AFRL-RH-WP-TR-2013-0078

Toxicity Evaluation of Engineered Nanomaterials (Phase I Studies)

Saber Hussain
Bioeffects Division
Molecular Bioeffects Branch

Nicole Schaeublin
Carol Garrett
Amanda Schrand
Monita Sharma
David Ellis
Henry M. Jackson Foundation
for the Advancement of Military Medicine
Wright-Patterson AFB OH

Christin Grabinski
Bradley Stacy
Jonathan Lin
ORISE

Michelle Kiyota
Catherine Kiyota
Air Force Academy

National Center for Toxicology Research
University of South Carolina
Wright State University
Jackson State University
University of Dayton
Collaborators

January 2012

Final Report for Jan 2009 – Dec 2011

Air Force Research Laboratory
711th Human Performance Wing
Human Effectiveness Directorate
Bioeffects Division
Molecular Bioeffects Branch

NOTICE PAGE

AFRL-RH-WP-TR-
2013-0078

THIS REPORT HAS BEEN REVIEWED AND IS APPROVED FOR PUBLICATION IN ACCORDANCE WITH ASSIGNED DISTRIBUTION STATEMENT.

_____
SABER HUSSAIN, Work Unit Manager
DAF Molecular Bioeffects Branch

_____
GARRETT   D.POLHAMUS,   Dr-IV,
Bioeffects Division
Human Effectiveness Directorate
711th Human Performance Wing
Air Force Research Laboratory

REPORT DOCUMENTATION PAGE

1. REPORT DATE *(DD-MM-YYYY)* 9-01-2012	2. REPORT TYPE Final Tech Report	3. DATES COVERED *(From - To)* 1-21-2009 to 12-31-2011

4. TITLE AND SUBTITLE
Toxicity Evaluation of Engineered Nanomaterials
(Phase I Studies)

5a. CONTRACT NUMBER

5b. GRANT NUMBER
NA

5c. PROGRAM ELEMENT NUMBER
62202F

6. AUTHOR(S)
Saber Hussain, Nicole Schaeublin, Carol Garrett, Amanda Schrand, Monita Sharma, David Ellis, Christin Grabinski, Bradley Stacy, Jonathan Lin , Michelle Kiyota, Catherine Kiyota

5d. PROJECT NUMBER
OAF

5e. TASK NUMBER
WP

5f. WORK UNIT NUMBER
OAFWP000

7. PERFORMING ORGANIZATION NAME(S) AND ADDRESS(ES)

711 HPW/RHDJ
2729 R Street
Wright-Patterson AFB OH 45433-5707

8. PERFORMING ORGANIZATION REPORT NUMBER

9. SPONSORING / MONITORING AGENCY NAME(S) AND ADDRESS(ES)
Air Force Materiel Command
Air Force Research Laboratory
711th Human Performance Wing
Human Effectiveness Directorate
Bioeffects Division
Molecular Bioeffects Branch
Wright-Patterson AFB OH 45433-5707

10. SPONSOR/MONITOR'S ACRONYM(S)
711 HPW/RHDJ

11. SPONSOR/MONITOR'S REPORT NUMBER(S)
AFRL-RH-WP-TR-2013-0078

12. DISTRIBUTION / AVAILABILITY STATEMENT

DISTRIBUTION A: Approved for public release; distribution unlimited. PA Case No. 88ABW-2013-4073

13. SUPPLEMENTARY NOTES

14. ABSTRACT
This project entitled "Toxicity Evaluation of Engineered Nanomaterials" focuses toward developing a fundamental understanding of the interaction of nanomaterials with biological molecules that can be exploited to predict the toxicological effects of engineered nanomaterials in relation to occupational human exposure. Nanoscale science is, by nature, an interdisciplinary venture with enormous implications and diverse DoD applications in areas such as medicine, energy, materials, communications, and electronics. The overarching goal of this effort was to develop a fundamental understanding of nanostructure-cellular interactions, and how these relationships are affected by nanostructure composition, size, and shape. The work focused on establishing the fundamental mechanisms of biological interactions of engineered nanomaterials, including toxicities arising from the physicochemical properties uniquely associated with nanoscale structures. This knowledge will not only help to improve nanomaterials' safety strategies for the protection of both human and environmental occupational health, but also help develop advanced nanobiotechnologies for both defense and civilian applications.

15. SUBJECT TERMS
Engineered Nanomaterials, toxicity, nanostructure-cellular interactions

16. SECURITY CLASSIFICATION OF:			17. LIMITATION OF ABSTRACT	18. NUMBER OF PAGES	19a. NAME OF RESPONSIBLE PERSON S. Hussain
a. REPORT U	b. ABSTRACT	c. THIS PAGE	SAR	158	19b. TELEPHONE NUMBER *(include area code)* NA

THIS PAGE INTENTIONALLY LEFT BLANK.

Table of Contents

List of Tables

List of Figures

Section I. Introduction

This project entitled "Toxicity Evaluation of Engineered Nanomaterials" focuses toward developing a fundamental understanding of the interaction of nanomaterials with biological molecules that can be exploited to predict the toxicological effects of engineered nanomaterials in relation to occupational human exposure. Dr. Saber Hussain served as the overall program manager as well as a Principal Investigator.

Nanoscale science is, by nature, an interdisciplinary venture with enormous implications and diverse DoD applications in areas such as medicine, energy, materials, communications, and electronics. The overarching goal of this effort was to develop a fundamental understanding of nanostructure-cellular interactions, and how these relationships are affected by nanostructure composition, size, and shape. The combined expertise of this research team, allowed an innovative and comprehensive approach to this important work. The work focused on establishing the fundamental mechanisms of biological interactions of engineered nanomaterials, including toxicities arising from the physicochemical properties uniquely associated with nanoscale structures. This knowledge will not only help to improve nanomaterials' safety strategies for the protection of both human and environmental occupational health, but also help develop advanced nanobiotechnologies for both defense and civilian applications.

Section II. Background

The composition, size, dimension, surface energy, and features of manufactured nanomaterials will have a significant effect on cellular structure and function. The effect of nanomaterials on structure and physiology of cells is expected to vary based on the nature of the nanomaterial, including size, surface area, physical and chemical characteristics. The surface energy properties of nanomaterials may contribute significantly to the generation of reactive oxygen species that are detrimental to living cells. The interaction of nanomaterials with cell membranes is likely to trigger signals through receptors that may result in oxidative stress in somatic and germline cells followed by apoptosis. As a result of the cellular responses induced by interactions with nanomaterials, there is a likely possibility for altered function at the level of tissue, organ, and organism. Therefore, there is a strong likelihood that biological interaction of nanomaterials depends primarily on physicochemical parameters that are usually not considered in toxicity studies with any other chemicals. The specific goals of the proposed research are to:

1.   Establish fundamental mechanism of interaction of nanomaterials with biological molecules and develop theoretical models to predict toxicity of engineered nanomaterials;

2.   Synthesize well-characterized nanomaterials with varied dimension and properties for toxicity assessment;

3.   Identify the exposure concentrations of nanomaterials that are lethal to specific cell types representing the lung, skin, liver and immune system, as well as the cellular effects generated post-exposure;

4.   Assess the cellular mechanisms generated from exposure to these nanoparticles at non-lethal doses, which is more representative of the occupational exposure;

5.   Assess the biocompatibility of nanomaterials based on toxicity data; and

6.   Establish the relationship between toxicity and size, morphology, and composition   of engineered nanomaterials.

A glossary of abbreviations used in this document is at Appendix I
A list of publications derived from this study is at Appendix II

Section III. Purpose
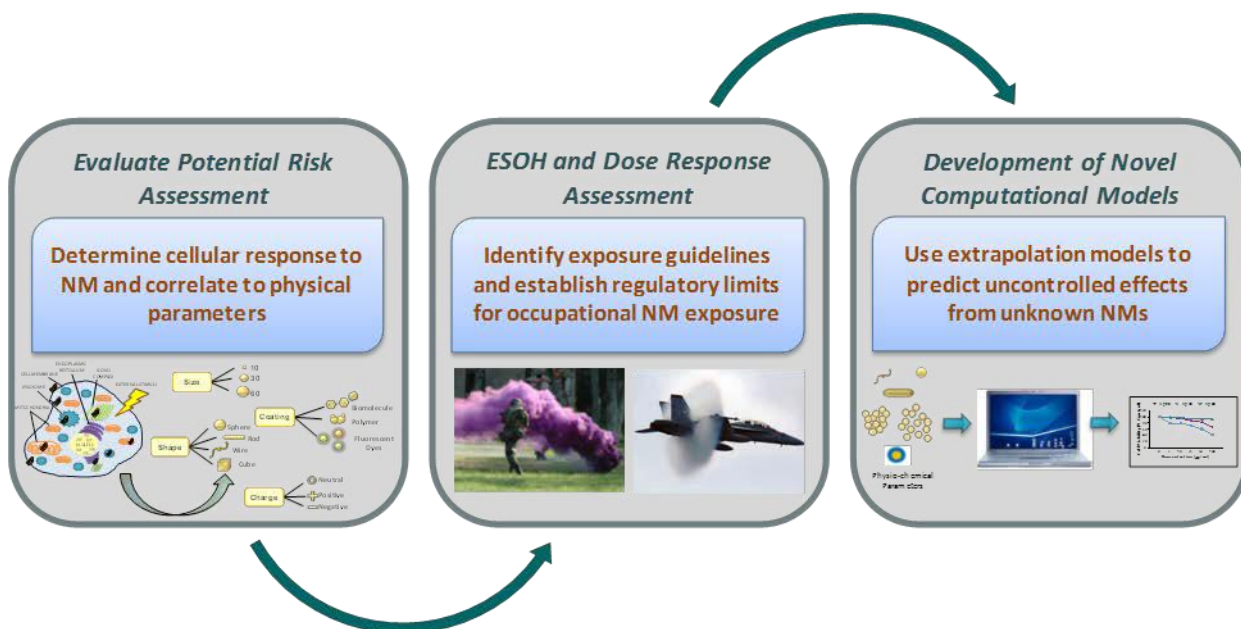
The purpose of this project was to establish dose-response relationships of the sized nanoparticles in biological systems using a tiered toxicological approach. This approach involves acellular, subcellular, and cellular systems. Biological or cytotoxic effects will be evaluated in relation to, i.e., NP number, NP surface, NP mass, and NP shape. The end points used will range from direct cytotoxicity (MTT, LDH, oxidative stress and apoptosis) to toxicogenomic and proteomic analyses. In addition, this project will

DISTRIBUTION A: Approved for public release; distribution unlimited. PA Case No. 88ABW-2013-4073

2

determine the efficacy of various surface coatings to enhance the biocompatibility and decrease toxicity of these materials. The physical and electromagnetic properties of NP were examined for their effect on the ability to bind specific cellular proteins, and alter cellular function. Studies were conducted on the kinetics of uptake and translocation in the cellular system by using electron microscopy and X-ray fluorescence microscopy to visualize nanoparticles.

Section IV. Studies

A. Gold Nanomaterials

1.   Evaluation of Gold Cytotoxicity Based on Shape
a. Purpose

Gold nanomaterials (AuNMs) have distinctive electronic and optical properties, making them ideal candidates for biological, medical, and defense applications. Therefore, it is imperative to evaluate the potential biological impact of AuNMs before employing them in any application. This study investigates two AuNMs with different aspect ratios (AR) on mediation of biological responses in the human keratinocyte cell line (HaCaT) to model potential skin exposure. The cellular responses were evaluated by cell viability, reactive oxygen species (ROS) generation, alteration in gene and protein expression, and inflammatory response. Gold nanospheres, nominally 20 nm in diameter and coated with mercaptopropane sulfonate (AuNS-MPS), formed agglomerates when dispersed in cell culture media, had a large fractal dimension ($D_f = 2.57 \pm 0.4$) (i.e., tightly bound and densely packed) and were found to be non-toxic even at the highest dose of 100 µg/mL. Highly uniform, 16.7 nm diameter and 43.8 nm long polyethylene glycol-capped gold nanorods (AuNR-PEG) also formed agglomerates when dispersed into the cell culture media. However, the agglomerates had a smaller fractal dimension ($D_f = 1.28 \pm 0.08$) (i.e., loosely bound) and were found to be cytotoxic to the HaCaT cells, with a significant decrease in cell viability occurring at 25 µg/mL and higher. Moreover, AuNR-PEG caused significant ROS production and up-regulated several genes involved in cellular stress and toxicity. These results, combined with increased levels of inflammatory and apoptotic proteins, demonstrated that the AuNR-PEG induced apoptosis. Exposure to AuNS-MPS, however, did not show any of the detrimental effects observed from the AuNR-PEG. Therefore, we conclude that shape appears to play a key role in mediating the cellular response to AuNMs.

b. Materials and Methods

Gold Nanoparticles

All glassware was cleaned in aqua regia and rinsed with copious amounts of deionized water prior to synthesis. Unless otherwise specified, all chemicals were ordered

from Sigma Aldrich (St. Louis, MO) and were of ACS reagent purity or higher and used as received. AuNSs (d_{core} ~ 20 nm) were synthesized through the citrate reduction of $HAuCl_4$ (i.e., the Turkevich method). Briefly, 68 mg of $HAuCl_4$ was dissolved in 400 mL of deionized water. Upon heating the solution to 100 °C, 400 mg sodium citrate hydrate (tribasic) dissolved in 20 mL deionized water was added to the reaction solution under vigorous stirring. The solution immediately turned from yellow to clear, to purple, and finally to wine red over the course of twenty min, at which time the reaction flask was removed from heat and cooled to room temperature. The solution was filtered through a clean 60 mL, medium porosity fritted funnel in order to remove any insoluble precipitates prior to further functionalization. This solution contained approximately 2.03×10^{-9} mol/L (M) AuNSs, calculated assuming total reaction of the gold precursor and the measured TEM diameter. The negatively charged citrate-stabilized AuNSs were functionalized through ligand exchange reactions employing MPS (also negative in charge) in a ratio of between 2:1 and 5:1 of the incoming thiol to the estimated number of available thiol "sites" on the nanoparticles in solution. The appropriate mass of thiol can be approximated using the estimated concentration of the AuNS solution, the total available surface area of the gold spheres, and the typical "footprint" of a thiol molecule on a gold surface (0.214 nm^2).[1] In this case, 2.5 mg MPS was added to the AuNS solution and stirred for 24 hr to allow completion of the ligand exchange reaction. The AuNSs were purified by 3 centrifugal wash cycles with deionized water. The morphologyof AuNS is shown in Figure 1b.
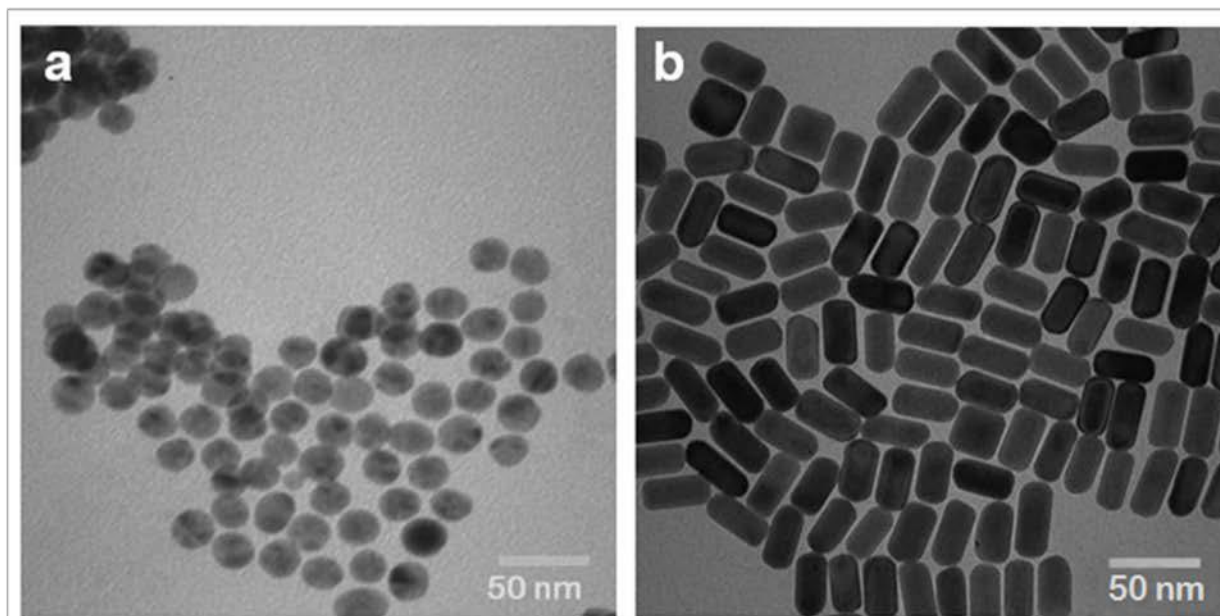
Figure 1 Morphology of Gold Nanomaterials (a-b) Representative bright field transmission electron microscope (BF-TEM) images of Au NMs taken at 120kV demonstrating rod and spherical morphologies (a) AuNS-MPS (b) AuNR-PEG

In order to synthesize AuNRs, briefly, the seed solution was made by adding a freshly prepared, ice-cold $NaBH_4$ solution (0.6 mL, 0.01 M) into a mixture solution composed of $HAuCl_4$ (0.025 mL, 0.1 M) and cetyltrimethyl-ammonium bromide (CTAB) (5 mL, 0.2 M). The growth solution was prepared separately by mixing $HAuCl_4$ (0.5 mL, 0.1 M), $AgNO_3$ (0.08 mL, 0.1 M), and CTAB (50 mL, 0.2 M) at room temperature. Next, ascorbic acid (0.55 mL, 0.1 M) was added to the growth solution as a mild reducing agent, followed by the seed solution (0.1 mL). The color of the growth solution slowly changed from clear to violet indicating the growth of AuNRs. The reaction condition stated above resulted in the AuNRs with aspect ratio of 2.6 (length: 43.8 nm, diameter: 16.7 nm) as shown in Figure 1b.

To prepare the AuNR-PEG, AuNR solution as made above containing CTAB (cationic) was centrifuged at 8000 g for 30 min, decanted, and resuspended in water to remove excess CTAB. Next, 100 µL of 1 mM thiol-functionalized PEG (PEG-SH) (approximate molecular weight 5000 g/mol) (neutral charge) was added to 10 mL of the 1 nM AuNR solution. The mixture was stirred for 24 h at room temperature. To ensure complete surface modification on the side as well as the end of the AuNRs, the excess PEG-SH was removed by centrifuge and the aforementioned procedure was repeated. Finally, excess PEG-SH was removed by multiple centrifugations.

Cell Culture

The Army Research Lab kindly provided the human keratinocyte cell line (HaCaT).[2] The cells were grown in a T-75 flask with RPMI-1640 media (ATCC, Manassas, VA), supplemented with 10 % (v/v) fetal bovine serum (FBS, ATCC) and 1 % (w/v) penicillin/streptomycin (Sigma, St. Louis, MO), and incubated at 37 °C in a humidified incubator with 5 % CO_2. For AuNM exposure procedures, media was supplemented with 1 % (w/v) penicillin/streptomycin but no serum.

Nanoparticle Characterization

To verify morphology and size, one drop of a 100 µg/mL solution was spotted on a formvar/carbon-coated TEM grid (EMS Diasum, Hatfield, PA) and allowed to dry. Once dried, the nanoparticles were viewed using a Philips/FEI CM200 TEM (Hillsboro, OR) at 120 kV.

Nanoparticle Characterization in Solution

In order to characterize nanoparticle size and zeta potential in solution dynamic light scattering (DLS) was performed on a Malvern Instruments Zetasizer Nano-ZS instrument according to the method described by Murdock et al.[3]

To perform static light scattering (SLS) measurements, AuNS-MPS and AuNR-PEG stock suspensions were diluted to obtain 25 mg/L concentrations in RPMI media in the presence of 1 % (w/v) streptomycin. Fractal dimension measurement was performed

using ALV-CGS/3 compact goniometer system (ALV-GmbH, Langen, Germany) equipped with a 22 mW He-Ne laser with a wavelength of 632.8 nm and coupled with an ALV/LSE-5004 digital auto correlator (ALV-GmbH, Langen, Germany). 2 mL of AuNM suspensions at 25 mg/L in media were added into pre-cleaned disposable borosilicate glass vials (Fisher Scientific, Pittsburg, PA). The rigorous cleaning procedure is described elsewhere.[4-6] This vial was kept in cell culture condition for 24 h (exposure time in toxicity analysis) to allow the particles to achieve a pseudo-equilibrium agglomerate structure. Scattered light intensity was measured at 37 °C by a photon counting module operating at 1.2 A and 5 V (Perkin Elmer, Dumberry, Canada) at scattering angles ranging from 12.5 ˚ to 100 ˚ maintaining 10 s time interval between consecutive readings. Triplicate measurements were performed for each scattering angle. The scattering intensity was plotted against scattering wave vector in a log-log plot. Fractal dimensions of the AuNM agglomerates were computed using the slope of the best-fit straight line using the method described elsewhere in the colloid literature.[7] The fractal dimension measurements were also replicated to confirm that results were reproducible.

Cellular Uptake of Gold Nanoparticles

HaCaT cells were processed for TEM according to Bozzola and Russell.[8] Briefly, the cells were seeded in six well plates at a density of 5×10^5 cells/well, allowed to grow overnight until ~90 % confluent and then treated with 25 µg/ml of the different shaped AuNMs. Twenty-four h later, the cells were removed from the plates via trypsin and centrifuged. The cell pellets were fixed in a mixture of 2 % (w/v) paraformaldehyde (EMS Diasum, Hatfield, PA) and 2.5 % (w/v) gluteraldehyde (EMS Diasum, Hatfield, PA) in phosphate buffered saline (PBS) for 2 h, then washed thoroughly with PBS to remove any residual aldehydes and subsequently stained with 1 % (w/v) osmium tetroxide (EMS Diasum, Hatfield, PA) for 1 h. After 3 additional PBS washes to remove any excess osmium, the cells were dehydrated using increasing concentrations of ethanol, with three final exchanges of 100 % ethanol. The samples then were placed in 100 % LR White resin (EMS Diasum, Hatfield, PA) and cured overnight at 60 °C in BEEM® capsules (EMS Diasum, Hatfield, PA) in a vacuum oven. The samples were thin-sectioned on a Leica ultramicrotome at a thickness of (50 to 100) nm, collected on formvar/carbon-coated TEM grids and imaged using a Philips/FEI CM200 TEM at 120 kV. Energy-dispersive x-ray (EDX) analysis was performed at various locations within the cells to confirm the presence of AuNMs with an EDAX system (Ametek, Mahwah, NJ). Controls consisted of cells not treated with nanoparticles for all experiments unless otherwise stated.

Mitochondrial Function

Mitochondrial function was assessed using the CellTiter 96 Aqueous One Solution Assay (Promega, Madison, WI). Cells were cultured in 96-well plates with 5×10^3 cells per well and allowed to grow at 37 °C with 5 % CO_2 for 24 h until ~80 %

confluent and then treated with AuNMs at concentrations of 0 to 100 µg/mL. After a 24 h exposure, mitochondrial function was assessed according to manufacturer's instructions and as described previously by Braydich-Stolle et al. [9] The plate was read on a SpectraMAX GeminiXS microplate reader at 490 nm to measure the absorbance. Each experiment was done in triplicate and the data are represented as the average of three independent trials ± one standard deviation.

Reactive Oxygen Species Generation

The generation of reactive oxygen species (ROS) was measured using the Image-iT Live Green Reactive Oxygen Species Detection Kit (Invitrogen, Carlsbad, CA). This kit uses a green fluorescent dye (carboxy-H_2DCFDA) to measure ROS generation in live cells. Additionally, the blue-fluorescent cell permanent nucleic acid stain, Hoechst, is used to visualize the nuclei. The cells were seeded with 5×10^3 cells per well in a 96- well black imaging plate (BD Biosciences, San Jose, CA) and allowed to grow overnight until ~80 % confluent. They then were exposed to 25 µg/mL of the AuNMs for 6 h. After 6 h, the media was removed and the cells were washed three times with PBS to eliminate any excess AuNMs that were not internalized or bound to the membrane. ROS production was induced in positive control cells by adding tert-butyl hydroperoxide (TBHP) for 90 min and incubating at 37 °C with 5 % CO_2. After 90 min, carboxy- H_2DCFDA solution was added to all cells and incubated at 37 °C with 5 % CO_2 in the dark for 30 min. After 25 min, Hoechst was added to all cells to stain the nuclei. After an additional 5 min incubation at 37 °C with 5 % CO_2 in the dark, the solution was removed; the cells were washed three times with PBS and imaged immediately on a BD Pathway435 confocal microscope (BD Biosciences, San Jose, CA). Each experiment was done in triplicate and the data are represented as the average of three independent trials ± one standard deviation.

Mitochondrial Membrane Potential (MMP)

Mitochondrial membrane potential was evaluated using the MitE-ψ Mitochondrial Permeability Detection Kit from BIOMOL (Plymouth Meeting, PA). This kit uses the cationic dye JC-1 to detect the depolarization of the mitochondrial membrane potential that occurs in apoptotic cells. The dye enters healthy mitochondria, aggregates and fluoresces red. When the mitochondria collapses, as in apoptotic cells, the dye becomes dispersed throughout the cell, assumes its monomeric form and fluoresces green, making it easy to distinguish between the red (non-apoptotic) cells and the green (apoptotic) cells. Additionally, Hoechst (Invitrogen, Carlsbad, CA) was added to MitE-ψ solution (1:1000 dilution) to visualize the nucleus. The cells were seeded as described above (ROS assay) in a 96-well black imaging plate, allowed to grow overnight until ~80 % confluent and exposed to 25 µg/ml of the AuNMs for 6 h. After 6 h, the media was removed and the cells were washed three times with PBS to eliminate any excess NMs that were not internalized or bound to the membrane. Next, the cells were incubated with the MitE-ψ solution for 15 min at 37 °C with 5 % CO_2. The solution was removed, the cells washed twice with PBS and imaged on a BD

DISTRIBUTION A: Approved for public release; distribution unlimited. PA Case No. 88ABW-2013-4073

7

Pathway435 confocal microscope (BD Biosciences, San Jose, CA). Each experiment was done in triplicate and the data are represented as the average of three independent trials ± one standard deviation.

Nanomaterial Solution Purity

The purity of the nanomaterial stock solutions was evaluated using Image-iT Live Green Reactive Oxygen Species Detection Kit (Invitrogen, Carlsbad, CA). The AuNS-MPS and AuNR-PEG nanomaterial solutions (in serum free media) were spun down at 12,000 × g for 30 min. After 30 min, the supernatant was removed and re-centrifuged for an additional 30 min to ensure all traces of the nanomaterials were removed from the solution. The remaining supernatant was used to treat the cells. The ROS assay was performed as described above except Hoechst was not added to stain the nucleus and the plate was read on a SpectraMAX GeminiXS microplate reader (Molecular Devices, Sunnyvale, CA) at 485 nm excitation wavelength and a 530 nm emission wavelength using the well scan setting of the instrument. Each experiment was done in triplicate and the data are represented as the average of three independent trials ± one standard deviation.

Annexin V Protein Binding

Annexin V protein binding was evaluated using the Apoptosis and Necrosis detection kit from Enzo Life Sciences. This kit utilizes an Annexin V-Enzo Gold conjugate that fluoresces green to detect cells in the early stages of apoptosis. The cells were seeded as described above in a 96-well black imaging plate (ROS assay), allowed to grow overnight until ~80 % confluent and exposed to 25 µg/ml of the AuNMs for 6 h. Additionally, 2µM staurosporine was added to the positive control wells for 4 h to induce apoptosis. After 6 h, they were incubated with the detection solution for 15 min at 37 °C with 5 % CO_2. The solution then was removed and the cells were washed twice with PBS and imaged on a BD Pathway435 confocal microscope (BD Biosciences, San Jose, CA). Each experiment was done in triplicate and the data are represented as the average of three independent trials ± one standard deviation.

Real Time PCR

The cells were plated in 6-well plates at 3×10^5 cells per plate and allowed to grow overnight until ~80 % confluent. The cells then were dosed with 25 µg/ml of the Au NMs and allowed to incubate for another 24 h. The RNA was isolated (RNeasy Mini Kit, Qiagen, Valencia, CA) and used in subsequent PCR reactions to assess cell stress and toxicity following manufacturer's instructions. The RNA was processed using SA Biosciences reagents (Frederick, MD) and the human stress and toxicity arrays (SA Biosciences) were run according to manufacturer's protocols. The data then was analyzed using SA Biosciences software. The data are represented as the average of three independent experiments ± the standard deviation, and gene changes were only reported if $p < 0.05$.

Expression of Caspase 1 and PCNA

The cells were seeded as described above in a 96-well black imaging plate, allowed to grow overnight until ~80 % confluent and exposed to 25 µg/ml of the AuNMs for 24 h. After exposure, the cells were fixed in 4 % (w/v) paraformaldehyde and immunostained with a caspase-1 or PCNA primary antibody (Santa Cruz Biotechnology, Santa Cruz, CA) and an AlexaFluor® 488 or 647 secondary antibody (Invitrogen, Carlsbad, CA) according to manufacturer's protocol. The nuclei also were stained with Hoechst (1:1000 dilution) (Invitrogen, Carlsbad, CA). The slides were visualized on a BD Pathway435 confocal microscope (BD Biosciences, San Jose, CA). Each experiment was done in triplicate and the data are represented as the average of three independent trials ± one standard deviation.

IL-18 Expression

Protein expression was examined using the IL-18 ELISA assay (Invitrogen, Carlsbad, CA). The cells were plated in 6-well plates at 3×10^5 cells per plate and allowed to grow overnight until ~80% confluent. The cells then were dosed with 25 µg/ml of the AuNMs and allowed to incubate for another 6 h. After 6 h, the media was collected and analyzed for protein following the manufacturer's instructions. The plate was read on a SpectraMAX GeminiXS microplate reader (Molecular Devices, Sunnyvale, CA) at 450 nm to measure the absorbance. Each experiment was done in triplicate and the data are represented as the average of three independent trials ± one standard deviation.

Image Acquisition and Data Analysis

For the endpoint assays, 16 fields in each well were imaged at 20X using the 4X4 montage option in the BD Pathway 435 software. The ROS assay and the PCNA antibody staining used the FITC and Hoechst filters, the MitE-ψ assay kit and the Apoptosis/Necrosis kit used the Rhodamine, FITC, and Hoechst filters, and the Caspase 1 antibody staining used the Rhodamine and Hoechst filters. Once the images were obtained, the confocal software allowed for segmenting the cells to measure only the fluorescent intensity within the designated portion. The images then were analyzed using the BD AttoVision™ v1.6 and the BD Image Data Explorer (BD Biosciences, San Jose, CA), which evaluated differences in fluorescent intensity between the samples. Each experiment was done in triplicate and the data are represented as the average of three independent trials ± one standard deviation.

Statistical Analysis

Each experiment was done in triplicate and the data are represented as the average of three independent trials ± one standard deviation. A two-way ANOVA was performed in GraphPad Prism to determine statistically significant differences in comparison to control values ($p < 0.05$).

c. Results and Discussion

Nanoparticle Characterization

Transmission electron microscopy (TEM) showed uniform, spherical AuNSs with a mean diameter and one standard deviation about the mean of 20 ± 4.6 nm, and AuNRs with 16.7 ± 4.3 nm x 43.8 ± 5.8 nm average dimensions yielding an aspect ratio of 2 based on no less than 100 particles (Table 1 and Figure 1). Additional characterization of the AuNS-MPS, including surface chemical analysis confirming MPS coating, has been reported elsewhere[10] and is considered relevant as the AuNS-MPS for this study were from the same batch. Dynamic light scattering (DLS) was performed to determine the agglomeration of the nanomaterials in water and in serum-free media (Table 1). Serum-free media was chosen in an attempt to keep as many parameters constant between the two AuNMs so that shape could accurately be assessed. Research has shown that the elevated amounts of protein found in serum can cause unwanted nanoparticle agglomeration due to the adsorption of serum proteins onto the surface of the nanoparticles.[11-13] The proteins on the nanoparticle surface are referred to as the protein corona, and are heavily dependent on nanoparticle size, surface and concentration.[12-13] The displacement of surface molecules with the protein corona causes a destabilization of the nanoparticle surface and results in an altered agglomeration state.[11] Changes in agglomeration then can lead to differences in nanoparticle uptake and cellular effects[14-20] and consequently masking possible shape outcomes. The DLS showed a highly stable colloidal suspension with no agglomeration of the gold nanorods and spheres in deionized water with average hydrodynamic diameters of 29.9 ± 0.4 nm for the AuNS-MPS and 17.2 ± 1.1 nm for AuNR-PEG, the mean and one standard deviation of three replicate measurements. Note the TEM standard deviation represents the width of the size distribution, while the DLS standard deviation represents the repeatability or precision of the measurements.[21] However, a considerable amount of agglomeration was observed in media as the particle size increased steadily to 514 nm for AuNS-MPS and 480 nm for AuNR-PEG. This agglomeration was caused by the high concentration of electrolytes in the media that effectively screened the electrostatic interaction between the gold nanomaterials and resulted in decreased colloidal stability.[20, 22-25] The agglomerate structure of the spheres and rods as determined by static light scattering (SLS) showed fractal dimension (D_f) of 2.57 ± 0.4 for the AuNS-MPS and 1.28 ± 0.08 for the AuNR-PEG (Table 2), the mean, and one standard deviation about the mean of three replicate measurements. The lower fractal dimension for the AuNR-PEG indicates that the agglomerates formed in media are loosely bound compared to more densely formed agglomerates in the case of AuNS-MPS, and the D_f of 2.57 suggests diffusion limited colloidal agglomeration was driving the formation of the AuNS-MPS

agglomerates.[26] This difference in the compactness of the agglomerates can have significant effect on particle suspension behavior and thereby their potential interaction with biological systems; this will be discussed in the subsequent section.

Zeta (ζ) potential measurements for AuNMs in water and media showed that AuNS- MPS acquired significantly higher negative electrostatic potential (-45.6 ± 1.6 mV in water and -19.2 ± 1.7 mV in media) compared to AuNR-PEG (-13.4 ± 1.1 mV in water and -7.31 ± 0.6 mV in media). In general, solutions with a ζ potential of < -30 mV or > +30 mV are considered to be electrostatically stable, meaning particles present in suspension will stay uniformly dispersed due to significant electrostatic repulsion.[27] However, a decrease in the magnitude of the ζ potential (i.e., lower than 30 mV in magnitude) caused by electrostatic screening in presence of salt reduces electrostatic barriers and results in agglomeration.[26, 4,5,28] The findings in this study are consistent with classical colloid literature, as AuNS-MPS were found to be relatively less stable compared to its counterpart AuNR-PEG NMs (Table 1) when introduced into cell culture media. The initial colloidal stability of the AuNS-MPS is primarily due to higher electrostatic repulsion emanating from the higher ζ potential in deionized (DI) water. The charged species in the cell culture media screened the surface charges of the AuNMs, and thereby caused agglomeration that is reflected in the ζ potential and DLS results (Table 1). However, the role of the surface coating also contributes. AuNR-PEG are more stable in both DI water and cell culture media due to the steric repulsion of the bulky PEG coating on the AuNR surface. Thus, the nature of the surface coating molecule impacts how tightly bound the agglomerated structures are. Additionally, as the question of dosimetry has recently come to light, the surface area and volume of a single rod and a single sphere was calculated, assuming perfect spherical or capped cylindrical geometries and a homogenous size distribution of only the mean values measured by TEM. The AuNS-MPS had a volume of 4.2×10^3 nm^3 and a surface area of 1.3×10^3 nm^2, while the AuNR-PEG had a volume of 8.4×10^3 nm^3 and a surface area of 2.3×10^3 nm^2. In both cases, the AuNR-PEG had a larger volume and surface area than the AuNS-MPS.

Table 1 Characterization of Gold Nanomaterials

Nanomaterial	Diameter Size (nm)	Length (nm)	Aspect Ratio	Particle Volume (nm³)	Particle Surface Area (nm²)	Capping Molecule	Z-Average Particle Diameter (nm)		Zeta Potential (mV)	
							Dispersed in Water	Dispersed in Serum Free Media	Dispersed in Water	Dispersed in Serum Free Media
Au Spheres (AuNS-MPS)	20 ± 4.6	***	***	4.2×10^3	1.3×10^3	MPS	29.9 ± 0.4	514.0	- 45.6 ± 1.6	-19.2 ± 1.7
Au Rods (AuNR-PEG)	16.7 ± 4.3	43.8 ± 5.8	2.6	8.4×10^3	2.3×10^3	PEG-SH	17.2 ± 1.1	479.7	-13.4 ± 1.1	-7.31 ± 0.6

Table 2 Characterization of Nanomaterial Agglomerates

Nanomaterial	Primary Particle Size (nm)	Particle Size in Media (nm)	Fractal Dimension	Agglomerate Shape
AuNS-MPS	20 ± 4.6	514.0	2.57 ± 0.4	Densely Packed
AuNR-PEG	16.7 ± 4.3	479.7	1.28 ± 0.1	Loosely Packed

Nanomaterial Uptake and Localization

TEM was performed to ascertain the internalization and localization of the AuNMs, and energy-dispersive x-ray (EDX) analysis was done to confirm the presence of Au. Representative TEM images verified internalization of all AuNMs into the cells after 24 h and agglomerates of the AuNS-MPS were found in cytoplasmic vacuoles located near the cell membrane (Figure 2a-c). EDX identified the elemental composition of the agglomerates as Au in specific places within the cell as compared to no presence of Au signal in control cells (Figure 2d). The cells also contained a background signal from the copper (Cu) TEM grid.

The TEM images demonstrated different amounts of material internalization in the cells. The AuNS-MPS appeared to be readily internalized, as shown by the large cluster of particles in a vacuole (Figure 2b) compared to a few individualized rods seen in the cells treated with AuNR-PEG (Figure 2c). It was recently shown that larger and positively charged NMs (both metallic and non-metallic) may penetrate cells in greater numbers and that spherical particles are taken up to a much higher extent than rods.[29-32] In addition, reports in the literature have revealed that exchange of PEG on the surface of nanorods reduces the interaction of particles with cells and leads to reduced uptake.[34-37] However, this limitation can be surmounted by using a lower molecular weight PEG.[38-40] The denser, longer chain length of the PEG$_{5000}$ used to functionalize the AuNR in this study could account for the low amount of AuNR-PEG in the cells. Furthermore, the lower fractal dimension, i.e., less-dense agglomerates or more-loosely-bound structure of the AuNR-PEG, also helps in speculating to the origins of the presence of individual AuNRs within the cells compared to larger clusters. The loosely bound nature of the agglomerates, likely a function of surface coating differences, most likely induced individual rod internalization of weakly bound AuNRs from the agglomerates, highlighting how surface coating, agglomeration state, and cellular uptake are inherently entangled parameters. Nevertheless, despite the lower uptake of the AuNR-PEG, any differences in cellular response between the two AuNMs used in this study should not be discounted as several recent studies have shown that NM uptake is not necessary to induce cellular effects.[41,42]
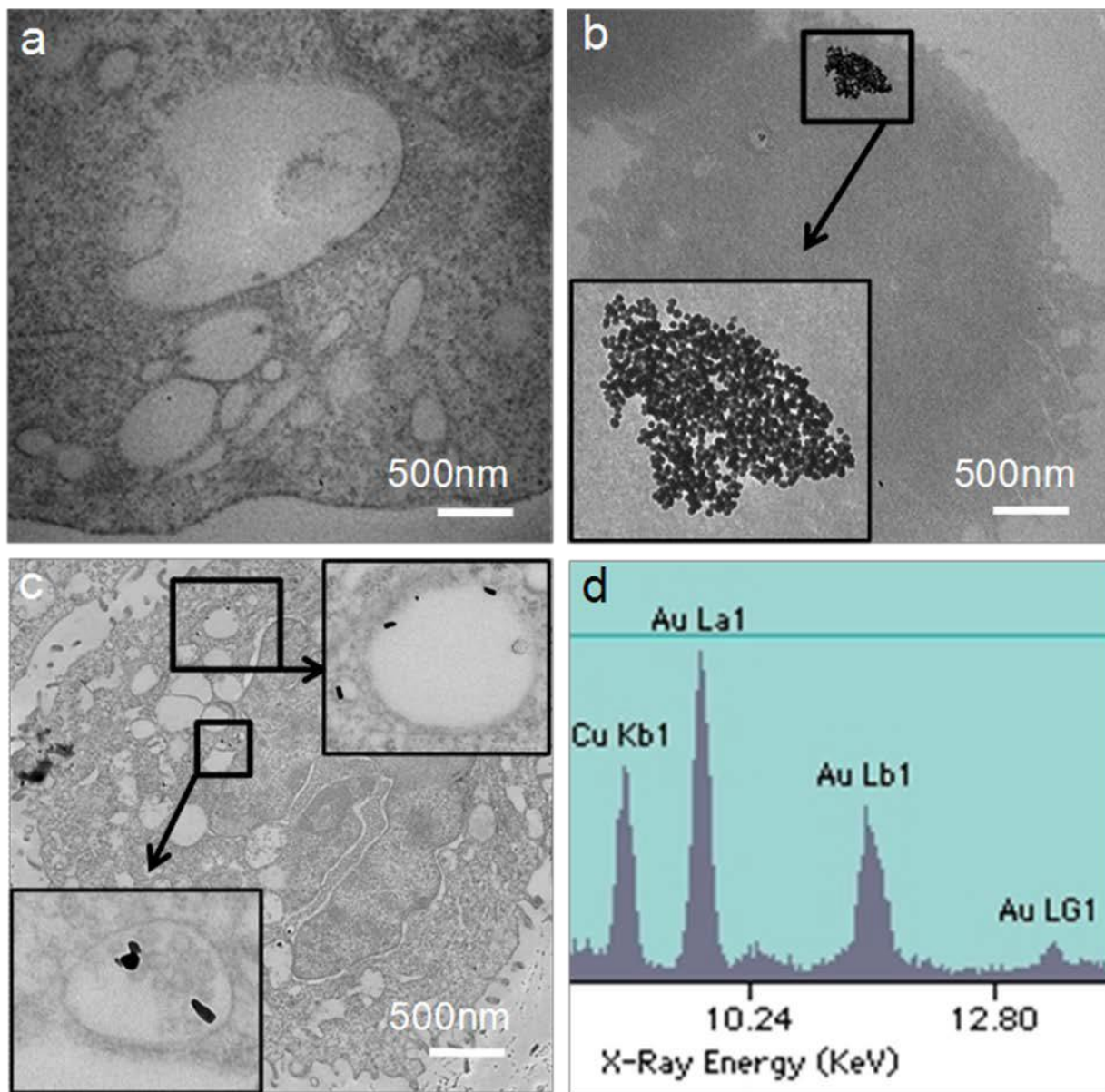
Figure 2 Gold Nanomaterial Uptake (a-c) Bright field transmission electron microscope (BF-TEM) images of Au NMs in human skin cells. (a) Control cells, no NMs (b) AuNS-MPS (c) Au NR-PEG (d) Energy-dispersive x-ray (EDX) spectra for localized elemental detection inside cells treated with AuNS-MPS.

Evaluation of Cellular Toxicity

The MTS assay was performed to determine the effect of the AuNMs on human keratinocyte mitochondrial function. The 24 h exposure results demonstrated a difference in the toxicity of the cells treated with the AuNR-PEG as compared to untreated control cells (Figure 3). The agglomerated AuNR-PEG caused a significant reduction in cell viability (down to 66 %) at 25 µg/mL whereas, after treatment with the

AuNS-MPS, no reduction in cell viability occurred, even at the highest dose of 100 µg/mL. These results were in contrast to Niidome et al.[43] and Grabinski et al.,[44] both of whom found that replacing the CTAB on the surface of the AuNR with PEG reduced the cytotoxicity.[43,44] However, the AuNRs used in both studies had much higher aspect ratios (5.9 and 3.5, respectively) and the authors did not provide data on the agglomeration patterns, therefore this could account for the discrepancy in cytotoxicity.
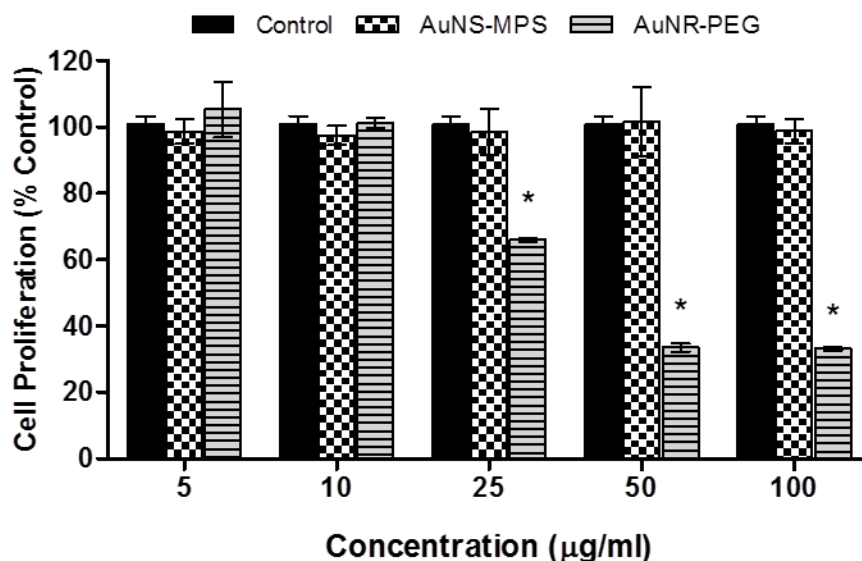
Figure 3 Cell Proliferation Following a 24 h Exposure to Gold Nanomaterials. The AuNS-MPS did not affect cell proliferation and demonstrated growth levels comparable to untreated control cells as high as 100 µg/ml. The AuNR-PEG initially did not demonstrate toxicity at low concentrations, but began to inhibit cell proliferation at 25 µg/ml. (*Denotes significance in comparison to control values p<0.05).
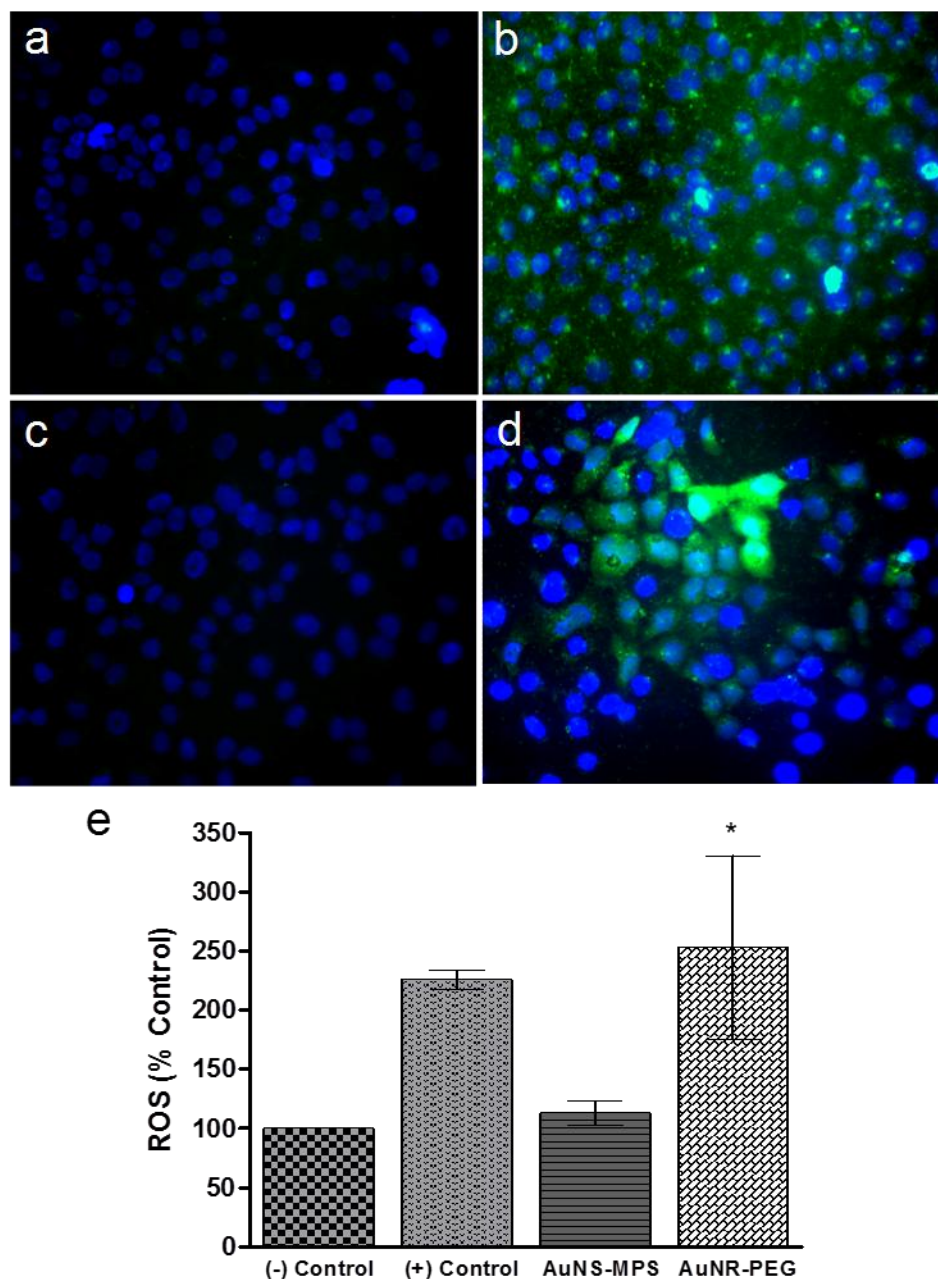
Figure 4 Generation of Reactive Oxygen Species Following Gold Nanomaterial Exposure (a) Negative Control (untreated cells) (b) Positive Control (Tert-butyl hydroperoxide) (c) AuNS-MPS (d) AuNR-PEG. The AuNS-MPS did not generate significant amounts of ROS while the AuNR-PEG displayed increased ROS when compared to the positive control. (e) Graph depicting the data shown in the images (*Denotes significance in comparison to negative (untreated) control values p<0.05).

Mitochondrial Stress

It is known that treatment with nanomaterials and other sources of cell stress can cause cells to generate reactive oxygen species (ROS).[45] Generation of ROS was therefore evaluated to determine if the AuNMs induced oxidative stress based on their shape. The ROS and remainder of the experiments were conducted with a dose of 25 µg/mL AuNMs (as toxicity began at this dose with the AuNR-PEG). It should be noted that the 50 µg/mL and 100 µg/mL doses were not tested due the high level of toxicity at these concentrations. As only ~30% of the cells were viable, it is unlikely that there would be a difference in the amount of ROS produced or change in MMP because the majority of the cells are dead.[46-48] The AuNR-PEG caused a significant amount of ROS to be formed, whereas AuNS-MPS did not (Figure 4). Since the production of ROS has been shown to disrupt the mitochondrial membrane potential (MMP) and indicate apoptosis,[49] the impact of AuNMs exposure on the MMP was examined. The MMP results corroborate the ROS results, as treatment with the AuNR-PEG triggered a significant disruption in the mitochondrial membrane potential while the AuNS-MPS left the membrane intact (Figure 5). Consequently, the ROS generated from the AuNR-PEG caused the depolarization of the mitochondrial membrane. When considered together, the results of the ROS and MMP assays strengthen the conclusion that the shape i.e., aspect ratio of the AuNM plays a key role in cellular toxicity with AuNR-PEG causing significantly higher stress to the cells.
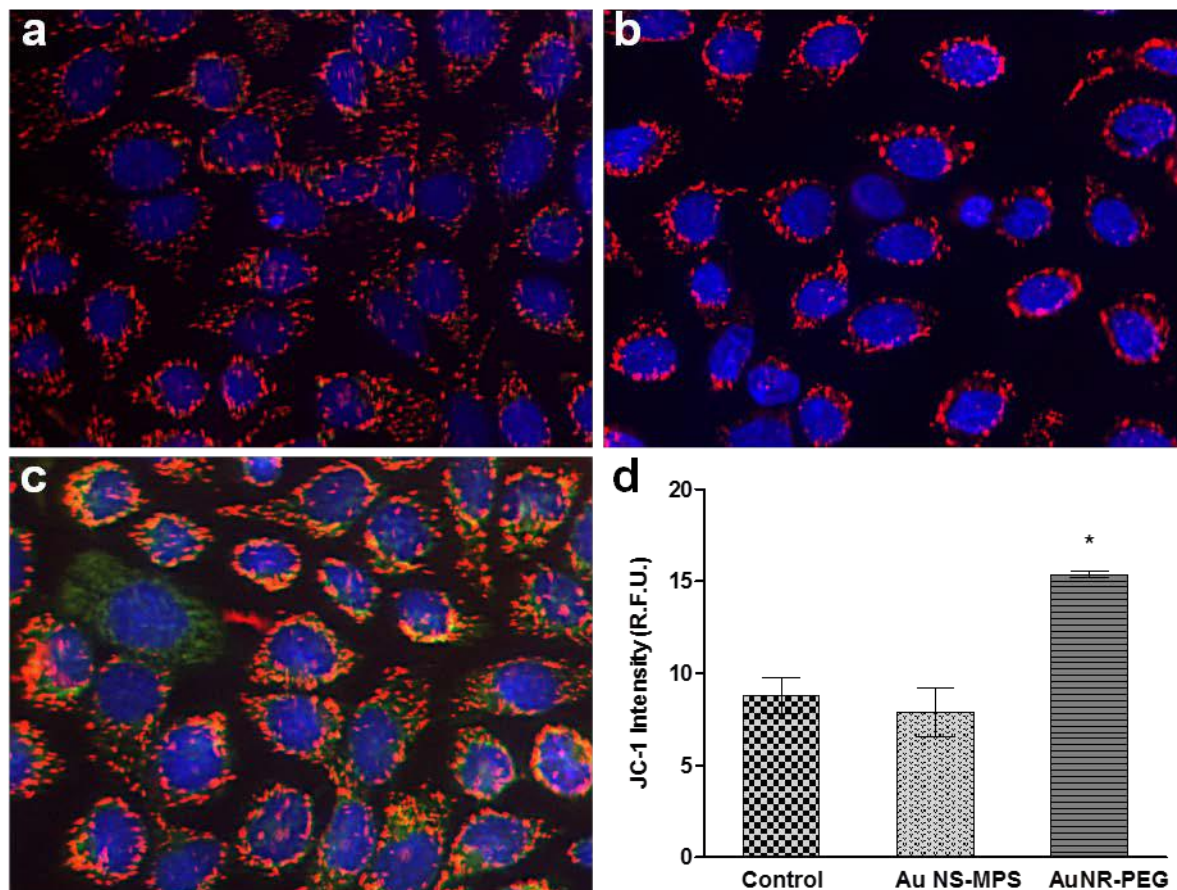
Figure 5 Evaluation of Mitochondrial Membrane Potential Following Gold Nanomaterial Exposure. This assay uses JC-1, which enters healthy mitochondria, aggregates and fluoresces red. Upon disruption of the mitochondrial membrane, the dye becomes dispersed throughout the cell and fluoresces green, indicating apoptotic cells. (a) Control Cells (untreated) (b) AuNS-MPS (c) AuNR-PEG. There was significant amount of MMP lost after exposure to the AuNR-PEG (d) Graph depicting the data shown in the images (*Denotes significance in comparison to control values p<0.05).

Nanomaterial Solution Purity and Surface Chemistry Control

Although several studies have shown that both MPS and PEG are biocompatible, in order to ensure that there were no residual impurities in the samples (MPS, PEG or CTAB), AuNMs were removed via centrifugation and cells were treated with the remaining media to ascertain toxic effects. The media from both the AuNR and AuNS stock did not generate the formation of reactive oxygen species (ROS), indicating that any changes in behavior of the cells would be linked to the AuNM morphology and not chemistry response to the molecules on the AuNM surface, whether still bound or dissociated (Figure 6a). Additionally, cellular viability was assessed on cells treated with 12 nm AuNS-PEG to further verify that the different surface chemistries were not contributing to any changes in cellular response. The results demonstrated no decrease in cellular viability after treatment with the AuNS-PEG (Figure 6b). Therefore, we can

confidently conclude that the different surface molecules coating the AuNM are not dissociating nor mediating the biological response.
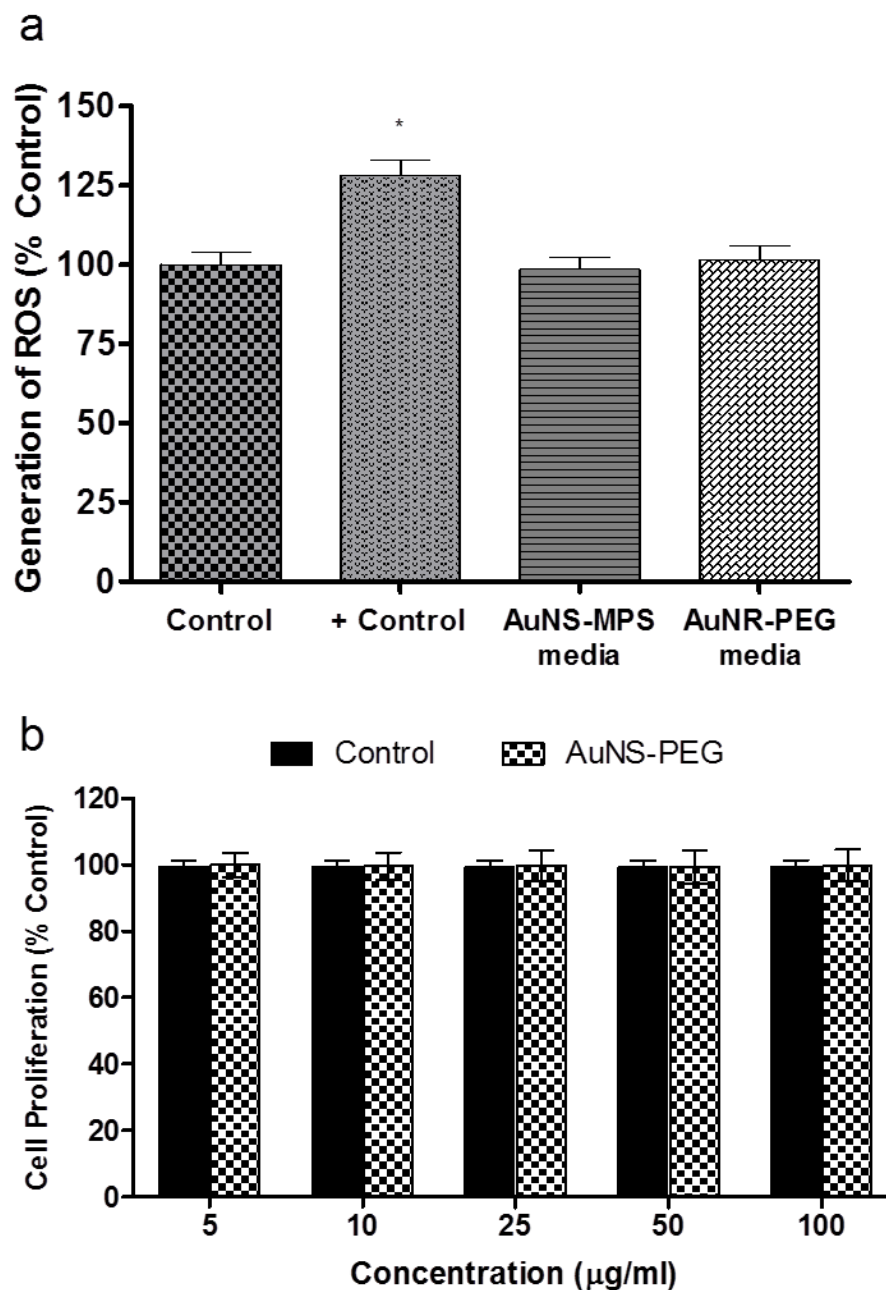
Figure 6 Assessment of Gold Nanomaterial Solution Purity and Surface Chemistry Toxicity. (a) ROS Generation of AuNM solution. Both the AuNS-MPS and AuNR-PEG solutions did not generate ROS as compared to the controls. (*Denotes significance in comparison to negative control values p<0.05) (b) Cellular Proliferation following a 24 h treatment with 12 nm AuNS-PEG. The AuNS-PEG did not cause a decrease in cellular proliferation and exhibited growth levels comparable to control cells as high as 100 µg/ml.

Evaluation of Changes in Gene Expression

The generation of ROS in small amounts is a common occurrence in cells and is easily neutralized by the cells antioxidant defenses, which include production of glutathione and antioxidant enzymes.[50] However, when significant amounts are generated, i.e. after treatment with NMs, an inflammatory response is triggered. If the inflammatory response, which is initiated through the activation of pro-inflammatory signaling cascades such as MAPK and NFkB, is unable to fix and repair the damage done by the ROS, then apoptotic factors (i.e. caspases) are released and cell death results.[50]

Upon exposure to the AuNR-PEG, the skin cells demonstrated considerable up-regulation of genes involved in cellular damage and stress (Table 3). Typically, GADD45A is transcribed following exposure to agents that can cause DNA damage, and the expression of this gene was up-regulated 184 fold by the AuNR-PEG. Similarly, the PCNA gene, which is known to interact with GADD45A and is involved in DNA synthesis and repair, was up-regulated 9 fold. RAD23A is also important in DNA damage repair and was up-regulated 400 fold. The increase in expression of these three genes suggested that the AuNR-PEG were damaging the cells, with the production of ROS most likely causing DNA damage. Additionally, the TNFSF10 gene, an activator of the extrinsic apoptotic pathway by acting as a ligand and binding cell death receptors was up-regulated ~4500 fold. The observed up-regulation suggested that apoptosis was initiated by these cells. This was further confirmed by the increase in expression of CASP8, which is a target for TNFSF10. Additionally, ANXA5, CASP1, and EGR1, whose expression is also associated with apoptosis, demonstrated an increase in gene expression (~20 fold). One function of CASP1 is to induce expression of certain pro-inflammatory cytokines such as IL-18 and IL-1β and both of these were significantly up-regulated by the AuNR-PEG (106 fold and 21 fold, respectively). Other inflammatory genes such as IL-1α and HSPA2 also were up-regulated showing that the AuNR-PEG triggered an immune response in the cells. In contrast, the AuNS-MPS demonstrated very little change in gene expression with the down-regulation of HSP90AB1 and SERPINE1, which are both responsible for inflammation. These results are not surprising as colloidal gold is widely used in the treatment of arthritic inflammation.[51]The evidence collected thus far demonstrated that the AuNR-PEG caused irreparable damage to the cells and initiated an immune response, which inevitably lead to cell death via the apoptotic pathway. These results are in contrast to those seen by Grabinski et al.[44] who found that AuNR-PEG (AR 3.5) caused down-regulation of genes involved in apoptosis, growth arrest, and cellular damage. However, as stated earlier, the AR is larger for these particles which could have an effect on the mechanism of uptake and consequently on cellular response.

DISTRIBUTION A: Approved for public release; distribution unlimited. PA Case No. 88ABW-2013-4073

19

Table 3 Changes in Gene Expression Following Treatment with Gold Nanomaterials

Nanomaterial	Gene	Function	Fold Regulation
AuNR-PEG	GADD45A	DNA Damage and Repair	184.57
	PCNA		9.2
	RAD23A		402.08
	TNFSF10	Activator of Immune Response and Apoptosis	4486.37
	HSPA2	Inflammation	78.87
	IL18		106.01
	IL1A		17.48
	IL1B		21.58
	ANXA5	Apoptosis	19.45
	CASP1		21.63
	CASP8		16.62
	EGR1		19.27
AuNS-MPS	HSP90AB1	Inflammation	-10.24
	SERPINE1		-2.91

Protein Expression Studies

In order to verify whether AuNR-PEGs were causing cell death by means of apoptosis (as suggested by the real-time PCR data); protein expression was evaluated for several of the genes with increased expression. An ELISA assay was performed to evaluate the protein level of interleukin 18 (IL-18), an inflammatory cytokine. Results of the ELISA revealed a significant amount of IL-18 protein expression after a 3 h exposure to the AuNR-PEG, but not to the AuNS-MPS as compared to control cells (Figure 7).

Additionally, immunofluorescence was performed to evaluate caspase 1 and PCNA protein expression (Figure 8). Caspase 1 is an enzyme that cleaves proteins, including IL-1β and IL-18, into active mature peptides, activates the inflammatory process and induces apoptosis. The caspase 1 assay revealed no protein expression in the control or the AuNS-MPS treated cells (Figure 8 a, b). Protein expression was, however found in the nucleus and the cytoplasm of the cells treated with AuNR-PEG (Figure 8 c). The PCNA protein is a cofactor of DNA polymerase delta, known to be found in small amounts in the nucleus of healthy, proliferating cells with a primary function of DNA replication and repair. Upon DNA damage, the protein is ubiquitinated and shuttled into the cytoplasm to facilitate RAD6-dependent DNA repair. Minimal PCNA expression was found in the nuclei of the control and AuNS-MPS treated cells signified that these cells were healthy and proliferating (Figure 8 d, e). However, there was a significant amount of PCNA found in the nuclei and cytoplasm of the cells treated with AuNR-PEG, suggestive of cell damage and repair (Figure 8 f). These data

DISTRIBUTION A: Approved for public release; distribution unlimited. PA Case No. 88ABW-2013-4073

20

correlate to the up- regulation of the CASP1 and PCNA genes in the real-time PCR studies and indicate that AuNR-PEG caused significant and irreparable damage to the cells while the AuNS- MPS did not. This lends further support to our hypothesis that the shape of the AuNMs is a major factor in mitigating the cellular response to the nanomaterials.
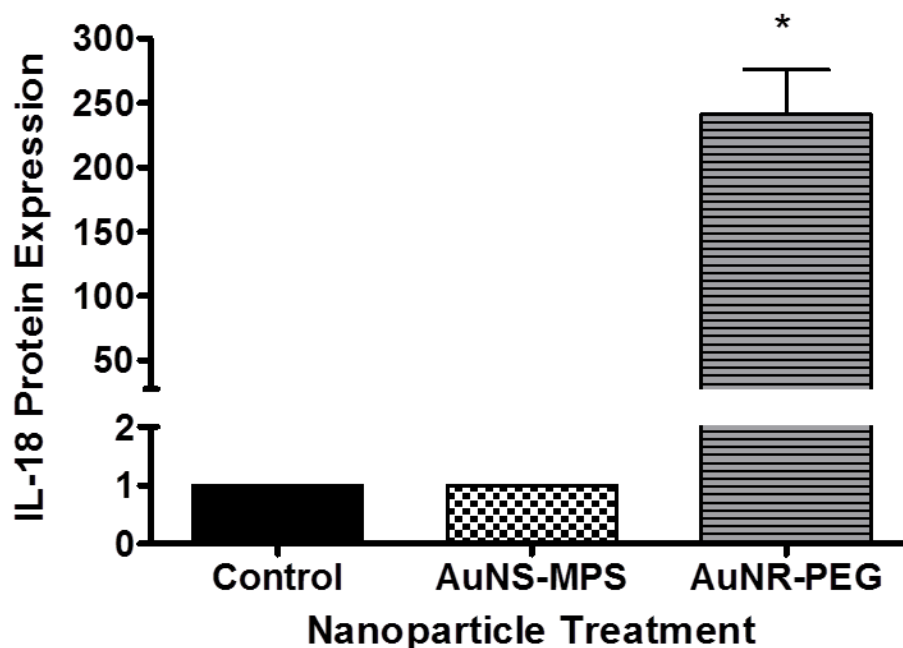
Figure 7 IL-18 Protein Expression after 6h Gold Nanomaterial Exposure. A significant amount of IL-18 protein was expressed after the cells were exposed to the AuNR-PEG but not the AuNS-MPS as compared to control cells. Data normalized to 1 for graphing purposes.
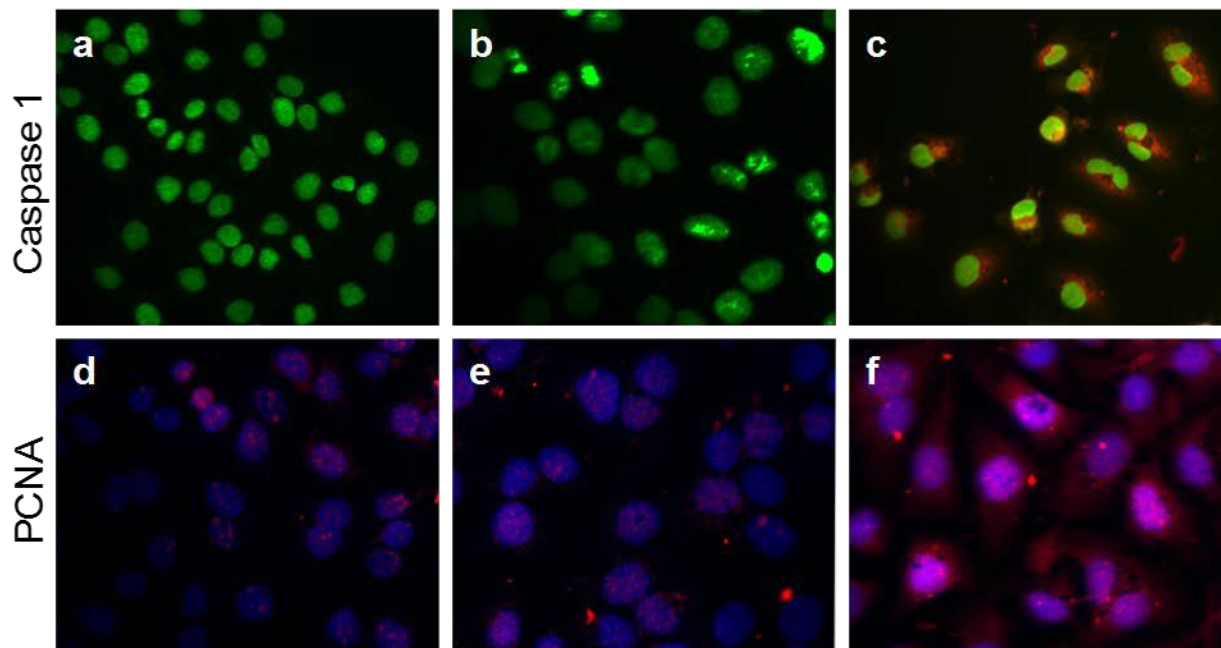
Figure 8 Caspase 1 and PCNA Protein Expression after Gold Nanomaterial Exposure. (a-c) Caspase 1 protein expression after 24 h exposure to Au NMs (a) Control cells, no nanomaterials (b) AuNS-MPS (c) AuNR-PEG. There is no caspase 1 expression in the control or the AuNS-MPS treated cells, however caspase 1 expression is found in the nucleus and the cytoplasm of the cells treated with AuNR-PEG (d-f) PCNA protein expression after 24 h exposure to Au NMs. (d) Control cells, no nanomaterials (e) AuNS-MPS (f) AuNR-PEG. There was minimal PCNA expression found in the nuclei of the control and AuNS-MPS treated cells, which signified that these cells were healthy and proliferating. However, there was a significant amount of PCNA found in the nuclei and the cytoplasm of the cells treated with AuNR-PEG.

Mechanism of Death Study

To verify that apoptosis was the mechanism of death for the cells exposed to the AuNR- PEG, annexin V protein expression was also evaluated (Figure 9). In healthy cells, the negatively charged phospholipid phosphatidylserine (PS) is located in the cytosolic leaflet of the plasma membrane lipid bilayer. However, during apoptosis the PS is displayed on the outer face of the membrane. Annexin has a high affinity to PS in the presence of physiological concentrations of calcium (Ca^{2+}). Given that annexin V is not cell permeable, the binding of externalized PS is selective for early apoptotic cells. There was no annexin V binding in the control cells or the cells treated with AuNS-MPS, however there was a significant amount of the protein bound in the cells treated with the AuNR-PEG. This further signified that the AuNR-PEG caused cell death via the apoptotic pathway.
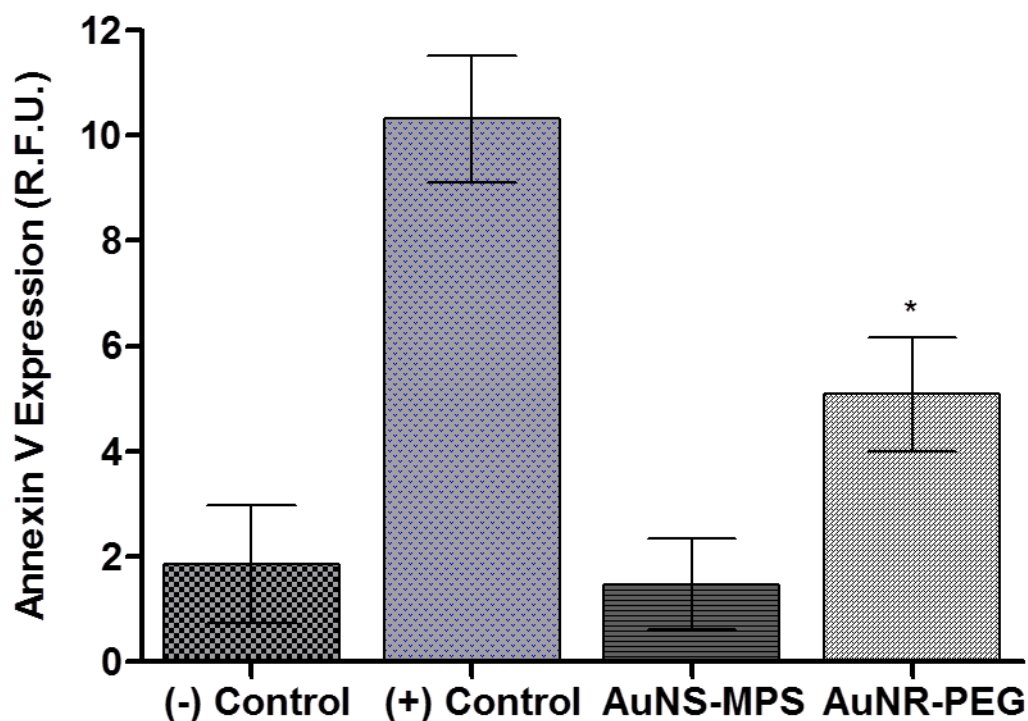
Figure 9 Binding of Annexin V after Gold Nanomaterial Exposure. There was significant (*p< 0.05) increase in annexin V binding after exposure to AuNR-PEG as compared to the negative control (untreated cells) which confirmed that apoptosis is the mechanism of death.

Linking Physiochemical Properties To Mechanism of Toxicity

The contrasting results observed between the AuNS-MPS and AuNR-PEG in the cytotoxicity, mitochondrial stress, gene, and protein studies indicated that the NM shape may play a role in the toxicity. A more difficult question to answer is why? One hypothesis is that in addition to the shape of the AuNMs, agglomerate size may play a key role in deciphering these differences. Several studies have demonstrated that cellular response to NM is dependent upon both agglomerate size and concentration.[14-20] While the present study showed that despite having a similar primary particle diameter and agglomerate size in media, the AuNR-PEG were found to be cytotoxic to human skin cells when compared to the AuNS-MPS. One of the major differences between these agglomerates was their fractal dimension (D_f), which indicates a significant difference in the compactness of the agglomerates between the two materials. Additionally, the AuNR-PEG had a higher aspect ratio with a larger calculated volume and surface area compared to the AuNS-MPS. Although there was not a sizable difference between the surface area of the AuNS-MPS and the AuNR-PEG (1.3×10^3 nm^2 and 2.3×10^3 nm^2, respectively), the AuNR-PEG had much more surface area available to interact with the cell membrane and multiple receptors. As a result, the AuNR-PEG could be causing the cell to generate more of a ROS and

MMP response than when it interacts with AuNS-MPS, through multiple receptors bound on the membrane. Moreover, the shape of the AuNM may affect the mechanism of uptake in the cell and could play a key role in cellular response. This is especially possible since despite similar agglomerate sizes in the media dosed to the cells, based on Figure 2 the AuNS-MPS were taken up as agglomerates while the AuNR-PEG were taken up more often as primary particles, i.e., single rods.

d. *Conclusion*

In conclusion, we have demonstrated that the shape is a major factor in establishing the biological response to AuNMs. Data from the viability, mitochondrial stress, gene, and protein studies attest that the AuNR-PEG had substantial detrimental effects on the cells, while exposure to the AuNS-MPS yielded distinctly different results and revealed them to be non-toxic. As a result, this study clearly indicates that shape of nanomaterial is a critical factor involved in mediating the cellular response to AuNMs.

e. *References*

[1]   Jadzinsky, P. D.; Calero, G.; Ackerson, C. J.; Bushnell, D. A.; Kornberg, R. D. Structure of a thiol monolayer-protected gold nanoparticle at 1.1 A resolution. *Science.* 2007, *318*, 430-433.

[2]   Boukamp, P.; Petrussevska, R. T.; Breitkreutz, D.; Hornung, J.; Markham, A.; Fusenig, N. E. Normal keratinization in a spontaneously immortalized aneuploid human keratinocyte cell line. *J. Cell Biol.* 1988, *106* (3), 761-771.

[3]   Murdock, R. C.; Braydich-Stolle, L.; Schrand, A. M.; Schlager, J. J.; Hussain, S. M. Characterization of nanomaterial dispersion in solution prior to in vitro exposure using dynamic light scattering technique. *Tox. Sci.* 2008, *101* (2), 239-253.

[4]   Saleh, N. B.; Pfefferle, L. D.; Elimelech, M. Aggregation kinetics of multiwalled carbon nanotubes in aquatic systems: measurements and environmental implications. *Environ. Sci. Technol.* 2008, *42*, 7963-7969.

[5]   Saleh, N. B.; Pfefferle, L. D.; Elimelech, M. Influence of biomacromolecules and humic acid on the aggregation kinetics of single-walled carbon nanotubes. *Environ. Sci. Technol.* 2010, *44*, 2412-2418.

[6]   Surdo, E. M.; Khan, I. A.; Choudhury, A. A.; Saleh, N. B.; Arnold, W. A. Barrier properties of poly(vinyl alcohol) membranes containing carbon nanotubes or activated carbon. *J. Hazard. Mater.* 2011, *188* (1-3), 334-340.

[7]   Kim, A. Y.; Berg, J. C. Fractal Aggregation: Scaling of Fractal Dimension with Stability Ratio *Langmuir* 2000, *16*, 2101-2104.

[8]   Bozzola, J. J.; Russell, L. D. Electron Microscopy. Principles and Techniques for Biologists. Jones and Bartlett Publishers, Boston, MA, 1992, pp. 16-37.

[9]   Braydich-Stolle, L.; Hussain, S.; Schlager, J. J.; Hofmann, M. C. In vitro cytotoxicity of nanoparticles in mammalian germline stem cells. *Tox. Sci.* 2005, *88* (2), 412-419.

[10] MacCuspie, R. I.; Elsen, A. M.; Diamanti, S. J.; Patton, S. T.; Altfeder, I.; Jacobs, J. D.; Voevodin A. A.; Vaia, R. A. Purification–chemical structure–electrical property relationship in gold nanoparticle liquids. *Appl. Organomet. Chem.* 2010, 24 (8), 590-599.

[11] Limbach, L. K.; Li, Y. C.; Grass, R. N.; Brunner, T. J.; Hintermann, M.A.; Muller, M.; Gunther, D.; Stark, W.J. Use Of Ultra-Low Cost Biodegradable Nanoparticles For The Transfection Of Mammalian Cells. *Environ. Sci. Technol.* 2005, 39, 9370-9376.

[12]   Lundqvist, M.; Stigler, J.; Elia, G.; Lynch, I.; Cedervall, T.; Dawson, K. A. Nanoparticle size and surface properties determine the protein corona with possible implications for biological impacts. *Proc. Natl. Acad. Sci.* U.S.A. 2008, 105, 14265-14270.

[13]   Cedervall, T.; Lynch, I.; Lindman, S.; Berggård, T.; Thulin, E.; Nilsson, H.; Dawson, K. A.; Linse, S. Understanding the nanoparticle-protein corona using methods to quantify exchange rates and affinities of proteins for nanoparticles. *Proc Natl Acad Sci* USA 2007. *104,* 2050-2055.

[14]   Albanese, A.; Chan, W.C. Effect of gold nanoparticle aggregation on cell uptake and toxicity. *ACS Nano* 2011, 26; 5(7):5478-89.

[15]   Qiu, Y.; Liu, Y.; Wang, L. M.; Xu, L. G.; Bai, R.; Ji, Y. L.; Wu, X. C.; Zhao, Y. L.; Li, Y. F.; Chen, C. Y. Surface chemistry and aspect ratio mediated cellular uptake of Au nanorods. *Biomaterials* 2010, *31*, 7606–7619.

[16]   Lacerda, S. H.; Park, J. J.; Meuse, C.; Pristinski, D.; Becker,M. L.; Karim, A.; Douglas, J. F. Interaction of gold nanoparticles with common human blood proteins. *ACS Nano* 2010, *4*, 365–379.

[17]   Rausch, K.; Reuter, A.; Fischer, K.; Schmidt, M. Fluorescent Analogs of Biomolecular Building Blocks: Design, Properties, and Applications. *Biomacromolecules* 2010, *11*, 2836–2839.

[18]   Maiorano, G.; Sabella, S.; Sorce, B.; Brunetti, V.; Malvindi, M. A.; Cingolani, R.; Pompa, P. P. Effects of Cell Culture Media on the Dynamic Formation of Protein-Nanoparticle Complexes and Influence on the Cellular Response. *ACS Nano* 2010, *4*, 7481-7491.

[19]   Kim, D.; El-Shall, H.; Dennis, D.; Morey, T. Interaction of PLGA nanoparticles with human blood constituents. *Colloids Surf. B* 2005, *40*, 83–91.

[20]   Zook, J. M.; MacCuspie, R. I.; Locascio, L. E.; Halter, M. D.; Elliott, J. T. Improved Characterization of Nanoparticle Clusters for EHS and Biosensors Research. *Nanotoxicol.* Early Online, 2011. DOI: 10.3109/17435390.2010.536615.

[21]   MacCuspie, R.I.; Rogers, K.; Patra, M.; Suo, Z.; Allen, A. J.; Martin, M. N.; Hackley, V.A. Challenges for physical characterization of silver nanoparticles under pristine and environmentally relevant conditions. *J. Environ. Monit. 2011*, *13*, 1212.

[22]   Phenrat, T.; Long, T. C.; Lowry, G. V.; Veronesi, B. Partial oxidation ("aging") and surface modification decrease the toxicity of nanosized zerovalent iron. *Environ. Sci. Technol.* 2009, *43*, 195–200.

[23]   Long, T. C.; Saleh, N.; Tilton, R. D.; Lowry, G. V.; Veronesi, B. Titanium Dioxide (P25) Produces Reactive Oxygen Species In Immortalized Microglia (Bv2): Implications For Nanoparticle Neurotoxicity. *Environ. Sci. Technol.* 2006, *40*, 4346-4352.

[24]   Long, T. C.; Tajuba, J.; Sama, P.; Saleh, N.; Swartz, C.; Parker, J.; Hester, S.; Lowry, G. V.; Veronesi, B. Nanosize Titanium Dioxide Stimulates Reactive Oxygen Species In Brain Microglia And Damages Neurons In Vitro. *Environ. Health Perspect.* 2007, *115*, 1631-1637.

[25]   Veronesi, B.; Tajuba, J.; Saleh, N.; Ward, W.; Hester, S.; Carter, J.; Lowry, G. V. Functionally charged polystyrene particles activate immortalized PV2 Microglia: Cellular and genomic response. *Nanotoxicology* 2008, *2*, 130-143.

[26]   Lin, M.Y.; Lindsay, H. M.; Weitz, D. A.; Ball, R. C.; Klein, R.; and Meakin, P. Universality in colloid aggregation. *Nature.* 1989, 339, 360-362.

[27]   Hunter RJ*, Introduction to Modern Colloid Science*, 1993, Oxford University Press, New York, p. 229.

[28]   Saleh, N.; Kim, H. J.; Phenrat, T.; Matyjaszewski, K.; Tilton, R. D.; Lowry, G. V. Aggregation Kinetics of Multiwalled Carbon Nanotubes in Aquatic Systems: Measurements and Environmental Implications. *Environ. Sci. Technol.* 2008, *42*, 3349-3355.

[29]   Chithrani, B. D.; Ghazani, A. A.; Chan, W. C. Determining the Size and Shape Dependence of Gold Nanoparticle Uptake into Mammalian Cells. *Nano Lett.* 2006, *6* (4), 662-668.

[30] Chithrani, B. D.; Chan, W. C. Elucidating the mechanism of cellular uptake and removal of protein-coated gold nanoparticles of different sizes and shapes. *Nano Lett.* 2007, *7* (6), 1542-1550.

[31] Orr, G.; Panther, D. J.; Phillips, J. L.; Tarasevich, B. J.; Dohnalkova, A.; Hu, D.; Teeguarden, J. G.; Pounds, J. G. Submicron and Nanoscale Inorganic Particles Exploit the Actin Machinery to be Propelled Along Microvilli like Structures into Alveolar Cells. *ACS Nano* 2007, *1* (5), 463-475.

[32] Gratton, S. E. A.; Ropp, P. A.; Pohlhaus, P. D.; Luft, J. C.; Madden, V. J.; Napier, M. E.; DeSimone, J. M. The effect of particle design on cellular internalization pathways. *PNAS* 2008, *105* (33), 11613-11618.

[33] Arnida; Malugin, A.; Ghandehari, H. Cellular uptake and toxicity of gold nanoparticles in prostate cancer cells: a comparative study of rods and spheres. *J. Appl. Toxicol.* 2010, *30* (3), 212-217.

[34] Hamblin, M. R.; Miller, J. L.; Rizvi, I.; Loew, H. G.; Hasan, T. Pegylation of charged polymer-photosensitiser conjugates: effects on photodynamic efficacy. *Br J Cancer* 0 AD, *89* (5), 937-943.

[35] Gref, R.; Minamitake, Y.; Peracchia, M. T; Trubetskoy, V.; Torchilin, V.; Langer, R. Lymph node localisation of biodegradable nanospheres surface modified with poloxamer and poloxamine block co-polymers. *Science* 1994 *263*, 1600-1603.

[36] Mosqueira, V.C.; Legrand, P.; Gref, R.; Heurtault, B.; Appel, M.; Barratt, G. Interactions between a macrophage cell line (J774A1) and surface-modified poly (D,L-lactide) nanocapsules bearing poly(ethylene glycol). *J Drug Target* 1999 *7*, 65-78.

[37] Mosqueira, V.C.; Legrand, P.; Morgat, J.L.; Vert, M.; Mysiakine, E.; Gref, R.; *et al.* Efficacy and Pharmacokinetics of Intravenous Nanocapsule Formulations of Halofantrine in Plasmodium berghei-Infected Mice. *Pharm Res* 2001 *18*, 1411-1419.

[38] Etame, A.B.; Smith, C; Chan, W.C.W; Rutka, J.T. Design and potential application of PEGylated gold nanoparticles with size-dependent permeation through brain microvasculature. *Nanomedicine* 2011, *7*, 992-1000.

[39] Lipka, J; Semmler-Behnke, M; Sperling R. A.; Wenk, A; Takenaka, S; Schleh, C; Kissel , T; Parak , W. J.; Kreyling, W.G. Biodistribution of PEG-modified gold nanoparticles following intratracheal instillation and intravenous injection. *Biomaterials* 2010, *31,* 6574-6581.

[40] Cruz, L. J.; Tacken, P. J.; Fokkink, R; Figdor, C. G. The influence of PEG chain length and targeting moiety on antibody-mediated delivery of nanoparticle vaccines to human dendritic cells. *Biomaterials* 2011, *32*, 6791-6803.

[41] Bhabra, G.; Sood, A.; Fisher, B.; Cartwright, L.; Saunders, M.; Evans, W.H.; Surprenant, A.; Lopez-Castejon, G.; Mann, S.; Davis, S.A.; Hails, L.A.; Ingham, E.; Verkade, P.; Lane, J.; Heesom, K.; Newson, R.; Case, C.P. Nanoparticles can cause DNA damage across a cellular barrier. *Nat. Nanotech.* 2009 *4*, 876 – 883.

[42] Sood, A.; Salih, S.; Roh, D.; Lacharme-Lora, L.; Parry, M.; Hardiman, B.; Keehan, R.; Grummer, R.; Winterhager, E.; Gokhale, P.J.; Andrews, P. W.; Abbott, C.; Forbes, K.; Westwood, M.; Aplin, J. D.; Ingham, E.; Papageorgiou, I.; Berry,M.; Liu, J.; Dick, A.D.; Garland, R.J.; Williams, N.; Singh, R.; Simon, A. K.; M. Lewis, M.; J. Ham, J.; L. Roger, L.; D. M. Baird, D.M.; L. A. Crompton, L.A.; M. A. Caldwell, M.A.; Swalwell, H.; Birch-Machin, M.; Lopez-Castejon, G.; Randall, A.; Lin, H.; Suleiman, M-S.; Evans, W.H.; Newson, R.; Case, C.P. Signaling of DNA damage and cytokines across cell barriers exposed to nanoparticles depends on barrier thickness. *Nat. Nanotech.* 2011 DOI: 10.1038/NNANO.2011.188

[43] Niidome, T.; Yamagata, M.; Okamoto, Y.; Akiyama, Y.; Takahashi, H.; Kawano, T.; Katayama, Y.; Niidome, Y. PEG-modified gold nanorods with a stealth character for in vivo applications. *J. Cont. Rel.* 2006, *114* (3), 343-347.

[44]   Grabinski, C.M.; Schaeublin, N.M.; Wijaya, A; D'Couto, H; Baxamusa, S.A.; Hamad-Schifferli, K; Hussain, S.M. Effect of gold nanorod surface chemistry on cellular response. *ACS Nano* 2011, *5* (4):2870-2879.

[45]   Nel, A.; Xia, T.; Mädler, L.; Li, N. Toxic potential of materials at the nanolevel. *Science* 2006, *311* (5761), 622-627.

[46]   Braydich-Stolle, L. K.; Speshock, J. L.; Castle, A.; Smith, M.; Murdock, R. C.; Hussain, S. M. Nanosized Aluminum Altered Immune Function. Nanosized aluminum altered immune function. *ACS Nano* 2010, *4* (7), 3661-3670.

[47]   Comfort, K. K.; Maurer, E. I.; Braydich-Stolle, L. K.; Hussain, S. M. Interference of silver, gold, and iron oxide nanoparticles on epidermal growth factor signal transduction in epithelial cells. *ACS Nano* 2011 doi 10.1021/nn203785a

[48]   Schaeublin, N. M.; Braydich-Stolle, L. K.; Schrand, A. M.; Miller, J. M.; Hutchison, J.; Schlager, J.J.; Hussain, S. M. Surface charge of gold nanoparticles mediates mechanism of toxicity. *Nanoscale* 2011, *3* (2), 410-420.

[49]   Green, D. R., and Reed, J. C. Mitochondria and apoptosis. *Science* 1998, *281* (5381), 1309-1312.

[50]   Halliwell, B. and Gutteridge, J. M. C. *Free Radicals in Biology and Medicine.* Oxford University Press, Oxford, UK, 1999.

[51]   Boisselier, E.; Astruc, D. Gold nanoparticles in nanomedicine: preparations, imaging, diagnostics, therapies, and toxicity. *Chem. Soc. Rev.* 2009, 38 (6), 1759-1782.

2.   *Evaluation of Surface Charge of Gold Nanoparticles Mediates Mechanism of Toxicity*

a.   *Purpose*

Recently, gold nanoparticles (AuNPs) have shown promising biological and military applications due to their unique electronic and optical properties. However, little is known about their biocompatibility in the event that they come into contact with a biological system. In the present study, we investigated whether modulating the surface charge of 1.5 nm AuNPs induced changes in cellular morphology, mitochondrial function, mitochondrial membrane potential (MMP), intracellular calcium levels, DNA damage-related gene expression, and of p53 and caspase-3 expression levels after exposure in a human keratinocyte cell line (HaCaT). The evaluation of three different AuNPs (positively charged, neutral, and negatively charged) showed that cell morphology was disrupted by all three NPs and that they demonstrated a dose-dependent toxicity; the charged AuNPs displayed toxicity as early as 10 µg/ml and the neutral at 25 µg/ml. Furthermore, there was significant mitochondrial stress (decreases in MMP and intracellular Ca^{++} levels) following exposure to the charged AuNPs, but not the neutral AuNPs. In addition to the differences observed in the MMP and Ca^{++} levels, up or down regulation of DNA damage related gene expression suggested a differential cell death mechanism based on whether or not the AuNPs were charged or neutral. Additionally, increased nuclear localization of p53 and caspase-3 expression were observed in cells exposed to the charged AuNPs, while the neutral AuNPs caused an increase in both nuclear and cytoplasmic p53 expression. In conclusion, these results indicate that surface charge is a major determinant of how AuNPs impact cellular processes, with the charged NPs inducing cell death through apoptosis and neutral NPs leading to necrosis.

b.   *Materials and Methods*

Gold Nanoparticles

AuNPs were synthesized in the laboratory of Dr. John Miller at the University of Oregon using previously published procedures in which gold NPs were produced through chemical reduction and subsequent stabilization using triphenylphosphine (TPP).[1-6] The nanoparticles consisted of a metallic gold core with primary diameters of 1.5 nm. AuNPs were functionalized with a water-soluble ligand to achieve different surface charges. The ligand 2-,2-mercaptoethoxyethoxyethanol (MEEE) conferred a neutral charge; N,N,N trimethylammoniumethanethiol (TMAT) conferred a positive, cationic charge; and a negative, anionic charged was obtained using 2-mercaptoethanesulfonate (MES) (Figure 10). A total of three nanoparticles were tested.
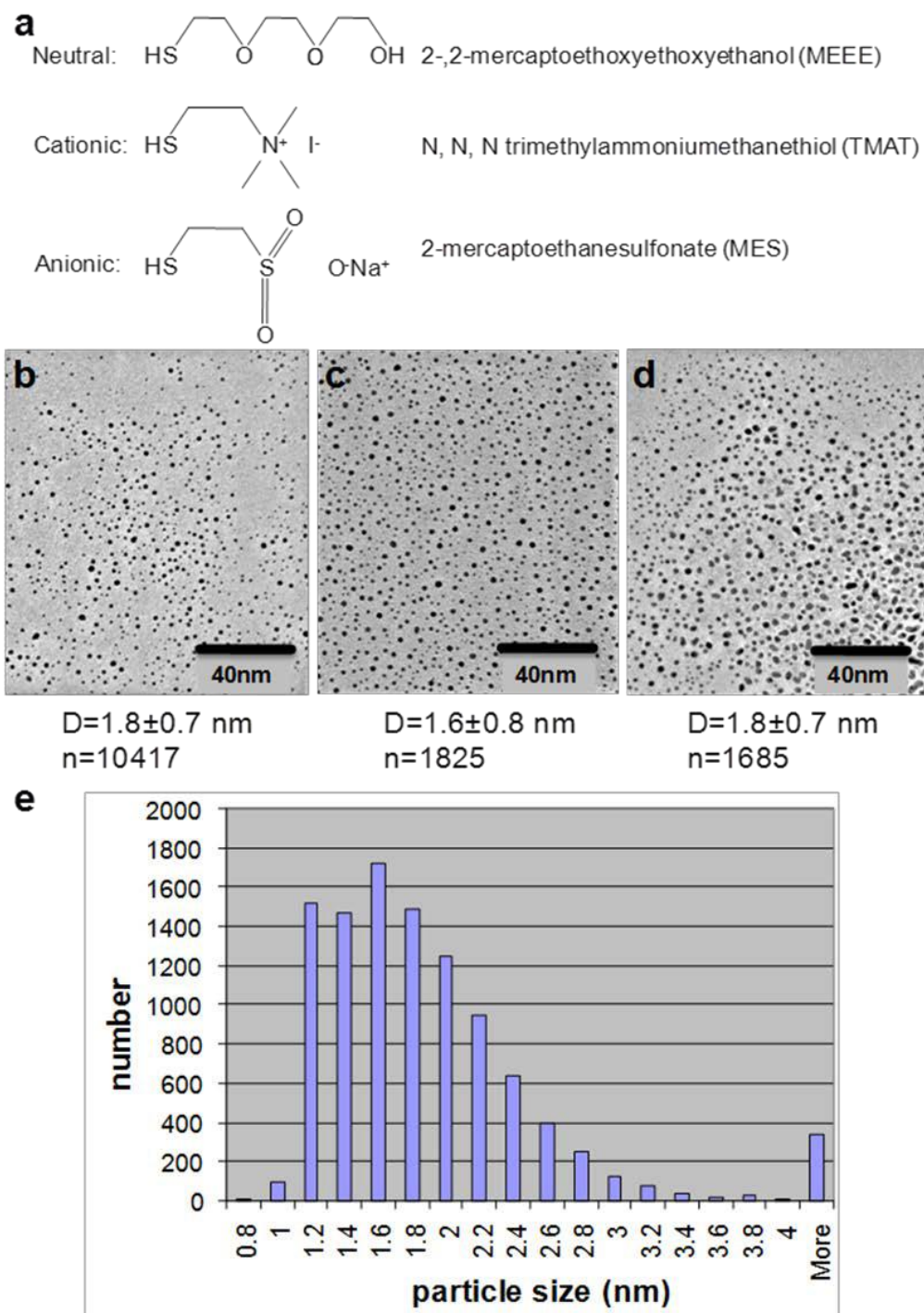
Figure 10 *Morphology of Gold Nanoparticle Modified with Different Surface Charges (a) Schematic of the water-soluble ligands used to functionalize the AuNPs with different charges, (b-d) representative bright field transmission electron microscope (BF-TEM) images of AuNPs taken at 120kV demonstrating spherical morphologies and sizes of ~1.5nm (b) MEEE (0) (c) TMAT (+), (d) MES (-), (e) histogram of particle size distribution of 1.5nm MEEE (0) particles.*

Cell Culture

The human keratinocyte cell line (HaCaT) was generously donated by the Army Research Lab.[7] The cells were cultured in a flask with RPMI-1640 media (ATCC, Manassas, VA), supplemented with 10% fetal bovine serum (FBS, ATCC) and 1% penicillin/streptomycin (Sigma, St. Louis, MO), and incubated at 37°C in a humidified incubator with 5% CO_2. For nanoparticle exposure procedures, media was supplemented with 1% penicillin/streptomycin but no serum. For the cytotoxicity assays, cells were cultured in 96-well plates with 5×10^3 cells per well and allowed to grow at 37°C with 5% CO_2 for 24 h until ~80% confluent.

Cellular Uptake of Gold Nanoparticles

HaCaT cells were processed for TEM according to Schrand et al., 2010.[8] Briefly, the cells were seeded in 100 mm tissue culture dishes, and at 85% confluency treated with 25 µg/ml of the different charged AuNPs. Twenty-four hours later, the cells were fixed in 2% paraformaldehyde/2.5% gluteraldehyde in PBS for 2 hours. Thereafter, the cells were post-fixed with 1% osmium tetroxide for 1 hour, and then the cells were scraped from the plate and centrifuged. The cells were dehydrated using increasing concentrations of ethanol with three changes of 100% ethanol. The samples then were placed in 100% LR White resin and cured overnight at 60°C in BEEM® capsules. The samples were thin-sectioned on a Leica ultramicrotome at a thickness of 50-100 nm, collected on formvar/carbon-coated TEM grids, and imaged using a Philips/FEI CM200 TEM at 200kV. Energy-dispersive x-ray (EDX) analysis was performed at various locations within the cells to confirm the presence of AuNPs with an EDAX system.

External Morphology and Nanoparticle Uptake by Ultra Resolution Imaging

HaCaT cells were plated on chambered slides at a density of 3×10^5 and allowed to grow at 37°C with 5% CO_2 for 24 h until ~80% confluent. They then were exposed to 10 µg/ml of each particle for 24 h. After exposure, the cells were fixed with 4% Paraformaldehyde and stained with the Alexa 555-phallodin stain and SYTOX green (Invitrogen, Carlsbad, CA) to visualize the actin and the nucleus, respectively. The slides were mounted in Prolong AntiFade reagent (Invitrogen), and images were taken using the CytoViva™ 150 ultra resolution attachment (Aetos Technologies, Inc., Auburn, AL) to determine if the particles were taken into the cell and to observe any morphological changes.

Quantification of Gold Nanoparticle Uptake

The cells were plated in 6-well plates at 5×10^5 cells per well and allowed to grow until ~80% confluent. The cells then were dosed with 25µg/ml of the AuNPs and incubated for another 24 h. After 24 h, the cells were washed to remove any excess or unbound

nanoparticles, digested with nitric acid, and analyzed using ICP-MS (iCAP 6500, Thermo-Fisher Scientific, Waltham, MA).

Mitochondrial Function

Mitochondrial function was assessed using the CellTiter 96 AQueous One Solution Assay (Promega, Madison, WI). The cells were seeded as described above and were treated with AuNPs at concentrations of 0-100 µg/ml. After a 24-h exposure mitochondrial function was assessed as described previously by Braydich-Stolle *et al.*[9] The plate was read on a SpectraMAX GeminiXS microplate reader at 490 nm to measure the absorbance. Each experiment was done in triplicate.

Reactive Oxygen Species Generation

Prior to treatment with AuNPs, a dichlorofluorescein diacetate probe was added and the cells were exposed AuNPs at a concentration of 10 µg/ml. Reactive oxygen species (ROS) production was assessed following the procedure described by Wang.[10] The plate then was read on a SpectraMAX GeminiXS microplate reader at a 486-nm excitation wavelength and a 530-nm emission wavelength, using the well scan setting of the instrument.

Real Time PCR

The cells were plated in 6-well plates at 3×10^5 cells per plate and allowed to grow overnight until ~80% confluent. The cells then were dosed with 25µg/ml of the AuNPs and allowed to incubate for another 24 h. The RNA then was isolated (RNeasy Mini Kit, Qiagen, Valencia, CA) and used in subsequent PCR reactions to assess DNA damage. The DNA-damage arrays were obtained from SA Biosciences (Frederick, MD) and the RNA was processed using SA Biosciences reagents following the manufacturer's instructions. Each experiment was performed in triplicate.

Expression of p53 and caspase-3

The cells were plated on chambered slides and exposed to 25µg/ml of the AuNPs for 24 h, or low concentration of H_2O_2 as a positive control for DNA damage. After exposure, the cells were fixed in 4% paraformaldehyde and immunostained with a p53 or caspase-3 primary antibody and an AlexaFluor® 647 secondary antibody. The nuclei also were stained with Hoechst. The slides then were visualized on a BD Pathway435 confocal microscope (BD Biosciences, San Jose, CA).

Mitochondrial Membrane Potential

Mitochondrial membrane potential was evaluated using the Mīt-EΨ Mitochondrial Permeability Detection Kit from BIOMOL (Plymouth Meeting, PA). The cells were seeded as described above in a 96-well black imaging plate, allowed to grow overnight

until ~80% confluent and exposed to 25µg/ml of the AuNPs for 6 h. After 4 h, the media was removed and the cells were washed three times with PBS to eliminate any excess NPs that were not internalized or bound to the membrane. The cells then were incubated with the M$\bar{\text{i}}$t-EΨ solution for 15 minutes at 37°C with 5% CO_2. The solution then was removed and the cells were washed twice with PBS and imaged on a BD Pathway435 confocal microscope (BD Biosciences, San Jose, CA).

Calcium Assay

Changes in intracellular calcium levels were measured using the Calcium Assay Kit from BD Biosciences (San Jose, CA). The cells were seeded as described above in a black 96-well plate and allowed to grow overnight. The next day they were incubated with dye-loading solution for one hour and then exposed to 25µg/ml of the AuNPs. The plate then was read on a SpectraMAX GeminiXS microplate reader at a 485-nm excitation wavelength and a 525-nm emission wavelength, using the well scan setting of the instrument at the following time points: 0 hour (background), 15min, 30 min, 45 min, 1 hour, and then every hour until 6 hours.

Image Acquisition and Data Analysis

For the endpoint assays, 16 fields in each well were imaged at 20X using the 4X4 montage option in the BD Pathway 435 software. The p53 and caspase 3 assays used the Rhodamine and Hoechst filters and the MitE-ψ assay kit used the Rhodamine, Hoechst and FITC filters. Once the images were obtained, the confocal software allowed for segmenting the cells to measure only the fluorescent intensity within the designated portion. The images then were analyzed using the BD AttoVision™ v1.6 and the BD Image Data Explorer, which evaluated differences in fluorescent intensity between the samples.

Statistical Analysis

Data are represented as the average of three independent trials + the standard deviation. A student t-test was performed in Microsoft Excel to determine differences in comparison to control values. For the ICP-MS analysis, one way ANOVA followed by Bonferroni analysis was performed in GraphPad Prism.

c.   *Results and Discussion*

Nanoparticle Synthesis and Characterization

The AuNPs used in this study were synthesized using previously published procedures in which gold NPs were produced through chemical reduction and subsequent stabilization using triphenylphosphine (TPP).[1-6] Subsequently, the particles underwent ligand exchange in the presence of thiol molecules with different terminal functional groups. In this project, we utilized Au-TPP NPs with a core diameter of 1.5nm to

DISTRIBUTION A: Approved for public release; distribution unlimited. PA Case No. 88ABW-2013-4073

32

produce thiol-stabilized particles with trimethylammoniumethanethiol (TMAT), mercaptoethanesulfonate (MES), and mercaptoethoxyethoxyethanol (MEEE) as the stabilizing ligands. The TMAT, MES, and MEEE ligands represent positively charged, negatively charged, and neutral ligand species respectively (Figure 10a). The approach employed in the production of these materials utilizes a single common precursor (Au-TPP NPs) to be used for the production of each of the tested materials, thus eliminating additional processing variances with the formation of the AuNP cores. This approach is unique in that we can independently control core diameter, ligand shell composition, and purity of the particles, giving us the unique ability to explore the relationship between each of these parameters and the toxicity. Moreover, the use of rigorous purification methods ensures that no un-reacted precursors or ligands remain in the NP solution.[6] In this study, we selected AuNPs with 1.5 nm diameter as these represent the most well-characterized NPs we have produced and because particles with diameter <10 nm have been shown to exhibit increased reactivity relative to their larger counterparts.

Transmission electron microscopy (TEM) confirmed the average size of the particles to be 1.8±0.7nm for the neutral (MEEE) particles, 1.6±0.8nm for the positive (TMAT) particles and 1.8±0.7nm for the negative (MES) particles (Figure 10b-d). As an example of the particle size distribution, a histogram for the neutral (MEEE) particles has been provided (Figure 10e).

Nanoparticle Uptake and Localization

Nanoparticle uptake and localization inside of the cells was confirmed using bright field transmission electron microscopy (BFTEM) and energy-dispersive x-ray (EDX) analysis was used to verify elemental composition. Representative images demonstrated internalization of AuNP aggregates into distinct cytoplasmic vacuoles, typically near the plasma membrane after 24h (Figure 11 arrows). However, smaller AuNP aggregates were also found free in the cytoplasm (Figure 11d, black boxes). The elemental composition of the aggregates was confirmed as Au at distinct spots with EDX inside the cells (Figure 11f) compared to no Au signal for the control cells (Figure 11e). Additionally all of the samples contained a background signal from the copper (Cu) TEM grid. The verification of the aggregate composition as Au is important because the heavy metals used in staining (i.e., Osmium) to obtain cellular contrast under high vacuum/high resolution TEM can contribute to nano-sized artifacts.[8]
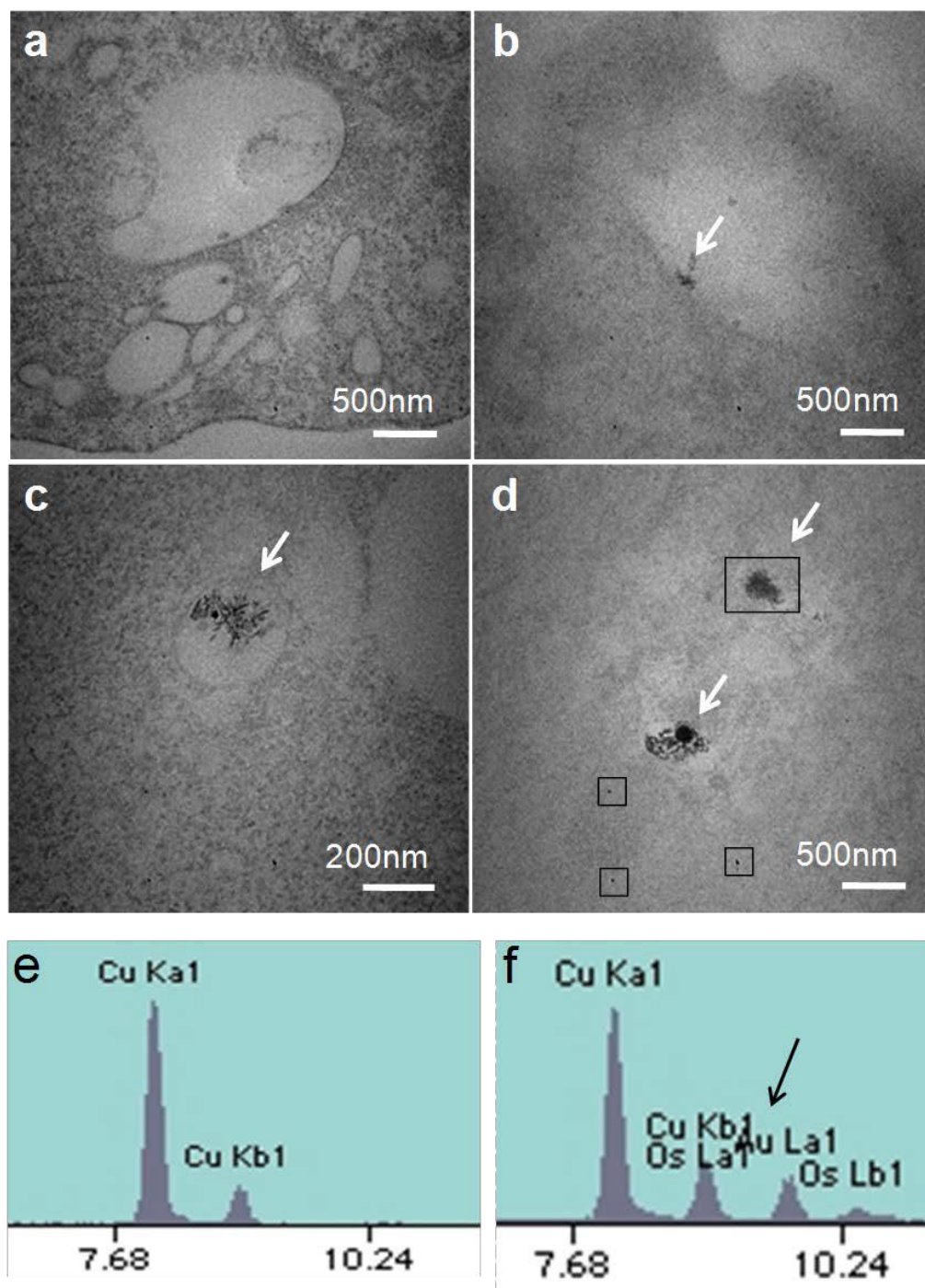
Figure 11 Gold Nanoparticle Uptake in HaCaT cells. (a-d) Representative bright field transmission electron microscope (BF-TEM) images of AuNPs in HaCaT cells. (a) Control (b) MEEE (0) (c) TMAT (+), and (d) MES (-). White arrows denote presence of AuNPs inside the cells (b, c, and d). Black boxes denote the presence of AuNPs inside the cells but not localized in vacuoles (d). (e, f) Representative energy-dispersive x-ray (EDX) spectra for localized elemental detection inside cells. (e) Control cells (f) Cells containing AuNPs inside cells. Images were taken at 200kV with a Philips/FEI CM200 Lab6 TEM and EDX spectra were obtained with an EDAX system.

The combination of both high illumination light microscopy and TEM imaging of cells exposed to AuNPs demonstrated minor interactions leading to low internalization. The amount of internalization was quantified using inductively coupled plasma mass spectroscopy (ICP-MS) (Figure 12). The ICP-MS data confirmed the presence of gold in the cells at 3.39 ±1.25, 3.27 ±0.83 and 5.90 ±1.21 μg/ml for the neutral (MEEE), positive (TMAT) and negative (MES) particles respectively. Despite the fact that it has been demonstrated recently that larger and positively charged NPs may enter other types of cells in greater numbers,[11-12] our analysis verified that there was no significant difference in the internalization based on surface charge. All three particles were found in the cell in relatively low amounts. Therefore, we strongly believe that the amount of uptake was not a deciding factor in the differences seen in cellular responses based on the different surface charges.
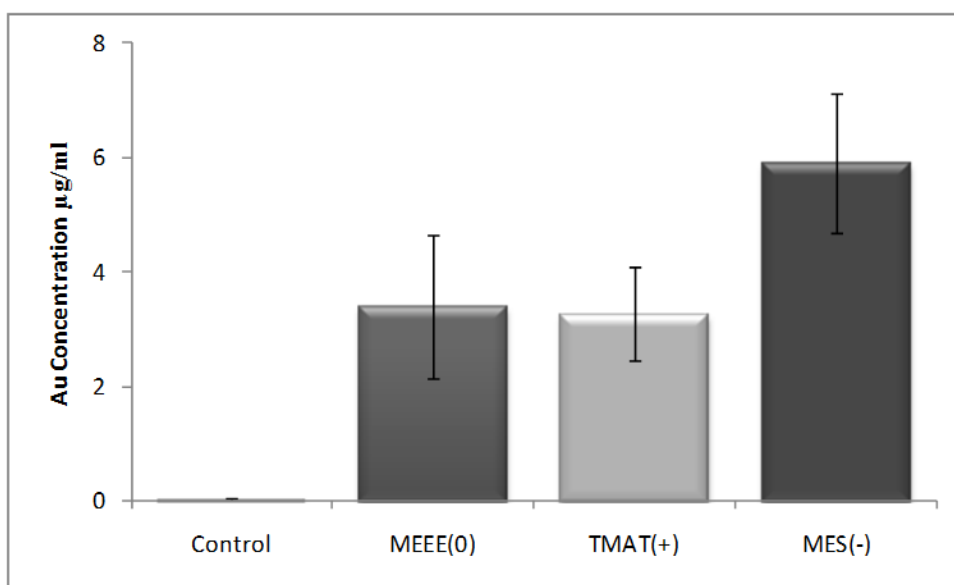
Figure 12 Quantification of Gold Nanoparticle Uptake in HaCaT Cells. The ICP-MS data confirmed the presence of AuNPs in the cells; however, the statistical analysis showed there was no significant difference in the amount of AuNP uptake in the cells based on surface charge.

Evaluation of Cellular Morphology & Cytotoxicity

Cell morphology studies were performed using ultrahigh resolution microscopy coupled with a fluorescence actin staining to detect the AuNPs inside the cells and associated with the cell membrane, as well as changes in cell morphology (Figure 13). In all three treatments of AuNPs, the cytoplasm of the cells were rounded and exhibited a loss of actin expression. Furthermore, when compared to the control cells, the cell monolayer was completely disrupted (Figure 13 b-d). Based on the abnormal cell morphology that was observed after exposure to AuNPs at 10 μg/ml, cytotoxicity was induced by these AuNPs regardless of charge. This cytotoxic effect was further demonstrated in the viability assays, where the AuNPs produced concentration-dependent cytotoxicity, regardless of charge (Figure 13e). A significant decrease in viability was seen with an

LD$_{50}$ < 10 µg/ml for both the charged particles (TMAT and MES) and an LD$_{50}$ = 25 µg/ml for the neutral MEEE particles. In order to confirm that the observed toxicity was due to the nanoparticles and not the ligands, just the ligands were tested and found to be nontoxic to the cells (Figure 13f). Since there was cytotoxicity demonstrated by all three AuNPs, the mechanism of cytotoxicity was further evaluated.
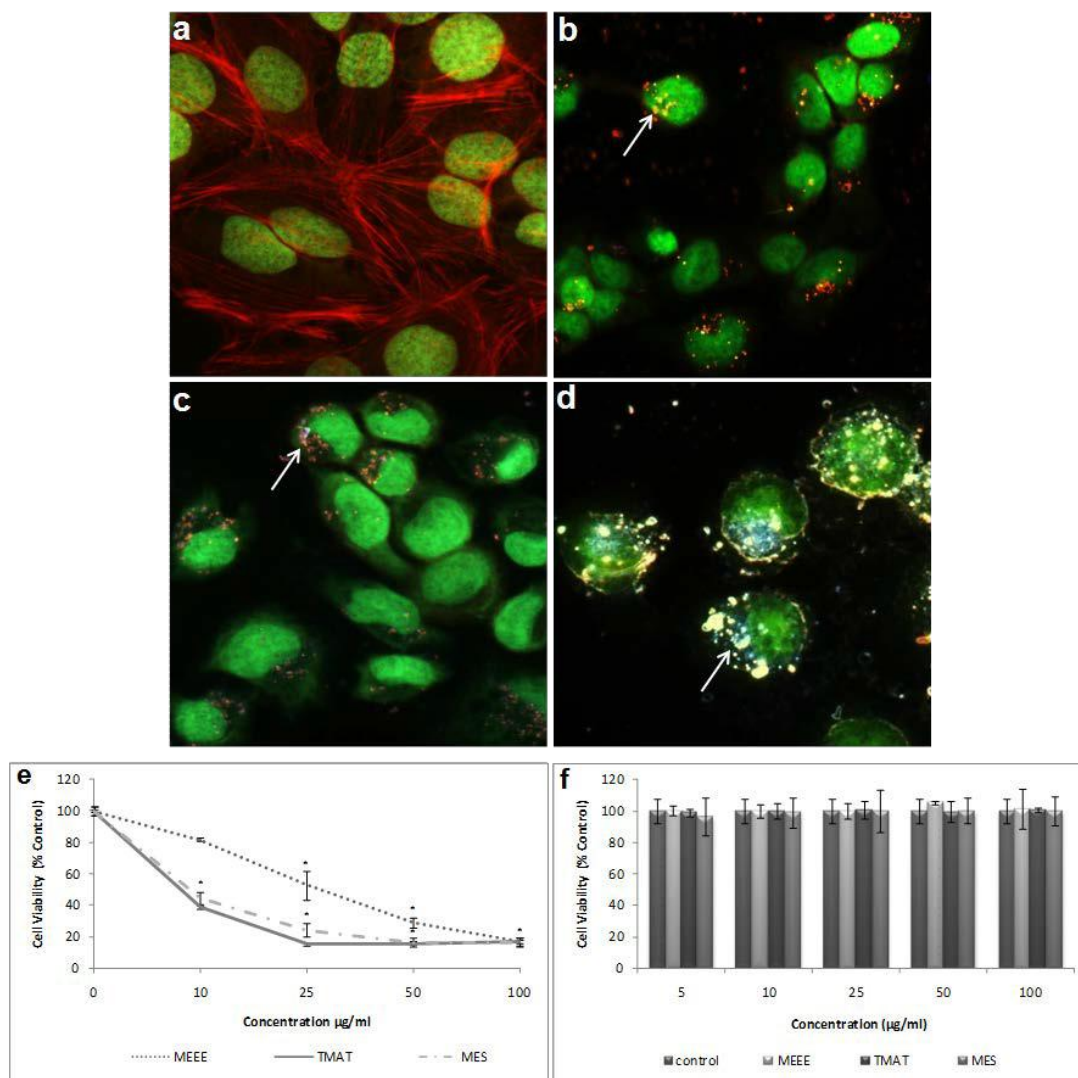
Figure 13 Changes in Morphology and Viability After Exposure to Charged Gold Nanoparticles and Ligands. (a) Untreated HaCaT cells, 96X. (b) HaCaT cells treated with MEEE AuNPs. (c) HaCaT cells treated with TMAT AuNPs. (d) HaCaT cells treated with MES AuNPs. High resolution imaging was able to detect AuNP agglomerates in all cells treated, as indicated by the arrows, as well as changes in cell morphology. (e) All of the AuNPs were toxic to the HaCaT cells in a concentration-dependent manner, with an LD50 < 10µg/ml for both charged particles and an LD50= 25 µg/ml for the neutral particles. (*Denotes significance in comparison to control values p<0.05). Cell viability was also plotted based on total surface area (cm2/ml) of the particles. See supplemental data. (f) HaCaT cells treated with the ligands used to produce the different charges. The ligands are not toxic to the HaCaT cells at the highest dose of 100 µg/ml.

Evaluation of Mitochondrial Stress

Nanoparticles have been shown to generate the formation of reactive oxygen species (ROS);[13] therefore, ROS formation was assessed to determine if oxidative damage was induced based on surface charge. For these studies, a concentration of 25 µg/ml was chosen, since at this concentration all of the AuNPs showed a significant decrease in cell viability. All the AuNPs particles induced formation of ROS and there was no difference in the levels induced based on charge (Figure 14). However, since the cell has the remarkable ability to try and repair itself following a stressful event such as the production of ROS, we wanted to evaluate the repair mechanisms following ROS production. Since the production of ROS has been shown to disrupt the MMP and indicate apoptosis,[14] we assessed the impact of AuNPs exposure on the MMP and intracellular Ca^{++} levels.

Following exposure to the neutral (MEEE) particles (Figure 14c) there was no change in the MMP when compared to control cells (Figure 14b); however, a significant alteration in the MMP was observed following exposure to the positive (TMAT) (Figure 14d) and negative (MES) AuNPs (Figure 14e). Despite the production of ROS by all three AuNPs, the difference in the MMP suggested that there was a differential cell death mechanism initiated based on whether the AuNPs had a neutral or charged surface chemistry. To further evaluate the difference of charge on the mitochondria, the intracellular Ca^{++} levels were evaluated since apoptosis can be induced by calcium.[15] After exposure to the NPs, there was no change in the intracellular levels of calcium for the neutral (MEEE) particles but there was a significant increase after exposure to both charged particles (Figure 14f). This set of experiments, which evaluated the impact of the differently charged AuNPs on the mitochondria, suggested that all the NPs produced oxidative stress within the cells, yet the charged NPs were inducing apoptosis through a depolarization of the MMP and release of Ca^{++}.

In this study, these differences can be related back to the surface chemistry of the ligands used to functionalize the particles and the different free radicals that could form within the cellular environment. For example, we hypothesize the highly reactive hydroxyl group on the neutral (MEEE) particles generated high amounts of ROS (Figure 10a). This elevated level of ROS increased production of superoxide dismutase (SOD) which is an important antioxidant defense in nearly all cells as it catalyzes the reaction of superoxide into oxygen and hydrogen peroxide.[16] Catalases, which are enzymes found in perixosomes, further breakdown oxygen and hydrogen peroxide into the benign products of water and oxygen.[17] The SOD acted as a scavenger and helped minimize the damage caused by the ROS and allowed the cells to try and repair themselves. However, the reactive groups on the charged particles produce different free radicals, and we hypothesize that the charged particles were unable to repair themselves. The positive (TMAT) particles have a free nitrogen that contains three reactive sites (Figure

10a), and this nitrogen can form nitric oxide and then react with superoxide (a normal by-product of the electron transport chain) to produce peroxynitrite, a potent oxidant that is toxic to cells.[18-19] It is likely that the majority of the damaging effects to the mitochondria result from the activity of peroxynitrite rather than OH^- because nitric oxide is the only biological molecule that is produced at a high enough concentration to outcompete SOD for superoxide.[20-21] Consequently, the SOD cannot scavenge the superoxide to prevent it from binding to the nitric oxide and producing the toxic peroxynitrite. Lastly, the negative (MES) particles contain a free oxygen and sodium ion. The sodium can be displaced by a free chloride ion, which leaves the oxygen free to form superoxide. These high levels of superoxide then produced other by-products that were detrimental to the cell.
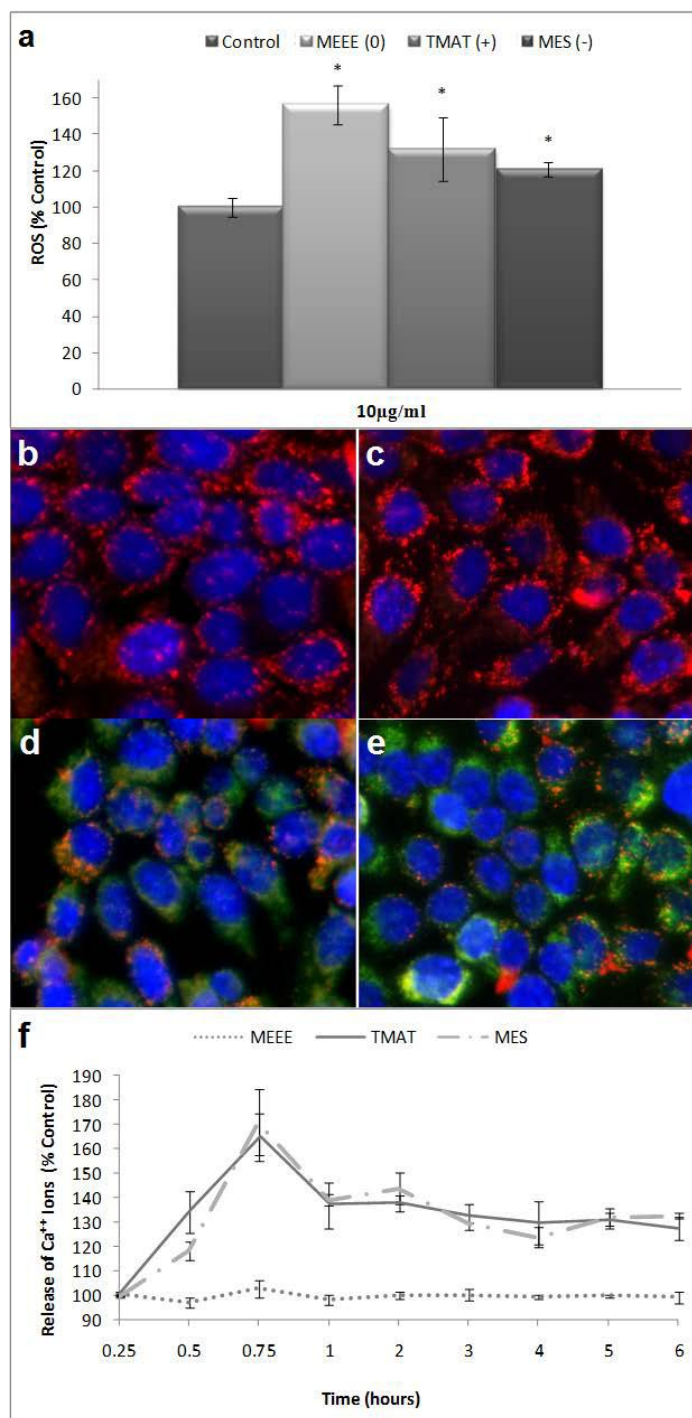
Figure 14 Evaluation of Mitochondrial Stress Following Gold Nanoparticle Exposure. (a) The AuNPs generated significant amounts of ROS, regardless of charge. (*Denotes significance in comparison to control values p<0.05). (b-e) Loss of mitochondrial membrane potential after exposure to 25 µg/ml AuNPs. (b) Control (c) MEEE (0) (d) TMAT (+) (e) MES (-). There was significant amount of MMP lost after exposure to both the TMAT (+) and MES (-) AuNPs. (f) Release of Calcium Ions into cytosol after exposure to 25 µg/ml AuNPs. There was a significant amount of Ca++ions into the cytosol after exposure to the (-) and (+) particles but not the MEEE (0) particles.

DISTRIBUTION A: Approved for public release; distribution unlimited. PA Case No. 88ABW-2013-4073

39

Evaluation of the Mechanism of Cell Death

Since there appeared to be a differential mechanism of cell death being initiated based on charge, further studies explored the changes in gene expression related to DNA damage and cell repair, as well as expression levels of p53 and caspase-3. A total of 12 genes exhibited significant changes in expression after exposure to the AuNPs (Table 4). In response to neutral (MEEE) particles, two genes involved in the cell cycle/apoptosis (TP73 and MAP2K6) were down-regulated, 7.01-fold and 2.86-fold, respectively. Changes in the expression of genes involved in DNA repair were also seen, with a slight down-regulation of RAD21 and MRE11A (1.74-fold and 2.26-fold, respectively), and a modest up-regulation (1.91-fold) of RAD51. The positively charged (TMAT) NPs also produced a down-regulation of several genes involved in the cell cycle/apoptosis (ATM, 4.10-fold; MAP2K6, 9.06-fold; SESN1, 2.85-fold) and DNA repair mechanisms (RAD21, 1.97-fold; MRE11A, 3.08-fold; MSH3, 2.11-fold). Negatively (MES) charged NPs had the most pronounced effects on gene expression, with all the genes being down-regulated. Exposure to these particles caused a massive down-regulation of the DNA repair genes RAD21, APEX1, REV1, and MSH3 (whose expression decreased by 2.58-fold, 2.43-fold, 29.87-fold, and 3.41-fold, respectively), which limited the cells ability to recruit DNA polymerases and repair DNA. Down-regulation also occurred in the apoptotic genes ATM, GTSE1, MAP2K6, RAP1, and SESN1 (3.79-fold, 19.94-fold, 19.48-fold, 1.63-fold, and 2.77-fold respectively.)

The data from this gene array suggested that apoptosis was induced by the charged AuNPs while the neutral AuNPs were down-regulating apoptotic genes and the cell death mechanism was most likely necrosis. When DNA damage is irreparable, p53 will induce apoptosis and caspase-3 is a key mediator in both the intrinsic and extrinsic apoptotic pathway. Therefore, to confirm the mechanism of cell death the expression levels of p53 and caspase-3 were evaluated. The neutral (MEEE) NPs demonstrated a 7-fold down-regulation of the p73 gene, a relative of p53 that induces apoptosis. This change in gene expression correlated with changes in p53 expression and cellular distribution, which showed a slight up-regulation relative to controls, but a shift toward cytoplasmic localization, indicated it was being shuttled out of the nucleus to prevent apoptosis (Figure 15).

Furthermore, there was minimal caspase-3 expression in the nucleus (Figure 15). This correlated with caspase-3 expression in the negative control cells, and was in contrast to the positive control cells that demonstrated strong cytoplasmic expression. After exposure to the positive (TMAT) NPs, p53 and caspase-3 expression was up-regulated compared to the negative control (Figure 15). Expression of p53 was seen only in the nucleus, and the lack of cytoplasmic expression indicated that p53 was building up in the nucleus and not being shuttled out to prevent apoptosis. Moreover, there was significant expression of caspase-3 in the cytoplasm, which was similar to the expression pattern in the caspase-3 positive controls. The p53 and caspase-3 expression data indicate that the changes at the RNA level are not carried through to the protein level. There was increased p53 expression in the nucleus of the cells after

exposure to the negative (MES) particles, but no cytoplasmic localization. This could be accounted for by the down-regulation of the apoptotic genes GTSE1 and MAP2K6, which customarily binds to p53, shuttles it out of the nucleus, and prevents apoptosis. 22 This was also confirmed by large amounts of caspase-3 in the cytoplasm.

*Table 4 Changes in DNA Damage Gene Expression following a 24 h treatment with AuNPs. ****denotes no expression. A total of 12 genes were differentially expressed in response to AuNP exposure.*

Gene Symbol	Functional Group	Function	Treatment		
			MEEE[0]	TMAT[+]	MES[-]
ATM	Apoptosis	Targets p53 in response to DNA double strand breaks	*****	-4.1	-3.79
GTSE1	Apoptosis	Binds to p53 and shuttles it out of the nucleus to repress apoptosis	*****	*****	-19.94
MAP2K6	Apoptosis	Activates p38 MAP kinase in response to stress	-2.86	-9.06	-19.48
TP73	Apoptosis/Cell Cycle	Related to p53 and induces apoptosis	-7.03	*****	*****
RPA1	Cell Cycle/DNA repair	Down-regulates DNA synthesis and allows DNA repair	*****	*****	-1.63
SESN1	Cell Cycle/Apoptosis	Target of p53, activates growth arrest	*****	-2.85	-2.77
RAD21	Damaged DNA Binding	Repairs double stranded DNA breaks	-1.74	-1.97	-2.58
RAD51	Damaged DNA Binding	Repairs double stranded DNA breaks	1.91	*****	*****
APEX1	DNA Repair	Intiates base exicision repair	*****	*****	-2.43
REV1	DNA Repair	Recruits DNA polymerases to repair DNA	*****	*****	-29.87
MRE11A	Double Strand Break Repair	Repairs double stranded DNA breaks	-2.26	-3.08	*****
MSH3	Mismatch Repair	DNA mismatch repair	*****	-2.11	-3.41

DISTRIBUTION A: Approved for public release; distribution unlimited. PA Case No. 88ABW-2013-4073

41
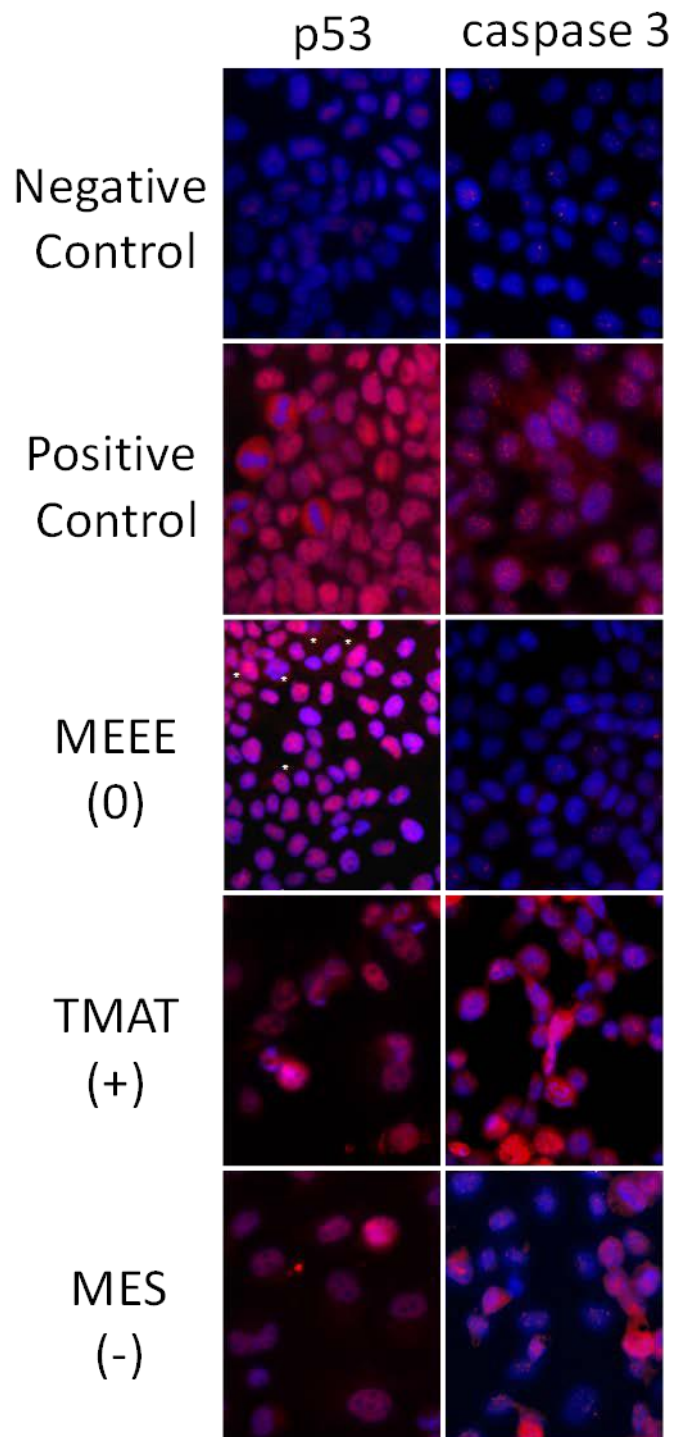
Figure 15 Expression of p53 and Caspase-3 after Exposure to Gold Nanoparticles. (The asterisks denote cytoplasmic localization of p53 in the MEEE treatment).

Proposed Mechanism of Cell Death Based on Gold Nanoparticle Surface Charge

A possible mechanism for the differences in cell death based on charge is illustrated in Figure 16, and a summary of the data used to create this model is presented in Table 5. Our data demonstrated a decline in mitochondrial function and an increase in expression for certain apoptotic markers, indicating that the AuNPs have the potential to interact with mitochondria. The mitochondria is a membrane bound organelle that consists of an outer membrane, an inter membrane space, an inner membrane, and an inner matrix. Aside from being the "powerhouse" of the cell where ATP is created, the mitochondria stores Ca^{++} as well as activators of apoptosis. The outer membrane has an electrochemical gradient very similar to the plasma membrane, and this gradient is very sensitive to change. The cytosolic side of the outer membrane has a slight negative charge as a result of the positive charge created by the proton pumps in the intermembrane space, which are responsible for storing energy needed for cellular respiration.[23] For the neutral AuNPs, we hypothesize that this membrane potential was not disrupted (Table 5, Figure 16a 1 & 2), and, therefore, mitochondrial-mediated apoptosis was not initiated and another form of cell death was activated upon AuNP internalization (Table 5, Figure 16a 3). This theory was supported by retention of the MMP, no increase of intracellular calcium levels, the absence of caspase-3 activation, and p53 nuclear accumulation. In contrast, the presence of the positive charge on the AuNPs may attract the nanoparticles to the slight negative charge on the outer portion of the mitochondrial membrane (Table 5, Figure 16b 1). If the AuNPs accumulated outside the mitochondria due to this attraction, this would create an imbalance in the MMP (Table 5, Figure 16b 2), which would damage the membrane (Table 5, Figure 15b 3) and allow apoptotic proteins from the inter-membrane space to leak into the cytosol (Table 5, Figure 16b 4). The damage to the membrane was confirmed with the MMP assay, which demonstrated a depolarization of the membrane (Table 5, Figure 14), and was further confirmed by the activation of caspase-3 following treatment with the positive (TMAT) AuNPs. Furthermore, the increased levels of intracellular calcium can be attributed to the increased expression of p53 and mitochondrial-mediated apoptosis is most likely the mechanism of toxicity. Similarly, the negatively charged (MES) AuNPs outside of the mitochondria would increase the negative charge of the outer surface of the membrane (Table 5, Figure 16c 1), and the mitochondria could attempt to correct this disruption in mitochondrial membrane potential (Table 5, Figure 16c 2) by releasing positively charged calcium ions from the matrix into the cytosol (Table 5, Figure 16c 3 & 4). Such a spike in calcium ions would trigger calcium-evoked apoptosis, as well as other calcium-induced signaling pathways (Table 5, Figure 16c). Based on the decline in mitochondrial function, the loss of MMP, the increase in the amount of intracellular calcium, the activation of caspase-3, and the increase in nuclear p53, it is most likely that apoptosis was activated by these negatively charged (MES) AuNPs.

DISTRIBUTION A: Approved for public release; distribution unlimited. PA Case No. 88ABW-2013-4073

43

Table 5 Summary of the Observed Cellular Responses Following Exposure to AuNPs with Different Surface Charges. Values that were not significant were excluded from this table and replaced with ***.

Particle	Cellular Response Following Treatment to 25 µg/ml of Gold Nanoparticles with Different Surface Charges							
	MTS	ROS	MMP	Ca^{++} Release at 45m	DNA Damage Gene Expression	p53 Expression	Caspase-3 Expression	Mechanism of Toxicity
MEEE^0	52.98	156.00	***	***	4 genes↓, 1 gene ↑	limited nuclear expression	no expression	Necrosis
TMAT$^+$	15.52	131.00	130.00	165.00	6 genes↓	nuclear accumulation	increased expression	Apoptosis
MES$^-$	24.41	121.00	136.00	171.00	9 genes↓	nuclear accumulation	increased expression	Apoptosis
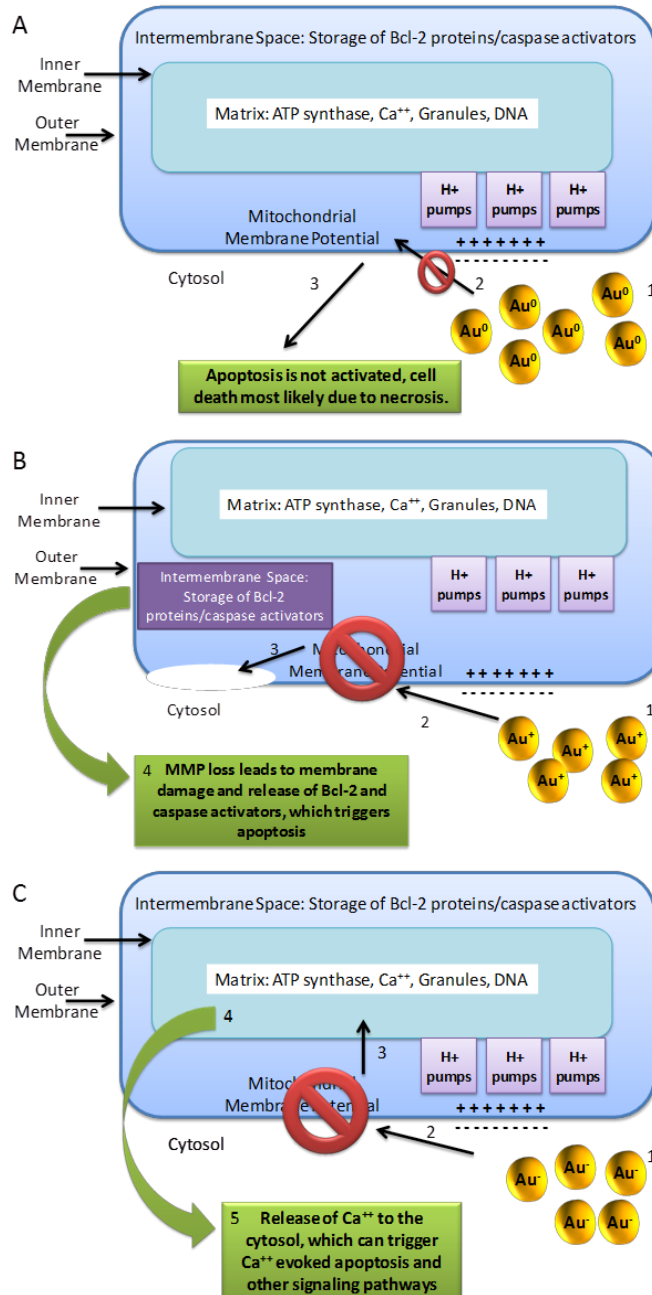
Figure 16 Proposed Mechanism of Cell Death Based on Gold Nanoparticles with Surface Charge. *(a) Neutral (MEEE) AuNPs. The neutral charge (1) does not disrupt the mitochondrial membrane potential (2), and therefore, apoptosis is not activated (3). (b) Positive (TMAT) AuNPs. The positive charge (1) disrupts the slight negative charge on the cytosolic side of the outer membrane, leading to a disruption in mitochondrial membrane potential (2). The disruption damages the membrane (3) and proteins, such as caspase activators, leak into the cytosol (4). (c) Negative (MES) AuNPs. The nanoparticles increase the negative charge on the outer membrane (1), which leads to a disruption in mitochondrial membrane potential (2). The mitochondria compensates by releasing calcium ions that were stored in the matrix of the mitochondria (3 & 4). The spike in calcium induces apoptosis (5).*

DISTRIBUTION A: Approved for public release; distribution unlimited. PA Case No. 88ABW-2013-4073

45

e.   Conclusions

The differences observed in the cellular morphology and cytotoxicity assays provided evidence that the charge of AuNPs plays a role in their toxicity. In contrast to Goodman *et al.*,[24] who found that cationic AuNPs were toxic while their anionic counterparts were not, we demonstrated that both the positively (TMAT) and negatively (MES) charged AuNPs were toxic, with the negative (MES) AuNPs evoking a greater response. In the Goodman study, the 2 nm gold cores were functionalized with 70 charged thiols and 30 uncharged thiols, while in this study thiol containing ligands were used to alter the surface charge. Both of these studies used gold nanospheres that were approximately the same size and functionalized with thiol groups to create a positive or negative surface charge, yet there were differences in the observed toxicity. When evaluating the actual chemistry of the thiol-based ligands, the negatively charged nanoparticles in our study had an outer chemistry that consisted of carbon, hydrogen, oxygen, and sulfur, while the ligands in Goodman's study contained an outer chemistry of just carbon, hydrogen, and oxygen. This difference in outer chemistry could account for the difference in toxicity based on how these elements can interact with cellular components. In comparison, the positively charged gold nanoparticles demonstrated similar trends in toxicity in the two studies, and they had a similar outer chemistry consisting of nitrogen, carbon, and hydrogen. The difference between these two studies demonstrates how the synthesis and functionalization methods can impact the biological response and how characterization of nanomaterials is imperative (reviewed by Hussain *et al.*[25] Furthermore, neutral (MEEE) AuNPs also displayed cytotoxicity, indicating that parameters other than charge contribute to toxicity (most likely size in this case, additional data not shown). Gene expression studies confirmed that charge was a factor in cell toxicity with irreparable DNA damage to the cells occurring after 24 h exposure to the AuNPs. However, the genes affected differed depending on particle charge. More importantly, the MMP data and DNA damage array, along with the p53 and caspase-3 expression, and intracellular calcium levels suggested that the mechanism of cell death varied depending on the surface charge. Both the positive (TMAT) and negative (MES) AuNPs increased the expression of apoptotic markers, indicating that the mechanism of cell death was apoptosis. In comparison, cell death in response to the neutral (MEEE) AuNPs was accompanied by cytoplasmic localization of p53 to prevent apoptosis, minimal expression of caspase-3 (comparable to control levels), and no significant increase in the loss of mitochondrial membrane potential or intracellular calcium levels thus suggesting necrosis instead of apoptosis as the mechanism of cytotoxicity. Consequently, the surface charge of the AuNPs played a critical role in determining the manner of cell death.

f.   References

[1]   Weare WW.; Reed SM.; Warner MG; Hutchison JE. Improved Synthesis of Small (dCORE =1.5 nm) Phosphine-stabilized Nanoparticles. *J. Am. Chem. Soc.* 2000. *122*, 12890-12891.

[2]   Woehrle GH.; Warner MG; Hutchison JE. Ligand Exchange Reactions Yield Subnanometer, Thiol-stabilized Gold Particles with Defined Optical Transitions. *J. Phys. Chem.* 2002. *106*, 9979-9981.

[3]   Warner MG; Hutchison JE. Synthesis, Functionalization, and Surface Treatment of Nanoparticles, ed. Baraton MI. *American Scientific Publishers* 2003. 67-89.

[4]   Hutchison JE.; Foster EW.; Warner MG.; Reed SM.; Weare WW.; Buhro W.; Yu H. Triphenylphosphine-Stabilized Gold Nanoparticles. *Inorg. Synth.* 2004. *34*,228-232.

[5]   Woehrle GH.; Brown LO.; Hutchison JE. Thiol-Functionalized, 1.5-nm Gold Nanoparticles through Ligand Exchange Reactions: Scope and Mechanism of Ligand Exchange. *J. Am. Chem. Soc.* 2005 *127*, 2172 - 2183.

[6]   Sweeney SF.; Woehrle G.; Hutchison JE. . Rapid Purification and Size Separation of Gold Nanoparticles via Diafiltration. *J. Am. Chem. Soc.* 2006 *128*, 3190-3197.

[7]   Boukamp P.; Petrussevska RT.; Breitkreutz D.; Hornung J.; Markham A.; Fusenig NE. Normal Keratinization in a Spontaneously Immortalized Aneuploid Human Keratinocyte Cell Line. *The Journal of Cell Biology*. 1988 *106*, 761-771.

[8]   Schrand AM.; Schlager JJ.; Dai L and Hussain SM. Preparing Cells Dosed with Nanomaterials for Assessment of Internalization and Localization with Transmission Electron Microscopy. *Nature Protocols* 2010, Apr;5(4):744-57.

[9]   Braydich-Stolle LK.; Hussain SM.; Schlager JJ.; and Hofmann MC. . In Vitro Cytotoxicity of Nanoparticles in Mammalian Germline Stem Cells. *Toxicol. Sci.* 2005 *88*(2), 412-419.

[10]   Wang H.; Joseph JA. . Quantitating cellular oxidative stress by dichlorofluorescein assay using microplate reader. *Free Rad Biol Med* 1999 *27*, 612-616.

[11]   Orr G.; Panther DJ.; Phillips JL.; Tarasevich BJ.; Dohnalkova A.; Hu D.; Teeguarden JG.; Pounds JG. . Submicrometer and Nanoscale Inorganic Particles Exploit the Actin Machinery to Be Propelled Along Microvilli-like Structures into Alveolar Cells. *ACS Nano* 2007 *1*(5), 463-475.

[12]   Gratton SE.; Ropp PA.; Pohlhaus PD.; Luft JC.; Madden VJ.; Napier ME.; DeSimone JM. . The effect of particle design on cellular internalization pathways. *PNAS* 2008 *105*(33), 11613-8.

[13]   Nel A.; Xia T.; Madler L.; Li N. Toxic Potential of Materials at the Nanolevel. *Science* 2006 *311*, 622.

[14]   Green DR and Reed JC. . Mitochondria and Apoptosis. *Science* 1998 *281*, 1309.

[15]   Wan-Cheng Li D.; Liu JP.; Mao YW.; Xiang H.; Wang J.; Ma WY.; Dong Z.; Pike HM.; Brown RE.; and Reed JC. . Calcium-activated RAF/MEK/ERK Signaling Pathway Mediates p53-dependent Apoptosis and Is Abrogated by αB-Crystallin through Inhibition of RAS Activation. *Mol Biol Cell.* 2005 *16*,4437–4453.

[16]   McCord JM.; Keele BBJ; Fridovich I. . An enzyme-based theory of obligate anaerobiosis: The physiological function of superoxide dismutase. *PNAS* 1971 *68*, 1024-1027.

[17]   Chelikani P.; Fita I.; Loewen PC. . Diversity of structures and properties among catalases. *Cell. Mol. Life Sci.* 2004 *61*(2), 192–208.

[18]   Blough NV.; Zafiriou OC: Reaction of superoxide with nitric oxide to form peroxonitrite in alkaline aqueous solution. *Inorg Chem* 1985 *24*, 3502-3504.

[19]   Beckman JS.; Beckman TW.; Chen J.; Marshall PA.; Freeman BA. . Apparent hydroxyl radical production by peroxynitrite: Implications for endothelial injury from nitric oxide and superoxide. *PNAS*. 1990 *87*, 1620-l624.

[20]   Robinson JP; and Babcock GF. . *Phagocyte Function: A Guide for Research and Clinical Evaluation.* New York: Wiley-Liss Inc. 1998 ISBN O-47 1- 12364- 1.

[21]   Pacher PA'L.; Beckman JS; Liaudet L. Nitric Oxide and Peroxynitrite in Health and *Disease. Physiol. Rev.* 2007 87, 315-424.

[22]   Monte M.; Benetti R.; Buscemi G.; Sandy P.; Del Sal G.; and Schneider C.. The Cell Cycle-regulated Protein Human GTSE-1 Controls DNA Damage-induced Apoptosis by Affecting p53 Function. *Journal Biol. Chem.* 2003 *278*(32), 30356-30364.

[23]   Alberts B.; Johnson A.; Lewis J.; Raff M.; Roberts K.; Walter P. *Molecular Biology of the Cell.* New York: Garland Publishing Inc. 1994 ISBN 0815332181.

[24]   Goodman CM.; McCusker CD.; Yilmaz T.; Rotello VM.Toxicity of gold nanoparticles functionalized with cationic and anionic side chains. *Bioconjug Chem.* 2004 *15*(4), 897-900.

[25]   Hussain SM.; Braydich-Stolle LK.; Schrand AM.; Murdock RC.; Yu KO.; Mattie DM.; Schlager JJ.; Terrones M. Toxicity evaluation for safe use of nanomaterials: recent achievements and technical challenges. *Adv. Mat.* 2009 *21*, 1-11.

3.   Evaluation of Effect of Gold Nanorod Surface Chemistry on Cellular Response

a.   Purpose

Gold nanorods (AuNRs) stabilized with cetyltrimethylammonium bromide (CTAB) and AuNR functionalized via a ligand exchange method with either thiolated polyethylene glycol (PEG5000) or mercaptohexadecanoic acid (MHDA) were investigated for their stability in biological media and subsequent toxicological effects to HaCaT cells. AuNR-PEG and AuNR-MHDA exhibited minimal effects on cell proliferation, whereas AuNR-CTAB reduced cell proliferation significantly due to the inherent toxicity of the cationic surfactant to cells. Cell uptake studies indicated relatively low uptake for AuNR-PEG and high uptake for AuNR-MHDA. Reverse transcriptase polymerase chain reaction (RT-PCR) revealed that AuNR-PEG induced significant down-regulation, while AuNR-MHDA exhibited significant up-regulation of the transcription levels of 84 genes related to stress and toxicity. The results demonstrate that, although cell proliferation was not affected by both particles, gene expression was affected uniquely by both particles.

b.   Materials and Methods

AuNR Synthesis.

AuNRs were synthesized using the seed mediated growth method.[28] The preparation of the seed solution used the following typical protocol. Seven and a half mL of 0.2 M CTAB solution was mixed with 0.25 mL of 0.01 M $HAuCl_4$ in a beaker. While the solution was stirred vigorously, 0.6 mL of ice-cold 0.01 M of $NaBH_4$ was added and the solution turned brownish yellow. Vigorous stirring continued for another 2 min, and then it was kept undisturbed at room temperature. Ten milliliters of 0.01 M of $HAuCl_4$ was added into 237.5 mL of 0.1 M CTAB in a glass bottle, and the solution turned orange. Then, 1.5 mL of 0.01 M $AgNO_3$ was added to the solution, followed by gentle mixing. Next, 1.6 mL of 0.1 M ascorbic acid was added into the solution, followed by gentle inversion until the solution turned colorless. Two milliliters of seed solution was gently added to the growth solution. The solution sat on the bench undisturbed overnight, during which it turned reddish brown.

AuNR Ligand Exchange.

The CTAB surfactant on the AuNR surface was replaced with mercaptohexanoic acid (MHA) by round-trip phase transfer ligand exchange as described in detail in ref 27. Briefly, a two-phase extraction method was utilized in which AuNR-CTAB in water was functionalized with dodecanethiol to pull them into an organic phase. Acetone was used to facilitate this phase transfer. The dodecanethiol functionalized AuNRs then were pulled back into the aqueous phase by the ligand mercaptohexanoic acid, MHA. This resulted in both nanocapsules and nanobones coated with MHA.

AuNR Characterization.

To visualize the structure and size of the AuNRs, a drop of the stock for each sample was placed on a TEM grid and viewed using a Hitachi H-7600 microscope at 100 kV. The length and width were averaged for 100 particles measured using ImageJ software.[48] The concentration of stock solutions was determined using UV/vis spectroscopy. The molar concentration of the AuNR samples was calculated based on the Beer-Lambert Law using an extinction coefficient of $4.6 \times 10^9 \, M^{-1} \, cm^{-1}$ at 800 nm. This result was multiplied by the dilution factor to yield the final molar concentration. To convert molar concentration to mass concentration, it was assumed that the AuNRs were cylindrical with dimensions of 11 nm in diameter and 44 nm in length and have a density of $19.30 \, g \, cm^{-3}$.

Cell Culture.

The human keratinocyte cell line (HaCaT) was generously donated by the Army Research Lab. The cells were cultured in a flask with RPMI-1640 media (ATCC) supplemented with 10% fetal bovine serum (FBS, ATCC) and 1% penicillin/ streptomycin (pen/strep, Sigma). For AuNR exposure, serum-free medium was supplemented with 1% penicillin/streptomycin and was labeled as the exposure media (EM). Cells were incubated at 37°C in a humidified incubator with 5% CO2.

Stability of AuNRs in Biological Media.

The relative stability of each AuNR sample was determined after dispersion in water or EM using UV/vis, DLS, and DF microscopy. For these studies, AuNRs were suspended at a concentration of 100 µg/mL in water or EM and vortexed 30 s upon dilution and again immediately before analysis. Samples were analyzed within 1 h of dilution. UV/vis measurements were performed using a Varian Cary Bio 300 UV/ vis spectrophotometer. A Malvern Zetasizer was used for zeta potential analysis of AuNRs dispersed in water based on laser Doppler electrophoresis. For DF imaging, a small volume of this sample was spotted on a microscope slide and allowed to dry in air. Imaging was performed using a DF condenser from CytoViva attached to an Olympus BX41 microscope and DAGE camera/software.

Biochemical Analysis.

For biochemical assays, cells were seeded in a 96-well plate at a concentration of 1.0 x 10^5 cells/cm^2 and allowed to proliferate and adhere for 24 h. Cells were dosed with varying concentrations of AuNRs (5, 50, and 100 μg/mL) in media without serum (EM). The addition of EM to cells served as negative controls. Biochemical assays were initiated after a 24 h exposure and included the MTS, LDH, and ROS assays. The MTS assay was performed using the CellTiter 96 Aqueous One Solution Cell Proliferation Assay (Promega). The solution reagent contains a tetrazolium compound 3-(4, 5-dimethylthiazol-2-yl)-5-(3-carboxymethoxyphenyl)-2-(4-sulfophenyl)-2H-tetrazolium,
inner salt; MTS and an electron coupling reagent (phenazine ethosulfate; PES). Metabolically active cells reduce the MTS compound into a colored formazan product that is soluble in tissue culture medium and can be measured using a standard microplate reader. After 24 h, the supernatant containing AuNRs was aspirated from the wells and the cells were washed three times with 1X PBS to remove residual AuNRs. Mitochondrial function then was assessed according to the manufacturer's instructions. Lactase dehydrogenase (LDH) leakage was evaluated to determine the integrity of the cell membrane using the CytoTox 96 Non-Radioactive Cytotoxicity Assay (Promega, Madison, WI). This is a colorimetric assay that quantitatively measures LDH, a stable cytosolic enzyme that is released upon cell lysis. Released LDH in culture supernatants is measured with a 30 min coupled enzymatic assay that results in the conversion of a tetrazolium salt into a red formazan product. For both the MTS and LDH assay, the formazan product was measured by the amount of absorbance at 490 nm with a standard microplate reader (SpectraMAX GeminiXS, Molecular Devices, Sunnyvale, CA). The absorbance is directly proportional to the number of metabolically active cells and the number of lysed cells in the MTS and LDH assays, respectively. The spectrophotometer was calibrated to zero absorbance using EM without cells, and a background reading was taken immediately after the addition of reagent to eliminate interference due to slight absorbance of AuNRs near 490 nm. In order to further investigate oxidative stress as a mechanism of cytotoxicity, the reactive oxygen species (ROS) assay was performed using the BD Pathway confocal microscope, which collects images and corresponding fluorescence intensity data. The generation of ROS was probed with the Image IT Live Green ROS detection kit (Molecular Probe, Invitrogen, Carlsbad, CA). This assay is based on a fluorescent marker for ROS in live cells (5-carboxy-20,70-dichlorodihydrofluoresceine diacetate; carboxy-H$_2$DCFDA). The oxidation product of carboxy- H$_2$DCFDA has excitation/emission maxima of approximately 495/529 nm. As a positive control, 0.03% of hydrogen peroxide was added for 1 h to induce cellular apoptosis. After incubation, the cells were washed with warm PBS, then the monolayers were covered with the working solutions (carboxy-H$_2$DCFDA for ROS staining: 25 μM; Hoechst solution for nuclear staining: 1 μM). The cells were incubated at 37 °C for 30 min, protected from light to avoid bleaching of the fluorophores. After rinsing with PBS, the cells were observed with 4',6-diamidino-2-phenylindole (DAPI) and fluorescein isothiocyanate (FITC) filters, and fluorescence intensity for each was quantified. The results were presented in the form of fold change in fluorescence intensity of FITC/DAPI from control. For each biochemical assay, three

DISTRIBUTION A: Approved for public release; distribution unlimited. PA Case No. 88ABW-2013-4073

50

trials were performed for each sample with a value of n = 3 per trial for a total of 9 data points for each sample. Statistical significance from the control was determined for biochemical data using a two-tailed t test in Excel with p < 0.05.

Cell Morphology and Uptake.

The interaction of AuNR-MHDA and AuNR-PEG cells was determined using DF imaging and transmission electron microscopy (TEM). For DF imaging, cells were plated in two-chambered slides (surface area = 4 cm^2) at a concentration of 1.0×10^5 cells/cm^2 and allowed to proliferate and adhere for 24-48 h or until ~80% confluent. For DF imaging experiments with AuNR-MHDA and AuNR-PEG, cells were dosed with AuNRs diluted in EM at a concentration of 10 µg/mL and exposed for 24 h. Following exposure, cells were washed with PBS and fixed in 4% paraformaldehyde for 10 min. The cells were washed again with PBS, a coverslip was added and sealed with clear nail polish, and the slide was imaged using the CytoViva Hyperspectral Imaging System attached to an Olympus BX41 microscope (Aetos Technologies, Inc., Auburn, AL). Data were collected using ENVI software. For TEM imaging, cells were seeded at a concentration of 1.0 × 10^5 cells/cm^2 in 6-well plates (surface area = 9.6 cm^2) and allowed to adhere and proliferate for 48 h. Cells were dosed with AuNRs diluted in EM at a concentration of 50 µg/mL and exposed for 24 h. At the completion of the exposure period, cells were washed with PBS, trypsinized from the plate, and centrifuged at 1000g for 10 min. The pellet was fixed in 2% paraformaldehyde overnight at 4 °C. The following day, the cell pellets were washed with PBS, stained with 4% osmium tetroxide, and dehydrated with ethanol in a standard dilution sequence. The final pellet was cured in a vacuum oven using LR White resin (EMS) at 60°C. The cured sample was sectioned using a Leica EM UC6 Ultramicrotome and imaged using a Hitachi H-7600 TEM at the University of Dayton.

Gene Expression Analysis.

Real-time reverse transcriptase polymerase chain reaction (RT-PCR) was used to determine the effect of AuNR-MHDA and AuNR-PEG exposure on HaCaT cells at nontoxic doses (50 µg/mL). Cells were seeded and exposed to AuNRs as described for TEM imaging (1 × 10^5 cells/cm^2 in 9.6 cm^2/well = ~1 ×10^6 cells/trial). After 24 h exposure, RNA was isolated from the cells using a RNA isolation kit from Qiagen. The RNA yield was determined using the NanoDrop spectrophotometer (Thermo Scientific). Following RNA isolation, c-DNA was prepared using the RT^2 First Strand kit (SABiosciences) according to manufacturer's instructions. The stress and toxicity array (SABiosciences) was used to evaluate the expression of 84 genes related to stress and toxicity production in human cells. Expression of genes that are directly regulated by oxidative or metabolic stress and heat shock, as well as genes, which are representative of pathways activated by prolonged stress, such as apoptosis and senescence, are among those evaluated in this array. Three trials were performed for each sample (control, AuNR-MHDA, and AuNR-PEG). Data were analyzed based on average threshold cycles (C$_t$), which is equal to the cycle number at which fluorescence

generated crosses the fluorescence threshold. The C_t values were normalized by subtracting the C_t for each gene of interest (GOI) by the arithmetic average of C_t values for a set of 5 housekeeping (HKG) genes (C_t (GOI) - C_t (HKG) = ΔC_t). The resulting ΔC_t values were averaged for triplicate trials for each test sample (AuNR-MHDA and AuNR-PEG). The averaged ΔC_t values were further manipulated by a factor to relate C_t to gene expression ($2^{-\Delta Ct}$). Fold regulation was determined by dividing $2^{-\Delta Ct}$ value for each test sample by the $2^{-\Delta Ct}$ value for the negative control sample and taking the negative inverse for values less than 1.00. A heat map for each AuNR sample is shown in Figure 21 based on fold regulation. Genes that were significantly different for AuNRs versus the negative control were determined by a Student's t test comparing the ΔC_t values for the triplicate trials for each test sample compared to the ΔC_t values for the negative control. Genes with $p < 0.05$ are shown in Table 8.

c.   *Results and Discussion*

Characterization of AuNRs and Stability in Biological Media.

AuNRs were synthesized using the seed-mediated method described in the literature.[28] Transmission electron microscopy (TEM) characterized the morphology and size distribution of AuNRs. The morphology for all AuNR samples is rod-like with a small amount of spheres. AuNR-MHDA and AuNR-PEG exhibited similar size distributions and ARs, but these values were slightly smaller for AuNR-CTAB due to synthesis batch variability (Figure 17a-c, Table 6). UV-Vis spectroscopy and darkfield (DF) images confirmed that AuNRs have different stabilities in RPMI-1640 exposure media (EM), which was used as dosing media for cell studies. AuNR-MHDA shows a loss in the longitudinal peak in the UV-Vis spectrum, indicating agglomeration (Figure 17d, dashed vs. solid). DF images of the AuNR-MHDA also show an increase in the size of the particles and reduced background containing individual AuNRs when the solution was changed from water to EM (Figure 17d, insets). The longitudinal peak of the AuNR-PEG did not decrease or shift upon exposure to EM (Figure 17e, dashed vs. solid), and the DF image of the AuNR-PEG did not change substantially from water to EM (Figure 17e, insets), indicating that AuNR-PEG exhibits increased stability in media versus AuNR-MHDA. Zeta potentials of the AuNRs were measured using laser Doppler electrophoresis (Table 7). AuNR-PEG exhibited the most neutral zeta potential of -11.1 (0.989mV, while AuNR-CTAB and AuNR-MHDA exhibited zeta potentials of +44.5 and -46.2 mV, respectively. These changes in zeta potential confirmed the ligand exchange to neutral and negatively charged ligands.

Table 6. Size Characterization of AuNRs by TEM

sample	GNR-CTAB	GNR-MHDA	GNR-PEG
average length (nm)	25.6 ± 3.6	35.5 ± 8.9	31.7 ± 9.6
average width (nm)	8.2 ± 1.1	10.1 ± 2.8	9.1 ± 3.2
aspect ratio (AR)	3.1	3.5	3.5

Table 7. Zeta Potential Data for AuNRs in Water

sample	Zeta Potential (mV)	
	water	EM
GNR-CTAB	+44.5 ± 0.354	N/A
GNR-MHDA	−46.2 ± 0.354	−8.37 ± 0.781
GNR-PEG	−11.1 ± 0.989	−4.97 ± 0.950

DISTRIBUTION A: Approved for public release; distribution unlimited. PA Case No. 88ABW-2013-4073

53

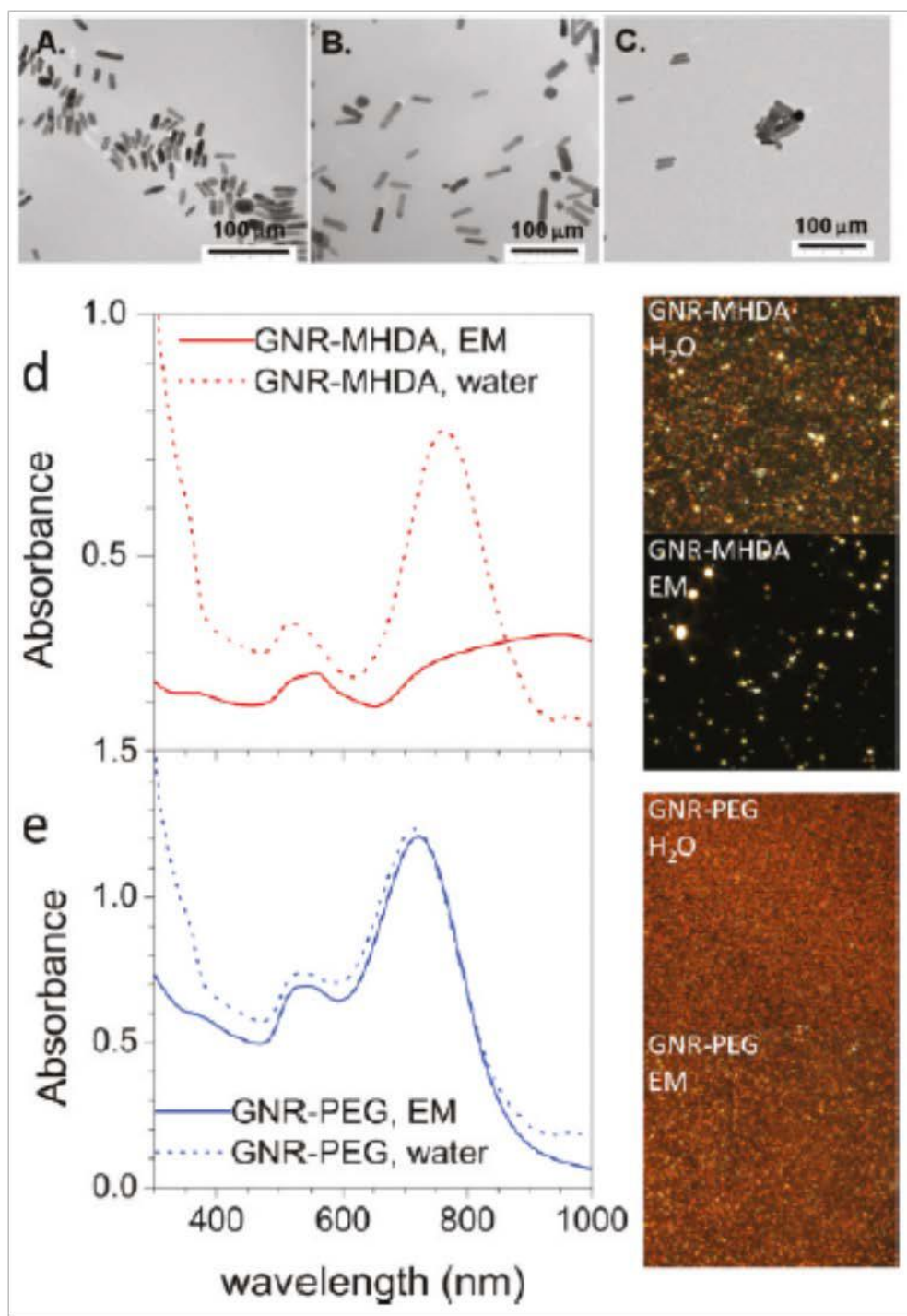***Figure 17. TEM characterization of AuNR morphology and size distribution. (a) AuNR-CTAB; (b) AuNR-MHDA; (c) AuNR-PEG. (d) UV/vis results for AuNR-PEG and (e) AuNR-MHDA in water (dashed) and EM (solid). Insets: DF images of AuNRs in water and media.***

When the AuNRs were exposed to EM, the zeta potentials for AuNR-MHDA and AuNR-PEG shifted closer to neutral, which has been observed by others and attributed to be

due to the amino acids in the EM adsorbing to the particles.[29] Because AuNR-CTAB precipitated in EM, it was not possible to measure its zeta potential, again demonstrating its poor stability in biological fluids.

Cell Proliferation

MTS assays were performed to determine the effect of 24 h exposure to AuNRs on the cell proliferation of HaCaT cells. After a 24 h exposure to AuNR-CTAB, cell proliferation was reduced by 80% from control at all concentrations, indicating that they are highly toxic (Figure 18a, solid red). Even at the lowest dose of 5 µg/mL, only 5-10% of the cells were still viable. There was no trend of a dose-dependent response. A similar response was shown by the CTAB alone (Figure 18c, solid gray). For AuNR-CTAB, the LDH membrane leakage assay was performed to verify MTS results (Figure 18b, solid red). There were high levels of membrane leakage at the lower doses, but at the higher doses, the amount of leakage was reduced. This is most likely caused by the fact that higher doses have a cytotoxic effect earlier than lower doses and thus result in lower LDH production by the cells. A similar trend was observed with the CTAB alone (Figure 18d, solid gray). Thus, the free CTAB inherent in the AuNR-CTAB sample is most likely responsible for the AuNR toxicity, as has been found by others.[13] Earlier times were probed for both MTS and LDH assays to determine whether LDH leakage could be observed at earlier times. Within 2 h of exposure to the AuNR-CTAB, there was a significant loss in cell proliferation (Figure 18a, hatched red) and an increase in membrane leakage (Figure 18b, hatched red). Again, these results were also observed after cellular exposure to CTAB alone (Figure 18c, d, hatched gray). The MTS assay was carried out for AuNR-PEG and AuNR-MHDA after a 24 h exposure to determine if surface functionalization could eliminate the toxic effects observed after exposure to AuNR-CTAB (Figure 18e). MTS results indicate that AuNR-MHDA (Figure 18e, orange) exhibited a slight proliferative effect (14%) on cells after a 24 h exposure period at low concentrations (5 µg/mL) and exhibited an inhibitive effect (12%) at high concentrations (100 µg/mL). AuNR-PEG (Figure 18e, blue) inhibited cell proliferation by only 10% at the highest concentration (100 µg/mL). These results show that changing the AuNR ligand can reduce their cytotoxic effect. The proliferative effect observed for AuNR-MHDA has been previously reported for gold nanostars.[30] This was also shown in another study where the MTS and Neutral Red assays showed increased proliferation after exposure to nanoparticles, but Trypan Blue exclusion assay and protein quantification did not show increased cell viability. It was hypothesized that the increase in proliferation observed by the mitochondrial-based assay is related to the high-energy demand for endocytosis, which increases mitochondrial enzyme activities.[31]
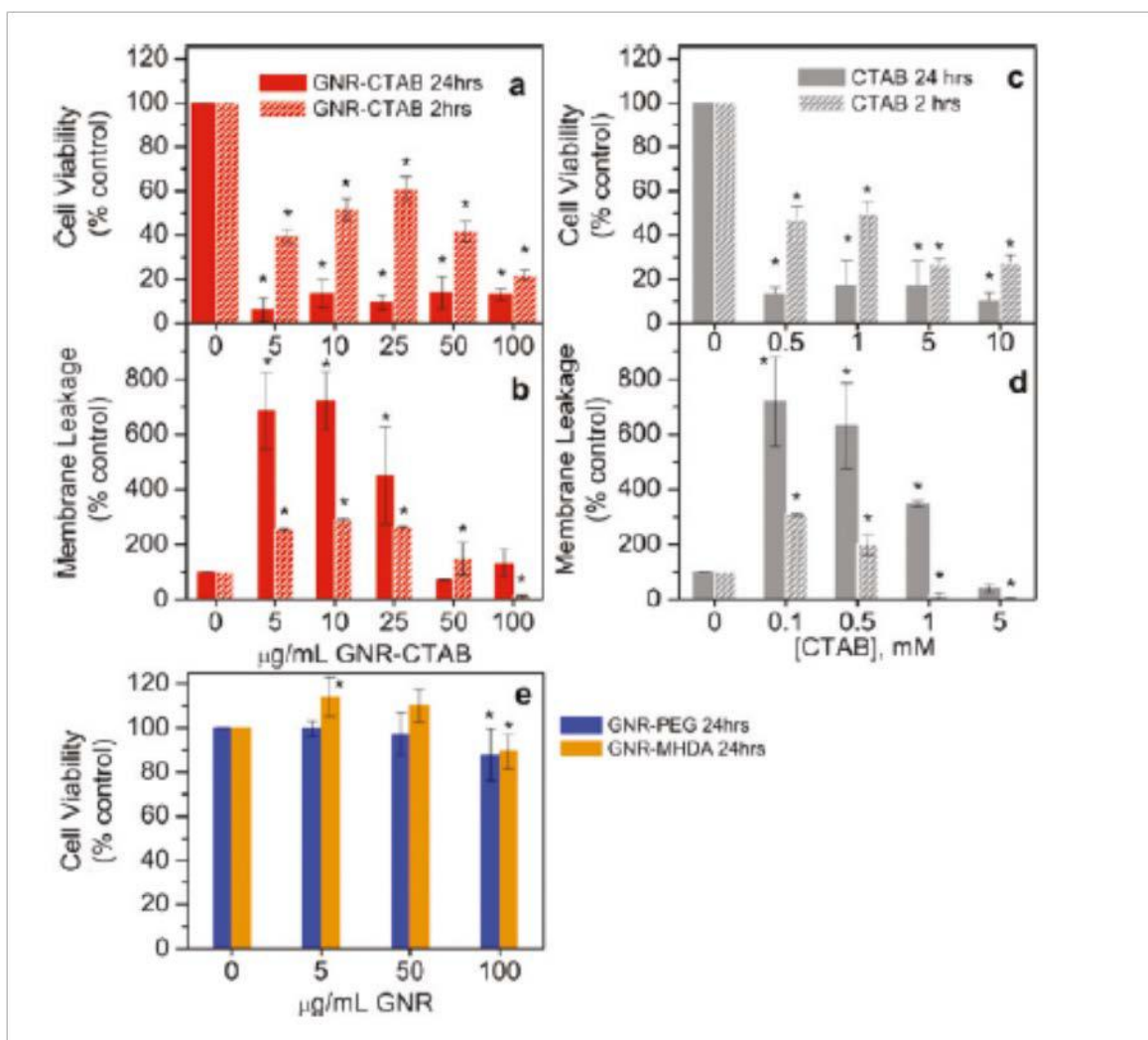
Figure 18. Cell proliferation following a 24 and 2 h treatment with AuNR-CTAB: (a) MTS assay; (b) LDH assay. Cell proliferation following a 24 and 2 h treatment with CTAB: (c) MTS assay; (d) LDH assay. (e) Cell proliferation following a 24 h treatment with AuNR-MHDA and AuNR-PEG measured via MTS assay. Error bars indicate standard deviation, asterisks denote significance (p < 0.05).

The ROS assay was performed to determine the oxidative stress response of cells exposed to AuNRs.9, 32 Qualitative data showed elevated production of ROS in cells exposed to AuNR-CTAB (Figure 19a-e). The negative control cells showed no ROS production as expected (Figure 19a), while the positive control cells showed ROS formation (Figure 19b). AuNR-CTAB exhibited a significant increase in ROS production, much higher than the positive control (Figure 19c). AuNR-PEG (Figure 19d) and AuNR-MHDA (Figure 19e) at 50 µg/mL resulted in no significant increase in ROS formation, as evidenced by the low green signal. Quantitative ROS data were collected for AuNR-CTAB, AuNR-MHDA, and AuNR-PEG in order to evaluate their effect on HaCaT cells. AuNR-CTAB at 5 µg/ mL showed a >40-fold increase of ROS formation relative to the

negative control (Figure 19f). Neither AuNR-MHDA (Figure 19g, orange) nor AuNR-PEG (Figure 19d, blue) over the concentration range of 0-100 µg/mL induced significant ROS after exposure, with ROS production showing only 0.9-1.01-fold differences.

Cell Morphology and Uptake.

DF imaging was used to probe cell morphology upon AuNR exposure and evaluate AuNR uptake relative to unexposed cells (Figure 20A). DF images indicated a high level of association of AuNR-MHDA with cells at the 24 h time point (Figure 20C) relative to AuNR-PEG (Figure 20E). Both AuNR-MHDA and AuNR-PEG appear to be internalized by cells, as determined by TEM (Figure 20D, F). AuNRs appear to have been taken up via endocytosis and are localized in endosomes within the cell. However, the number of AuNRs taken up is considerably greater for AuNR-MHDA than AuNR-PEG. This result is expected due to the nearly neutral zeta potential of PEGylated surfaces and relative inertness of PEGylated AuNRs in biological media. Additionally, larger agglomerates of AuNR-MHDA were exposed to cells, which could also play a role in the increased level of uptake due to an increased rate of gravitational settling versus AuNR-PEG.[33]

Stress and Toxicity Array Analysis.

Real-time reverse transcriptase polymerase chain reaction (RT-PCR) was used to determine the effect of AuNR-PEG and AuNR-MHDA on HaCaT cells at nontoxic doses (50 µg/mL), in addition to AuNR-MHDA at 5 µg/mL, to further investigate the proliferative effect observed by the MTS assay for cells exposed at that concentration. The stress and toxicity array was used to evaluate the expression of genes directly regulated by oxidative or metabolic stress and heat shock, as well as genes that are representative of pathways activated by prolonged stress, such as apoptosis and senescence. The expression of genes was determined based on their average threshold cycles (C_t), which is equal to the cycle number at which fluorescence generated crosses a threshold. The C_t values were normalized based on the mean of C_t values for a set of 5 housekeeping genes for each trial. Fold regulation was determined for each test sample (AuNR-PEG and AuNR-MHDA) versus the negative control based on an inverse relationship of the normalized C_t values, which were averaged for triplicate trials. A heat map for each AuNR sample is shown in Figure 21A-C based on fold regulation between ~5 and 10.
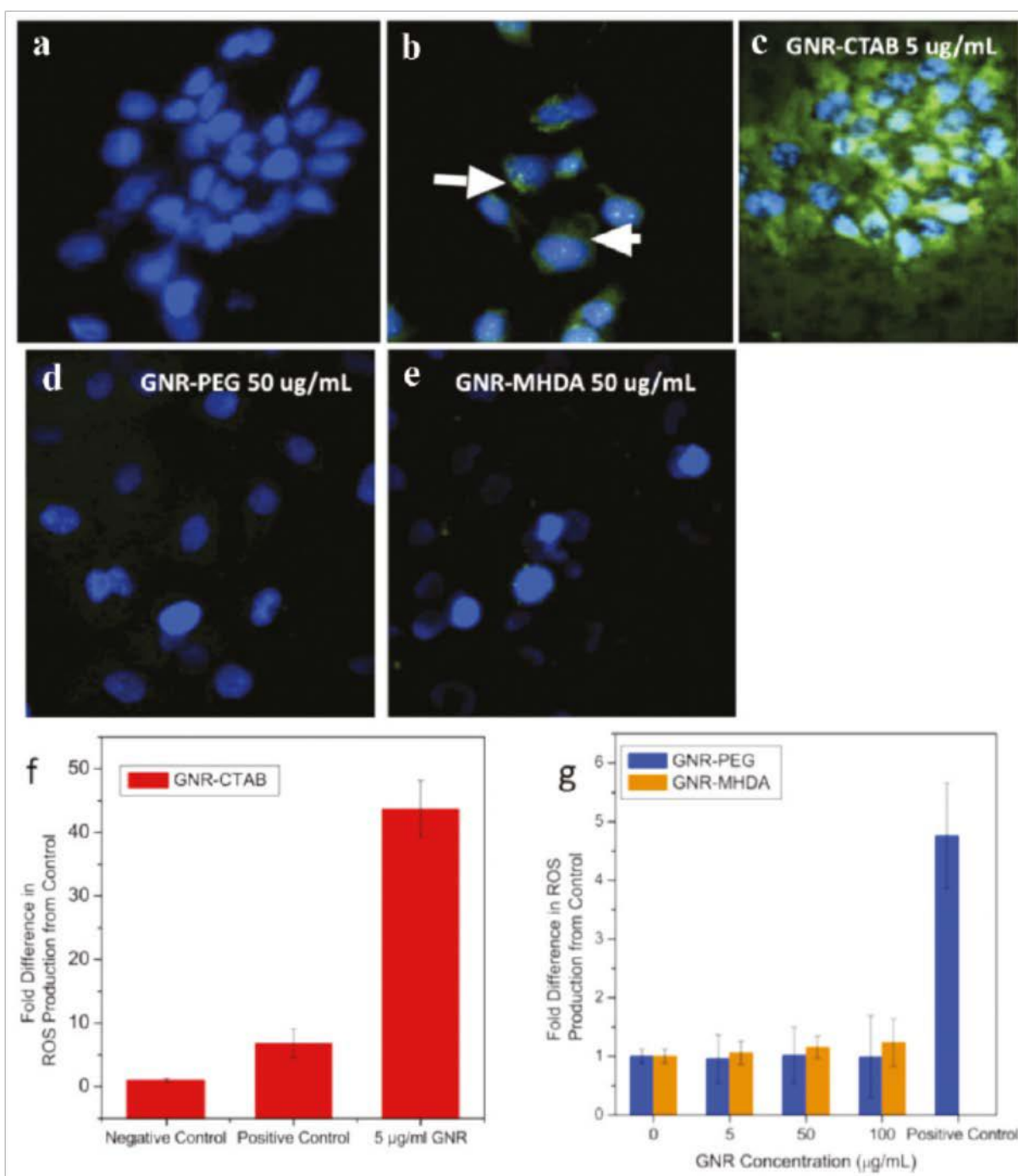
Figure 19. Oxidative stress production after exposure to AuNR-CTAB. (a) Negative control; (b) positive control (0.03% H2O2); (c) 5 µg/mL AuNR-CTAB, (d) 50 µg/mL AuNR-PEG, (e) 50 µg/mL AuNR-MHDA. Nuclei are stained with Hoechst, and the DCFH probe fluoresces green in the presence of ROS. White arrows indicate green fluorescence produced in positive control. (f) Oxidative stress production after exposure to AuNR-CTAB and (g) AuNR-MHDA and AuNR-PEG. Data were normalized FITC intensity to Hoechst intensity to account for cell number.

Genes that were significantly different for AuNRs versus the negative control were determined by a Student's t test comparing the normalized C_t values for each test sample to the negative control. Genes with $p < 0.05$ and fold regulation with magnitude >3 are shown in Table 8. Exposure to AuNR-PEG and AuNR-MHDA induced unique gene regulation patterns. AuNR-PEG induced down regulation of genes associated with apoptosis, DNA damage, and growth arrest, including those that encode for apoptosis-related cysteine peptidase, also known as interleukin 1, beta, convertase (CASP1), serine/threonine protein kinase (CHEK1), and growth arrest and DNA damage inducible protein, alpha (GADD45R) in the range of ~4.0 to ~5.6 (Table 8). CASP1 proteolytically cleaves pro-IL-1β to its mature, active form. Over expression of CASP1 leads to apoptosis; however, this gene was down-regulated, which has been found to occur in cancer cells.[34] CHEK1 is a DNA damage response, and its decrease allows survival by reducing the apoptosis pathway.[35] GADD45R down-regulation also occurs in tumor tissues. It is related to growth arrest and senescence but also plays a role in inducing apoptosis. It's down-regulation could be related to cell survival.[36] These results show that AuNR-PEG do have some effect on cellular response.

Figure 20. Cell uptake of AuNR-MHDA and AuNR-PEG in HaCaT cells via DF imaging (A,C,E)

and TEM (B,D,F). (A,B) Control (no particle exposure); (C,D) AuNR-MHDA; (E,F) AuNR-PEG.
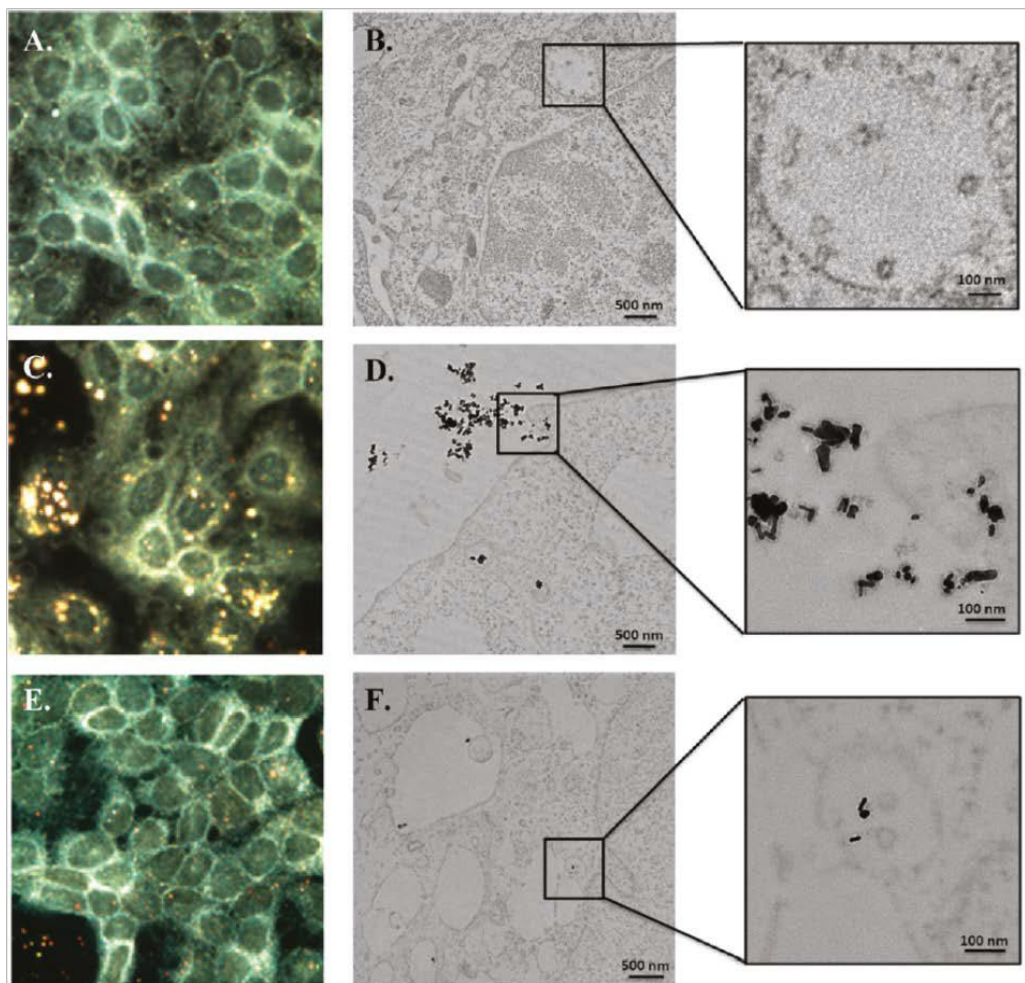In comparison, AuNR-MHDA at 50 µg/mL induced significant up-regulation of genes associated with heat shock and inflammation. Up-regulation of genes related to heat shock indicates that the cells exhibited stress responses upon exposure to AuNR-MHDA. When exposed at the high concentration (50 µg/mL), genes encoding for both heat shock 70 kDa protein 8 (HSPA8) and heat shock protein 90 (HSP90RA2) were up-regulated by 7.2 and 25.5, respectively. HSPA8 and HSP90RA2 are known to work as a molecular chaperone system, which facilitates correct protein folding.[37] HSPA8 has also been shown to enhance survival of cells and prevent apoptosis under stress conditions.[38] AuNR-MHDA exposure also up-regulated two genes associated with inflammation. IL-1R, which was up regulated by 7.8-fold, is in the interleukin 1 cytokine family and indicates a pro-inflammatory response. IL-1 is involved in modulating the immune response, and production of this protein affects many signal transduction pathways.[39] The other gene is Serpine1, a serine protease inhibitor, which was up-regulated 21.1-fold, which acts by inducing the synthesis of a protein that inhibits the activity of tissue plasminogen activator. Plasminogen activator plays a role in cell movement and inflammation.

Table 8. Genes Significantly Affected by Exposure to AuNRs (Boldface Indicates Significant Changes, (Student's t test, p < 0.05)

gene symbol	gene type	fold regulation (compared to control)		
		GNR-PEG 50 μg/mL	GNR-MHDA 50 μg/mL	GNR-MHDA 5 μg/mL
CASP1	apoptosis signaling	−5.6↓	1.0	−1.2
TNFRSF1A	apoptosis signaling	−1.5	1.5	8.4↑
CHEK2	DNA damage and repair	−5.0↓	1.2	1.2
XRCC2	DNA damage and repair	1.2	5.7↑	1.4
GADD45α	growth arrest and senescence	−4.0↓	−2.0	−2.2
HSPA8	heat shock	−3.0	7.2↑	1.8
HSP90αA2	heat shock	−1.7	25.5↑	18.8↑
IL-1α	inflammation	1.1	7.8↑	6.8↑
IL-1β	inflammation	−1.2	3.2	8.5↑
IL-6	inflammation	−1.9	1.4	6.4↑
SERPINE1	inflammation	−1.7	21.1↑	1.3

DISTRIBUTION A: Approved for public release; distribution unlimited. PA Case No. 88ABW-2013-4073

60
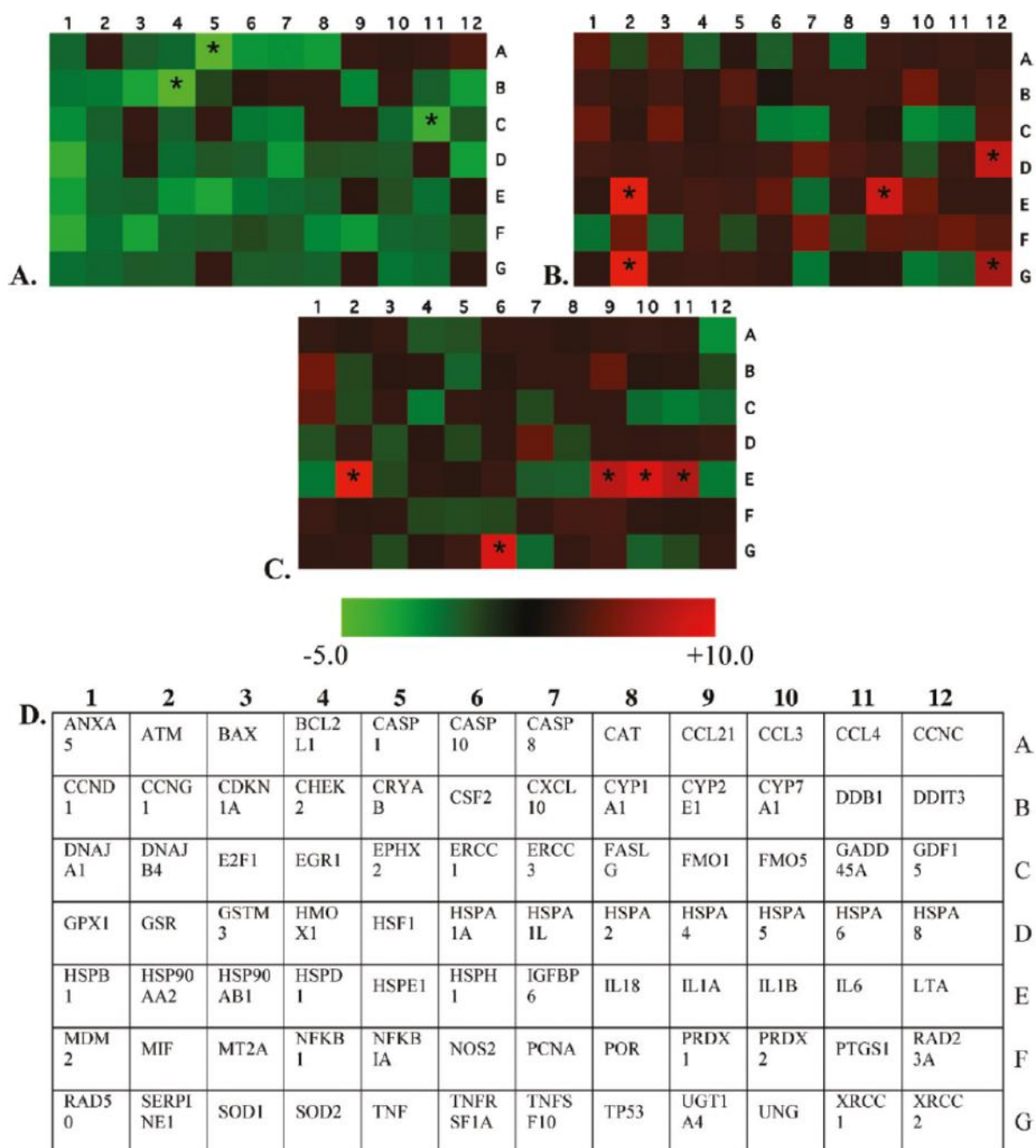
Figure 21. Representative heatmaps based on fold regulation of stress and toxicity genes after exposure to AuNRs compared to negative control sample. (A) AuNR-PEG 50 µg/mL; (B) AuNR-MHDA 50 µg/mL; (C) AuNR-MHDA 5 µg/mL. (D) Stress and toxicity array layout. Asterisks in the heat map correlate with p < 0.05 and fold regulation magnitude >3 for n g 3.

This suggests a significant anti-inflammatory effect induced by exposure to AuNR-MHDA after a 24 h exposure period. Serpine1 has been shown to stimulate keratinocyte adhesion and migration, in addition to rescue keratinocytes from plasminogen-induced

substrate detachment.[40] Interaction of AuNR-MHDA with the cell membrane could affect cell movement, which may play a role in the inhibition of plasminogen activator. Cell uptake could also be related to this inflammation response. In addition to heat shock and inflammation-related genes, one gene that plays a role in DNA damage repair was up-regulated significantly. XRCC2 was up-regulated by 5.7, which induces the synthesis of a protein, and is involved in DNA damage repair.[41] The reason for translation of this gene is unknown but could be related to insult suffered by HaCaT cells after significant cell uptake of AuNR-MHDA at 50 µg/mL. There were unique genes up-regulated by the low concentration of AuNR-MHDA (5 µg/mL). Cells exposed to the lower concentration of AuNR-MHDA shared upregulation of heat shock and inflammation genes HSP90RA2 and IL-1R, but not the other genes effect by AuNR-MHDA at 50 µg/mL. Interleukin 6 (IL-6) has been shown to increase the proliferation of keratinocytes, so the up-regulation of the gene encoding this protein could be related to the proliferation observed at low concentration exposure to AuNR-MHDA.[42] IL-1R and β are involved in a variety of cellular activities, including cell proliferation, differentiation, and apoptosis. Although keratinocytes produce both IL-1R and β mRNA in vitro, they do not process IL-1β, so the up-regulation observed does not likely indicate a route for cell proliferation.[43] The gene encoding for tumor necrosis factor (TNF), TNFRSF1A, was also up-regulated. TNF is a major mediator of apoptosis, inflammation, and immunity, which indicates additional cell signaling changes in the cells that are not indicated by the cell proliferation and morphology data.[44] Overall, the changes in gene expression for each test sample is likely caused by many different aspects of AuNR exposure to HaCaT cells. Direct interactions, such as binding to the cell membrane and uptake into intracellular organelles are one cause for changes in gene expression. However, these changes could also be related to indirect interactions. For example, one study in the literature showed that nanoparticles caused DNA damage to cells indirectly, without ever being directly exposed to or taken up by the cells.[45] It is hypothesized in this report that damage is due to transmission of purine nucleotides and intercellular signaling. Thus, it is possible that AuNRs could interact with macromolecules in the extracellular environment, which could affect cell signaling and therefore affect gene expression. AuNR interaction with macromolecules has been reported and is suggested to be a dynamic process that occurs in any biological environment.[30] In order to provide a threshold for the significance of the gene expression data, it may be useful to compare the results to data available in the literature for a material that is known to be toxic, such as asbestos. A study investigating the toxicity of asbestos using the stress and toxicity array showed up-regulation of genes related to inflammation and down regulation for genes associated with oxidative or metabolic stress with fold regulation in the range of 50-fold for increase to 10-fold for decrease, with an overall pro-inflammatory response.[46] In a study investigating the regulation of 5 genes related to inflammation in macrophages after exposure to AuNRs, positively charged end groups led to anti-inflammatory response, whereas negatively charged end groups led to pro-inflammatory effects, and neutral end groups seemed to exhibit minor effects with fold regulation of 33-fold for increase and 20-fold for decrease.[23] This indicates that up-regulation of Serpine1 to 21.1 after exposure to AuNR-MHDA is in line with previous assays and

indicates a less significant response than asbestos and equal to slightly more significant response compared to other AuNR surface chemistries.

d.   Conclusions

AuNRs coated with different ligands induced unique responses in HaCaT cells, supporting the strong influence of surface functionality on biological effects. Ligand exchange to MHDA and PEG resulted in improved viability and lower toxicity compared to AuNR-CTAB. However, while AuNR-PEG and AuNR-MHDA did not result in significant decreases in cell proliferation by the MTS test, they significantly affected the expression of genes related to stress and toxicity. These changes in gene expression were more significant for AuNR-MHDA, which could be due to the higher level interaction with serum proteins in the biological media, which are likely dynamically exchanged with different macromolecules once introduced into the cellular environment.[21,47] Additionally, AuNR-MHDA exhibited greater interaction with the cell membrane and uptake into the cells than that observed for AuNR-PEG. If changes in gene expression persist for long exposure, there is likely to be more severe toxicity for chronic exposures to AuNR-MHDA. AuNR-PEG shows promise for applications due to high level of stability in biological media and low level of cytotoxicity compared to AuNR-MHDA. However, PCR results suggest that AuNR-PEGs are not entirely inert, and the uptake is low, so for applications requiring more significant cell uptake, further studies into the effect of PEG molecular weight, different surface ligands, and the use of targeting moieties should be further investigated.

e.   References

[1]   Huang, X.; El-Sayed, I. H.; Qian, W.; El-Sayed, M. A. Cancer Cell Imaging and Photothermal Therapy in the Near- Infrared Region by Using Gold Nanorods. *J. Am. Chem. Soc.* 2006, 128, 2115–2120.

[2]   Wijaya, A.; Schaffer, S. B.; Pallares, I. G.; Hamad-Schifferli, K. Selective Release of Multiple DNA Oligonucleotides from Gold Nanorods. *ACS Nano* 2009, 3, 80–86.

[3]   Chen, C.-C.; Lin, Y.-P.; Wang, C.-W.; Tzeng, H.-C.; Wu, C.-H.; Chen, Y.-C.; Chen, C.-P.; Chen, L.-C.; Wu, Y.-C. DNA Gold Nanorod Conjugates for Remote Control of Localized Gene Expression by Near Infrared Irradiation. *J. Am. Chem. Soc.* 2006, 128, 3709–3715.

[4]   Agarwal, A.; Huang, S. W.; O'Donnell, M.; Day, K. C.; Day, M.; Kotov, N.; Ashkenazi, S. Targeted Gold Nanorod Contrast Agent for Prostate Cancer Detection by Photoacoustic Imaging. *J. Appl. Phys.* 2007, 102, 064701-4.

[5]   Lee, S. E.; Sasaki, D. Y.; Perroud, T. D.; Yoo, D.; Patel, K. D.; Lee, L. P. Biologically Functional Cationic Phospholipid- Gold Nanoplasmonic Carriers of RNA. *J. Am. Chem. Soc.* 2009, 131, 14066–14074.

[6]   Murphy, C. J.; Gole, A. M.; Stone, J. W.; Sisco, P. N.; Alkilany, A. M.; Goldsmith, E. C.; Baxter, S. C. Gold Nanoparticles in Biology: Beyond Toxicity to Cellular Imaging. *Acc. Chem. Res.* 2008, 41, 1721–1730.

[7]   Lewinski, N.; Colvin, V.; Drezek, R. Cytotoxicity of Nanoparticles. *Small* 2008, 4, 26–49.

[8]   Hussain, S. M.; Braydich-Stolle, L. K.; Schrand, A. M.; Murdock, R. C.; Yu, K. O.; Mattie, D. M.; Schlager, J. J.; Terrones, M. Toxicity Evaluation for Safe Use of Nanomaterials: Recent Achievements and Technical Challenges. *Adv. Mater.* 2009, 21, 1549–1559.

[9]   Carlson, C.; Hussain, S. M.; Schrand, A. M.; Braydich-Stolle, K. L.; Hess, K. L.; Jones, R. L.; Schlager, J. J. Unique Cellular Interaction of Silver Nanoparticles: Size-Dependent

DISTRIBUTION A: Approved for public release; distribution unlimited. PA Case No. 88ABW-2013-4073

63

Generation of Reactive Oxygen Species. *J. Phys. Chem.* B 2008, 112, 13608–13619.

[10]   Niidome, T.; Yamagata, M.; Okamoto, Y.; Akiyama, Y.; Takahashi, H.; Kawano, T.; Katayama, Y.; Niidome, Y. PEG Modified Gold Nanorods with a Stealth Character for In Vivo Applications. *J. Controlled Release* 2006, 114, 343–347.

[11]   Huff, T. B.; Hansen, M. N.; Zhao, Y.; Cheng, J.-X.; Wei, A. Controlling the Cellular Uptake of Gold Nanorods. *Langmuir* 2007, 23, 1596–1599.

[12]   Chithrani, B. D.; Ghazani, A. A.; Chan, W. C. W. Determining the Size and Shape Dependence of Gold Nanoparticle Uptake into Mammalian Cells. *Nano Lett.* 2006, 6, 662–668.

[13]   Alkilany, A. M.; Nagaria, P. K.; Hexel, C. R.; Shaw, T. J.; Murphy, C. J.; Wyatt, M. D. Cellular Uptake and Cytotoxicity of Gold Nanorods: Molecular Origin of Cytotoxicity and Surface Effects. *Small* 2009, 5, 701–708.

[14]   Hauck, T.; Ghazani, A.; Chan, W. C. W. Assessing the Effect of Surface Chemistry on Gold Nanorod Uptake, Toxicity, and Gene Expression in Mammalian Cells. *Small* 2008, 4, 153–159.

[15]   Manohar, S.; Rayavarapu, R.; Petersen, W.; van Leeuwen, T. G. Cell Viability Studies of PEG-Thiol Treated Gold Nanorods As Optoacoustic Contrast Agents. *SPIE Proc.* 2009, 7177, 71772D.

[16]   Smith, D. K.; Korgel, B. A. The Importance of the CTAB Surfactant on the Colloidal Seed-Mediated Synthesis of Gold Nanorods. *Langmuir* 2008, 24, 644–649.

[17]   Parab, H. J.; Chen, H. M.; Lai, T.-C.; Huang, J. H.; Chen, P. H.; Liu, R.-S.; Hsiao, M.; Chen, C.-H.; Tsai, D.-P.; Hwu, Y.-K. Biosensing, Cytotoxicity, and Cellular Uptake Studies of Surface-Modified Gold Nanorods. *J. Phys. Chem.* C 2009, 113, 7574–7578.

[18]   Leonov, A. P.; Zheng, J.; Clogston, J. D.; Stern, S. T.; Patri, A. K.; Wei, A. Detoxification of Gold Nanorods by Treatment with Polystyrenesulfonate. *ACS Nano* 2008, 2, 2481– 2488.

[19]   Goodman, C. M.; McCusker, C. D.; Yilmaz, T.; Rotello, V. M. Toxicity of Gold Nanoparticles Functionalized with Cationic and Anionic Side Chains. *Bioconjugate Chem.* 2004, 15, 897–900.

[20]   Connor, E. E.; Mwamuka, J.; Gole, A.; Murphy, C. J.; Wyatt, M. D. Gold Nanoparticles Are Taken Up by Human Cells but Do Not Cause Acute Cytotoxicity. *Small* 2005, 1, 325–327.

[21]   Lynch, I.; Cedervall, T.; Lundqvist, M.; Cabaleiro-Lago, C.; Linse, S.; Dawson, K. A. The Nanoparticle Protein Complex as a Biological Entity; A Complex Fluids and Surface Science Challenge For the 21st Century. *Adv. Colloid Interface Sci.* 2007, 134-135, 167-174.

[22]   Barnes, C. A.; Elsaesser, A.; Arkusz, J.; Smok, A.; Palus, J.; Lesniak, A.; Salvati, A.; Hanrahan, J. P.; Jong, W. H. D.; Dziubaltowska, E.; et al. Reproducible Comet Assay of Amorphous Silica Nanoparticles Detects No Genotoxicity. *Nano Lett.* 2008, *8*, 3069-3074.

[23]   Bartneck, M.; Keul, H. A.; Singh, S.; Czaja, K.; Bornemann, J.; Bockstaller, M.; Moeller, M.; Zwadlo-Klarwasser, G.; Groll, J. Rapid Uptake of Gold Nanorods by Primary Human Blood Phagocytes and Immunomodulatory Effects of Surface Chemistry. *ACS Nano* 2010, 4, 3073–3086.

[24]   Pan, Y.; Leifert, A.; Ruau, D.; Neuss, S.; Bornemann, J.; Schmid, G.; Brandau, W.; Simon, U.; Jahnen-Dechent, W. Gold Nanoparticles of Diameter 1.4 nm Trigger Necrosis by Oxidative Stress and Mitochondrial Damage. *Small* 2009, 5, 2067–2076.

[25]   Balasubramanian, S. K.; Jittiwat, J.; Manikandan, J.; Ong, C.-N.; Yu, L. E.; Ong, W.-Y. Biodistribution of Gold Nanoparticles and Gene Expression Changes in the Liver and Spleen after Intravenous Administration in Rats. *Biomaterials* 2010, 31, 2034–2042.

[26]   Arikawa, E.; Pan, H.; Sun, Y.; Wang, J.; Zhou, Q.; Prabhakar, S.; Wang, Y. B.; Dial, S.; Ning, B.; Guo, L.; et al. P53-M Real-Time PCR Array for Multi-Gene Expression Profiling and Microarray Data Validation: RT2 Profiler PCR Array. *J. Biomol. Tech.* 2007, 18, 18–19.

[27]   Wijaya, A.; Hamad-Schifferli, K. Ligand Customization and DNA Functionalization of Gold

Nanorods via Roundtrip Phase Transfer Ligand Exchange. *Langmuir* 2008, 24, 9966–9969.

[28] Sau, T. K.; Murphy, C. J. Seeded High Yield Synthesis of Short Au Nanorods in Aqueous Solution. *Langmuir* 2004, 20, 6414–6420.

[29] Phenrat, T.; Long, T. C.; Lowry, G. V.; Veronesi, B. Partial Oxidation ("Aging") and Surface Modification Decrease the Toxicity of Nanosized Zerovalent Iron. *Environ. Sci. Technol.* 2009, 43, 195–200.

[30] Wei, Q.; Song, H.-M.; Leonov, A. P.; Hale, J. A.; Oh, D.; Ong, Q. K.; Ritchie, K.; Wei, A. Gyromagnetic Imaging: Dynamic Optical Contrast Using Gold Nanostars with Magnetic Cores. *J. Am. Chem. Soc.* 2009, 131, 9728–9734.

[31] Di Virgilio, A. L.; Reigosa, M.; de Mele, M. F. L. Response of UMR 106 Cells Exposed to Titanium Oxide and Aluminum Oxide Nanoparticles. *J. Biomed. Mater. Res. A* 2010, 92A, 80–86.

[32] Shukla, R.; Bansal, V.; Chaudhary, M.; Basu, A.; Bhonde, R. R.; Sastry, M. Biocompatibility of Gold Nanoparticles and Their Endocytotic Fate Inside the Cellular Compartment: A Microscopic Overview. *Langmuir* 2005, 21, 10644–10654.

[33] Teeguarden, J. G.; Hinderliter, P. M.; Orr, G.; Thrall, B. D.; Pounds, J. G. Particokinetics In Vitro: Dosimetry Considerations for In Vitro Nanoparticle Toxicity Assessments. *Toxicol. Sci.* 2007, 95, 300–312.

[34] Feng, Q.; Li, P.; Salamanca, C.; Huntsman, D.; Leung, P. C. K.; Auersperg, N. Caspase-1R Is Down-Regulated in Human Ovarian Cancer Cells and the Overexpression of Caspase- 1R Induces Apoptosis. *Cancer Res.* 2005, 65, 8591–8596.

[35] Peng, G.; Lin., S.-Y. Exploiting the Homologous Recombination DNA Repair Network for Targeted Cancer Therapy. World *J. Clin. Oncol.* 2011, 2, 73–79.

[36] Higashi, H.; Vallb€ohmer, D.; Warnecke-Eberz, U.; Hokita, S.; Xi, H.; Brabender, J.; Metzger, R.; Baldus, S. E.; Natsugoe, S.; Aikou, T.; et al. Down-Regulation of Gadd45 Expression Is Associated with Tumor Differentiation in Non-small Cell Lung Cancer. *Anticancer Res.* 2006, 26, 2143–2147.

[37] Brychzy, A.; Rein, T.; Winklhofer, K. F.; Hartl, F. U.; Young, J. C.; Obermann, W. M. J. Cofactor Tpr2 Combines Two TPR Domains and a J Domain To Regulate the Hsp70/Hsp90 Chaperone System. *EMBO J.* 2003, 22, 3613–3623.

[38] Jolly, C.; Morimoto, R. I. Role of the Heat Shock Response and Molecular Chaperones in Oncogenesis and Cell Death. *J. Natl. Cancer I* 2000, 92, 1564–1572.

[39] Bankers-Fulbright, J. L.; Kalli, K. R.; McKean, D. J. Interleukin-1 Signal Transduction. *Life Sci.* 1996, 59, 61–83.

[40] Providence, K.; Higgins, S.; Mullen, A.; Battista, A.; Samarakoon, R.; Higgins, C.; Wilkins-Port, C.; Higgins, P. SERPINE1 (PAI-1) Is Deposited into Keratinocyte Migration "Trails" and Required for Optimal Monolayer Wound Repair. *Arch. Dermatol. Res.* 2008, 300, 303–310.

[41] Tambini, C. E.; Spink, K. G.; Ross, C. J.; Hill, M. A.; Thacker, J. The Importance of XRCC2 in RAD51-Related DNA Damage Repair. *DNA Repair* 2010, 9, 517–525.

[42] Takahashi, H.; Tsuji, H.; Hashimoto, Y.; Ishida-Yamamoto, A.; Iizuka, H. Cell Proliferation and Cytokine Induction by TNF-R of Psoriatic Keratinocytes Are Not Different from Normal Keratinocytes In Vitro. *Indian J. Dermatol.* 2009, 54, 237–239.

[43] Mizutani, H.; Black, R.; Kupper, T. S. Human Keratinocytes Produce but Do Not Process Pro-interleukin-1 (IL-1) beta. Different Strategies of IL-1 Production and Processing in Monocytes and Keratinocytes. *J. Clin. Invest.* 1991, 87, 1066–1071.

[44] Chen, G.; Goeddel, D. V. TNF-R1 Signaling: A Beautiful Pathway. *Science* 2002, 296, 1634–1635.

[45] Bhabra, G.; Sood, A.; Fisher, B.; Cartwright, L.; Saunders, M.; Evans, W. H.; Surprenant, A.; Lopez-Castejon, G.; Mann, S.; Davis, S. A.; et al. Nanoparticles Can Cause DNA Damage Across a Cellular Barrier. *Nat. Nanotechnol.* 2009, 4, 876–883.

[46]   Duncan, K. E.; Ghio, A. J.; Dailey, L. A.; Bern, A. M.; Gibbs-Flournoy, E. A.; Padilla-Carlin, D. J.; Roggli, V. L.; Devlin, R. B. Effect of Size Fractionation on the Toxicity of Amosite and Libby Amphibole Asbestos. *Toxicol. Sci.* 2010, 118, 420–434.

[47]   Cedervall, T.; Lynch, I.; Lindman, S.; Thulin, T. B. E.; Nilsson, H.; Dawson, K. A.; Linse, S. Understanding the Nanoparticle-Protein Corona Using Methods to Quantify Exchange Rates and Affinities of Proteins for Nanoparticles. *Proc. Natl. Acad. Sci. U.S.A.* 2007, 104, 2050–2055.

[48]   Abramoff, M. D.; Magelhaes, P. J.; Ram, S. J. Image Processing with ImageJ. *Biophotonics Int.* 2004, 11, 36–42.

4.   Evaluation of Global Gene Expression in Response to Different Sizes of Gold Nanoparticles

a.   Purpose

Gold nanoparticles (AuNPs), with relatively low toxicity, have shown promise as novel materials for therapeutics, imaging, diagnostics, and delivery systems. Unanticipated alterations at the genomic level, however, still may contribute to long-term health consequences. This study investigated genomic alterations induced in HaCaT cells exposed to AuNPs of highly uniform sizes. Exposure to low levels of AuNPs led to minimal uptake, readily visualized in intracellular vacuoles. The 60 nm AuNPs suppressed homeostasis genes, i.e., genes that are responsible for maintaining intracellular stability, cell signaling, and cell cycle regulation. The physicochemical characterization of the AuNPs showed significant differences in aggregate structures between 30 and 60 nm AuNPs—30 nm AuNPs forming comparatively more densely packed aggregates—that is likely to be responsible for the gene suppression. The discrete size effects were further evidenced by changes in G-protein coupled receptor signaling produced upon exposure to the 30nm gold particles. These results provide with strong evidence for fractal dimension of nanoparticles being a strong contributor to observed biological responses and changes in gene expression.

b.   Materials and Methods

Cell Culture

The human keratinocyte cell line, HaCaT, was purchased from ATCC (Manassas, Virginia). The cells were cultured in flasks with RPMI Medium 1640 cell culture media (Invitrogen, Carlsbad, CA) supplemented with 10% fetal bovine serum (ATCC) and 1% penicillin/streptomycin (Sigma St Louis, MO), and incubated at 37^0C in a humidified incubator with 5% $CO2$. For nanoparticle exposure protocols, the RPMI Medium 1640 media was supplemented with 1% penicillin/streptomycin and no serum.

Nanoparticles

Gold nanoparticles (AuNPs) of 30nm and 60nm were purchased from the National Institute of Standards and Technology (NIST, Gaithersburg, MD). Each standard reference material was supplied as 5mL of approximately 50µg/mL citrate-stabilized

AuNPs in an aqueous suspension in a sealed pre-scored glass ampoule sterilized by gamma irradiation. Verification of the size and morphology of the AuNPs was performed with transmission electron microscopy (TEM) on a Philips/FEI CM200 Lab6 instrument at 200kV. Charge was verified via zeta potential (ZP) measurements on a Malvern Zetasizer machine. The changes in dispersion/agglomeration of the AuNPs were examined with DLS after suspension in RMPI cell culture media (+1% penicillin/streptomycin) in the as-received form (50 µg/ml in water) and at a final concentration of 2.5µg/ml.

Fractal Dimension Determination

An ALV-CGS 3 compact goniometer system (ALV-GmbH, Langen, Germany) was used to perform SLS measurements of AuNPs in cellular media condition. This equipment uses a 22mW He-Ne laser having wavelength of 632.8 nm along with ALV/LSE-5004 digital auto correlator (ALV-GmbH, Langen, Germany) to de-convolute the scattering data. Stock suspensions of nanoparticles of two different nominal diameter (nominal diameter of 30 nm and 60 nm) were diluted at 2.5 mg/L concentration in RPMI media in presence of 1% Streptomycin. A 2mL nanoparticle suspension was added to previously cleaned disposable borosilicate glass vials (Fisher Scientific, Pittsburg, PA). The cleaning procedure is described elsewhere[1-3]. The particles were exposed to cell culture condition for 1hr (to allow for achieving stable aggregate structure) prior to initiating the light scattering measurements. The Photon counting module (Perkin Elmer; Dumberry, Canada) which was appended to the equipment operating at 1.2 amperes and 5 V, measured the light intensity at 37 °C for a scattering angle range of 12.5° to 100° at 10s time interval between consecutive readings. Triplicate measurements were performed for each scattering angle. Fractal dimension of the aggregate was computed using a log-log plot of the scattering intensity vs. scattering wave vector magnitude. Linear angular range for scattering was identified and the slope of the best-fit line yielded in D_f.

RNA Isolation & Quantification

Total RNA was extracted from cultured human keratinocytes using an E.Z.N.A.® Total RNA Kit (Omega Bio-Tek, Inc. Norcross GA USA) according to the manufacturer's instructions. For gene expression studies, 500,000 cells were seeded into each well of a 6-well plate and allowed to adhere for 24h. Cells then were incubated with 2.5µg/mL of 10nm, 30nm or 60nm AuNPs in a total volume of 2mL exposure media in triplicate. Control cells were incubated with 2mL exposure media alone. After 24 hours, medium containing AuNPs not taken up by the cells was aspirated and TRK lysis buffer was added directly to the 6 well plate. Buffer and lysed cells then were transferred to a 1.5mL RNase free Eppendorf tube and the remainder of the protocol was completed per manufacturer's instructions. The concentration and quality of total RNA were determined using the Agilent 2100 Bioanalyzer and the RNA 6000 Nano Chip kit (Agilent, Santa Clara CA) which allows for the detection of total RNA down to 5ng.

Affymetrix 3'expression analysis

Affymetrix 3' expression arrays have probe sets targeted to the 3' end of the transcript. One hundred nanograms of total RNA was amplified and labeled for hybridization to these arrays using the Affymetrix 3' IVT express kit. Briefly, a single stranded cDNA was synthesized using an oligo-dT primer with an attached T7 promoter sequence. After making the complementary second strand, the double-stranded cDNA molecule was amplified in a linear fashion by in vitro transcription (IVT) using T7 RNA polymerase. As the aRNA (amplified RNA, also commonly referred to as cRNA) was being made, a biotinylated nucleotide analog was incorporated and served as a label for the message. After fragmentation, 40µg of this labeled anti-sense aRNA was hybridized to the HG U133 plus 2.0 microarray. This microarray allows the researcher to analyze gene expression across the entire human genome for one sample. It is comprised of more than 54,000 probe sets and 1,300,000 distinct oligonucleotide features. After overnight hybridization to the array, the chips were washed to remove any non-bound target and stained with a streptavidin phycoerythrin conjugate to amplify the signal intensity. Chips then were scanned using the GeneChip® Scanner 3000.

Data Analysis

Upon review of the report file for each chip (Table S3 Supplemental Information, Appendix III) and confirmation that the chip image was not smeared or distorted, the Affymetrix .CEL file for each sample was imported into GeneSpring™ GX using Guided Workflow. By default, the Guided Workflow option does RMA and baseline transformation to the median of all samples. Additionally, the lowest 20th percentile of all the raw intensity values was removed and a profile plot of filtered entities was generated. Gene expression in each treatment (10nm, 30nm and 60nm AuNPs) was individually compared with the sham-treated control group. The ratio of signal to control (used for fold changes) and log of ratio of signal to control (used for clustering and statistics) were assigned to each gene. Statistically significant difference from control was determined using analysis of variance (ANOVA) with post hoc comparisons (Student Newman Keuls).

Next, data were analyzed through the use of Ingenuity Pathways Analysis (IPA) (Ingenuity Systems®, www.ingenuity.com). A dataset containing gene identifiers and corresponding expression values was uploaded into IPA. Each identifier was mapped to its corresponding gene object in the Ingenuity® knowledge base. A fold change cutoff of 1.5 was set to identify genes whose expression was significantly different from control. These genes, called focus genes, were overlaid onto a global molecular network developed from information contained in the Ingenuity knowledge base. Networks of these focus genes then were algorithmically generated based on their connectivity. Canonical pathways analysis identified the pathways from the IPA library of canonical pathways that were most significant to each of the data sets. A pathway is a graphical representation of the molecular relationships between genes/gene products. Genes or

gene products are represented as nodes, and the biological relationship between two nodes is represented as a line. All lines are supported by at least 1 reference from the literature, from a textbook, or from canonical information stored in the Ingenuity knowledge base. The intensity of the node color indicates the degree of up- (red) or down- (green) regulation.

The Functional Analysis of a network identified the biological functions and/or diseases that were most significant to the genes in the network. The network genes associated with biological functions and/or diseases in the Ingenuity knowledge base were considered for the analysis. Benjamini-Hochman Multiple Testing Correction was used to calculate a p-value determining the probability that the significant functions within a dataset are due to chance alone and to indicate the fraction of false positives among significant functions.

Canonical Pathways Analysis identified the pathways from the Ingenuity Pathways Analysis library of canonical pathways that were most significant to the dataset. Genes from the dataset that met the fold change cutoff of 1.5 and were associated with a canonical pathway in the Ingenuity knowledge base were considered for the analysis. The significance of the association between the dataset and the canonical pathway was measured in 2 ways: 1) A ratio of the number of genes from the dataset that met the expression value cutoff that map to the pathway divided by the total number of molecules that exist in the canonical pathway is displayed. 2) Benjamini-Hochman Multiple Testing Correction was used to calculate a p-value determining the probability that the association between the genes in the dataset and the canonical pathway is explained by chance alone.

c.   *Results and Discussion*

Characterization of Gold Nanoparticles

In order to verify the primary nanoparticle diameter and spherical morphology, TEM imaging was performed on the 30 and 60 nm AuNPs, respectively (Figure 22 A, D). Both the AuNPs showed highly uniform sizes that are close to the manufacturer reported values. The extent of aggregation at low concentrations (2.5 µg/mL) was evaluated using DLS over time (Figure S2A-B, Appendix III). After 24 hours in exposure conditions, both the 30 and 60 nm AuNPs aggregated to micron sized aggregates (Figure S2A), with the nanoparticles only demonstrating a nano-size during the first 6 hours following dispersion (Figure S2B, Appendix III). The SLS data demonstrated that the fractal dimensions (D_f) for the 30 and 60 nm AuNPs were 2.61 ± 0.22 and 2.15 ± 0.32, respectively. This is a large difference in packing density where the smaller 30 nm AuNPs are found to have significantly higher packing density compared to the larger 60 nm ones.
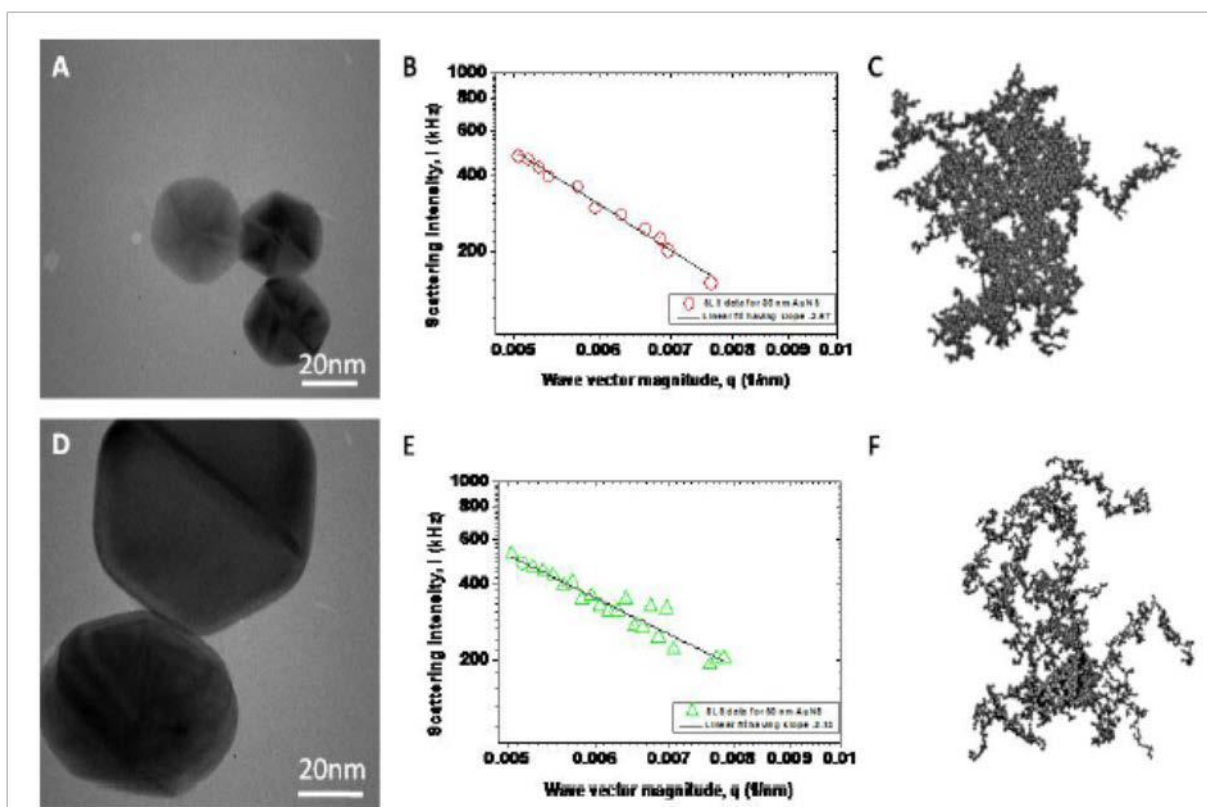
Figure 22. Characterization of NIST Gold Nanoparticles. A-C 30 nm NIST Gold. D-F 60 nm NIST Gold. A,D Representive TEM images that demonstrated the spherical morphology and primary diameter. B,E SLS data for the 30 nm and 60 nm NIST gold, respectively. C,F Cartoon depicting the fractal dimension pattern of the gold nanoparticle aggregates based on the SLS data (30 nm and 60 nm respectively).

Gene Expression

The changes in gene expression for human cultured keratinocytes exposed to 2 different sizes of AuNPs over 24 hours were examined in an attempt to understand the molecular interaction of nanomaterials within biological systems (Figure 23). A principal component analysis (PCA) shows that the probe sets changed after nanoparticle treatment clustered together according to size (Figure 23A). Table S2 (Appendix III) shows the cellular location and molecular function of some of the common genes changed upon AuNP treatment. The AuNP modulated genes were involved in high-level biological functions such as Cell Death, Cell Cycle, Cellular Growth and Proliferation, Cellular Development, and Cellular Movement.

Although many genes were commonly affected for both samples, there were also unique changes observed. Table S3 (Appendix III) shows the cellular location and molecular function of genes uniquely changed by each size AuNP treatment. The 30nm AuNP treatment modulated prostaglandin E receptor G (PTGER), a gene involved with

high-level biological functions such as cell morphology, cell development, molecular transport, cell signaling, and cellular assembly and organization. The 60nm AuNPmodulated several genes that are involved in cellular development, cell growth and proliferation, cell cycle, and cell death.

Figure 23B shows average fold change for currently mapped gene identifications (IDs) for each treatment group. Treatment with 30nm or 60nm particles caused equal amounts of upward and downward expression. The 60nm particles caused the greatest number of genes to be changed with differential expression being mostly down regulated (Figure 23C).
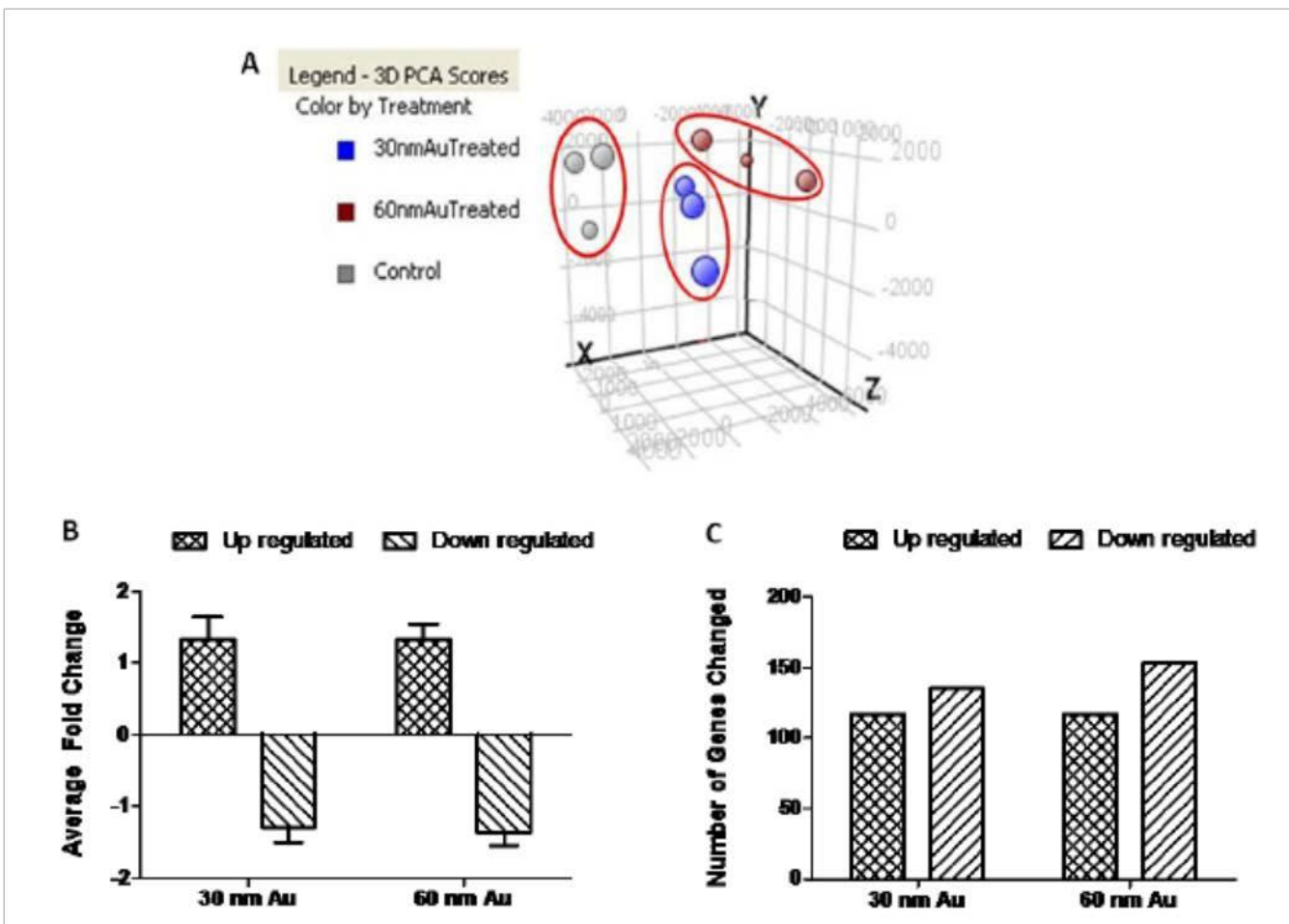

Figure 23. Overview and Changes in Gene Expression. (A) Principal Component Analysis (PCA) plot demonstrating that the altered transcripts cluster according to AuNP size, (B) Average Fold Change observed with each treatment group. (C) Number of genes changed by each treatment group.

Size effects on Canonical Pathways

Due to the unique gene changes for each size of AuNP, further core analysis was performed on each set of genes from Table S3 (Appendix III). The observed effect of 30nm AuNPs treatment was up-regulation of signaling pathways, specifically Eicosanoid, cAMP signaling, and G-protein receptor signaling (Figure 24A). In contrast, the 60nm AuNPs caused down-regulation of cell cycle, regulatory and signaling pathways (Figure 24B). Based on this data, it is demonstrated that AuNPs of well-defined sizes have unique gene expression profiles. Exposure to the AuNPs led to low levels of uptake readily visualized in intracellular vacuoles (Figure S1, Appendix III). The largest particles (60 nm) suppressed genes responsible for maintaining intracellular stability, cell signaling, and cell cycle regulation, which act to inhibit genes that maintain homeostasis. The discrete size effects are further evidenced by changes in G-protein coupled receptor signaling produced upon exposure to the 30nm AuNPs.
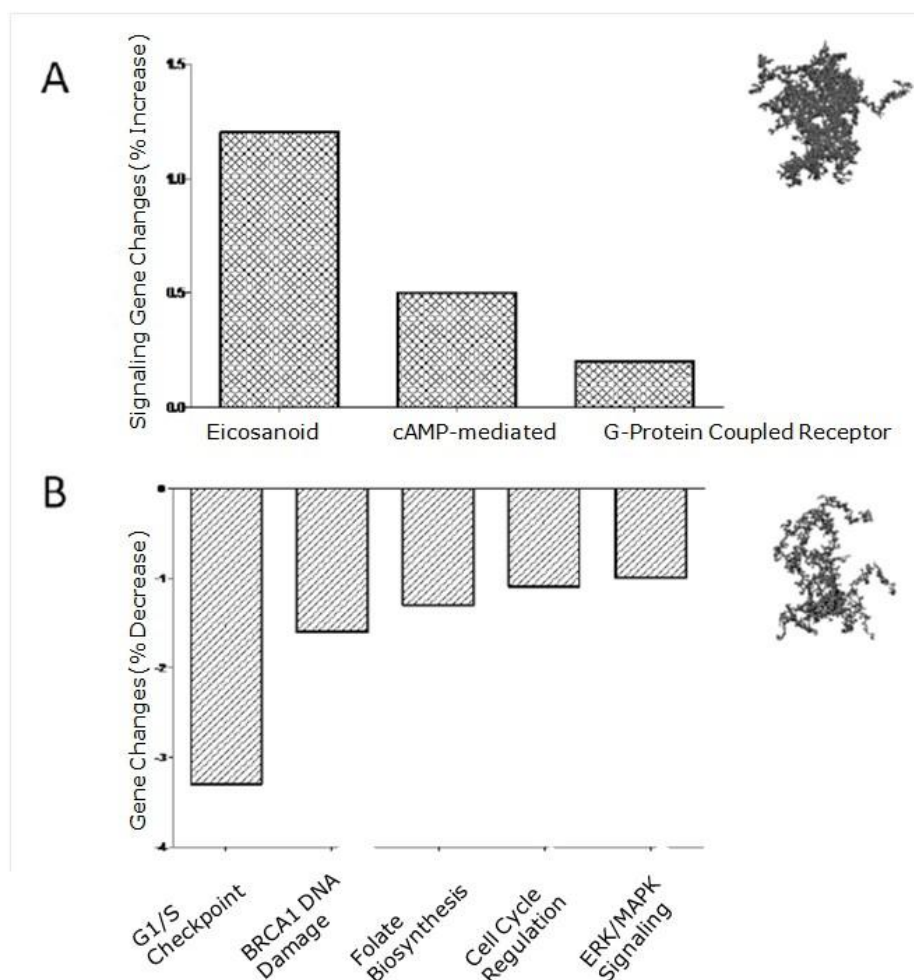

Figure 24. Metabolic and Signaling Pathways Affected by AuNP. Chart displays the most significant Canonical Pathways across multiple AuNP treatments. Results are plotted as

percent of genes changed in dataset versus all genes in pathway. (A) Pathways affected only by 30nm AuNP and (B) Pathways affected only by 60nm AuNP.

Since the AuNPs aggregated to micron sizes once dispersed in media (Figure S2A, Appendix III) there was not a clear size dependent effect when the aggregate size alone was evaluated. However, SLS data that estimated the fractal dimension patterns showed significant differences in aggregate packing density— densely packed structure for 30 nm particles showed higher Df compared to more loosely packed 60 nm AuNPs. Despite forming aggregates of similar size range (in 10s of microns), clear differences were observed in the biological responses. One explanation for such differences can be attributed to discrete cell recognition and response to uniquely different fractal patterns. For the densely packed 30 nm Au, cAMP mediated signaling, Eicosanoid Signaling, and G-Protein Receptor Signaling were up-regulated and this has implications in immune signaling responses (Figure 25A). Treatment with 30 nm AuNP uniquely up regulated the prostaglandin E receptor (PTGER3) that affects intracellular and second messenger signaling mechanisms and involves cellular functions relating to Cell Death, Cell Signaling, Molecular Transport, and Vitamin and Mineral Metabolism. Pathways identified to be directly or indirectly associated with PTGER3 are cAMP mediated signaling, Eicosanoid Signaling, and G-Protein Receptor Signaling. The G proteins are key players in trans-membrane signaling by coupling a multitude of receptors to enzymes. The members of the Gs family couple many receptors to adenyl cyclase activation resulting in increases in the intracellular cAMP concentration. The G proteins of the Gi/Go family are widely expressed and have been shown to mediate receptor-dependent inhibition of various types of adenyl cyclases. G protein-mediated signaling is centrally involved in diverse physiological functions such as perception of sensory information, modulation of synaptic transmission, hormone release and actions, regulation of cell contraction, and migration, or cell growth and differentiation. In addition to the G protein signaling being up-regulated, the 3'-5'-cyclic adenosine monophosphate (cAMP), second messenger central to a number of biological processes, including eicosanoid signaling was also up-regulated. cAMP is produced by the catalytic action of adenyl cyclase (AC) on ATP. AC activity is regulated via its interaction with G-coupled receptor PTGER3. Furthermore, some of the eicosanoids receptors include BLT-1,-2 and CYSLTR1 and CYSLTR2 for leukotrienes, PTGERs for Prostaglandin E2, PTGFR for prostaglandin F2, PTGDR for prostaglandin D2 and TBXA2R for thromboxane A2. Signaling components in this pathway were up-regulated and the eicosanoids transduce signals via their membrane receptors and mediate complex biological processes like inflammation, vascular permeability, allergic reactions, induction of labor and carcinogenesis. Therefore, it is most likely that the exposure to the 30 nm AuNPs initiated an inflammatory response (Figure 25A).

In this study, the 60 nm AuNP elicited the greatest number of uniquely changed genes (Figure 23C). Overall, the loosely packed 60 nm AuNPs caused a down-regulation in gene expression in multiple categories relating to the cell cycle and cell growth. Cell cycle checkpoint regulation ensures the reliability of cell division. Progression through the eukaryotic cell cycle is driven by oscillations in the activities of Cyclin-dependent kinases (CDK). CDK activity is controlled by periodic synthesis and degradation of positive regulatory subunits named cyclins. The key components involved in the G1/S

checkpoint are CDK4/6-cyclin D, CDK2-cyclin E, and the transcription complex that includes the retinoblastoma protein (Rb) and transcription factor E2F. Genes for CDK2 and Rb are suppressed by treatment with 60 nm AuNPs. Interestingly, Busse et al. studied the effect of quinazoline inhibitors on cell cycle progression in the A431 skin cells and demonstrated that these small molecule inhibitors negatively impacted the cell cycle progress with specific emphasis on the G1 to S phase transition.[19] The results presented in this study demonstrates a similar trend with the 60 nm AuNPs (Figure 25B).
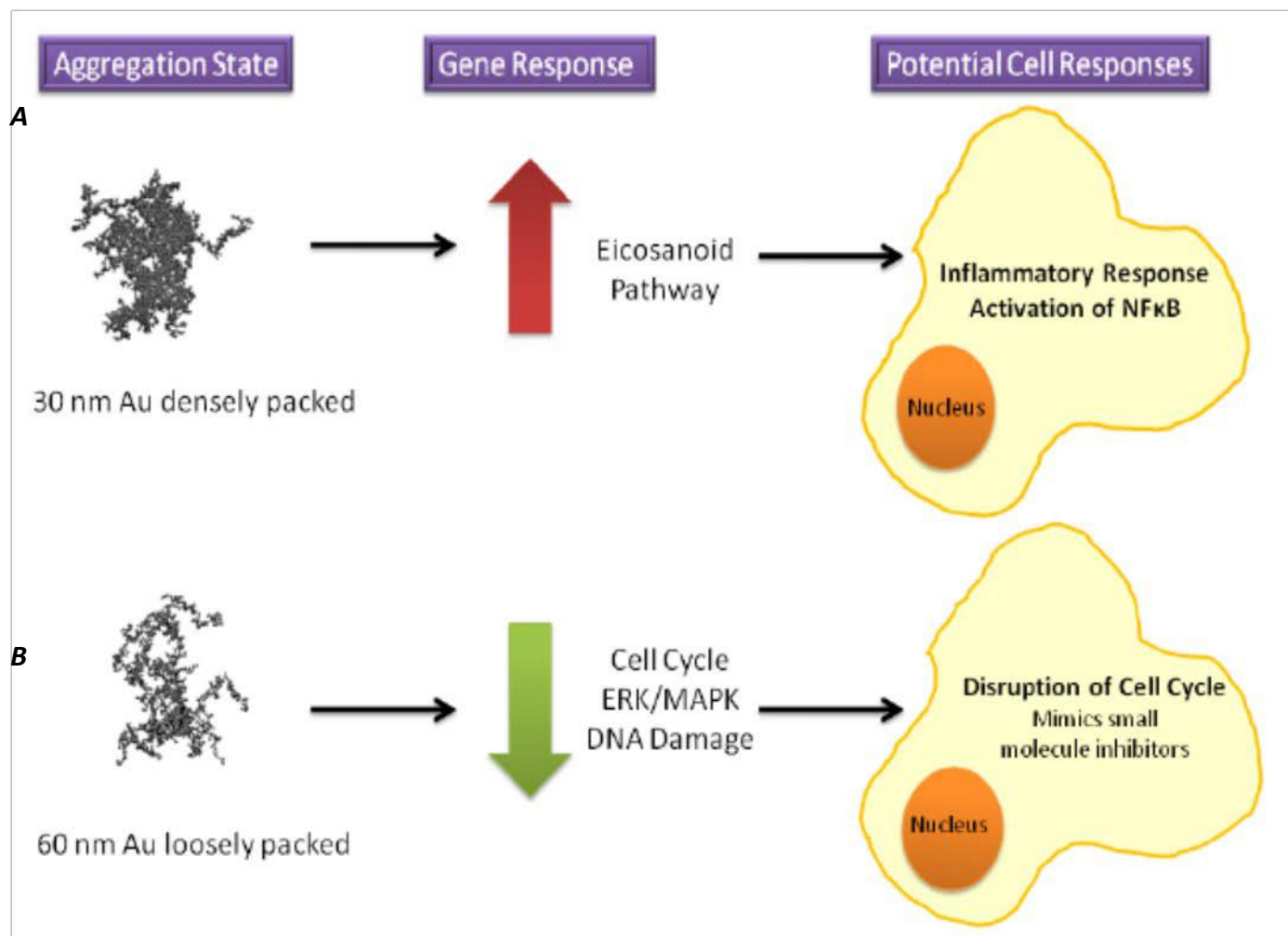

Figure 25. *Potential Cellular Responses Based on Observed Gene Expression Changes. The aggregation patterns demonstrated differences in gene expression changes and potential biological responses. The 30 nm Au activated inflammatory responses while the 60 nm Au disrupted cell proliferation similarly to small molecule inhibitors.*

d.   *Conclusions*

We have demonstrated that although engineered AuNPs do not elicit cytotoxicity at low doses, they induce significant changes in global gene expression, *in vitro*, based on their primary nanoparticle diameter, which influences their fractal dimension or aggregate pattern. Further, these gene expression changes can be analyzed from a systems biology perspective to determine unique molecular pathway involvement of nanomaterials in model systems. We showed that 60nm particles elicited widespread gene changes despite having the lowest uptake of particles into the cell suggesting that NPs of different sizes may selectively alter gene expression through different molecular mechanisms. Changes with 60nm particles were predominantly in the form of suppression of genes related to cell cycle checkpoint regulation, small molecule biochemistry, and cell signaling (Figure 25B). The 30nm AuNP treated group had only one gene that was uniquely changed at 24h. The gene, a prostaglandin E receptor, is involved in receptor-mediated cell signaling pathways, signal transduction and inflammation, indicating that the 30 nm Au most likely initiated an inflammatory response (Figure 25A). This finding provides critical insight to understanding the interaction of NPs prior to exposure through the formation of aggregates with distinct differences in pattern formation and the biological effects that were a result of these aggregate formations.

e.   *References*

[1]   Zook J, MacCuspie R, Locascio L, Halter M, Elliott J. Stable nanoparticle aggregates/agglomerates of different sizes and the effect of their size on hemolytic cytotoxicity. *Nanotoxicology.* 2010, Dec 13.

[2]   Boisselier E, Astruc D, Gold nanoparticles in nanomedicine: preparations, imaging, diagnostics, therapies, and toxicity. *Chem Soc Rev.* 2009, 38(6), 1759.

[3]   Alkilany A, Murphy C. Toxicity and cellular uptake of gold nanoparticles: what we have learned so far? *Nanopart Res.* 2010, 12(7), 2313.

[4]   Schrand A, Schlager J, Dai L, Hussain S. Preparation of cells for assessing ultrastructural localization of nanoparticles with transmission electron microscopy. *Nature Protocols* 2010 5, 744.

[7]   Khlebtsov N, Dykman L, Biodistribution and toxicity of engineered gold nanoparticles: a review of in vitro and in vivo studies. *Chem Soc Rev.* 2011, 40(3), 1647.

[8]   Pan Y, Neuss S, Leifert A, Fischler M, Wen F, Simon U, Schmid G, Brandau W, Jahnen-Dechent W. Size-dependent cytotoxicity of gold nanoparticles. *Small.* 2007, 3(11), 1941.

[9]   Sadauskas E, Jacobsen N, Danscher G, Stoltenberg M, Vogel U, Larsen A, Kreyling W, Wallin H. Biodistribution of gold nanoparticles in mouse lung following intratracheal instillation. *Chem Cent J.* 2009 3, 16.

[10]   De Jong W, Hagens W, Krystek P, Burger M, Sips A, Geertsma R. Particle size-dependent organ distribution of gold nanoparticles after intravenous administration. *Biomaterials* 2008, 29, 1912.

[11]   Sonavane G, Tomoda K, Makino K. Biodistribution of colloidal gold nanoparticles after intravenous administration: effect of particle size. *Biointerfaces* 2008. 66, 274.

[12]   Zhang G, Yang Z, Lu W, Zhang R, Huang Q, Tian M, Li L, Liang D, Li C. Influence of anchoring ligands and particle size on the colloidal stability and in vivo biodistribution of polyethylene glycol-coated gold nanoparticles in tumor-xenografted mice. *Biomaterials.*

2009 30(10), 1928.

[13]   Pan Y, Leifert A, Ruau D, Neuss S, Bornemann J, Schmid G, Brandau W, Simon U, Jahnen-Dechent W. Gold nanoparticles of diameter 1.4 nm trigger necrosis by oxidative stress and mitochondrial damage. *Small.* 2009 , 5(18), 2067.

[14]   Yen H, Hsu S, Tsai C. Cytotoxicity and immunological response of gold and silver nanoparticles of different sizes. *Small.* 2009, 5(13), 1553.

[15]   Li J, Wang L, Liu X, Zhang Z, Guo H, Liu W, Tang S. In vitro cancer cell imaging and therapy using transferrin-conjugated gold nanoparticles. *Cancer Lett*. 2009, 274(2), 319.

[16]   Cho W, Kim S, Han B, Son W, Jeong J. Comparison of gene expression profiles in mice liver following intravenous injection of 4 and 100 nm-sized PEG-coated gold nanoparticles. *Toxicol Lett.* 2009, 191(1), 96.

[17]   Zhang X, Zhang J, Wang H, Hao Y, Zhang X, Wang T, Wang Y, Zhao R, Zhang H, Yang B. Thermal-induced surface plasmon band shift of gold nanoparticle monolayer: morphology and refractive index sensitivity. *Nanotechnology.* 2010, 21(46), 465702. Epub 2010 Oct 25

[18]   Busch W, Kühnel D, Schirmer K, Scholz S, Tungsten carbide cobalt nanoparticles exert hypoxia-like effects on the gene expression level in human keratinocytes. *BMC Genomics.* 2010, 11, 65.

[19]   Murdock R, Braydich-Stolle L, Schrand A, Schlager J, Hussain S, Characterization of nanomaterial dispersion in solution prior to in vitro exposure using dynamic light scattering technique. *Toxicol Sci.* 2008, 101(2), 239. Epub 2007 Sep 13.

[20]   Sugimoto Y, Nakato T, Kita A, Takahashi Y, Hatae N, Tabata H, Tanaka S, Ichikawa A. A cluster of aromatic amino acids in the i2 loop plays a key role for Gs coupling in prostaglandin EP2 and EP3 receptors. *J Biol Chem* 2004, 279(12), 11016.

[21]   Busse D, Doughty R, Ramsey T, Russell W, Price J, Flanagan W, Shawver L, Arteaga C, Reversible G(1) arrest induced by inhibition of the epidermal growth factor receptor tyrosine kinase requires up-regulation of p27(KIP1) independent of MAPK activity. *J Biol Chem.* 2000, 275(10), 6987.

[22]   Levitzki A, and Gazit A. Tyrosine kinase inhibition: an approach to drug development. *Science* 1995 267, 1782–1788

[23]   Fry D, Kraker A, McMichael A, Ambroso L, Nelson J, Leopold W, Connors R, and Bridges A. A specific inhibitor of the epidermal growth factor receptor tyrosine kinase. *Science.* 1994, 265, 1093.

5.   Gold nanoparticles induce transcriptional activity of NF-κβ In a B-lymphocyte cell line

a.   Purpose

The advent of nanomaterials came with the realization of their enormous potential to many interdisciplinary sciences, especially nano-medicine. The specific properties of nanomaterials (electronic, mechanical, physio-chemical) have shown to be primarily dependent on their shape and dimensions.[1] Of all the metallic nanoparticles available today, gold has attracted special interest owing to its plasmonic properties in conjunction with low or no immediate toxicity towards biological systems. Moreover, the ease of synthesis and chemical stability, adds to the overall advantages of gold nanoparticles (Au-NPs). Over the years, the primary focus has been to evaluate the material properties of nanoparticles (NPs), which led to the development of state of the art synthesis and characterization techniques. However, with the ever-growing increase in the nano-bio applications of Au-NPs, there is a need to understand their effect on

biological systems. Immune cells such as lymphocytes circulate through the blood and lymph and therefore are likely cellular components to come in contact with Au-NPs. Additionally, the non-inert nature of these nanomaterials has been revealed in both in vitro and in vivo studies demonstrating toxic effects or altered cellular function following Au-NP exposure.[2-8] Au-NPs are chemically active towards biomolecules[9-13] and have the capability to alter the fate of chemical reactions and modulate cellular signaling pathways and cellular function.

NF-κB/Rel proteins represent a family of transcription factors that not only regulate inflammatory responses but also the expression of a wide variety of genes encompassing a spectrum of cellular activities such as proliferation, differentiation, and apoptosis.[14, 15] Immune function, including the regulation of humoral immunity, has been linked to NF-κB/Rel activity.[16] B-lymphocytes, the main effector cells of humoral immunity, secrete antibodies that bind antigens or invading pathogens and non-self molecules with specificity and facilitate the clearance of these antigens from the host.

Antibody production in B lymphocytes may be partially mediated through NF-κB/Rel binding to κB motifs in enhancer regions that regulate transcription of the immunoglobulin (Ig) heavy and light chains (primary components of antibodies). Within the immunoglobulin heavy chain (*Igh*) gene, a transcriptional regulatory region 3' of the heavy chain constant regions (referred to as 3'*Igh*RR) mediates *Igh* expression and therefore overall antibody levels; furthermore, 3'*Igh*RR activity is influenced by NF-κB.[17-19] IκK plays a pivotal role in intracellular signaling, as it is a point of convergence for a large number of signaling cascades including the activation of the NF-κB pathway.[14] Gold compounds have long been used as anti-inflammatory agents. Although the exact mechanism is unclear, gold compounds have been shown to inhibit NF-κB and IκK activity.[20-24]

The main aim of this study was to determine the impact of Au-NPs on B-lymphocyte cells. Because of the inherent property of gold to bind to –thiol groups, we hypothesized that potential protein interactions with Au-NPs could alter both NF-κB signaling pathways and antibody expression. A review of the available literature suggests that proteins adsorb to NP surface depending on the material properties such as charge, size, hydrophobicity, and conductivity.[25] Utilizing a well-characterized murine B-lymphocyte cell line (CH12.LX), we identified intracellular 10 nm Au-NPs through the use of TEM, demonstrating that the Au-NPs could cross the cellular membrane and physically interact with cellular proteins. Through transient transfection studies utilizing an NF-κB-regulated luciferase reporter, we demonstrated that Au-NP treatment of the CH12.LX cells induced NF-κB activation. In CH12.γ2b-3'*Igh* cells (a variant of the CH12.LX), ELISA analysis of Ig expression correlated to the increase in NF-κB activation with an increase in both 3'*Igh*RR activity and IgA expression suggesting a potential for Au-NP-mediated immune dysfunction. Additionally, through Western blot analysis, we identified a physical interaction between Au-NPs and IκK in cellular lysate, likely due to binding the cysteine residues on IκK.[26, 27] Taken together, these results

demonstrate that not only are B lymphocytes a sensitive and direct target of Au-NPs, but further investigation of Au-NPs and their interactions with intracellular proteins are required.

b.   *Materials and Methods*

Protein Isolation for Protein Corona Analysis.

CH12.LX cells (1.5×10^7 cells) were pelleted via centrifugation at 3000 rpm and washed once with 1x PBS. The cells were resuspended in 1 mL of mild lysis buffer (150 mM NaCl, 10 mM Sodium Phosphate pH 7.2, 2 mM EDTA, 1% Nonidet P-40) supplemented with Complete Mini Protease Inhibitor Cocktail (Roche Diagnostics, Indianapolis, IN) and frozen at -80°C for at least 1 hr. For protein quantification, the lysate was thawed on ice and resuspended briefly then centrifuged at 14,000 rpm for 5 min. The whole cell lysates were removed from the pelleted cell debris, and quantified by the Bio-Rad Protein Assay (Bio Rad, Hercules, CA) according to manufacturer specifications. 10 nm AuNPs (100 µg/mL) were added to 1 mL of the cleared whole cell lysate and incubated at room temperature with rotation for one hour. Samples then were centrifuged at 14,000 rpm for 10 min. The AuNP pellet was washed with 1x PBS four times and centrifuged for 7 min at 14,000 rpm between washes. For the final wash, the AuNP pellet then was transferred to a new 1.5 mL eppendorf and centrifuged a final time. The supernatant was discarded and 50 µL of 2x loading dye (50 mM Tris-HCl, 10% Glycerol, 4% SDS, and 0.4% of 14.2 M stock β-mercaptoethanol) was added to the AuNP pellet and boiled at 95°C for 7 min then vortexed for 30 seconds and centrifuged at 14,000 rpm for 10 min. The supernatant was collected for further analysis (i.e. UV-Vis and Western blot).

SDS-PAGE and Western Blot Analysis.

Whole cell lysates and the supernatant from the boiled AuNP pellet were thawed on ice and 50 µg of protein from the whole cell lysate control and 40 µL of eluent from the AuNPs were electrophoresed through a 12.5% polyacrylamide gel at 130 volts for 90 min. The proteins then were transferred to a polyvinylidene fluoride (PVDF) membrane (Millipore, Bedford, MA) using an electric current of 100 volts for 75 min. The membrane was immediately washed two times with double distilled water and stained with Sigma Aldrich's Reversible Protein Detection Kit for Membranes and Polyacrylamide Gels per manufacturer's directions. Gel blot images were captured using a Fotodyne Foto/Eclipse imager with incandescent background lighting. To probe for IκKαthe membrane was de-stained and immersed in 3% BSA (bovine serum albumin)/TTBS (tris-buffered saline with 0.05% Tween-20) blocking solution and rocked overnight at 4°C. The membranes were incubated at room temperature for 1 hr with a rabbit anti-IκKα (47453 Abcam Cambridge, MA) at a 1:1000 dilution in 3% BSA/TTBS. The membrane then was washed four times in TTBS at 10 min intervals, and the blot was incubated with the appropriate HRP-conjugated secondary antibody (goat anti-rabbit at 1:2500) for 1 hr. The blot was washed again four times in TTBS, then

subjected to ECL substrate (Thermo scientific, Waltham, MA), and analyzed on a Fuji LAS-3000 Bioimager (Tokyo, Japan).

Transient Transfection and Luciferase Assay.

CH12.LX cells ($1.0x10^7$) were resuspended in 200 µL of culture media with 10 µg of 3x-NF-κB plasmid,[25] and transferred to a 2-mm gap electroporation cuvette (Molecular BioProducts, San Diego, CA). Cells were electroporated using an electro cell manipulator (ECM 630; BTX, San Diego, CA) with the following voltage, capacitance and resistance: 250 V, 150 µF, and 75 Ω. Multiple transfections were pooled and 2 mL of cells were aliquoted into 12-well plates at $2.0x10^5$ cells/mL. Immediately after transfection, cells were treated with 0.05, 0.5 and 5 µg/ml of AuNPs for 24 or 48 hrs then lysed with 1x reporter lysis buffer (Promega Corp., Madison WI), and stored at -80°C. To measure luciferase activity, the whole cell lysate was thawed and cleared of cellular debris by centrifugation at 14,000 rpm then 20 µL of whole cell lysate was mixed with 100 µL of luciferase assay reagent (Promega Corp., Madison WI) and luciferase activity was measured with a luminometer (Berthold detection systems). Results are represented in relative light units (RLU) with the naive control set to 100 percent effect.

ELISA for γ2b and IgA Expression.

CH12.γ2b-3′Igh cells were treated with varying concentrations of 10 nm AuNPs then seeded (2 mL/well) into 48-well plates. To evaluate γ2b protein production, cells were seeded at a concentration of $3.0x10^4$ cells/mL and incubated for 48 hrs. For IgA protein detection, cells were seeded at a concentration of $2.0x10^5$ cells/mL and incubated for 24 hrs. Following the incubation period, cells were centrifuged at 3000 rpm then lysed with mild lysis buffer containing freshly added protease inhibitors. Lysed cells were cleared via centrifugation at 14,000 rpm. Supernatants were collected and stored at −80 °C until analysis. To measure γ2b or IgA, cell lysates were thawed on ice and protein concentrations were determined by Bio-Rad Protein Assay (Bio Rad, Hercules, CA). Samples were diluted to 2 or 3 µg of total protein/100 µL and analyzed for IgA or γ2b, respectively, by ELISA as previously described (all antibodies were purchased from Bethyl Industries, Inc.).

c.   Results

Since the 10 nm Au-NPs are taken up by the CH12.LX B cells Au-NPs could interact with membrane-bound and/or intracellular proteins potentially altering signal transduction pathways and normal cellular function. To determine if Au-NPs and cellular proteins physically interact, the dispersion and aggregation pattern of Au-NPs before and after incubation with whole cell protein lysate was assessed using UV-Vis spectroscopy and TEM. Cell lysate was incubated with Au-NPs for 1 hr then either analyzed immediately by UV-Vis (Fig. 26A, curve a) or after proteins that specifically bound the Au-NPs were extracted as described above (Fig. 26A, curve b). The UV-Vis absorption spectra demonstrated a characteristic peak for 10 nm Au-NPs at ~525 nm

for the samples containing Au-NPs. Interestingly, proteins extracted from the Au-NP induced more distinct peaks as compared to the whole cell lysate (Fig. 26 A, compare curves a and b) which likely reflects selective binding of specific proteins to the Au-NPs. Additionally, no absorption for Au could be seen in the protein sample extracted from the Au-NP pellet after heating under reducing conditions (Fig. 26 A, curve b), indicating little or no contamination of the sample with Au-NPs. These results suggest that a protein corona is formed on the surface of the Au-NP, which is further supported by TEM analysis of Au-NPs before and after incubation with whole cell protein lysate. After incubation with cell lysate, the Au-NPs are less agglomerated perhaps due to a protein corona, which keeps them separated from each other (Fig. 26 C). Once the proteins are removed from the surface of the particles by heating under reducing conditions, the Au-NPs agglomerate (Fig. 26 D). This agglomeration of Au-NPs can be attributed to the absence of the stabilizing agent (i.e. sodium citrate or protein corona).
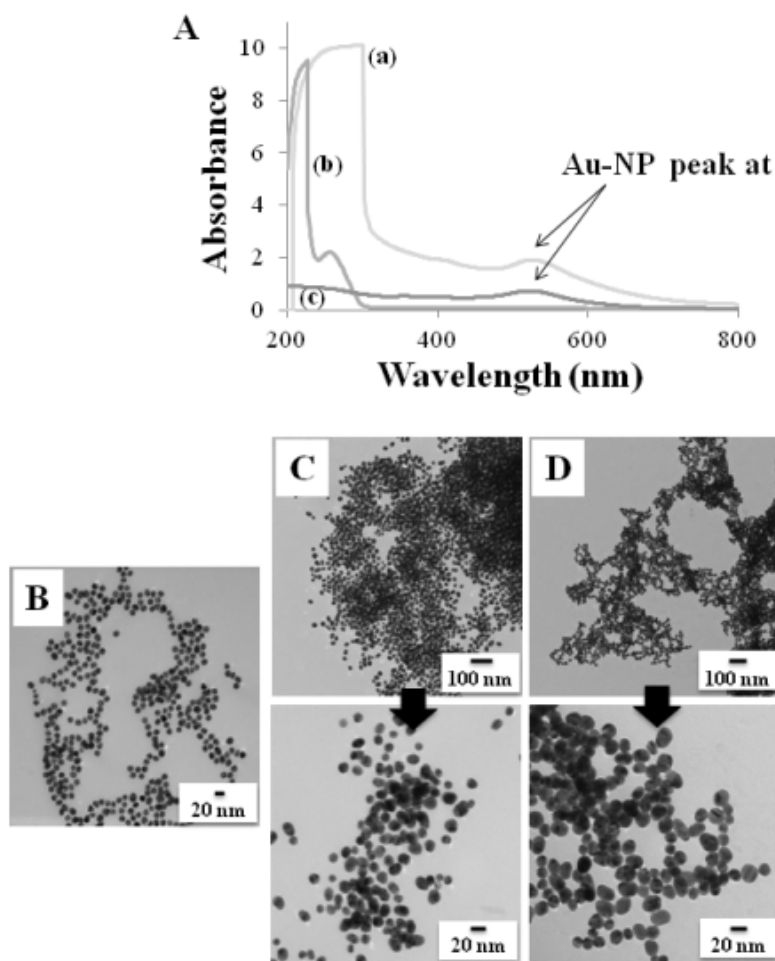

Figure 26 Protein corona characterization using UV-Vis spectroscopy and TEM imaging. A) Whole cell lysate from CH12.LX cells was incubated with 10 nm AuNPs for 1 hr then analyzed by UV-Vis either immediately (curve a) or following extraction of proteins that specifically bound the AuNPs (curve b). Curve c represents the AuNPs alone control (absence of cell lysate). B-D) Corresponding TEM imaging for AuNPs prior to (B) and after (C) incubation with whole cell lysate from CH12.LX cells and following removal of the protein corona (D). Results are representative of three separate experiments.

To further investigate the association of Au-NPs with intracellular proteins, whole cell protein lysate isolated from the CH12.LX B-lymphocyte cell line was incubated for 1 hr with Au-NPs. Proteins that specifically associated with Au-NPs were eluted by heating under reducing conditions and resolved by SDS-PAGE and Western blot analysis. Reversible membrane staining revealed several protein bands, suggesting a broad spectrum of proteins binding to the Au-NPs (Fig. 27 A, lane 3). However, there was less banding as compared to the whole cell lysate control (Fig. 27 A, compare lanes 2 and 3) supporting protein specificity for the Au-NPs. Additionally, the absence of detectable bands in the Au-NP only (in lysis buffer) control (Fig. 27 A, lane 4) demonstrated that the elucidated bands are not merely an artifact from the Au-NPs or the protein extraction process.

Previous studies have demonstrated inhibition by gold therapeutics (i.e. aurothiomalate) of over-expressed IκK activity in COS cells and since an inherent property of gold is to bind to –thiol groups, the presence of cysteine residues on IκK makes it a likely protein target for binding to Au-NPs. Therefore, to determine if IκK was one of the many proteins binding to Au-NPs, the Western blot was probed with an antibody specific for IκKα and IκKβ, two catalytic subunits of the IκK complex. Strong IκKα and IκKβ bands were detected in the protein sample eluted from the Au-NPs (Fig. 27 B, lane 3 and Fig. 27 C, lanes n1-n3) that was also detected in the whole cell lysate sample (Fig. 27 B, lane 2 and Fig. 27 C, lane 1) but not in the Au-NP in lysis buffer control sample (Fig. 27 B, lane 4). These results support a direct interaction between IκK and Au-NPs which may alter NF-κB signaling in the CH12.LX B-lymphocyte cell line and lead to B-lymphocyte dysfunction (i.e. altered Ig expression and antibody formation).
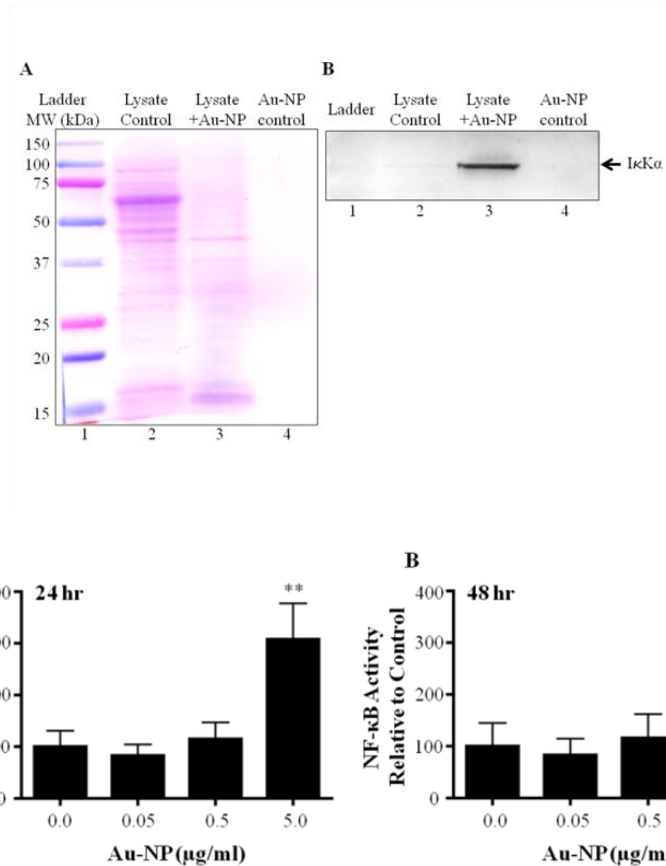
Figure 27. The AuNP protein corona contains IκKα. Whole cell lysate from CH12.LX cells was incubated with 10 nm AuNPs for 1 hr. The protein corona was extracted from the AuNP surface and subjected to Western blot analysis. The membrane was subject to reversible protein staining (A) then washed and probed with anti-IκKα antibodies (B). Lane 1: ladder; lane 2: 50 μg whole cell lysate without AuNP; lane 3: 40 μL of protein extracted from the AuNP surface; lane 4: 40 μL of extract from AuNPs incubated in lysis buffer alone. Results are representative of four separate experiments.

Using a 3x-NF-κB luciferase reporter plasmid, we evaluated the effect of Au-NPs on NF-κB activity in the CH12.LX B-lymphocyte cell line. CH12.LX cells were treated with varying concentrations of 10 nm Au-NPs for 24 or 48 hr. Surprisingly, Au-NP significantly induced 3x-NF-κB reporter activity at both time points and this effect was limited to the highest Au-NP concentration (5 μg/ml) with no effect at lower concentrations (Fig. 28A and B).
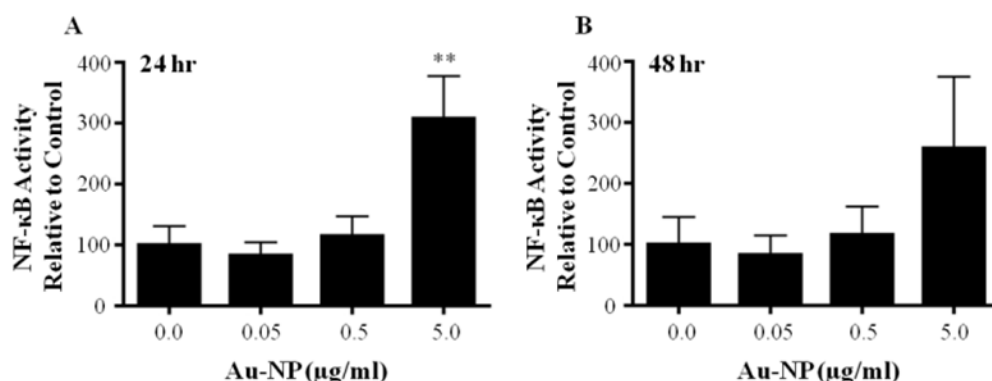
Figure 28 AuNPs activate the NF-κB transcriptional pathway. CH12.LX cells were transiently transfected with the 3x-NF-κB luciferase reporter plasmid then cultured at 2.0x105 cells/ml with varying concentrations (0.0, 0.05, 0.5, and 5 μg/ml) of 10 nm AuNPs. After a 24 hr (A) or 48 hr (B) incubation, cells were lysed and cellular extracts evaluated for luciferase enzyme activity as measured in relative light units (RLU) and represented on the y-axis as luciferase activity (mean ± SEM) relative to the naïve control (0.0 μg/ml AuNP , set to 100%). The results are representative of at least three separate experiments (n=3 for each treatment group). **, statistical significance at p<0.01 compared to 0.0 μg/ml AuNP control via 1-way ANOVA and a Dunnett's post- hoc test.

We utilized a variant of the CH12.LX B-lymphocyte cell line that stably expresses an Ig heavy chain (γ2b) under the transcriptional regulation of the 3'IghRR to determine if treatment with Au- NP leads to a functional effect on Ig transcriptional regulatory elements (i.e. 3'IghRR) and on endogenous antibody production. The CH12.γ2b-3'Igh cells have been previously characterized and shown to endogenously express IgA antibodies as well as one copy of the γ2b transgene. The CH12.γ2b-3'Igh cells were treated with varying concentrations of 10 nm Au-NPs and evaluated by ELISA for γ2b and IgA protein levels. Similar to the effect on NFκB, 5 μg/mL AuNP significantly increased 3'IghRR-regulated γ2b transgene expression (Fig. 29A). IgA levels were also significantly increased.
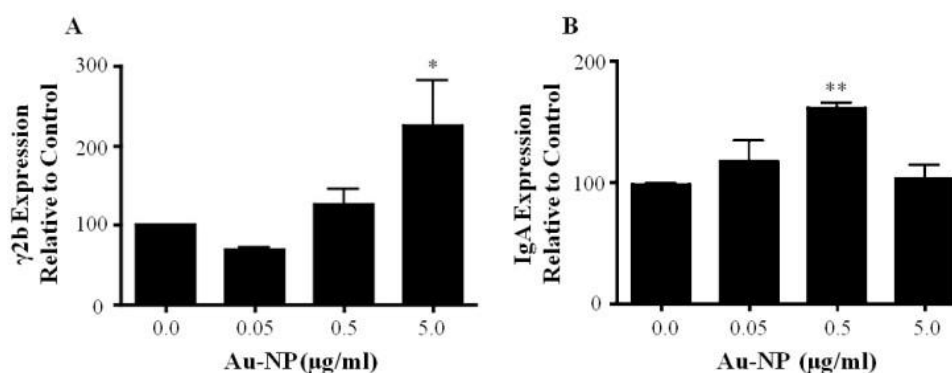
DISTRIBUTION A: Approved for public release; distribution unlimited. PA Case No. 88ABW-2013-4073

83

Figure 29. AuNPs increase 3'IghRR-regulated γ2b transgene expression and IgA secretion. CH12.γ2b-3'Igh cells at 3.0×10^4 cells/mL were cultured with varying concentrations (0.0, 0.05, 0.5 and 5 µg/ml) of 10 nm AuNPs. After a 48 hr (γ2B) or 24 hr (IgA) incubation, cells were lysed and diluted to 3 or 2 µg whole cell protein/100 µL and evaluated by ELISA to determine ng of γ2B per 3 µg protein (A) or ng of IgA per 2 µg protein (B). Expression of γ2b or IgA relative to the naïve control (0.0 µg/ml AuNP, set to 100%) is represented on the y-axis. * and **, statistical significance at $p<0.05$ or $p<0.01$, respectively, compared to 0.0 µg/ml AuNP control via 1-way ANOVA and a Dunnett's post-hoc test.

d. Discussion

We demonstrate a direct interaction of AuNPs with IκKα that correlated with a significant effect on NF-κB activity and altered cellular function (i.e. increased immunoglobulin (Ig) expression). The exact mechanism for this effect is unclear and appears to be contrasted with previous results in studies demonstrating an inhibition of NF-κB activity by gold compounds and nanoparticles. Future experiments will focus on defining the effects of AuNP on the IκK complex and IκBα.

e. Conclusions

The results presented here suggest an alternative way to study the nanoparticle interaction with the biological environment. By identifying the protein targets first, IκK in this study, and then evaluating the downstream effects on cell signaling might prove to be a direct approach to assess bio impact of nanoparticles. Results also demonstrate that the gold nanoparticles are not inert as previously thought. Although we did not see any change in cell viability, we saw modulation of cell function in presence of gold nanoparticles.

B. Copper Nanomaterials

1. Characterization and in vitro Toxicity Of Copper Nanoparticles (Cu-NPs) In Murine Neuroblastoma (N2a) Cells Nanoparticles

a.   Purpose

The purpose of this investigation was to thoroughly characterize Cu-NPs, Cu-MSPs, and CuO-NPs upon their suspension in water and to determine the toxic effect of these copper nanoparticles on Murine Neuroblastoma (N2A) Cells. Specifically, the following issues were addressed:

1. Characterization of copper nanomaterial's physiochemical properties (morphology, shape, agglomeration, spectral signature).
2. Toxicity assessment of Cu-NPs, Cu-MSPs and CuO-NPs on the murine neuroblastoma (N2A) cell line.

b.   Materials and Methods

Prior to *in vitro* cell culture experiments, the effect of the cell culture media upon the copper nanoparticles was investigated. Previous research has demonstrated that suspension of nanoparticles in cell culture media generally leads to the aggregation of most compositions of nanoparticles[1].

In vitro cell culture and aseptic techniques were used in this research. Murine neuroblastoma (N2A) cells were cultured in T-75 plastic flasks and exposed to various concentrations of Cu-NPs (25 nm), CuO-NPs (40 nm) and Cu-MSPs (500 nm) over certain time periods. The viability of the N2A cells after exposure to each type of Cu-NPs, Cu-MSPs, and CuO-NPs at various concentrations was determined by measuring the mitochondrial function of the cell. Mitochondrial function acts as an indicator of metabolic activity and therefore elucidates cell viability. The 3-(4,5- dimethylthiazol- 2-yl)-5-(3-carboxymethoxyphenyl)-2-(4-sulfophenyl)-2H-tetrazolium (MTS) assay was used for the assessment of cellular viability based on mitochondrial function. Morphological characteristics of the cells after exposure to each type of Cu particle, were observed with three different imaging techniques – two forms of Scanning Electron Microscopy (SEM), high resolution and environmental, and two forms of Transmission Electron Microscopy (TEM), high resolution and low voltage. Agglomeration characteristics were observed by using Dynamic Light Scattering (DLS) in dosing media along with the endocytosis inhibitor Dynasore.

c.   Results and Discussion

MTS data

MTS was performed on the three types of Cu particles and CuCl2. The results of this cellular proliferation assay can be seen in Figure 30.
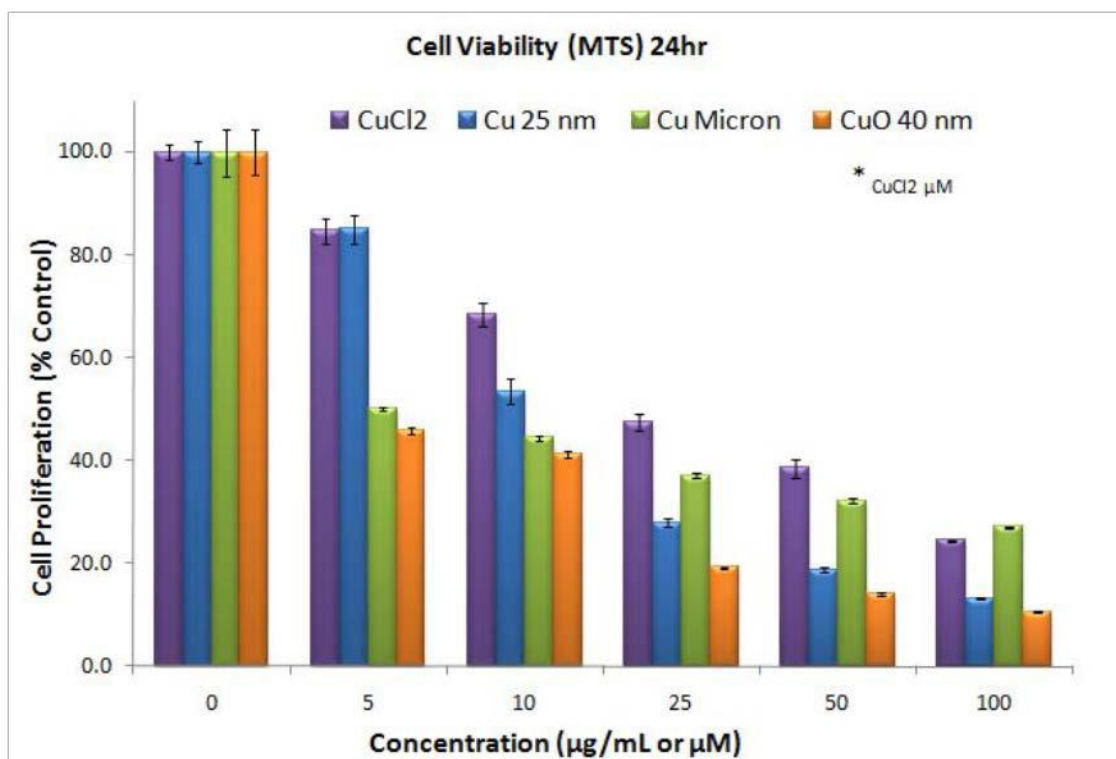
Figure 30. MTS assay for the three types of Cu particles and CuCl2. (Concentration in µg/mL for NPs and µM for CuCl2)

In terms of cellular viability, CuCl2 is the least toxic at all concentrations. Cu-NP 25 nm is less toxic at low concentrations (< 25 µg/mL) than Cu-MSP 500 nm and CuO-NP 40 nm. At concentrations above 25 µg/mL, Cu-NP 25 nm becomes comparable in toxicity to CuO-NP 40 nm and more toxic than Cu-MSP 500 nm. From further characterization, it is not surprising that the Cu-NP 25 nm and CuO-NP 40 nm share similar toxicities. As these two particles become suspended in water for longer periods of time, they both become oxidize, especially Cu-NP 25 nm, which may explain the similarities in toxicities.

Dynamic Light Scattering Experiments

Dynamic Light Scattering Experiments were conducted in order to observe changes in the dynamic size of Cu-NPs, CuO-NP, and Cu-MSP under cell culture conditions. An initial trial of DLS was conducted for the particles at 50 µg/mL concentration with dosing media. The general conclusion is that at these conditions there is a trend for the Cu particle sizes to increase. The surprising aspect of size observation in solution is that it follows an inverse trend compared to the primary size of the particles: CuO-NPs **>** Cu-NPs **>** Cu-MSPs[3]. Previous studies show limited cellular modulation with co-incubation with the endocytosis inhibitor, Dynasore. An initial experiment was conducted to serve as a control for change in particle agglomeration for the Cu-NP (25 nm), CuO-NP (40 nm), and Cu-MSP (500 nm) with 3 and 24 hour incubation times without the use of Dynasore. Cu particles were freshly diluted from 1 mg/mL stock

solutions prior to readings. Table 9 shows concentration and incubation times. In general, agglomerations became larger as incubation time increased from 3 to 24 hours with the exception of the Cu-NP 25 nm. Dynamic sizes of the particles under cell culture conditions are CuO-NPs > Cu-MSPs > Cu-NPs, which is similar to the sizes measured earlier by Schrand *et al*[3].

Table 9. Concentration and incubation times used for DLS control experiment without Dynasore

Sample & concentration	Cu particle volume, dosing media volume	0 hour incubation	3 hour incubation	24 hour incubation
Cu-NP (25 nm) 25 μg/mL	25 μg/mL Cu 975 μL dosing media	0 hour incubation	3 hour incubation	24 hour incubation
CuO-NP (40 nm) 25 μg/mL	25 μg/mL Cu 975 μL dosing media	0 hour incubation	3 hour incubation	24 hour incubation
Cu-MSP (500 nm) 25 μg/mL	25 μg/mL Cu 975 μL dosing media	0 hour incubation	3 hour incubation	24 hour incubation

DISTRIBUTION A: Approved for public release; distribution unlimited. PA Case No. 88ABW-2013-4073

87

Figures 31 A-C show the results of this initial DLS experiment.
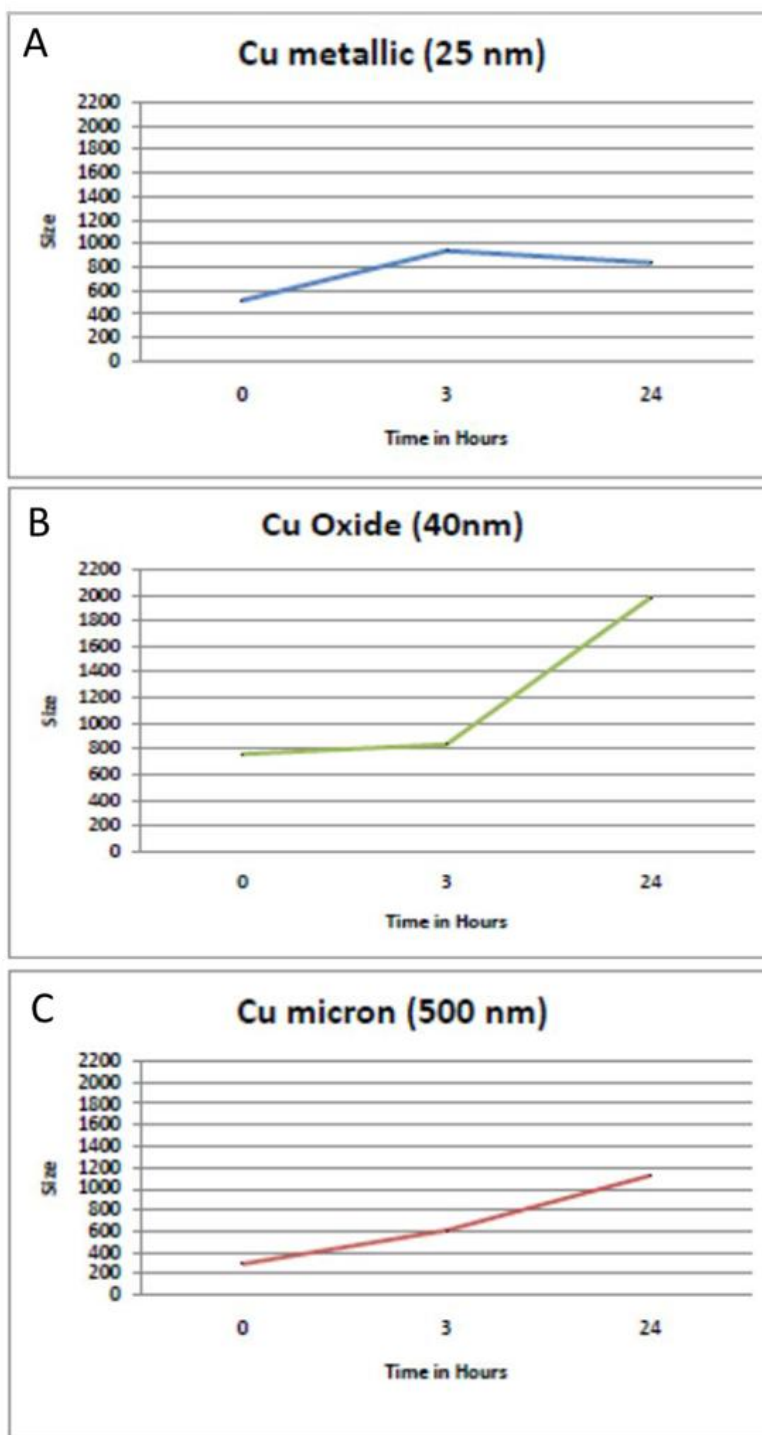

Figure 31. Results of initial DLS experiment

The next set of DLS experiments involve three trials of Cu-NP, CuO-NP, and Cu-MSP in dosing media at three different concentrations of 25 µg/mL, 50 µg/mL, and 100 µg/mL as seen in Table 10. Measurements were taken at 0 and 3 hours for each particle at each concentration. 25 µM of the endocytosis inhibitor Dynasore was also added to each sample because ultimately the goal is to understand if the chemical has any effect on the viability of the N2A cells as seen in previous studies.

Table 10. Cu particle, Dynasore, and dosing media volumes

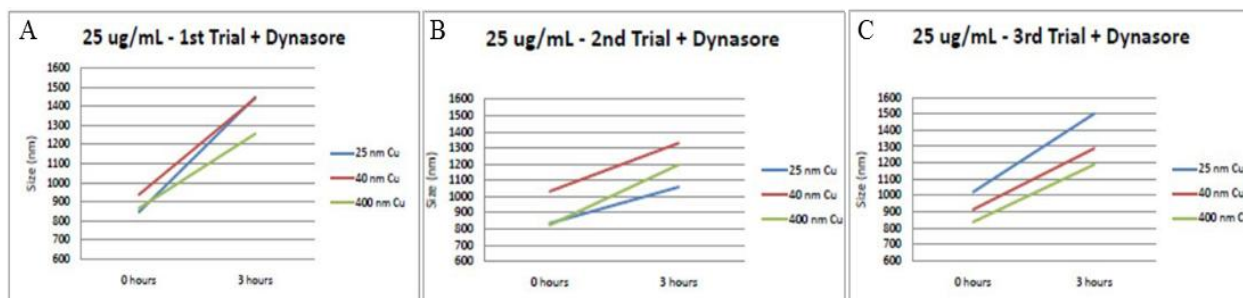| Final concentration for samples	Cu particle volume	Dynasore volume	Dosing media	Total volume
25 µg/mL Cu particle + 25 µM Dynasore	25µL	25µL	950µL	1000µL
50 µg/mL Cu particle + 25 µM Dynasore	50µL	25µL	925µL	1000µL
100 µg/mL Cu particle + 25 µM Dynasore	100µL	25µL	875µL	1000µL

Figure 32. Size distributions from DLS experiment 25 µg/mL A). Size distribution of Cu particles at a concentration of 25 µg/mL and Dynasore at both 0 and 3 hours of incubation, 1st trial B.) Size distribution of Cu particles at a concentration of 25 µg/mL and Dynasore at both 0 and 3 hours of incubation, 2nd trial C). Size distribution of Cu particles at a concentration of 25 µg/mL and Dynasore at both 0 and 3 hours of incubation, 3rd trial.
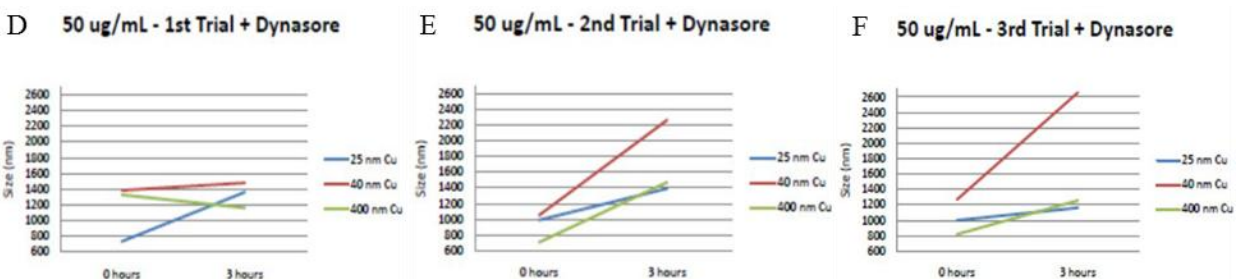
Figure 33. Size distributions from DLS experiment 50 µg/mL. D). Size distribution of Cu particles at a concentration of 50 µg/mL and Dynasore at both 0 and 3 hours of incubation, 1ˢᵗ trial E). Size distribution of Cu particles at a concentration of 50 µg/mL and Dynasore at both 0 and 3 hours of incubation, 2ⁿᵈ trial F). Size distribution of Cu particles at a concentration of 50 µg/mL and Dynasore at both 0 and 3 hours of incubation, 3ʳᵈ trial.
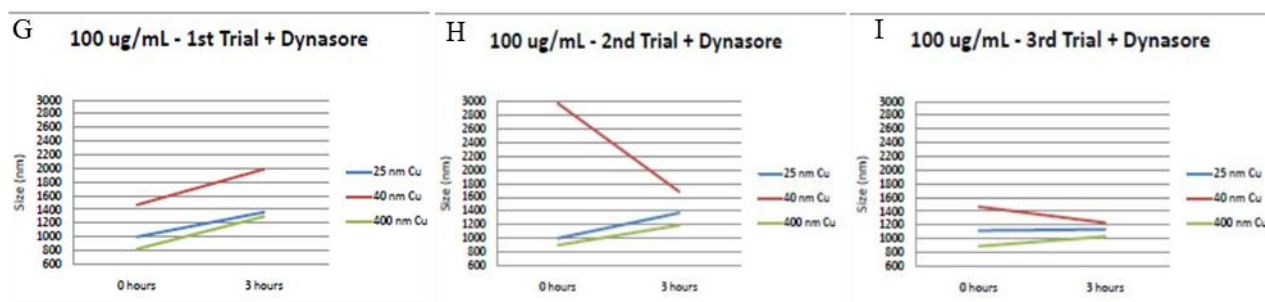

Figure 34. Size distributions from DLS experiment 100 µg/mL G). Size distribution of Cu particles at a concentration of 100 µg/mL and Dynasore at both 0 and 3 hours of incubation, 1ˢᵗ trial H). Size distribution of Cu particles at a concentration of 100 µg/mL and Dynasore at both 0 and 3 hours of incubation, 2ⁿᵈ trial I). Size distribution of Cu particles at a concentration of 100 µg/mL and Dynasore at both 0 and 3 hours of incubation, 3ʳᵈ trial.

Low Voltage Electron Microscopy (LVEM) Imaging

In Figure 35 A-C, LVEM images of the three particles are shown. The LVEM may not produce the sharpest images but the process is not time consuming or difficult to set up. From these images basic particle morphology and agglomeration behavior can be observed.

DISTRIBUTION A: Approved for public release; distribution unlimited. PA Case No. 88ABW-2013-4073
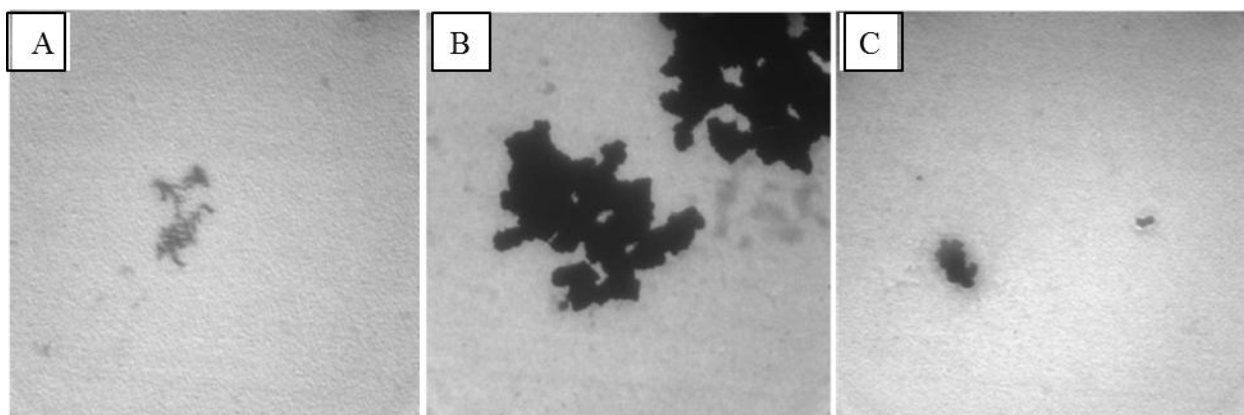
90

Figure 35. LVEM images of the three copper particles. A) CuNP 25nm at 202 kx magnification B) CuO NP 40nm at 202kx magnification, C) CuMSP 500nm at 202 kx magnification.

Environmental Scanning Electron Microscopy (ESEM) Imaging

Environmental Scanning Electron Microscopy was conducted on Cu-NPs, CuO-NPs, and Cu-MSPs 3 months after suspension in water. The particles were diluted from stock solutions and the goal of the microscopy was to aid in the characterization of the physiochemical properties of the particles themselves. Examination of surface roughness is an indicator of the amount of oxidization the particles experience and may elucidate particle uptake sizes. Figures 36A-B illustrate the original images captured.
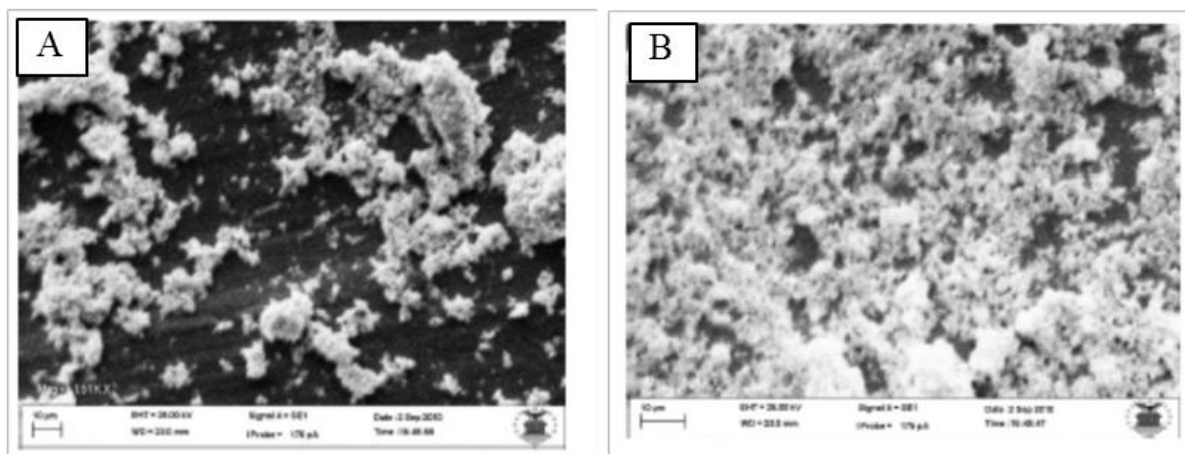

Figure 36. Environmental Scanning Electron Microscopy images of Cu-NPs, CuO-NPs, and Cu-MSPs 3 months after suspension in water. A)CuNP 25nm at 3 months, B) CuO NP 40nm at 3 months.

Scanning Electron Microscopy (SEM) Imaging

SEM images were taken after N2A cells were dosed with Cu particles in an experiment to visually determine the placement of particles and cells in dosing media. All particles

were dosed at a concentration of 25 µg/mL. Fig 37A-D show a series of images including a control image and that of the three particles.
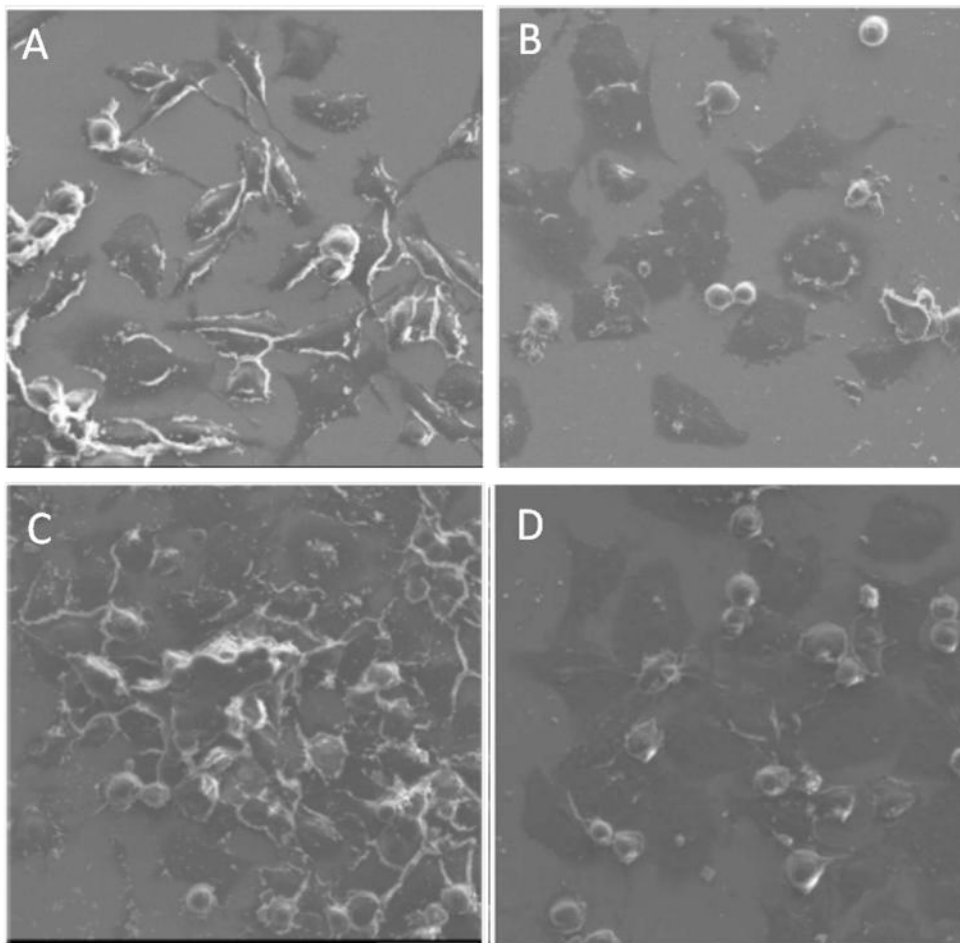

Figure 37. SEM images of N2A cells dosed with Cu particles. A)Control cells with no CuNP, B)CuNP 25nm, C) CuO 40nm, D) CuMSP 500nm. (images provided by Dr Amanda Schrand)

Although some charging is seen in the image, the Cu-NP 25 nm can be seen fairly clearly with the N2A cells showing up as darker shadowy figures. In scanning electron microscopy, charging effects are described where excess negative charge accumulates on the specimens and image artifacts arise from excess surface charge and produce poor images. At times, it may be necessary to prepare poorly conducting specimens with a metallic coating such as gold[7].

The control image shows the cells without any CuNP dosing, and the cells are observed be more adherent and neuron like with more dendrites present. As the N2A cells are dosed with the Cu particles they are under more oxidative stress and thus start to become rounder and less adherent to the glass cover-slip surfaces.

Transmission Electron Microscopy (TEM) Imaging

TEM Imaging was conducted on the Philips Lab 6 TEM at the Air Force Research Laboratory (AFRL) Materials Laboratory. The following figures show the morphology and sizes of the particles suspended in water: initially after preparation, at 2 or 3 months after preparation, and again at 6 months. The surface oxidation, agglomeration, and sizes indicate changes the particles experience over time.

It is worth noting that initial TEM imaging was conducted along with a brief study on the size distribution of the particles. Interestingly, as was also found in the study by Schrand *et al.* referred to earlier, the Cu-NP 25 nm has a larger average size than the CuO-NP 40 nm$_3$. This is important to realize; nominal sizes provided by the manufacturer may not be indicative of the true particle size. The stock particles, in powder form, are preserved under Argon gas, but even so, properties of the particles may change over time.

The three different types of particles were imaged again after 2 or 3 months to look for any changes in oxidation, morphology, and overall surface properties. Figure 38A-C show images of the three types of particles.
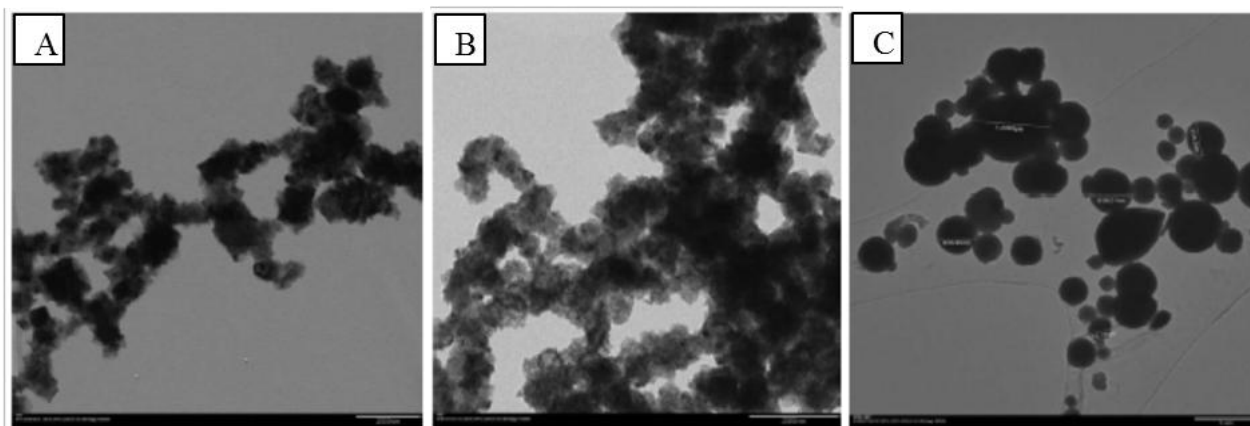

Figure 38. TEM Images showing the morphology and sizes of the particles suspended in water. A)CuNP 25nm at 2 months, B) CuO NP 40nm at 3 months, C) CuO MSP 500nm at 3 months.

Figures 39-41 show the comparison images of the three particles at 6 months. Comparison images were taken at standard magnifications of 3800x, 8800x, 15000x, 50,000x, and 80,000x so improved observations can be made.
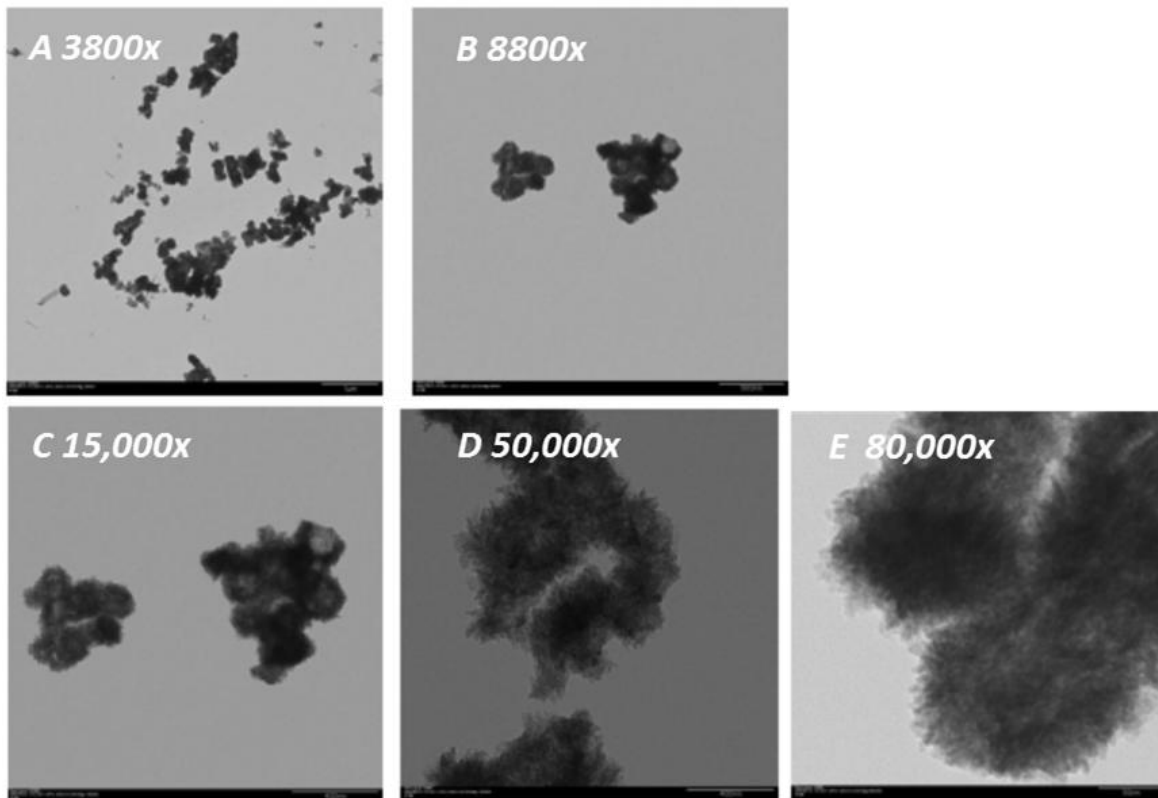
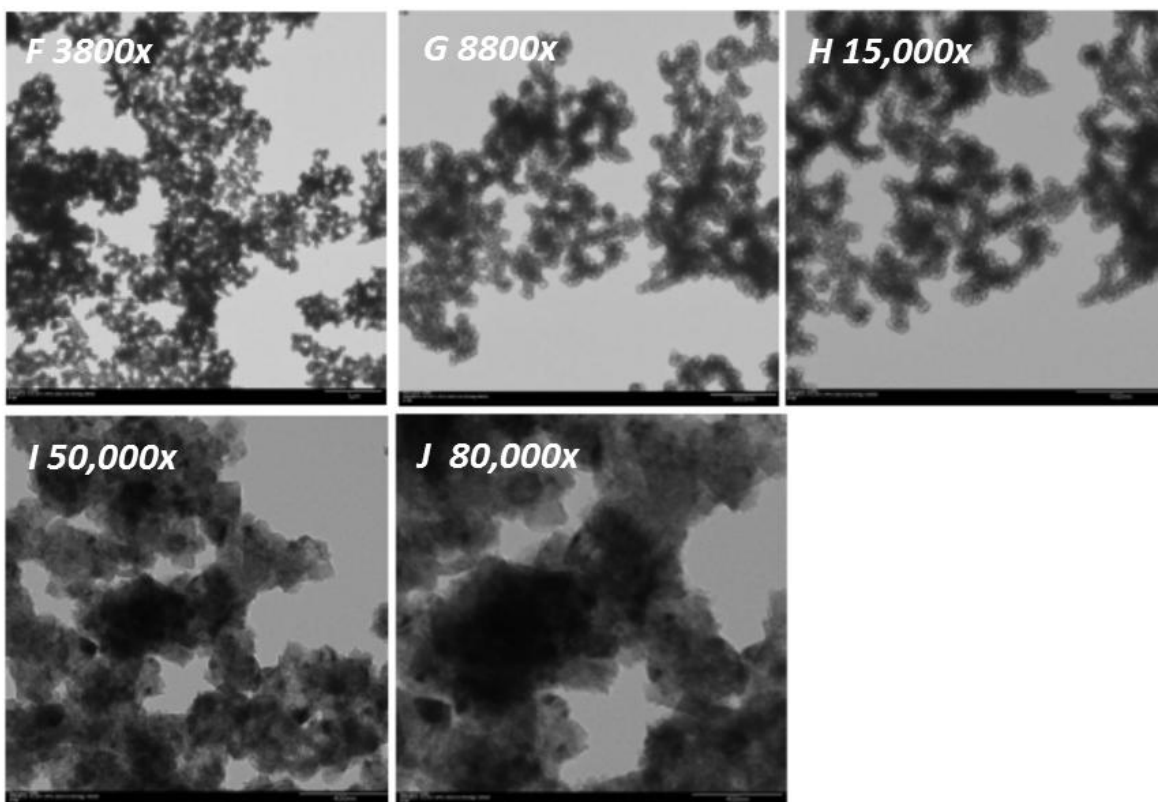**Figure 39. Comparison images of CuNP 25nm at 6 months.**

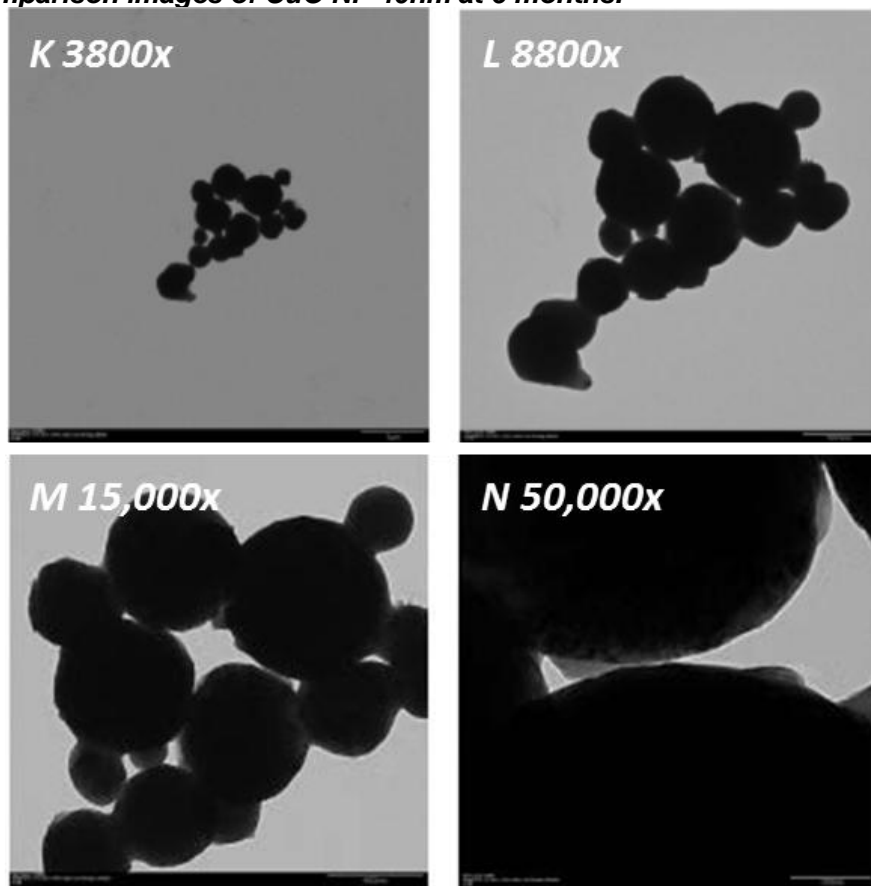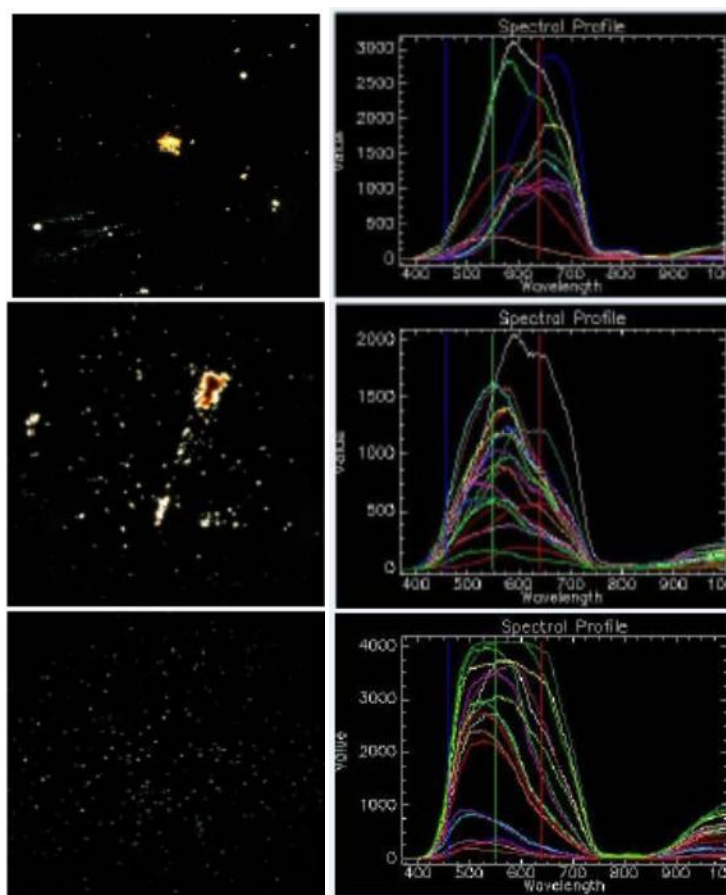*Figure 40. Comparison images of CuO NP 40nm at 6 months.*

Figure 41. Comparison images of Cu MSP 500nm at 6 months.

Hyperspectral Imaging

Figures 42. Hyperspectral imaging of copper nanomaterials. From top to bottom; CuNP 25nm, CuO NP 40nm, and Cu MSP 500nm. Corresponding spectral profiles are in the right hand column.

Unfortunately, it has been shown that copper does not have a "prominent light-scattering or absorption peak in the visible region of the spectrum".[8] This makes it very difficult to draw any conclusions from the HSI data as there is not a clear plasmonic peak for copper and the collected spectra of dissimilar sizes of copper nano and micron-sized particles would not give much information. Careful inspection of the three spectral profiles (figure 42) shows that there are very broad peaks and it is difficult to pinpoint any specific peaks. From chapter 3, Yguerabide and Yguerabide.[8] show that the copper band should fall somewhere between 380-530 nanometers, yet the spectra in figure 42 show broad bands between 500-800 nanometers. This could be due to agglomeration of the particles but regrettably, no additional information is provided such as oxide content between the various particles as no clear "shift" can be observed.

d. Conclusions

This research compared the effects upon N2A cellular viability by the three types of Cu particles and characterized these particles using a variety of techniques. Toxicity changed for the N2A cells at different concentrations and for different particles. At high concentrations, N2A cells fared better when dosed with Cu-MSP 500 nm. This may be related to cellular mechanisms where cellular uptake is generally limited for large particles around 500 nm, thus enabling smaller Cu particles to be uptaken easier. Characterization showed a general increase in size when the particles were incubated with the endocytosis inhibitor Dynasore. This may also explain apparent "rescue" effects seen in previous research, where there was increased cellular viability in the presence of Dynasore. At higher concentrations of particles (100 µg/mL) with 25 µM Dynasore trends are somewhat more inconclusive, suggesting possible interferences in the solution or between the particles themselves as far as forming agglomerations. Additionally, this research seeks to observe *in vitro* effects upon murine neuroblastoma cells (N2A) by these three types of particles as well as by CuCl2. Microscopy techniques indicate observable changes in oxidation for Cu-NP 25 nm and CuO-NP 40 nm after suspension in water over long incubation. In general, agglomerations of the particles increase when dosed with the endocytosis inhibitor Dynasore. In terms of cellular viability, CuCl2 is the least toxic at all concentrations. Cu-NP 25 nm is less toxic at low concentrations (< 25 µg/mL) than Cu-MSP 500 nm and CuO-NP 40 nm. At concentrations above 25 µg/mL, Cu-NP 25 nm becomes comparable in toxicity to CuO-NP 40 nm and more toxic than Cu-MSP 500 nm.

e. References

[1]   Murdock, R. C.; Braydich-Stolle, L.; Schrand, A. M.; Schlager, J. J.; Hussain, S. M. Characterization of nanomaterial dispersion in solution prior to in vitro exposure using dynamic light scattering technique. *Tox. Sci.* 2008, *101* (2), 239-253

[2]   Schrand AM.; Schlager JJ.; Dai L and Hussain SM. Preparing Cells Dosed with Nanomaterials for Assessment of Internalization and Localization with Transmission Electron Microscopy. *Nature Protocols* 2010, Apr;5(4):744-57.

[3]   Schrand AM, Lin JB, Hussain SM. Assessment of Cytotoxicity of Carbon Nanoparticles Using 3-(4,5-Dimethylthiazol-2-yl)-5-(3-Carboxymethoxyphenyl)-2-(4-Sulfophenyl)-2H-Tetrazolium (MTS) Cell Viability Assay. *Methods Mol Biol.* 2012; 906:395-402.

[4]   Schrand AM, Dai L, Schlager JJ, Hussain SM Toxicity testing of nanomaterials. *Adv Exp Med Biol.* 2012; 745:58-75. Review

[5]   Schrand AM, Lin JB, Hens SC, Hussain SM. Temporal and mechanistic tracking of cellular uptake dynamics with novel surface fluorophore-bound nanodiamonds. Nanoscale. 2011 Feb;3(2):435-45.

[6]   Schrand AM, Rahman MF, Hussain SM, Schlager JJ, Smith DA, Syed AF. Metal-based nanoparticles and their toxicity assessment. *Wiley Interdiscip Rev Nanomed Nanobiotechnol.* 2010 Sep-Oct;2(5):544-68

[7]   T J Shaffner and R D Van Veld. 'Charging' effects in the scanning electron microscope *J. Phys. E: Sci. Instrum.* 1971. 4 633

[8]   Yguerabide J, Yguerabide EE. Light-scattering submicroscopic particles as highly fluorescent analogs and their use as tracer labels in clinical and biological applications. *Anal Biochem.* 1998 Sep 10; 262(2):157-76.

2. Relationship Between Physicochemical Properties and Nanotoxicity of CuNPs Nanoparticles

a. Purpose

The far-reaching applications of nanoparticles (NPs) in drug delivery, medical imaging, diagnostics, and therapeutics have led to an increased potential for interfacing with a diverse range of biological environments. While metallic NPs such as copper NPs have been explored for their antimicrobial and catalytic properties, they have been shown to induce undesirable toxic effects. Nonetheless, bio-modulators may be employed to control this cytotoxicity. Dynasore is a dynamin GTPase inhibitor that has been shown to rapidly and reversibly block clathrin-dependent endocytic traffic within minutes of application. Here, we demonstrate that Dynasore can chemically bio-modulate the toxic effects of copper nanoparticles (CuNPs) but not through reducing CuNP internalization. In fact, Dynasore seems to possess secondary effects that have been unreported to date. We propose and test three potential mechanisms of cytotoxicity modulation: 1) through changes in agglomeration pattern, 2) through potential quenching of reactive oxygen species (ROS), and 3) through Cu^{+2} ion chelation. These results have far-reaching implications for understanding the complex interactions that occur with NPs in biological environments, especially during mechanistic chemical modification strategies.

b. Materials and Methods

Copper Samples:

The particulate copper samples consisted of small metallic Cu nanoparticles (Cu 90, ~80-90 nm, American Elements, 99% metals basis, PN: CU-M-02M-NP.025N) and large metallic Cu nanoparticles (Cu 480, ~500 nm, American Elements, 99% metals basis, PN: CU-M-02-MP.01UM). The soluble salt form of copper was copper (II) chloride dehydrate, purchased from Sigma Aldrich (C3279).

Nanoparticle Characterization:

Transmission Electron Microscopy (TEM):

Copper nanoparticles (CuNPs) were dispersed in water and drop-cast onto formvar-carbon coated TEM grids, then imaged with a Philips/FEI CM200 TEM at 200kV. Final bright-field TEM (BF-TEM) images were obtained with Revolution software and saved as tiff images. Analysis of approximately one hundred individual CuNPs from each sample yielded average sizes of 88 ± 30 nm for Cu 90 and 477 ± 184 nm for Cu 480. Therefore, based upon these values, the CuNP samples – although fairly polydisperse in size – were appropriately categorized as either small (~90 nm) or large (~480 nm).

Powder X-ray Diffraction (XRD):

Copper nanoparticles (CuNPs) were sprinkled onto slides coated with silicone grease prior to analysis on a Rigaku 2500 x-ray diffraction unit. All of the data was acquired under the following parameters: divergence slit = scatter slit = 1 degree, divergence height limiting slit = 10 mm, receiving slit = 0.6 mm. Powders were scanned in 2theta-theta geometry (also known as Bragg-Brentano geometry) from 2 theta 20 degrees to 100 degrees. The sampling interval was 0.05 degrees, and the scan speed was 3 degrees per minute with continuous scan. The power parameters were 50 KV, 300 mA, so 15 KW.

Dynamic Light Scattering (DLS):

Particle solutions were prepared and analyzed as previously described[1]. Briefly, Cu particles were suspended in DMEM/F12 cell culture media at a final concentration of 50 µg/mL and immediately analyzed for initial agglomerate sizes (0 h). Then, the samples were incubated at 37°C for 3 h to observe alterations in agglomerate size in solution (Figure S1, Appendix III, B). Data are presented as the most prevalent agglomerate size over 3 h based on scattering intensity.

Nanoparticle Size Measurements:

Average particle size measurement and particle size distribution of the Cu 90 and Cu 480 nanoparticles in cell culture media was determined using ALV-CGS 3 compact goniometer system (ALV-GmbH, Langen, Germany), equipped with a 22mW, 632.8 nm He-Ne laser and coupled with ALV/LSE-5004 digital auto correlator (ALV-GmbH, Langen, Germany). Approximately 2 mL of a 25 mg/L nanoparticle solution in DMEM/F12+1% streptomycin was added into previously cleaned disposable borosilicate glass vials (Fisher Scientific, Pittsburg, PA). The cleaning procedure is described elsewhere.[14] Scattered light intensity was measured at 37°C by a photon counting module (Perkin Elmer, Dumberry, Canada) operating at 1.2 amperes and 5 volts. The scattering angle of 90° was used for 1 h, with a 15 s time interval between consecutive readings. The scattering intensity was interpreted as hydrodynamic radius using second order cumulant analysis.[15] A similar procedure was followed to perform DLS measurements of CuNPs in presence of Dynasore with DMEM/F12+1% streptomycin.

Acellular ROS:

In order to measure the amount of ROS generated by CuNPs independently of the cellular system, an acellular ROS was performed as described in Braydich-Stolle et al., 2009.[18]   The ROS probe was made by deacetylating the 2',7'-dichlorofluorescein diacetate (DCFH-DA) probe in NaOH. Immediately prior to analysis, horseradish peroxidase (HRP) reagent was added to the DCFH-DA solution. To measure ROS, the

DCFH-HRP probe was added to different concentrations of nanoparticles in cell culture media and incubated at 37°C for 30 min (Fig S2, Appendix III, B).

Cell Culture and Related Experiments:

Cell Culture:

Neuroblastoma (N2A) cells were purchased from ATCC (Neuro-2a line, CCL-131) and grown in an atmosphere of 5% CO_2 at 37°C. Growth media for the neuroblastoma cells was DMEM/F12 supplemented with 10% normal fetal bovine serum (FBS) and 1% Pencillin-streptomyocin (ATCC). Other cell culture supplies included 10x Phosphate buffered saline (pH 7.4) and 2.5% trypsin (Gibco Invitrogen™ Corporation, Carlsbad, CA).

Endocytosis Inhibitor Dynasore:

Murine neuroblastoma (N2A) cells were pre-treated with 25 µM Dynasore for 1 h, followed by 3 h of exposure to CuNPs. This concentration was chosen based on literature values and control experiments, which are described in the supporting information (Fig S3-S4, Appendix III, B).

MTS Assay for Mitochondrial Function:

The 3-(4,5-dimethylthiazol-2-yl)-5-(3-carboxymethoxyphenyl)-2-(4-sulfophenyl)-2H-tetrazolium (MTS) assay assesses cellular viability based on mitochondrial function. After 1 h of incubation with MTS, a dark purple color developed within the cells, indicating the formation of a water-soluble formazan product by active mitochondria in live cells. The formazan product was quantified with a microplate reader at 490 nm. A reading from 0 minutes was subtracted out of the final reading to account for background absorbance due to the NPs or the solution. The percent reduction of MTS was compared to controls (cells not exposed to particles), which represented 100% MTS reduction.

Cellular Reactive Oxygen Species (ROS):

The generation of intracellular reactive oxygen species (ROS) was determined using the fluorescent probe 2,7-dichlorohydrofluorescein diacetate (DCHF-DA) under a light controlled environment as described by Wang and Joseph (1999), with minor modifications as previously described by Hussain and Frazier (2002). The reactivity of the DCFH probe was evaluated with the positive control, hydrogen peroxide, by serial dilutions of stock 30% H_2O_2 (Sigma) in dosing media (Fig S6, Appendix III, B).

Cellular Uptake of Copper Particles with Transmission Electron Microscopy:

N2A cells were processed for TEM according to Schrand et al.[21] Briefly, the cells were seeded in T-75 flasks and, at 85% confluency, incubated with 25 µg/mL of the CuNPs with or without 25 µM Dynasore pretreatment. Three hours later, the cells were fixed in 2% paraformaldehyde/2.5% gluteraldehyde in PBS for 2 h. Thereafter, the cells were post-fixed with 1% osmium tetroxide for 1 h and then scraped from the plate and centrifuged. The cells were dehydrated using increasing concentrations of ethanol with three changes of 100% ethanol. The samples then were placed in 100% LR White resin and cured overnight at 60°C in BEEM® capsules. The samples were thin- sectioned on a Leica Ultra cut ultramicrotome at a thickness of ~100 nm and imaged using a Philips/FEI CM200 TEM at 200kV.

Atomic Absorption Spectroscopy for Quantification of Cu Uptake

Approximately 2×10^6 cells were seeded in T-75 cell culture flasks and exposed to Cu particles. The samples were washed, centrifuged, and counted on a hemocytometer prior to acid digestion and dilution. The samples were analyzed on a Varian AA240 atomic absorption spectrometer for total amount of copper in a standardized 5-10 mL sample, and the data was collected as micrograms/milliliter (equivalent to parts per million) with atomic absorption spectroscopy (AAS).

Inductively Coupled Plasma – Mass Spectroscopy (ICP-MS) for Ionic Dissolution:

Characterization of ionic release from CuNPs was performed after filtration with MicroKros hollow fiber membranes from Spectrum Laboratories, Inc. The pore rating used was 10kDa to ensure only ions could pass through the membrane. The fibers were rinsed with ethanol to produce a hydrophilic surface, and then rinsed with water thoroughly to remove all trace amounts of alcohol. After the preparation of the filter, the solutions were passed through the fibers repeatedly to remove the disassociated ions. ICP-MS was conducted to obtain ionic concentrations. Samples were diluted in 1% nitric acid prior to running on a Perkin Elmer Elan DRC-e ICP-MS. The DRC gas was methane at 0.55 mL/min.

High-Performance Liquid Chromatography (HPLC):

Solutions were prepared and incubated at 5% CO_2 and 37°C in dosing media to simulate the potential reaction conditions during chemical bio-modulation. Samples were analyzed using Zorbax XDB-C_{18} columns and the Agilent 1100 series liquid chromatography system coupled with UV detection. The mobile phases were A) water with 0.1% Trifluoro acetic acid (TFA) and B) 100% methanol with 0.1% TFA, with an initial concentration of 100% A increasing up to 100% B in 40 minutes. Detection was carried out with UV at 254 nm.

c.   Results and Discussion

Copper samples were first characterized to understand the role of size and aggregation behavior on cellular end-points of viability, oxidative stress, and uptake. Transmission electron micrographs (TEM) reveal small and large CuNPs with an average size of ~90nm (88±30nm, Cu 90, Figure 43A) and ~480nm (477± 184nm, Cu 480, Figure 43B), respectively. The Cu 480 displayed a more homogenous spherical morphology compared to the Cu 90, which appeared to be more fused and agglomerated. The metallic composition of these two samples was confirmed with powder x-ray diffraction (XRD): both spectra revealed minimal surface oxidation on the CuNPs (Figure 43C-D).
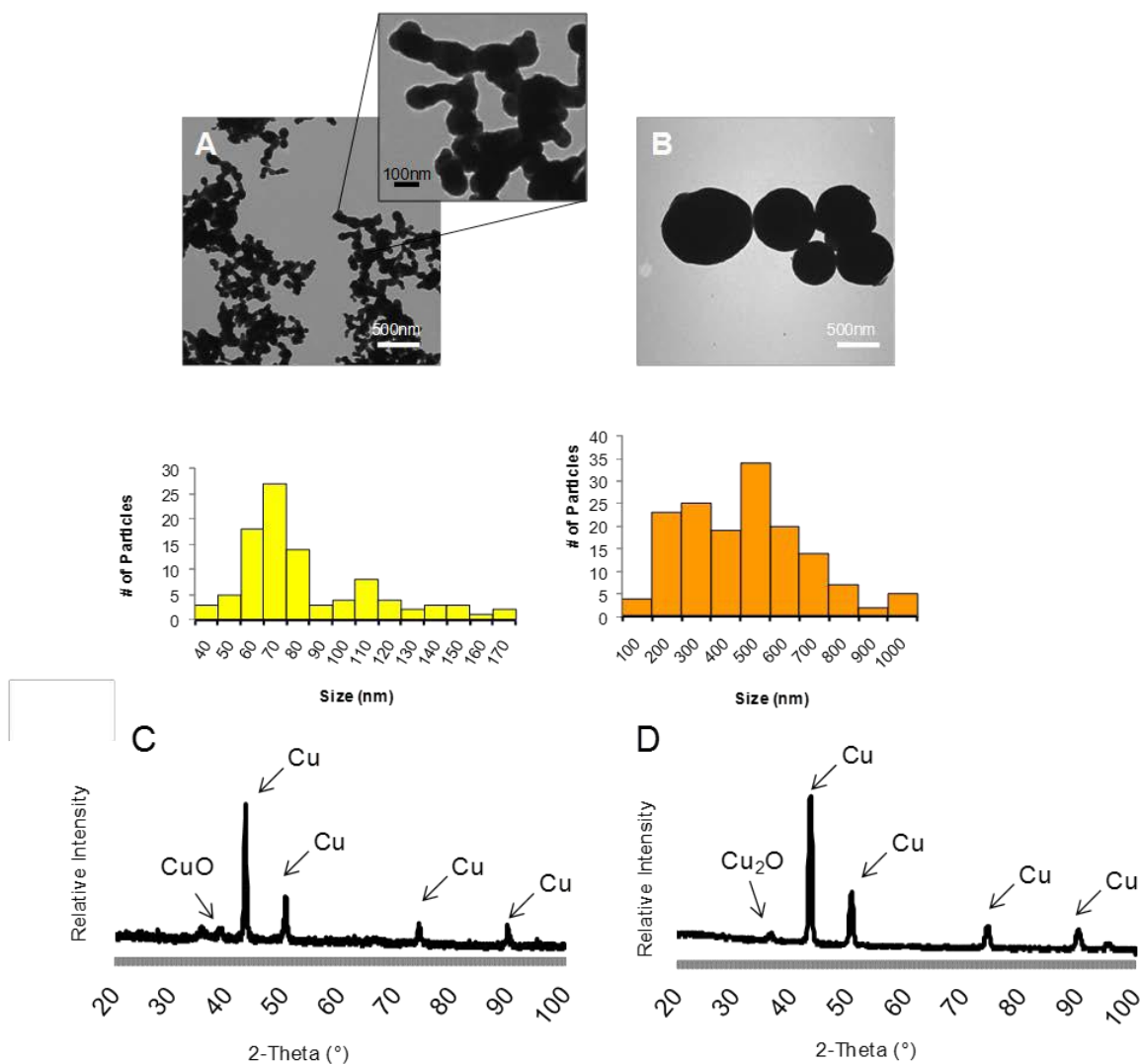

Figure 43. Characterization of CuNPs. (A-B) Bright field transmission electron micrographs and associated size distributions of CuNPs. (A) Cu 90 with average diameter of 88 ± 30 nm and (B) Cu 480 with average size of 477 ± 184 nm. Inset in (A) shows details of surface morphology compared to original image, which was taken at the same magnification to demonstrate the size difference between samples. (C-D) Powder x-ray diffraction (XRD) patterns demonstrating negligible amounts of surface oxidation in both the (C) Cu 90 and the (D) Cu 480.

In accordance with previous studies that expound on the cytotoxicity of CuNPs *in vitro*[22-25] both sizes of CuNP yielded cell viability values of less than 50% at concentrations ranging from 25-100 µg/mL following 3 h exposures as measured with MTS (Figure 44A-B). This cytotoxicity was greater for Cu 90 (Figure 44A) compared to Cu 480 (Figure 44B), with a steeper drop in viability at the lower concentrations. Similarly, the production of reactive oxygen species (ROS) increased in a dose-dependent manner at the same concentrations and exposure end points (Figure 44C-D). However, pre-incubation of the cells for 1 h with the endocytosis inhibitor Dynasore followed by 3 h of exposure to NPs significantly reduced the cytotoxic effects of both sizes of CuNPs (Figure 44A-B) and quenched ROS generation (Figure 44C-D). These beneficial effects were not evident with co-incubation when Dynasore and the NPs were applied to the cells at the same time (Figure S3-S4, Appendix III, B). These results indicate that Dynasore pretreatment is necessary for bio-modulation and the rescue effect, which is consistent with other similar studies.[4-11]
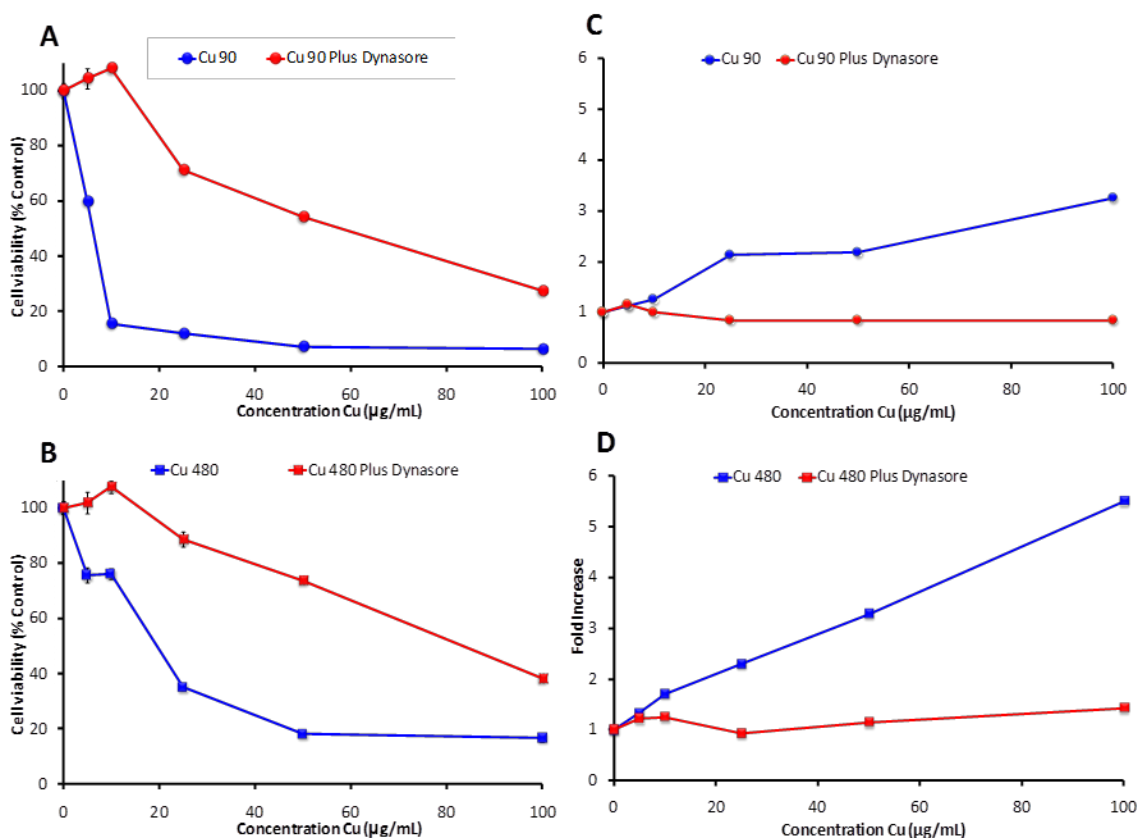

Figure 44. Rescue of cell viability and quenching of ROS after 25 µM Dynasore pretreatment for 1 h. (A-B) Cell viability assessment and (C-D) Cellular ROS production (Red = with 25 µM Dynasore, Blue = without Dynasore). Note that viability is significantly increased at all concentrations with 25 µM Dynasore pretreatment for 1 h for both (A) Cu 90 and (B) Cu 480

NPs (paired t-test one-tailed, p < 0.05). Similarly, ROS production is significantly reduced after pretreatment with 25 μM Dynasore for both (C) Cu 90 and (D) Cu 480 NPs (paired t-test one-tailed, p < 0.05).

Because Dynasore has been primarily used for its function as an endocytosis inhibitor, it would seem that the observed cytotoxicity modulation by Dynasore pretreatment is due, at least in part, to blockage of CuNP internalization. However, as a chemical inhibitor, Dynasore may possess other secondary effects that are unreported to date. For example, Dynasore may be reducing toxicity through other mechanisms. Therefore, we sought to confirm visible alterations in uptake with transmission electron microscopy (TEM) and assess quantifiable changes in the amount of internalized Cu with atomic absorption spectroscopy (AAS). High resolution TEM has been previously used to track various NPs inside individual cells[26,27,12] and can be used in conjunction with energy-dispersive x-ray spectroscopy (EDXS) to provide morphological and elemental verification of the NPs.[21] In this case, we found very low internalization of both sizes of CuNPs with and without short-term inhibition of endocytosis after evaluation of over 100 cells from each sample (Figure 45). Nonetheless, the CuNPs that did enter cells were localized to intracellular vacuoles (V), such as endosomes and lysosomes, confirming the transient effects of a pretreatment blocking methodology. Quantification with AAS corroborates minimal differences in uptake for cells pretreated with Dynasore (Figure 45, associated table). Therefore, uptake inhibition does not seem to be the mechanism at work reducing cytotoxicity.
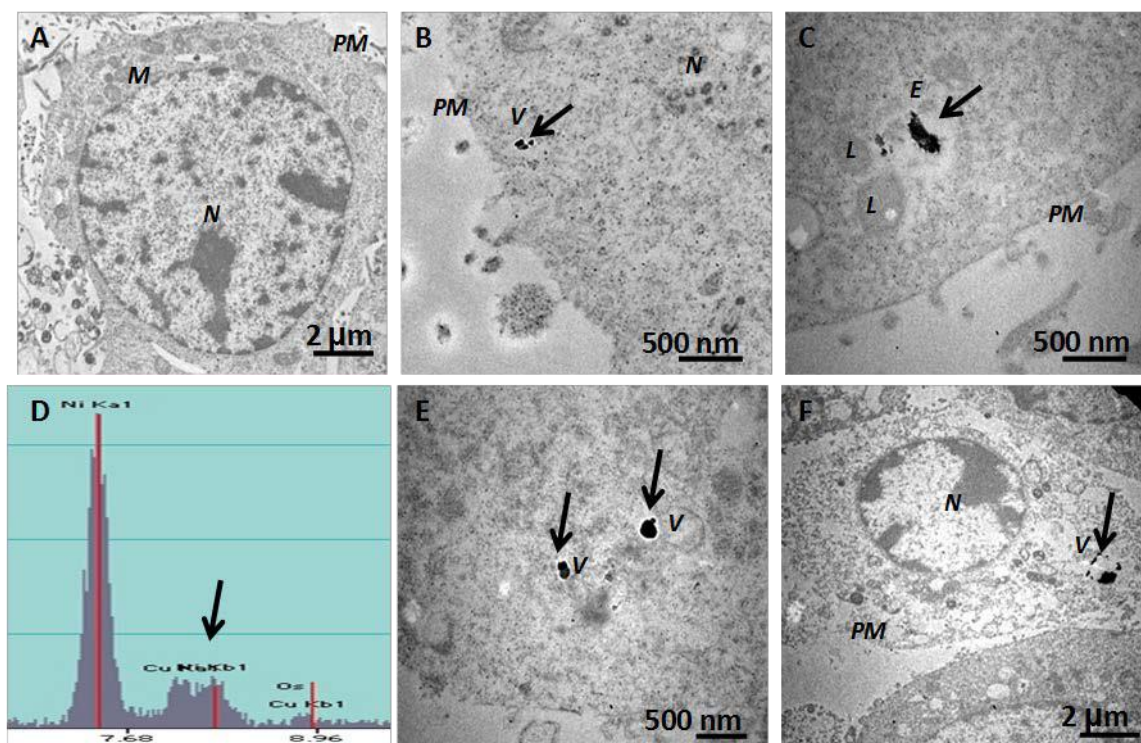
Sample	Cu Uptake (µg/ml)	Cu Uptake (+Dynasore)
Cu 90	12.8 ± 3.5	13.5 ± 4.9
Cu 480	23.2 ± 11.9	21.4 ± 4.4
CuCl₂	N/A	N/A

Figure 45. Selected TEM micrographs, representative EDXS spectra demonstrating low CuNP uptake and localization inside cells with or without 25 µM Dynasore pretreatment for 1 h and quantification of low uptake with AAS. (A) Control, (B) Cu 90, (C) Cu 480, (D) Representative EDXS: Large Ni signal from TEM grid, representative Cu signal (black arrow) from CuNP identified inside cell and background Os signal from cell staining procedure, (E) Cu 90 plus 25 µM Dynasore pretreatment for 1 h, (F) Cu 480 plus 25 µM Dynasore pretreatment for 1 h. Note that the uptake of CuNPs was very low under both treatment conditions. Associated Table containing AAS data demonstrates no quantifiable differences in Cu uptake with or without Dynasore pretreatment. Abbreviations: PM: plasma membrane, N: nucleus, M: mitochondria, V: vacuole, E: endosome, L: lysosome. Black arrows denote intracellular CuNPs.

Other potential interactions of Dynasore with the CuNPs such as alterations in fundamental aggregation behavior and surface interaction of CuNPs under biological conditions were examined in order to more firmly establish a relationship between effects on physicochemical properties and the observed cytotoxicity rescue (Figure 46). Changes in size after dispersion in cell culture media is caused by transient clustering of the NPs, which may directly affect the NP's chemical properties and/or limit cellular uptake by normal mechanisms such as clathrin-dependent endocytosis. In conventional

uptake mechanisms, the upper threshold of internalization size is typically limited to ~500 nm. Changes in aggregation after addition of Dynasore may reflect a change in physicochemical properties, which may affect potential for cytotoxicity. We examined the aggregation behavior of the two different sizes of CuNPs (90 nm and 480 nm) with and without the addition of Dynasore over a 3-hour period at 37°C in biological exposure conditions with time-resolved dynamic light scattering.[15,16]

The CuNP colloidal stability analysis demonstrated that the smaller Cu 90 NPs (Figure 46A) had a slower increase in size over time with less variability in their average size compared to their larger Cu 480 NP counterpart (Figure 46B). The Cu 480 NPs aggregated soon after addition to the exposure medium and continued to demonstrate large variability in particle aggregate size throughout the exposure time period. Furthermore, the Cu 90 NPs continued to increase in size over the duration of the experiments, yet remained smaller in hydrodynamic diameter compared to the Cu 480 NPs, confirming a true size difference for the two CuNPs under biological conditions. In agreement, the primary size and size distributions obtained with high resolution TEM (HRTEM) ranged from 40-170 nm for the Cu 90 NPs and 100-1000 nm for the Cu 480 NPs (Figure 43A-B), where the Cu 480 NPs showed a wider size distribution compared to the Cu 90 NPs. Both suspensions demonstrated the presence of much larger agglomerate sizes compared to the primary size of the CuNPs, suggesting that the cells are exposed to a variety of aggregates sizes for both samples. Similar results were obtained with traditional DLS (Figure S1, Appendix III, B).

Interestingly, the addition of the chemical Dynasore resulted in the formation of CuNP networks, which were more widely distributed in their size. For example, both the Cu 90 and Cu 480 with Dynasore formed aggregates with sizes up to 10 microns (Figure 46C-D). In general, it appears that addition of Dynasore increased network formation, which caused reduced toxicity of the CuNP samples independent of their initial primary size. For example, the overall dispersion trends follow the cell viability trends: Cu 480/Dynasore > Cu 90/Dynasore > Cu 480 > Cu 90 (Figure 44). These networks may be related to ions from the media bridging the OH- groups that exist within the Dynasore molecules and contribute to the reduction of cytotoxicity observed in this way.
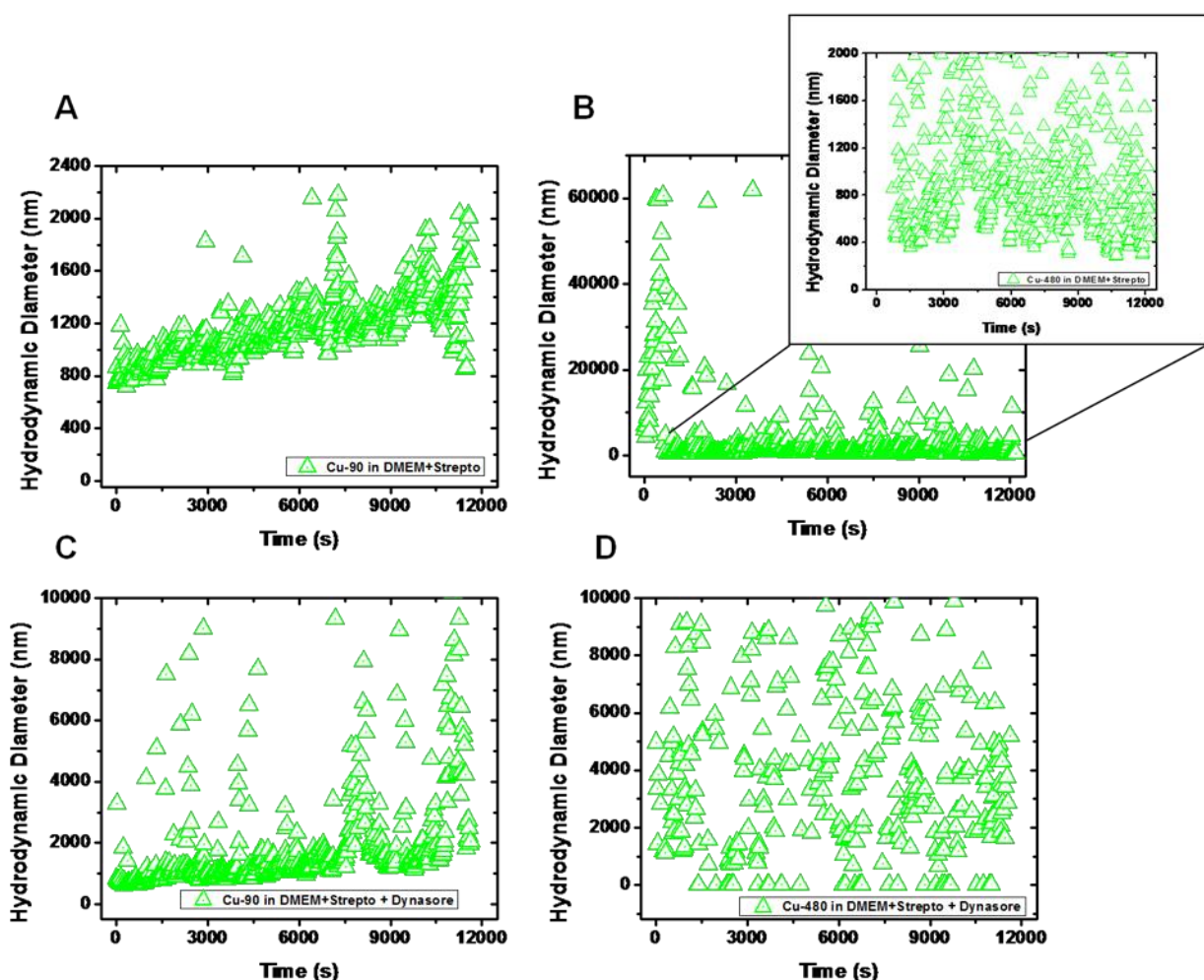
Figure 46. Time-dependent aggregation behavior of CuNPs under cell culture conditions (37 °C, 0-3h). (A) Cu 90 NPs and (B) Cu 480 NPs, (C) Cu 90 NPs + 25 µM Dynasore and (D) Cu 480 NPs +25 µM Dynasore. Inset in (B) is enlargement of lower condensed values. All values presented are average hydrodynamic diameters of the particle suspension at respective time point. Note that the addition of Dynasore increases the size distribution of both CuNP samples (C-D).

However, Dynasore may affect not only the physical properties of the CuNPs but also their chemical reactivity. While we originally hypothesized that ROS reduction may be caused by blocking uptake (Figure 44C-D), Dynasore may instead be acting as an ROS quencher, leading to increased cell viability. Dynasore can potentially act as a free radical scavenger because of the three hydroxyl groups in its chemical structure (Figure 47A). In this case, free radicals generated at the surface of the CuNPs[17] may be scavenged by Dynasore under biological conditions by abstracting a hydrogen atom from one of the ortho-phenolic hydroxyl groups of Dynasore, thereby inactivating the radical species responsible for cellular damage. In support of this, we found that CuNP-induced reactive oxygen species (ROS) in an acellular environment was significantly

quenched after the addition of Dynasore (Figure S2, Appendix III, B). To further confirm this potential mechanism, we tested a known ROS quencher, N-acetyl-cysteine (NAC). As expected, there was a significant quenching of ROS upon pre-incubation with 50 mM

NAC for 1 h prior to exposure to 100 µg/mL of Cu 90 or Cu 480 NPs (Figure 47B-C). The similar type of ROS reduction with both NAC and Dynasore corroborate this ROS quenching as a potential mechanism of cytotoxicity modulation.
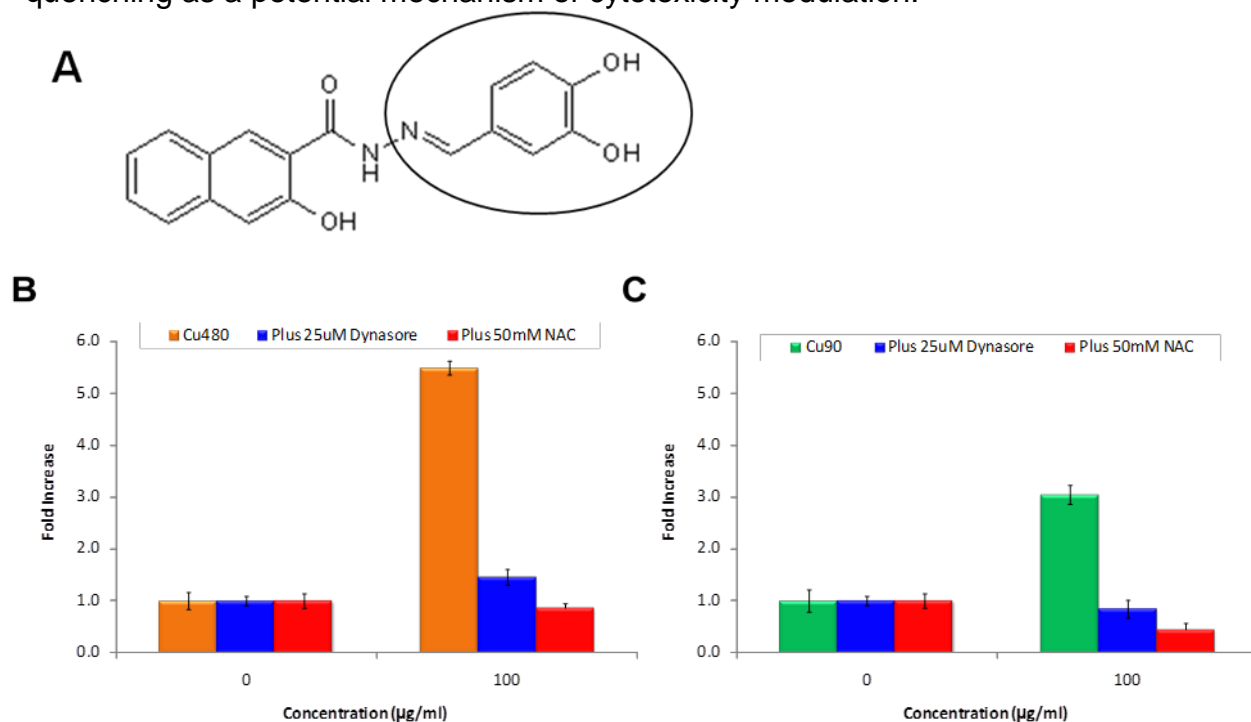

Figure 47. Proposed potential mechanism of Dynasore cytotoxicity rescue ROS quenching with reactive phenolic hydroxyl end groups as free radical chain reaction terminators. (A) Dynasore chemical structure with reactive end groups circled. (B) Comparison of ROS quenching ability of Dynasore to known ROS-quencher NAC in Cu 90. (C) Comparison of ROS quenching ability of Dynasore to known ROS-quencher NAC in Cu 480. In both cases, it appears that Dynasore functions similarly to NAC to significantly reduce ROS levels.

Another possible mechanism for the apparent rescue effect of Dynasore may be related to its complexing with Cu ions released by the CuNPs, thereby reducing the concentration of free Cu ions in the media and their availability to induce damaging effects to the cells (Figure 48). It is well known that copper NPs generate ROS and cytotoxicity that is linked to dissolution and ionic release.[28-32] Removal of metallic ions from the cellular environment through chelation has been used to alleviate conditions involving toxic levels of metallic ions such as Wilson's disease.[33,34] In this case, Dynasore's polyphenolic structure may allow for Cu+2 ion chelation by forming 5- or 6-membered rings. Some antioxidants with similar polyphenolic structural features, such as the flavonoids rutin and quercetin, were reported to behave via similar mechanisms.[35] Recently, additional phenolic compounds have demonstrated specific

antioxidant reactivity towards hydrogen peroxide and copper ions.[36] Through tangential flow filtration, we found that both of the CuNP samples produced significant concentrations of ions under cell culture conditions (Figure 48B). The toxicity of these Cu ions alone was corroborated by the finding that comparable amount of Cu^{+2} ions from $CuCl_2$ were also highly toxic (Figure S5, Appendix III, B).

To corroborate this potential mechanism via ion chelation, we performed high-performance liquid chromatography to characterize electronic configuration. Our spectrographs show a clear peak for the Dynasore molecule at roughly 20.64-20.67 min (Figure S7, Appendix III, B). In addition, the peak for the Dynasore molecule through HPLC was split after the addition of Cu 90, Cu 480, and $CuCl_2$ (Figure 48C-F), indicating a change in electronic configuration that may be related to the ion chelation. This splitting is not based on the mere presence of any chemical species in the media (Figure S8, Appendix III, B) nor the particles themselves (Figure S9-S11, Appendix III, B), since none of these samples by themselves have a peak near this region. The similar peak splitting for both particles that release ions and pure ions suggests that similar chelation mechanisms may be occurring in all three cases. Therefore, it is possible that Dynasore may form complexes with the Cu ions to reduce their bio-availability and toxic potential. These complexes may be related to the networks observed through time-resolved DLS (Figure 46C-D).
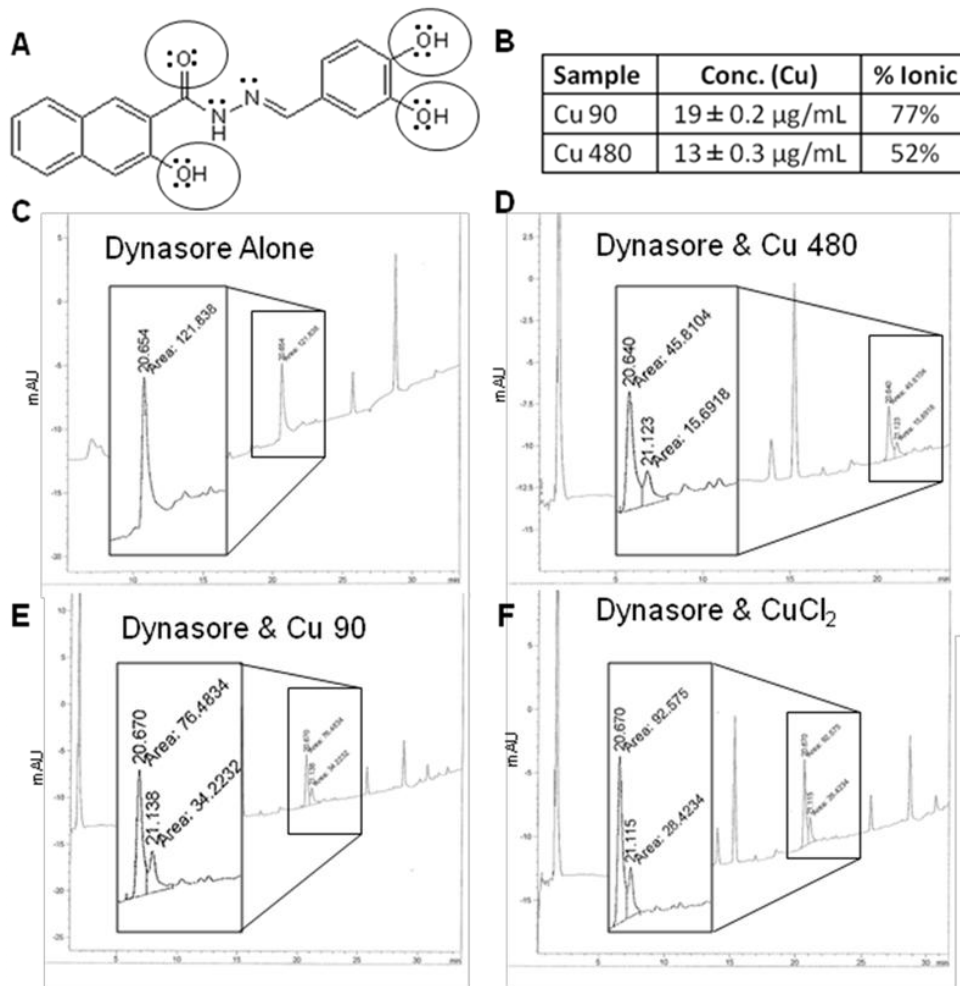
Figure 48. Potential mechanism of Dynasore cytotoxicity rescue through Cu^{2+} chelating by 5- or 6-membered rings. (A) Dynasore chemical structure with lone pairs that can chelate Cu ions indicated. (B) Significant amount of dissolution and release of Cu ions for both Cu 90 and Cu 480. (C) Corroboration of potential Cu^{+2} ion chelation with HPLC; similar splitting of the Dynasore peak after addition of (D) Cu 480, (E) Cu 90, and (F) $CuCl_2$, indicates a change in electronic structure. Inset images are enlargements

d.   Conclusions

In summary, we provide evidence that Dynasore reduces the cytotoxicity of CuNPs, but not through uptake inhibition. Instead, Dynasore's ability to rescue cells from CuNP-induced toxicity is based on other secondary effects. We have proposed and provided evidence to support three possible mechanisms that are independent of the CuNP size or form: physical alterations in aggregation (Figure 46), chemical ROS quenching (Figure 47), and chemical ion chelation (Figure 48). Furthermore, the cell viability rescue effect of Dynasore also extends to the soluble form of copper in $CuCl_2$ (Figure S5, Appendix III, B). All in all, our results suggest that some of the beneficial effects previously observed during Dynasore treatment strategies[11] may be due, in part, to the

physicochemical alterations brought forth in this work. Nonetheless, pretreatment with Dynasore for 1 h is not sufficient to fully recover cell viability to control levels after 3 h of continuous exposure to CuNP concentrations exceeding 10 µg/mL. This indicates that high doses of CuNPs may overwhelm the short-term protective effects of Dynasore leading to alternative mechanisms of CuNP-induced cell death. Cumulatively, our results aid in mechanistically explaining nanomaterial interactions with biological species at the cellular level. These results have far-reaching implications for understanding the complex interactions that occur with NPs in biological environments, especially during mechanistic chemical modification strategies.

e.   *References*

[1]   Cioffi N, Torsi L., Ditaranto N., Tantillo G., Ghibelli L., Sabbatini L., Bleve-Zacheo T., D'Alessio M., Zambonin P G, Traversa E. Copper Nanoparticle/Polymer Composites with Antifungal and Bacteriostatic Properties. *Chem. Mater.* 2005, 17, 5255-62.

[2]   Anyaogu, K. C.; Fedorov, A. V.; Neckers, D. C. Synthesis, characterization, and antifouling potential of functionalized copper nanoparticles. *Langmuir* 2008, 24, 4340-46.

[3]   Schrand AM, Rahman MF, Hussain SM, Schlager JJ, Smith DA, Syed AF. Metal-based nanoparticles and their toxicity assessment. *Wiley Interdiscip Rev Nanomed Nanobiotechnol.* 2010a, 2, 544-68.

[4]   Macia, E.; Ehrlich, M.; Massol, R.; Boucrot, E.; Brunner, C.; Kirchhausen, T. Dynasore, a cell-permeable inhibitor of dynamin. *Dev. Cell* 2006, 10, 839-50.

[5]   Kirchhausen, T.; Macia, E.; Pelish, H. E. Use of dynasore, the small molecule inhibitor of dynamin, in the regulation of endocytosis. *Methods Enzymol.* 2008, 438, 77-93.

[6]   Thompson, H. M.; McNiven, M. A. Discovery of a new 'dynasore'. *Nat. Chem. Biol.* 2006, 2, 355-56.

[7]   Newton, A. J.; Kirchhausen, T.; Murthy, V. N. Inhibition of dynamin completely blocks compensatory synaptic vesicle endocytosis. *Proc. Natl. Acad. Sci. U.S.A.* 2006, 103, 17955-60.

[8]   Martinez-Argudo, I.; Jepson, M. A. Salmonella translocates across an in vitro M cell model independently of SPI-1 and SPI-2. *Microbiology* 2008, 154, 3887-94.

[9]   Gratton, S. E. A.; Ropp, P. A.; Pohlhaus, P. D.; Luft, J. C.; Madden, V. J.; Napier, M. E.; DeSimone, J. M. The effect of particle design on cellular internalization pathways. *Proc.Natl. Acad. Sci. U.S.A.* 2008, 105, 11613-18.

[10]   Jiang, X.; Dausend, J.; Hafner, M.; Musyanovych, A.; Rocker, C.; Landfester, K.; Mailander, V.; Nienhaus, G. U. Specific effects of surface amines on polystyrene nanoparticles in their interactions with mesenchymal stem cells. *Biomacromolecules* 2010, 11, 748-53.

[11]   Soriano, J.; Stockert, J. C.; Villanueva, A.; Canete, M. Cell uptake of Zn(II)-phthalocyanine-containing liposomes by clathrin-mediated endocytosis. *Histochem. Cell Bio.* 2010, 133, 449-54.

[12]   Schrand, A. M.; Lin, J. B.; Ciftan Hens, S.; Hussain, S. M. Temporal and mechanistic tracking of cellular uptake dynamics with novel surface fluorophore-bound nanodiamonds. *Nanoscale* 2011, 3, 435-45.

[13]   Murdock, R.C.; Braydich-Stolle, L.; Schrand, A. M.; Schlager, J. J.; Hussain, S. M. Characterization of nanomaterial dispersion in solution prior to in vitro exposure using dynamic light scattering technique. *Toxicol. Sci.* 2007, 101, 239-53.

[14]   Surdo, E. M.; Khan, I. A.; Choudhury, A. A.; Saleh, N. B.; Arnold, W. A. Barrier properties of poly(vinyl alcohol) membranes containing carbon nanotubes or activated carbon. *J. Haz. Mat.* 2011, 188, 334-40.

[15]   Saleh, N. B.; Pfefferle, L. D.; Elimelech, M. Aggregation kinetics of multiwalled carbon nanotubes in aquatic systems: measurements and environmental implications. *Environ. Sci. Technol.* 2008, 42, 7963-69.

[16]   Saleh, N. B.; Pfefferle, L. D.; Elimelech, M. Influence of biomacromolecules and humic acid on the aggregation kinetics of single-walled carbon nanotubes. *Environ. Sci. Technol.* 2010, 44, 2412-18.

[17]   Nel, A.; Xia, T.; Mädler, L.; Li, N. Toxic potential of materials at the nanolevel. *Science* 2006, 311, 622-27.

[18]   Braydich-Stolle LK. Schaeublin NM, Murdock RC, Jiang J, Biswas P, Schlager JJ, Hussain SM. Crystal structure mediates mode of cell death in titanium dioxide nanotoxicity. *J. Nanopart. Res.* 2009, 11, 1361-74.

[19]   Wang, H.; Joseph, J. A. Quantifying cellular oxidative stress by dichlorofluorescein assay using microplate reader. *Free Radic. Biol. Med.* 1999, 27, 612-16.

[20]   Hussain, S. M.; Frazier, J. M. Cellular toxicity of hydrazine in primary rat hepatocytes. *Toxicol. Sci.* 2002, 69, 424-32.

[21]   Schrand, A. M.; Schlager, J. J.; Dai, L.; Hussain, S. M. Preparation of cells for assessing ultrastructural localization of nanoparticles with transmission electron microscopy. *Nat. Protoc.* 2010b, 5, 744-57.

[22]   Midander, K.; Cronholm, P.; Karlsson, H. L.; Elihn, K.; Möller, L.; Leygraf, C.; Wallinder, I. O. Surface characteristics, copper release, and toxicity of nano- and micrometer-sized copper and copper (II) oxide particles: a cross-disciplinary study. *Small* 2009, 5, 389-99.

[23]   Lanone, S.; Rogerieux, F.; Geys, J.; Dupomt, A.; Maillot-Marechal, E.; Boczkowski, J.; Lacroix, G.; Hoet, P. Comparative toxicity of 24 manufactured nanoparticles in human alveolar epithelial and macrophage cell lines. *Part, Fibre Toxicol.* 2009, 6.

[24]   Fahmy, B.; Cormier, S. A. Copper oxide nanoparticles induce oxidative stress and cytotoxicity in airway epithelial cells. *Toxicol. In Vitro* 2009, 23, 1365-71.

[25]   Karlsson, H. L.; Gustafsson, J.; Cronholm, P.; Möller, L. Size-dependent toxicity of metal oxide particles--a comparison between nano- and micrometer size. *Toxicol. Lett.* 2009, 188, 112-18.

[26]   Schrand AM, Huang H, Carlson C, Schlager JJ, Omacr Sawa E, Hussain SM, Dai L. Are diamond nanoparticles cytotoxic? *J. Phys. Chem. B.* 2007, 111, 2-7.

[27]   Schrand, A. M.; Braydich-Stolle, L. K.; Schlager, J. J.; Dai, L.; Hussain, S. M. Can silver nanoparticles be useful as potential biological labels? *Nanotechnology* 2008, 19, 1-13.

[28]   Griffitt RJ, Weil R, Hyndman KA, Denslow ND, Powers K, Taylor D, Barber DS. Exposure to copper nanoparticles causes gill injury and acute lethality in zebrafish (Danio rerio). *Environ. Sci. Technol.* 2007, 41, 8178-86.

[29]   Kasemets, K.; Ivask, A.; Dubourguier, H. C.; Kahru, A. Toxicity of nanoparticles of ZnO, CuO and TiO2 to yeast Saccharomyces cerevisiae. *Toxicol. In Vitro* 2009, 23, 1116-22.

[30]   Heinlaan M, Ivask A, Blinova I, Dubourguier HC, Kahru A. Toxicity of nanosized and bulk ZnO, CuO and TiO2 to bacteria Vibrio fischeri and crustaceans Daphnia magna and Thamnocephalus platyurus. *Chemosphere* 2008, 71, 1308-16.

[31]   Meng H, Chen Z, Xing G, Yuan H, Chen C, Zhao F, Zhang C, Wang Y, Zhao Y. Ultrahigh reactivity and grave nanotoxicity of copper nanoparticles. *J. Radioanal. Nucl.* Ch. 2007, 272, 595-98.

[32]   Meng H, Chen Z, Xing G, Yuan H, Chen C, Zhao F, Zhang C, Zhao Y. Ultrahigh reactivity provokes nanotoxicity: explanation of oral toxicity of nano-copper particles. Toxicol. Lett. 2007, 175, 102-10.

[33]   Thompson, K. H.; Orvig, C. Boon and bane of metal ions in medicine. *Science* 2003, 300, 936-39.

[34]   Subramanian, I.; Vanek, Z. F.; Bronstein, J. M. Diagnosis and treatment of Wilson's disease. *Curr. Neurol. Neurosci. Rep.* 2002, 2, 317-23.

[35]   Afanas'ev, I. G.; Dorozhko, A. I.; Brodskii, A. V.; Kostyuk, V. A.; Potapovitch, A. I.

Chelating and free radical scavenging mechanisms of inhibitory action of rutin and quercetin in lipid peroxidation. *Biochem. Pharmacol.* 1989, 38, 1763-69.

[36] Labieniec, M.; Gabryelak, T. Study of interactions between phenolic compounds and H2O2 or Cu(II) ions in B14 Chinese hamster cells. *Cell Biol. Int.* 2006, 30, 761-68.

C. Other Nanomaterials

1. Cellular Uptake and Effects of Engineered Nanoceria Based on Surface Charge

a. Introduction

The goal of this project is to evaluate the effect of surface charge on cellular uptake and bioeffects of nanoparticles using fluorescence-labeled nanoceria particles. Cells have a negative membrane potential and are decorated with negatively charged glycoproteins. Since nanoparticles can be coated with different molecules to give them specific surface charges, it follows that nanoparticles can be engineered for greater or less cellular uptake based on their surface charge. Moreover, different surface charges may target particles to different uptake pathways and alter their intracellular fate and therefore their bioeffect. Localization to acidic lysosomes can result from clathrin-mediated or fluid-phase endocytosis while cargo taken up by caveolae-mediated endocytosis is not trafficked to lysosomes (1). In fact, positively charged nanoceria particles have greater uptake and lysosomal association than negative or neutral particles (2) and nanoceria is expected to act as an oxidant in acidic lysosomal fluids but as an antioxidant in the pH-neutral cytoplasm (3). Changing the surface charge on nanoceria particles should, therefore, affect their uptake pathway, intracellular fate, and effect on the cell. This study examines the difference in uptake pathway and bioeffects of 4 nm cerium oxide nanoparticles which are coated with dextran, poly(acrylic acid), or aminated-poly(acrylic acid) producing a neutral, negative, or positive surface charge, respectively. DiI fluorescent dye attached to each particle allows intracellular visualization..

b. Nanoceria Uptake

1) **Purpose:** The purpose of this aim is to determine if the particle surface charge affects the internalization rate of nanoparticles.

2) **Materials and Methods:** The nanoceria particles were synthesized by Dr. Perez (University of Central Florida, Orlando, FL). They have a 4 nm core of cerium oxide and are coated with dextran for a neutral surface charge, or poly (acrylic acid) for a negative surface charge, or aminated-poly(acrylic acid) for a positive surface charge. They are designated DNC(0), PNC(-), and ANC(+), respectively. DiI fluorescent dye is bound to the coating for visualization. Cells were counterstained with Hoechst nuclear stain and Cell Mask Deep Red plasma membrane stain (Invitrogen) and visualized using a BD Pathway 435 nipkow-spinning-disc confocal microscope. The cell lines studied were HaCaT (human keratinocyte) and A549 (human pulmonary epithelium)

cells. Each was cultured in RPMI 1640 (ATCC) supplemented with 1% Penicillin/Streptomycin and 10% FBS (normal FBS for HaCaT and heat inactivated FBS for A549 cells). Particle uptake was measured after 100 µg/mL treatment for 5 minutes to 2 hours.

3)   **Results:** A greater number of neutrally charged DNC(0) particles were taken internally by both A549 and HaCaT cells than negatively charged PNC(-) particles. This difference was apparent in HaCaT cells from 10 minutes to 2 hours after exposure (Figure 49) and in A549 cells after 1 hour (Figure 50). The positively charged ANC(+) particles were taken up to about the same extent as PNC(-); however, the particles were later found to have equivalent, negative surface charges. No particle uptake was apparent during the first 5 minutes of exposure in HaCaT cells (Figure 49).
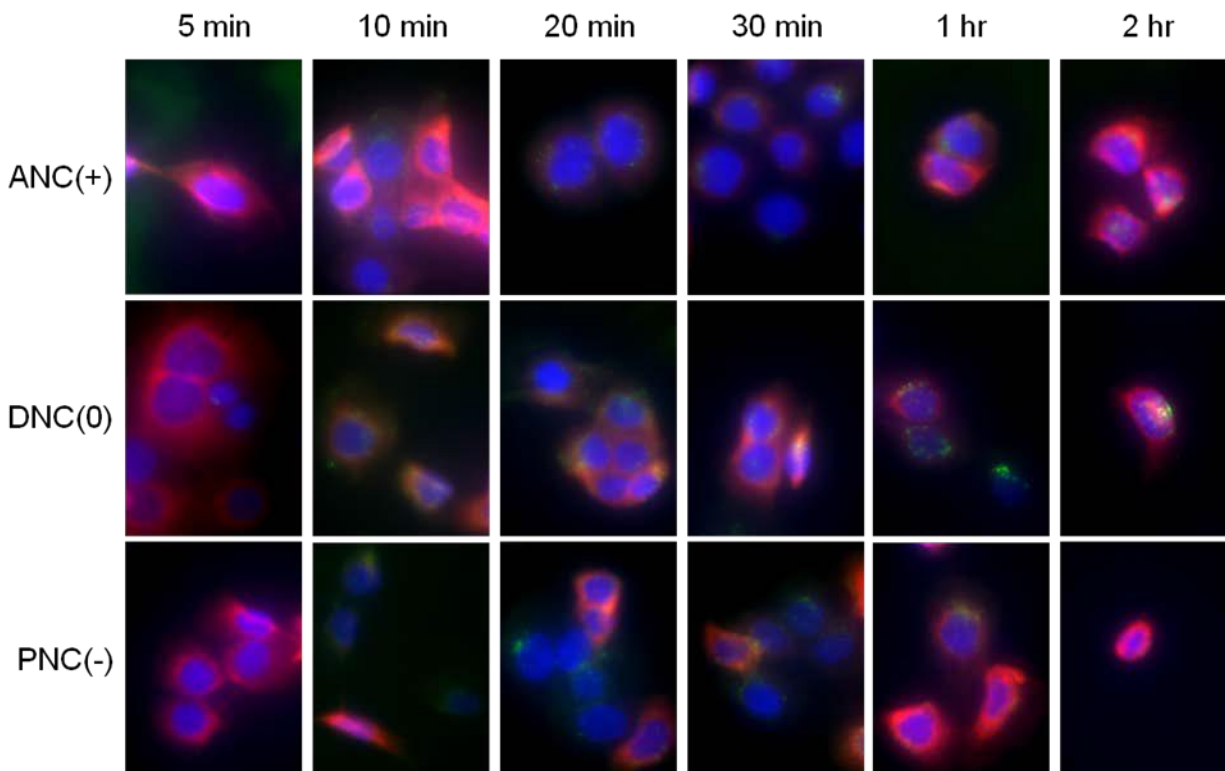

Figure 49: Uptake of nanoceria particles by HaCaT cells over time. Blue = nucleus, Red = plasma membrane, Green = nanoceria particle.

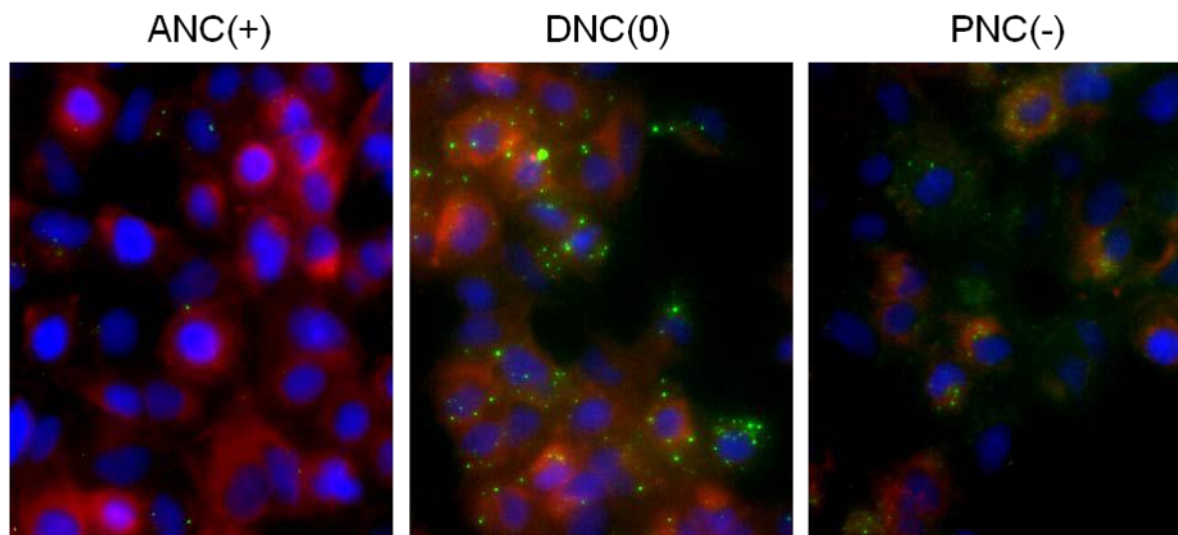DISTRIBUTION A: Approved for public release; distribution unlimited. PA Case No. 88ABW-2013-4073

114

Figure 50: Uptake of nanoceria particles by A549 cells after 1 hour of treatment. Blue = nucleus, Red = plasma membrane, Green = nanoceria particle.

4)   **Discussion:** Greater uptake of DNC(0) over PNC(-) demonstrated here was expected based on the overall negative surface charge of the cell membrane and anticipated repulsion of negative charges. Greater uptake was expected for the ANC(+) particles, but subsequent characterization of ANC(+) revealed a negative surface charge equivalent to PNC(-). This suggests a lack of amine groups on the aminated-poly (acrylic acid) coating and explains the lower than expected uptake of these particles. Further uptake studies with ANC(+) particles is pending the arrival of newly synthesized particles.

5)   **Conclusions:** Uncharged DNC(0) particles were internalized more than negatively charged PNC(-) from 10 minutes to 3 hours post-exposure.

c.   **Nanoceria Cytotoxicity**

1)   **Purpose:** The purpose of this aim is to determine if the particle surface charge affects the cytotoxicity of nanoparticles.

2)   **Materials and Methods**: The nanoceria particles were synthesized by Dr.Perez (University of Central Florida, Orlando, FL). They have a 4 nm core of cerium oxide and are coated with dextran for a neutral surface charge, or poly (acrylic acid) for a negative surface charge, or aminated-poly(acrylic acid) for a positive surface charge. They are designated DNC(0), PNC(-), and ANC(+), respectively. DiI fluorescent dye is also bound to the coating. The cell lines studied were HaCaT (human keratinocyte) and A549 (human pulmonary epithelium) cells. Each was cultured in RPMI 1640 (ATCC) supplemented with 1% Penicillin/Streptomycin and 10% FBS (normal FBS for HaCaT and heat inactivated FBS for A549 cells). Cytotoxicity was studied using the standard MTT assay after 24 hour exposure to 12.5 to 200 μg/mL nanoceria. DMSO was used to dissolve formazan crystals and measure their absorbance at 600 nm.

3)   **Results:** The results are presented in Figure 51. In HaCaT cells, DNC(0) particles caused significant cytotoxicity at or above 25 µg/mL but only reduced cellular activity bellow 80% of control at concentrations greater than 50 µg/mL. Every concentration of PNC (-) particles reduced cellular activity bellow 80% of control. No concentration of DNC (0) negatively impacted A549 cells and only the highest concentration of PNC (-) (200 µg/mL) significantly reduced cellular activity. Results for ANC (+) particles were the same as PNC(-) particles which is explained by the later discovery that both particles have the same negative surface charge.

4)   **Discussion:** Although DNC (0) particles were internalized more than PNC (-) particles (see section "b. Nanoceria Uptake" above), they caused less cytotoxicity in both cell lines. This may be due to the pathway of uptake utilized by each particle and their intrinsic oxidant/antioxidant properties. Since PNC (-) particles are likely repelled by the negatively charged cell surface, their interaction with the cell membrane leading to internalization is likely very specific: binding to a moiety on the cell surface with enough force to overcome the electrostatic repulsion. Therefore, PNC (-) are likely taken up by a receptor mediated process which typically involves clathrin-mediated uptake and targeting to lysosomes. DNC (0) are more likely to have non-specific interactions with the cell surface and be taken up by both receptor-mediated and incidental processes like fluid phase endocytosis which may not target the particles to lysosomes. In this way, PNC (-) particles are more likely to localize in acidic lysosomes and cause oxidative stress to cells than DNC (0) particles. A more detailed examination of intracellular localization and oxidative stress is necessary to confirm this hypothesis.

5)   **Conclusions:** Cytotoxicity was greatest for PNC (-) particles in both A549 and HaCaT cell lines, and HaCaT cells were more sensitive to nanoceria exposure.
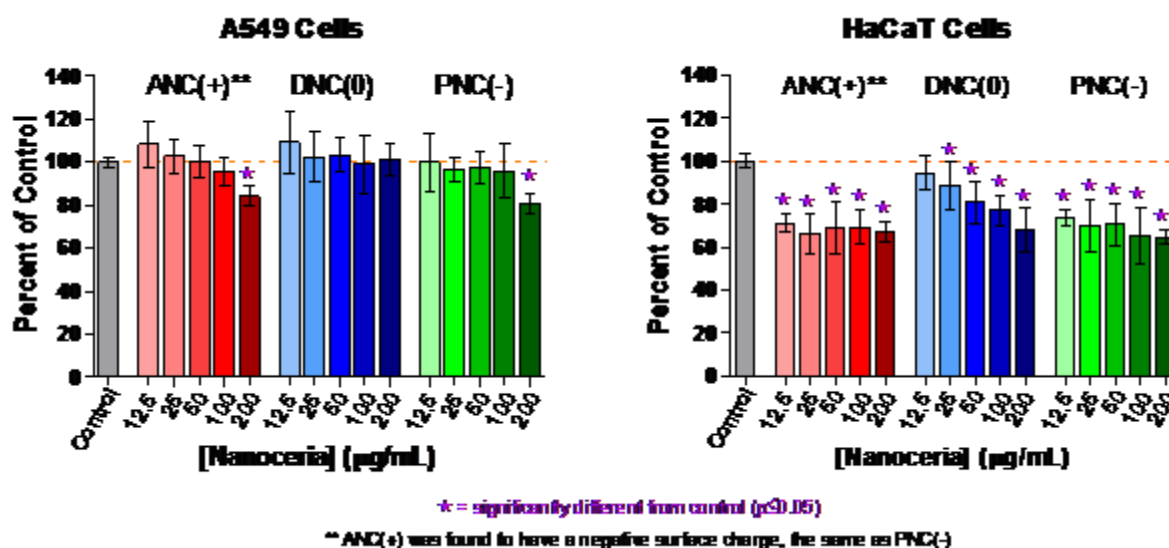
DISTRIBUTION A: Approved for public release; distribution unlimited. PA Case No. 88ABW-2013-4073

116

Figure 51: Cytotoxicity of nanoceria particles in HaCaT and A549 cells after 24 hour exposure, assessed by MTT assay.

d.   Determining Uptake Pathway

1)   **Purpose:** The purpose of this study was to determine if the particle surface charge affects the uptake pathway utilized for internalization of nanoparticles.

2)   **Materials and Methods:** Nanoceria particles with neutral, negative, and positive surface charge produced by dextran, poly(acrylic acid) or aminated- poly(acrylic acid) coating, respectively, were provided by Dr. Perez (University of Central Florida, Orlando, FL). The cell lines studied were HaCaT (human keratinocyte) and A549 (human pulmonary epithelium) cells. Each was cultured in RPMI 1640 (ATCC) supplemented with 1% Penicillin/Streptomycin and 10% FBS (normal FBS for HaCaT and heat inactivated FBS for A549 cells). Inhibitors of endocytosis utilized for pathway analysis were Chlorpromazine (clathrin-mediated uptake), Genistein (caveolin-mediated uptake), and EIPA and Rottlerin (fluid phase uptake). In order to find the optimal inhibitory concentration which does not cause overt cytotoxicity, cells were treated with endocytosis inhibitors for 30 minutes and activity measured by MTS assay.

3)   **Results:** Treatment conditions for inhibition of endocytosis have been optimized but further studies are required using of newly synthesized particles.

4)   **Discussion:** Due to the discovery that ANC(+) particles did not have a positive surface charge and in fact had the same surface charge as PNC(-) particles, uptake pathway studies were postponed.

5) References

[1]   Khalil, I.A., Kogure, K., Hidetaka, A., Harashima, H. 2006 "Uptake Pathways and Subsequent Intracellular Trafficking in Nonviral Gene Delivery." Pharmacol Rev. 58(1): 32-45.

[2]   Asati, A., Santra, S., Kaittanis, C., Perez, J.M. 2010 "Surface-Charge-Dependent Cell Localization and Cytotoxicity of Cerium Oxide Nanoparticles." ACS Nano 4(9): 5321-31.

[3]   Perez, J.M., Asati, A., Nath, S., Kaittanis, C. 2008 "Synthesis of Biocompatible Dextran-Coated Nanoceria with pH-Dependent Antioxidant Properties." Small 4(5): 552-6.

2.   *Respiratory Effects of Silver Nanowires*

a.   *Purpose*

Silver nanoparticles (AgNPs) possess antibacterial and antimicrobial properties, thus making them the most abundant nanomaterials used in the biomedical field today.[1-3] They are incorporated into numerous medical devices such as catheters, wound dressings and antiseptic creams and consumer products including socks, t-shirts, hand sanitizer, cosmetics, and toothpaste.[4-7] AgNPs also possess unique plasmon-resonance optical scattering properties that make them ideal for use in sensors, optics, and electronics.[8, 9]

Due to their widespread use in consumer products, AgNPs are being released into the environment at an alarming rate, henceforth making toxicity assessment extremely important. Numerous studies in the literature have shown AgNPs to be cytotoxic to many cell types (ie. keratinocytes, fibroblasts, and hepatocytes) because of their ability to induce the formation of reactive oxygen species (ROS) and cause apoptosis.[10-22] Additionally, nanomaterials have been shown to penetrate deep into the alveolar regions of the lung, however, previous *in vitro* studies on AgNP toxicity in the lungs have focused exclusively on one type of lung cell. This approach presents an incomplete picture of toxic potential as the human lungs are primarily composed of three types of cells: type I pneumocytes, which are simple squamous epithelial cells that provide structure in the alveolar wall; type II pneumocytes which are cuboidal, surfactant-secreting epithelial cells; and alveolar macrophages that phagocytize foreign or dead material.[23] Therefore, in this study we used a human alveolar lung co-culture model previously established in our lab as our model for inhalation exposure and evaluated the bioeffects of two silver nanowires (AgNWs) with a similar diameter of ~90 nm and lengths of 4 and 20 μm from nanoComposix. The co-culture model was examined for changes in cellular morphology, cell viability, mitochondrial membrane potential (MMP), oxidized glutathione, and inflammatory response. Results indicated that both AgNWs did not alter cell viability and that there was no toxicity. However, both AgNWs did cause a loss of MMP, an increase in the GSH:GSSG ratio, and an increase in cytokine production. Therefore, while the AgNWs were not toxic to the cells, they did

cause irritation and triggered an inflammatory response. Furthermore, *in vivo* studies are currently underway in collaboration with Dr. Jenny Roberts (CDC/NIOSH) in order to compare the *in vivo* and *in vitro* results. . Dr. Roberts is a Research Biologist in the Health Effects Laboratory Division (HELD) at the National Institute for Occupational Safety and Health (NIOSH) in Morgantown, WV. Her expertise lies in using *in vivo* models to evaluate lung inflammation, injury, immunomodulation, and development of pulmonary disease that may occur after exposures to a variety of different occupational particulates, including nanomaterials. Dr. Roberts is studying the effects of the same AgNWs in rat lungs. The results of this collaboration will be extremely valuable in correlating *in vivo* and *in vitro* studies.

b. *Materials and Methods*

Silver Nanowires
nanoComposix synthesized two different AgNWs with lengths of 4 and 20 μm and diameters of ~80nm. The AgNWs were dispersed in an artificial lung surfactant in order to simulate their passage through the respiratory tract into the cultured cells that would form the respiratory lining in the alveoli (Table 11).[24]

Table 11 Artificial Lung Fluid Composition

Compound	Formula Wt.	Milli-moles/L	g/L
NaCl	58.4	116	6.779
NH_4Cl	53.49	10	0.5349
$NaHCO_3$	84.01	27	2.2683
$NaH_2PO_4-H_2O$	137.998	0.2	0.1656
Na_3 Citrate-H2O	294.19	0.2	0.0558
Glycine	75.07	5	0.3754
L-Cysteine Hyrdochloride	175.63	1	0.1756
DTPA	393.35	1	0.0787
H_2SO_4 (Con)	98.08	0.01	0.03 mL/L
$CaCl_2-_2H_2O$	146.92	0.2	0.294
ABDC	0.005	5.0e-3	0.1mL/10L

DTPA- diethylenetriaminepentaacetic acid
ABDC- alkylbenzyl-dimethyl-ammonium chloride

Dosing Concentrations
The dosing concentrations for these experiments were chosen to represent realistic dosing exposures and were derived based on the current American Conference of

DISTRIBUTION A: Approved for public release; distribution unlimited. PA Case No. 88ABW-2013-4073

119

Governmental Industrial Hygenists (ACGIH) [25] threshold exposure limit value - time weighted average (TLV-TWA) for insoluble Ag (0.1 mg/m^3 for an 8 hour work day). The doses were calculated based on an equation provided by Dr. Jenny Roberts and Mr. Bean Chen (CDC/NIOSH) that converts the amount of Ag inhaled in a standard worker in an 8-hour workday into a single dose to be administered via intratracheal instillation to a rat. The equation normalizes for minute ventilation (20,000 ml/min), pulmonary deposition efficacy of an 80 nm x 4 µm and an 80 nm x 20 µm nanowire (~12.8 and 13.2 % respectively) and lung surface area (human = ~ 102.2 m2; rat = ~0.40 m2).

Particle Deposition in a standard worker (75 kg, male) = (minute ventilation) x (air to liquid volume conversion) x (TLV-TWA) x (exposure time) x (particle lung deposition efficiency) = (20,000 ml/min) x (10^{-6}m^3/ml) x (0.1 mg/m^3) x (480 min/day) x (0.128) = 0.123 mg deposited /work day for the short wire and 0.127 mg deposited /work day for the long wire (substitute 0.132 for 0.128 in the equation).

Normalization for amount deposited per work day for rat body weight (300 g) relative to the lung surface area of a 75 kg worker = (0.123 mg/ 102.2 m^2) x (0.40 m^2) = 0.481µg per work day for the short wire and 0.496 µg per work day.

The resulting doses represented approximate exposures for 1 month, 5.5 months, 1 year and 4 years (10, 50, 125, and 500 µg per ~0.40 m^2 of rat lung, i.e., 2.5, 12.5, 31.25, and 125 ng/cm^2, respectively).

** Note- The deposition efficiency was similar enough between the long and the short wire that it did not change the approximate exposure lengths. Additionally, Dr. Roberts originally decided to dose with 10, 25, 100, 250, and 500 µg per ~0.40 m^2 of rat lung (2.5, 6.25, 25, 62.5, and 125 ng/cm^2) respectively, which represented 1 month, 2.5 months, 10 months, 2 years, and 4 years but due to funding issues, chose to use the former doses. However, since the *in vitro* study started before the *in vivo* study, the doses for the *in vitro* study were based on the latter concentrations. These doses then were adjusted based on the surface area of one well in a 96 well plate (0.32cm^2) (4, 10, 40, 100, 200 ng/ml, respectively). To match the *in vivo* concentrations the concentrations should have been 4, 20, 50, and 200ng/ml. The 4 and 200 ng doses match exactly and the 50 ng dose is very close to the 40 ng dose that was used, therefore, comparisons between the 2 studies should still be able to be made.

Human Lung Co-cultures

In this study, the A549 (ATCC, CCL-185, Manassas, VA) cell line and the U937 (ATCC, CRL-1593.2) cell line were chosen as an *in vitro* model for inhalation. To mimic the alveoli microenvironment, the A549 epithelial cells were co-cultured with the U937 cells in a 3:1 (A549:U937) ratio,[26] and grown in RPMI-1640 (ATCC) media supplemented with 1% penicillin/streptomycin (Sigma, St. Louis, MO), and 10% heat-inactivated FBS

DISTRIBUTION A: Approved for public release; distribution unlimited. PA Case No. 88ABW-2013-4073

120

(ATCC) and incubated at 37°C in a humidified incubator with 5% CO_2. Prior to preparing the co-cultures, the U937 cells were stimulated with 100 ng/mL of phorbol-12- myristate-13-acetate (PMA) for 48 h to induce differentiation into macrophages. The A549 cells and the stimulated U937 cells were plated in the same tissue culture plates at a ratio of 3:1 (epithelial cells to macrophages) with 1×10^5 total cells per well. Twenty-four hours after plating, the co-cultures were dosed with the AgNWs for 24 h.

External Morphology and Nanoparticle Uptake by Ultra Resolution Imaging

The A549 cells and stimulated U937 cells were plated on chambered slides (3:1 ratio) at a density of 3×10^5 total cells and allowed to grow at 37°C with 5% CO_2 for 24 h. They then were exposed to 200 ng/ml of each wire for 24 h. All further processing of the cells was done at room temperature. After exposure, the cells were fixed with 4% paraformaldehyde for 15 min, washed twice with PBS and then 0.1 % Triton X was added to permeablize the membrane. After 20 min, the Triton X was removed, and the cells were blocked with blocking buffer (Thermo, Rockford, IL) for 20 min. to prevent non-specific binding. Next, the cells were stained with the Alexa 555-phallodin stain for 15 min (Invitrogen, Carlsbad, CA) to visualize the actin. After washing with PBS, CD68 (an antibody specific to macrophages) was added to the wells at a concentration of 1:100 and incubated for 1.5 h. After several washes, a goat anti-mouse secondary antibody was added at 1:100 dilution for 1 h. Finally, the slides were washed several times with PBS and mounted in Prolong AntiFade with Dapi reagent (Invitrogen), and images were taken using the CytoViva^{TM} 150 ultra resolution attachment (Aetos Technologies, Inc., Auburn, AL) to determine if the particles were taken into the cell and to observe any morphological changes.

Cellular Viability

Cell viability was measured using the CytoTox-Glo Cytotoxicity Assay from Promega (Madison, WI). This assay utilizes a luminogenic peptide substrate alanyl-alanyl-phenylalanyl-aminoluciferin (AAF-Glo) to measure dead cell protease activity from cells that have lost membrane integrity and is unable to penetrate the intact membrane of healthy cells. The cells were seeded in a 3:1 ratio of A549 and U937 in a 96-well plate, allowed to grow overnight and exposed to varying concentrations of AgNWs for 24 h. After 24 h, the cells were incubated with the AAF-Glo solution for 15 min at room temperature in the dark. The plate was read using the luminescence setting on the plate reader. Following the reading, lysis buffer (provided in the kit) was added to the plate and incubated an additional 15 min at room temperature in the dark. After 15 min, the plate was re-read using the luminescence setting on the plate reader. Cell viability was determined using the following equation to normalize data for total cell number:

Viable cell luminescence=Total luminescence (after lysis) – Experimental dead cell luminescence

Mitochondrial Membrane Potential (MMP)

Mitochondrial membrane potential was evaluated using the M̄īt-EΨ Mitochondrial Permeability Detection Kit from BIOMOL (Plymouth Meeting, PA). This kit utilizes a cationic fluorescent dye called JC-1. The dye penetrates cells and enters the healthy mitochondria where it aggregates and fluoresces red. When the mitochondria collapses, as in apoptotic cells, the dye no longer accumulates in the mitochondria. Instead, it is distributed throughout the cell, assumes its monomeric form, and fluoresces green. The cells were seeded in a 96-well black imaging plate, allowed to grow overnight until~80% confluent and exposed to 10 ng/ml and 100 ng/ml of the AgNWs for 24 h. After 24 h, the media was removed and the cells were washed three times with PBS to eliminate any excess NPs that were not internalized or bound to the membrane. The cells then were incubated with the M̄īt-EΨ solution for 15 min at 37°C with 5% CO_2. The cells were washed twice with PBS and imaged on a BD Pathway435 confocal microscope (BD Biosciences, San Jose, CA).

Protein Expression

Changes in protein expression were evaluated using the Inflammatory Cytokines Multi-Analyte ELISArray kit. This kit analyzes 12 pro-inflammatory cytokines at one time. The cytokines in the kit are IL-1α, IL-β, IL-2, IL-4, IL-6, IL-8, IL-10, IL-12, IL-17A, INFγ, TNFα, and GMCSF. The cells were seeded in a 3:1 ratio of A549 and U937 cells in 6 well plates at a density of ~500,000 total cells per well and allowed to grow overnight. The cells then were dosed with a high (100 ng/ml) and a low (10 ng/ml) concentration of AgNWs for 24h. After 24h, the media was removed, aliquoted, and stored at -80°C until the ELISA was performed. To perform the assay, the media was thawed and the procedure was carried out following manufacturer's instructions.

Glutathione Assay

The cells were seeded in 6-well plates (~500,000 cells/well), allowed to grow overnight until ~80% confluent and exposed to 10 µg/ml and 100µg/ml of the AgNWs for 24h.
After 24 h, the media was removed and the cells were prepared for storage. All steps were done on ice to prevent the cells from oxidizing the GSH content. Briefly, 300 µl of ice-cold glutathione buffer was added to each well and the cells were homogenized by scraping the dish using the back of a large eppendorf tip. The homogenate (180 µl) was added to a pre-chilled tube containing 60 µl of perchloric acid (PCA) and vortexed to get a uniform emulsion. Each tube was incubated on ice for 5 min and then spun down for 2 min at 13,000 x g at 4°C. The resulting supernatant was collected and stored at -80°C until use (stable for one month). To begin the assay, the GSH standard curve was prepared by adding 10 µl of the GSH standard to 990 µl assay buffer to generate a 0.2 µg/µl stock and then diluted further with the appropriate amount of assay buffer to get 0, 0.4, 0.8, 1.2, 1.6, and 2.0 µg/ml. Next the samples were prepared by adding 40 µl of ice cold 3N KOH to 80 µl of the frozen samples, incubated on ice for 5 mins and then centrifuged for 2 min at 13,000 x g at 4°C. 10 µl of each sample was transferred to a 96

well plate (each sample was placed in multiple wells to assay total glutathione, GSH and GSSG in 5 replicates). To detect GSH, the sample volume in each well was brought up to 90 µl with assay buffer while sample volume was brought up to 80 µl with assay buffer and 10 µl of reducing agent was added and incubated at room temperature for 10 min to detect total glutathione. To detect GSSG, sample volume was brought up to 70 µl with assay buffer and 10 µl of GSH quencher was added and allowed to incubate at room temperature for 10 min. After 10 min, 10 µl of the reducing agent was added and incubated at room temperature for an additional 10 min. Lastly, 10 µl of OPA probe was added to all wells and incubated at room temperature for 40 min, and then the plate was read on the plate reader using the fluorescent setting at 340nm excitation and 420 emission wavelengths.

c.   Results and Discussion

Nanowire re-suspension
Prior to the start of any experiment, the AgNWs were first re-suspended in an artificial lung fluid to simulate their passage through the respiratory tract into the cultured cells that would form the respiratory lining in the alveoli (Table 11) [24] and then further diluted down to the final concentrations in cell culture media.

Nanowire Characterization
The AgNWs used in this study were synthesized by nanoComposix. TEM imaging confirmed the 4 µm wires length to be 4910 nm ± 1560 nm with a width of 97.2 ± 17.7 nm and the 20 µm wires to be 19.2 ± 7.3 nm in length with a width of 75.9 ±16 nm (Figure 52).
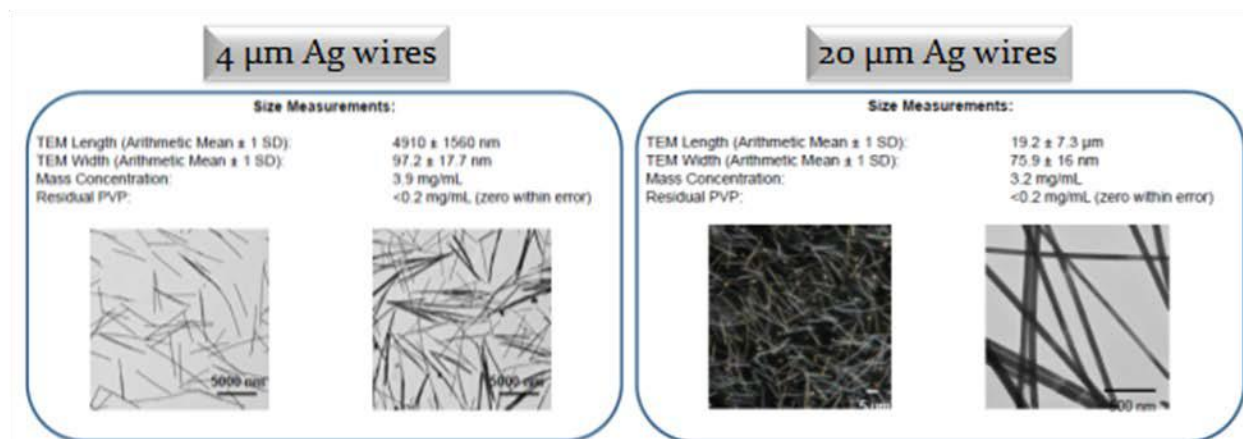
Figure 52. Transmission electron microscope images of AgNWs confirming their size and distribution.

Evaluation of Cellular Morphology & Cytotoxicity

Cell morphology studies were performed using ultrahigh resolution microscopy coupled with fluorescent staining to detect the AgNWs inside the cells and associated with the

cell membrane, as well as changes in cell morphology (Figure 53). The different cell types were discernible via differences in the fluorescent staining. The nuclei of both cell types were stained with Dapi to make them blue, however the difference can be seen in the location of the red and green stains. The A549 epithelial cells contain a lot of actin, thus the presence of the red phalloidin. The U937 cells however, contain almost no cytoplasm and were stained with the primary antibody CD68 (green). In both AgNW treatments, cell morphology of both cell types appeared normal and the wires could be seen interacting with the cells. There appeared to be some localization of the wires in the A549 epithelial cells (white arrows, Figure 53c), however the majority of the wires were engulfed by the U937 macrophages (yellow arrows, Figure 53b and c).
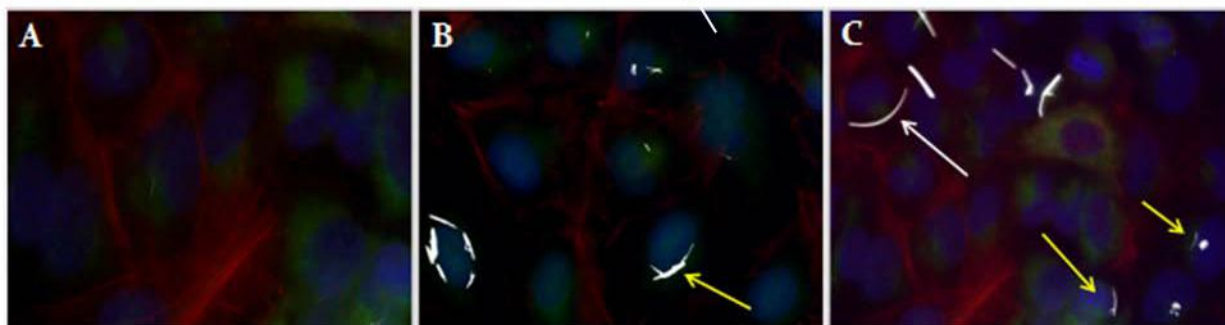
Figure 53. CytoViva images of AgNWs in the lung co-culture model. (A) Untreated cells 96X (B) Co-culture treated with 4µm AgNW(C) Co-culture treated with 20µm AgNW. CytoViva was able to detect AgNWs in the co-culture. While there appeared to be some localization in the A549 epithelial cells the majority of the particles were engulfed by the U937 macrophages.

Cellular Viability

The luminescence tests show a small, but significant toxic effect of both AgNWs at all concentrations tested in the A549 cell line (Figure 54a). There was no dose dependent effect – the presence of only 4ng/ml had just as strong a toxic effect as the 200ng/ml. Furthermore, there was no significant difference in toxicity between the 4µm and the 20µm nanowires. In the U937 cell line, neither the 4µm nor the 20µm wires exhibited any significant decrease in viability (Figure 54b). Similarly, the co-culture presented no evidence of toxicity from the exposure to either of the wires (Figure 54c). These results indicate that the macrophages are protecting the epithelial cells from the toxic effects caused by the AgNWs as they would *in vivo*, thus proving the co-culture is a more realistic scenario in which to test the compatibility of nanoparticles.
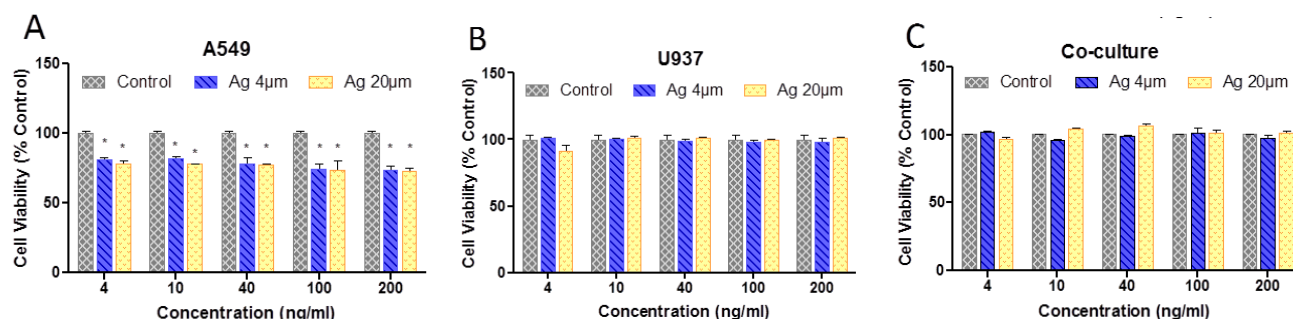
Figure 54. Cellular Viability after 24h Exposure to AgNWs in the Lung Co-Culture Model (A) A549 cells. Both the 4 µm and 20 µm wires were toxic to the cells starting at the lowest dose of 4ng/ml (B) U937 cells. Neither the 4 µm nor the 20 µm wires were toxic to these cells (C) Co-culture model. The AgNWs were not toxic to the cells in the co-culture. These results suggested that when the macrophages (U937) are cultured with the epithelial (A549) cells they offer protection from the toxicity caused by exposure to the AgNWs. (*Denotes significance in comparison to control values p<0.05).

Mitochondrial Membrane Potential

The generation of ROS is a normal cellular response to stress and is often indicative of apoptosis.[27] However, because these studies were conducted in the co-culture model, normal ROS assays were not feasible. In order to stimulate the U937 monocytes to differentiate into macrophages, they were stimulated with 100ug/mL of phorbol 12-myristate 13-acetate (PMA) for 2 days. However, PMA causes the U937 cells to generate ROS to stimulate differentiation and makes it difficult to distinguish how much of the ROS is from the NW treatment or from the PMA. The generation of ROS in small amounts is a common occurrence in cells and is easily neutralized by the cells antioxidant defenses, which include production of glutathione and antioxidant enzymes.[28] However, excess amounts of ROS cause the mitochondrial membrane to depolarize and this can be used to evaluate ROS production. Results demonstrated significant amounts of mitochondrial membrane potential lost after exposure to both the 4µm and the 20µm AgNWs at both 10 and 100ng/ml (Figure 55).
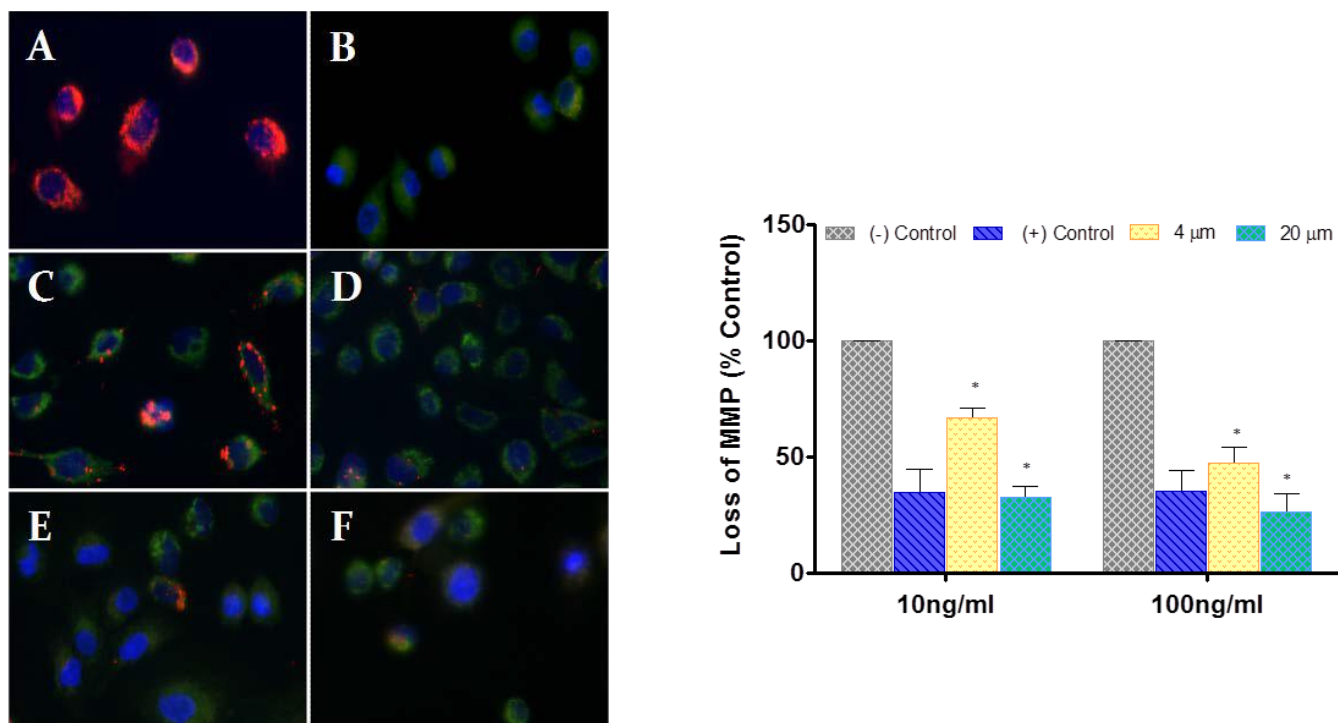
Figure 55 Loss of Mitochondrial Membrane Potential after 24-hour exposure AgNWs. (A) Negative control (B) Positive Control (C)4µm wires 10ng/ml (D) 4µm wires 100ng/ml (E) 20µm wires 10ng/ml (F)20µm wires 100ng/ml (G) Graph depicting data in images. There was significant amount of mitochondrial membrane potential lost after exposure to both the 4µm and the 20µm AgNWs at 10 and 100ng/ml. (*Denotes significance in comparison to control values p<0.05).

Protein Expression

Changes in protein expression were evaluated using the Inflammatory Cytokines Multi-Analyte ELISArray kit. This kit analyzes 12 pro-inflammatory cytokines at one time. The cytokines in the kit are IL-1α, IL-β, IL-2, IL-4, IL-6, IL-8, IL-10, IL-12, IL-17A, INFγ, TNFα, and GMCSF. Results showed that exposure to both the 4µm and 20µm AgNWs at both concentrations caused a significant increase in IL-6 protein expression and a significant decrease in IL-10 protein expression (Figure 56). IL-6 is a pro-inflammatory cytokine and has important roles in acute phase reactions, inflammation, hematopoiesis, bone metabolism, and cancer progression. IL-6 activity is essential for the transition from acute inflammation to either acquired immunity or chronic inflammatory disease. IL-10 on the other hand is an anti-inflammatory cytokine. It is capable of inhibiting synthesis of pro-inflammatory cytokines like IFN-γ, IL-2, IL-3, TNFα, and GM-CSF made by cells such as macrophages and regulatory T-cells.
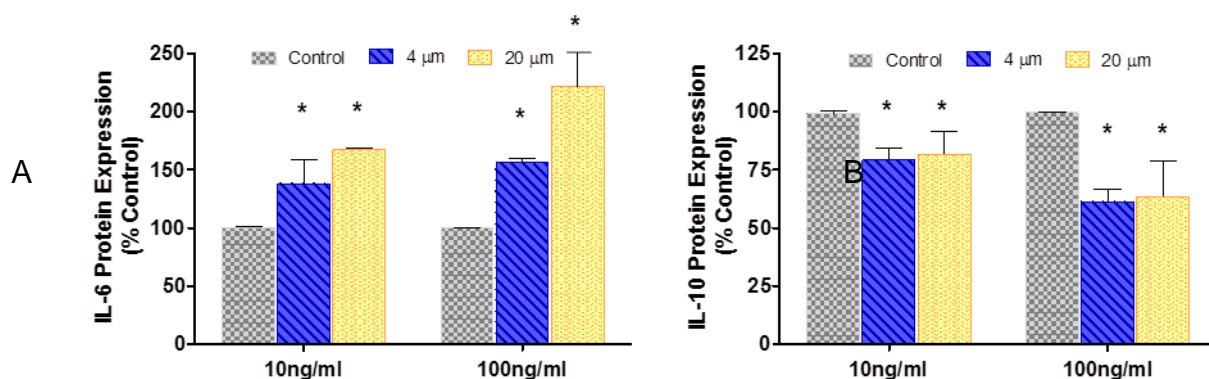
Figure 56. Evaluation of Inflammatory Protein Expression after 24h Exposure to AgNWs. (A) There was an increase in IL-6 protein expression after exposure to both AgNWs at both concentrations. (B) There was a decrease in IL-10 expression after exposure both AgNWs at both concentrations (*Denotes significance in comparison to control values p<0.05).

Glutathione Activity

Glutathione (GSH) is a tripeptide (γ-glutamylcysteinylglycine) that contains a free thiol group. It is a major antioxidant found in the body and helps prevent cell damage caused by ROS and other free radicals by acting as a scavenger.[28] Glutathione exists in two states: reduced (GSH) and oxidized (GSSG). However, more than 90% of the glutathione in healthy cells occurs in the reduced (GSH) form. This is because the enzyme that reverts it from its oxidized form (GSSG) glutathione reductase, is constitutively active and inducible upon oxidative stress. During times of stress, the free thiol group on the cysteine of the reduced GSH donates an electron to any unstable molecule (i.e., ROS or free radical), thus quenching the free radical and neutralizing it. After donating an electron, the glutathione itself becomes reactive and binds to another reactive glutathione via a disulfide bond to form glutathione disulfide (GSSG, the oxidized form). Since GSSG levels in healthy cells are usually low, an increased GSH:GSSG ratio is often used as an indicator of oxidative stress. Results demonstrated that both the 4 μm and 20 μm AgNWs cause a decrease in the GSH:GSSG ratio as compared to control cells, thus providing additional evidence that the AgNWs are causing oxidative stress to the cells (Figure 57).
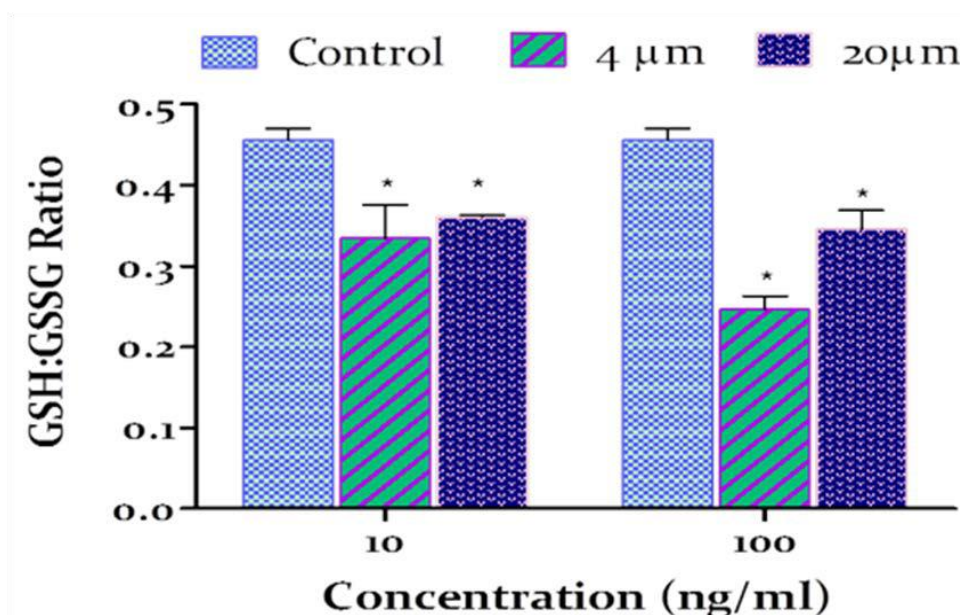
Figure 57. GSH:GSSG ratio after exposure to AgNWs. Both the 4 µm and 20 µm AgNWs showed a significant decrease in the GSH:GSSG ratio when compared to the control cells.

e. Conclusions

The AgNWs were toxic to the A549 epithelial cells at low doses, but not to the U937 cells or the co-culture. The presence of the U937 cells appeared to rescue the A549 cells from the toxic effects of the AgNWs when the two cell lines were cultured together. These results are promising, and suggest that the co-culture is a more realistic in vitro model and could be comparable to in vivo results. However, although the co-culture appeared to mitigate the decrease in cell viability, both the 4 and 20 µm wires caused the cells stress and triggered an inflammatory response. These results suggest that multiple assays and end-points should be evaluated when determining the bioeffects of different nanomaterials.

f. References

[1]   Silver, S.; Phung, L. T.; Silver, G. Silver as Biocides in Burn and Wound Dressings and Bacterial Resistance to Silver Compounds. *J. Ind. Microbiol. Biotechnol.* 2006, 33,627–634.

[2]   Chen, X.; Schluesener, H. J. Nanosilver: A Nanoproduct in Medical Application. *Toxicol. Lett.* 2008, 176, 1–12.

[3]   Eby D, Schaeublin N, Farrington K, Hussain S, Johnson, G. Lysozyme Catalyzes the Formation of Antimicrobial Silver Nanoparticles. *ACS Nano* 2009, 3(4), 984-994.

[4]   Dibrov, P.; Dzioba, J.; Gosink, K. K.; Hase, C. C. Chemiosmotic Mechanism of Antimicrobial Activity of Ag(+) in Vibrio cholerae. *Antimicrob. Agents Chemother.* 2002, 46, 2668–2670.

[5]   Feng, Q. L.; Wu, J.; Chen, G. Q.; Cui, F. Z.; Kim, T. N.; Kim, J. O. A Mechanistic Study of the Antibacterial Effect of Silver Ions on Escherichia coli and Staphylococcus aureus. *J. Biomed. Mater. Res.* 2000, 52, 662–668.

[6] Lok, C. N.; Ho, C. M.; Chen, R.; He, Q. Y.; Yu, W. Y.; Sun, H.; Tam, P. K.; Chiu, J. F.; Che, C. M. Silver Nanoparticles: Partial Oxidation and Antibacterial Activities. *J. Biol. Inorg. Chem.* 2007, 12, 527–534.

[7] The Project on Emerging Nanotechnologies. Nanotechnology Consumer Product Inventory. Washington, DC: The Woodrow Wilson International Center for Scholars (2010). Available: http://tinyurl.com/5sa88q

[8] Dubas ST, Pimpan V. Humic acid assisted synthesis of silver nanoparticles and its application to herbicide detection. *Mater Lett* 2008, 62, 2661–3.

[9] Schrand AM, Braydich-Stolle LK, Schlager JJ, Dai L, Hussain SM. Can silver nanoparticles be useful as potential biological labels? *Nanotechnology* 2008, 19, 235104.

[10] Kulthong K, Srisung S, Boonpavanitchakul K, Kangwansupamonkon W, Maniratanachote R. Determination of silver nanoparticle release from antibacterial fabrics into artificial sweat. *Parte Fibre Toxicol* 2010, 7, 8.

[11] Paddle-Ledinek JE, Nasa Z, Cleland HJ. Effect of different wound dressings on cell viability and proliferation. *Plast Reconstr Surg* 2006, 117:110S–8S.

[12] Lam PK, Chan ES, Ho WS, Liew CT. In vitro cytotoxicity testing of a nanocrystalline silver dressing (acticoat) on cultured keratinocytes. *Br J Biomed Sci* 2004, 61, 125–7.

[13] Poon VK, Burd A. In vitro cytotoxity of silver: implication for clinical wound care. *Burns* 2004, 30, 140–7.

[14] Arora S, Jain J, Rajwade JM, Paknikar KM. Cellular responses induced by silver nanoparticles: in vitro studies. *Toxicol Lett 2008,* 179, 93–100.

[15] Arora S, Jain J, Rajwade JM, Paknikar KM. Interactions of silver nanoparticles with primary mouse fibroblasts and liver cells. *Toxicol Appl Pharmacol* 2009, 236, 310–8.

[16] Hsin YH, Chen CF, Huang S, Shih TS, Lai PS, Chueh PJ. The apoptotic effect of nanosilver is mediated by a ROS- and JNK-dependent mechanism involving the mitochondrial pathway in NIH3T3 cells. *Toxicol Lett* 2008, 179, 130–9.

[17] Gopinath P, Gogoi SK, Sanpuic P, Paul A, Chattopadhyay A, Ghosh SS. Signaling gene cascade in silver nanoparticle induced apoptosis. *Colloids Surf B* 2010, 77, 240–5.

[18] Takenaka S, Karg E, Roth C, et al. Pulmonary and systemic distribution of inhaled ultrafine silver particles in rats. *Environ Health Perspect* 2001, 4, 547–51.

[19] Sung JH, Ji JH, Yun JU, et al. Lung function changes in Sprague-Dawley rats after prolonged inhalation exposure to silver nanoparticles. *Inhal Toxicol* 2008, 20, 567–74.

[20] Hussain SM, Hess KL, Gearhart JM, Geiss KT, Schlager JJ. In vitro toxity of nanoparticles in BRL 3A rat liver cells. *Toxicol In Vitro* 2005, 19, 975–83.

[21] Carlson C, Hussain S, Schrand A, Braydich-Stolle L, Hess K, Jones R and Schlager J. Unique cellular interaction of silver nanoparticles: size-dependent generation of reactive oxygen species. *J Phys Chem B* 2008, 112, 13608–19.

[22] Braydich-Stolle L, Hussain S, Schlager JJ, Hofmann MC. In vitro cytotoxicity of nanoparticles in mammalian germline stem cells. *Toxicol Sci* 2005, 88, 412–9.

[23] http://en.wikipedia.org/wiki/Pulmonary_alveolus

[24] Ansoborlo et al. Review and Critical Analysis of Available In Vitro Dissolution Tests. *Health Physics* 1999, 77, 638-645.

[25] ACGIH (2001). TLVs and BEIs: Based on the documentation of the threshold limit values for chemical substances and physical agents and biological exposure indices. American Conference of Governmental Industrial Hygienists. Cincinnati, Ohio.

[26] Wang S, Young R, Sun N, and Witten M. In Vitro Cytokine Release from Rat Type II Pneumocytes and Alveolar Macrophages Following Exposure to JP-8 Jet Fuel in Co- Culture. *Toxicology* 2002 173, 211-219.

[27] Nel A, Xia T, Madler L, Li N. Toxic Potential of Materials at the Nanolevel. *Science* 2006 311, 622.

[28] Halliwell, B. and Gutteridge, J. M. C. Free Radicals in Biology and Medicine. Oxford University Press, Oxford, UK, 1999.

[29]   Pompella A, Visvikis A,   Paolicchi A, De Tata V, Casini AF. The changing faces of glutathione, a cellular protagonist. *Biochemical Pharmacology* 2003 66 (8): 1499–503

Section V. Discussion (overall discussion of all studies)

The overarching goal of this effort was to develop a fundamental understanding of nanostructure- cellular interactions, and how these relationships were affected by nanostructure composition, size, and shape. Specifically, this effort focused on establishing a link between the fundamental mechanisms of biological interactions of engineered nanomaterials and the physicochemical properties uniquely associated with nanoscale structures. The first several studies in this report focus specifically on different physicochemical properties of gold and how they affect the biological interactions with the cells. Unlike other studies in the literature, these studies used a very systematic approach to address these fundamental questions. All the studies were performed using the human keratinocyte (HaCaT) cell line as a model for dermal exposure and utilized many of the same end- points. This approach allowed for direct comparison between the studies. These four studies demonstrated that size, charge, shape, and surface chemistry all affected how the AuNPs interacted with the HaCaT cells. The AuNPs exhibited differences in toxicity and the mechanism of toxicity based on the different physical parameters in each study. Another gold study demonstrated direct interaction of AuNPs with specific proteins that correlated with altered cellular function, suggesting that the AuNPs are not the only possible factor in determining the bioeffects with the cell. Proteins can adsorb to the surface of the NPs and cause disruptions in cellular signaling. Furthermore, the two copper studies revealed additional parameters that may affect how the cell reacts to nanoparticles: agglomeration size, and oxidation of the particles/ion released. These results, combined with the findings from the ceria studies established that nanotoxicology requires extensive and complete characterization of the NPs before, during and after all studies because the bioeffects are directly linked to these physical parameters.

Lastly, the study on AgNWs addressed a more specific objective of the proposal. This study assessed the cellular mechanisms generated from exposure to nanoparticles at non-lethal doses, which is more representative of the occupational exposure. Results showed that, while not directly toxic to the cells at a low dose, the AgNWs triggered an inflammatory response in the cells, which suggested that the AgNWs had a detrimental effect to the cells. These results validate the need for multiple assays and end-points when determining the bioeffects of different nanomaterials as the effects may not be obvious

Section VI. Summary/Conclusion (based on all studies)

In conclusion, the studies put forth in this effort demonstrated that the physiochemical parameters, such as shape, size (both primary particle and agglomeration), charge, and coating (surface functionalization and/or protein adsorbed from the media and cells) can contribute to the chemical reactivity and bioeffects of the nanomaterial. Therefore,

it is essential to thoroughly characterize all nanoparticles prior to and throughout the entire screening process as the nanoparticles can change drastically during the duration of the study.

Appendices

Appendix I: Glossary of abbreviations

1.	*AAS*	*Absorption Spectroscopy*
2.	*AAS*	*Atomic Absorption Spectroscopy*
3.	*ABDC*	*Alkyldenzyl-Dimethyl-Ammonium Chloride*
4.	*Ag NP*	*Silver Nanoparticles*
5.	*ANC*	*Positive Surface Charge*
6.	*ANOVA*	*Analysis Of Variance*
7.	*Au*	*Np Gold Nanoparticles*
8.	*AuNMs*	*Gold Nanomaterials*
9.	*AuNR-PEG*	*Polyethylene Glycol-Capped Gold Nanorods*
10.	*AuNS-MPS*	*Mercaptopropane Sulfonate Coated Gold Spheres*
11.	*BFTEM*	*Bright Field Transmission Electron Microscopy*
12.	*Ca*	*Calcium*
13.	*cAMP*	*Cyclic Adenosine Triphosphate*
14.	*carboxy-H2DCFDA*	*5-Carboxy-20,70-Dichlorodihydrofluoresceine Diacetate*
15.	*CDK*	*Cyclin-Dependent Kinases*
16.	*CO2*	*Carbon Dioxide*
17.	*Ct*	*Threshold Cycle*
18.	*CTAB*	*Cetyltrimethylammonium Bromide*

DISTRIBUTION A: Approved for public release; distribution unlimited. PA Case No. 88ABW-2013-4073

131

19. *Cu*   *Copper*

20. *Cu MSP*   *Copper Micron Sized Particles*

21. *CuNP*   *Copper Nanoparticles*

22. *CuO NPs*   *Copper Oxide Nanoparticles*

23. *DAPI*   *4'6-Diamidin-2-Phenylindole*

24. *DCHF-DA*   *2,7-Dichlorohydrofluorescein Diacetate*

25. *Df*   *Fractal Dimension*

26. *DLS*   *Dynamic Light Scattering*

27. *DMSO*   *Dimethyl Sulfoxide*

28. *DNA*   *Deoxyribonucleic Acid*

29. *DNC*   *Neutral Surface Charge*

30. *DoD*   *Department Of Defense*

31. *DPTA*   *Diethylenetriaminepentaacedic Acid*

32. *EDX*   *Energy-Dispersive X-Ray*

33. *EM*   *Exposure Media*

34. *ESEM*   *Environmental Scanning Electron Microscopy*

35. *FBS*   *Fetal Bovine Serum*

36. *FITC*   *Fluorcein Isothiocyanate*

37. *GNR*   *Gold Nanorod*

38. *GSH*   *Glutathione*

39. *GSSG*   *Reduced Glutathione*

40. *GTPase*   *Guanosine-5'-Triphosphate*

41.	H2O2	Hydrogen Peroxide
42.	HAADF-STEM	High Angle Angular Dark Field Scanning Transmission Electron Microscopy
43.	HaCaT	Human Keratinocyte Cell Line
44.	HKG	Housekeeping Genes
45.	ICP	Inductively-Coupled Plasma
46.	ICP-OES	Inductively-Coupled Plasma Optical Emission Spectroscopy
47.	IPA	Ingenuity® Pathway Assist
48.	LDH	Lactase Dehydrogenase Leakage
49.	LVEM	Low Voltage Electron Microscopy
50.	MEEE	2-, 2-Mercaptoethoxyethoxyethanol
51.	MEEE	2-, 2-Mercaptoethoxyethoxyethanol
52.	MES	2-Mercaptoethanesulfonate
53.	MHDA	Mercaptohexadecanoic Acid
54.	MMP	Mitochondrial Membrane Potential
55.	MPS	Mercaptopropane Sulfonate
56.	MTS	3-(4,5-Dimethylthiazol-2-Yl)-5-(3-Carboxymethoxyphenyl)-2-(4-Sulfophenyl)-2H-Tetrazolium
57.	N2A Cells	Murine Neuroblastoma Cells
58.	NM	Nanomaterial
59.	NP	Nanoparticle
60.	PBS	Phosphate Buffered Saline
61.	PCR	Polymerase Chain Reaction

DISTRIBUTION A: Approved for public release; distribution unlimited. PA Case No. 88ABW-2013-4073

133

62.	PEG	Polyethylene Glycol
63.	PNC	Negative Surface Charge
64.	PTGDR	Prostaglandin D2
65.	PTGER3	Prostaglandin E Receptor
66.	PTGFR	Prostaglandin F2
67.	RLU	Relative Light Units
68.	RNA	Ribonucleic Acid
69.	ROS	Reactive Oxygen Species
70.	SEM	Scanning Electron Microscopy
71.	SLS	Static Light Scattering
72.	SOD	Superoxide Dismutase
73.	TBXA2R	Thromboxane A2
74.	TEM	Transmission Electron Microscopy
75.	TMAT	N, N, N Trimethylammoniumethanethiol
76.	TNF	Necrosis Factor
77.	TPP	Triphenylphosphine
78.	XRD	X-Ray Diffraction

Appendix II - List of Publications Derived from this Study
<u>2009:</u>

1. Yu KO, Grabinski CM, Schrand AM, Murdock RC, Wang W, Gu B, Schlager JJ and Hussain SM (2009) Toxicity of amorphous silica nanoparticles in mouse keratinocytes. J Nanopart Res 11, 15-24, 2009

DISTRIBUTION A: Approved for public release; distribution unlimited. PA Case No. 88ABW-2013-4073

134

2.   Braydich-Stolle LK. Schaeublin NM, Murdock RC, Jiang J, Biswas P, Schlager JJ, Hussain SM (2009). Crystal structure mediates mode of cell death in titanium dioxide nanotoxicity. J Nanopart Res 11: 1361-1374

3.   M. F. Rahman, J. Wang, T. A. Patterson, B. Robinson, G. D. Newport, R. C. Murdock, J. J Schlager, S. M. Hussain, and S. F. Ali (2009) Expression of genes related to oxidative stress in the mouse brain after exposure to silver-25 nanoparticles. Toxicol Lett 187 15–21

4.   Ryan Posgai, Maqusood Ahamed, Saber M. Hussain, John J. Rowe, Mark G. Nielsen (2009): Inhalation method for delivery of nanoparticles to 1 the Drosophila respiratory system for toxicity testing. Science of the Total Environment (408)2:439-443

5.   Ahamed M, Posgai R, Gorey TJ, Nielsen M, Hussain SM, and Rowe JJ (2009) Silver nanoparticles induced heat shock protein 70, oxidative stress, and apoptosis in Drosophila melanogaster. Toxicol and Appl Pharm 242(3):263-9

6.   Wang J, Rahman MF, Duhart HM, Newport GD, Patterson TA, Murdock RC. Hussain SM, Schlager JJ, Ali F. (2009) Expression Changes of Dopaminergic System-Related Genes in PC12 Cells Induced by Manganese, Silver, or Copper Nanoparticles. NeuroToxicology 30(6):926-33

7.   Rosas-Hernández H, Jiménez-Badill S, Martínez-Cuevas PP, Eduard Gracia-Espino, Humbert Terrones, Mauricio Terrones, Saber M. Hussain, Syed F. Ali, Carmen González (2009) Effects of 45-nm Silver Nanoparticles on Coronary Endothelial Cells and Isolated Rat Aortic Rings. Toxicol Lett 191(2-3):305-13

_2010:_

1.   Braydich-Stolle LK, Speshock JL, Castle A, Smith M, Murdock RC, and Hussain SM. (2010). Nanosized Aluminum Altered Immune Function. ACS Nano, 4 (7): 3661-3670.

2.   Braydich-Stolle LK, Lucas B, Schrand AM, Murdock RC, Lee T, Schlager JJ, Hussain SM, Hofmann MC (2010). Silver nanoparticles disrupt GDNF/Fyn kinase signaling in spermatogonial stem cells. Tox Sci, 116 (2): 577-589.

3.   Nadagouda MN, Rajender VS, Castle AB, Murdock RC, Hussain SM. (2010) In vitro biocompatibility of nanoscale zerovalent iron particles (NZVI) synthesized using tea polyphenols. Green Chem. 12:114-122

4.   Prabhu BM, Ali SF, Murdock RC, Hussain SM, & Srivatsan M (2010) Copper nanoparticles exert size and concentration dependent toxicity on somatosensory neurons of Rat. Nanotoxicology 1;4 (2): 150-160

5.   Moulton MC, Braydich-Stolle LK, Nadagouda NM, Kunzelman S, Hussain SM and Varma RS (2010). Synthesis, characterization, and biocompatibility of "green" synthesized silver nanoparticles using tea polyphenols. Nanoscale 2:763-770

6.   Trickler WJ, Lantz SM, Murdock RC, Schrand AM, Robinson BL, Newport GD, Schlager JJ, Oldenburg SJ, Paule MG, Slikker, Jr. W, Hussain SM, and Ali SF (2010). Silver Nanoparticle Induced Blood-brain Barrier Inflammation and Increased Permeability in Primary Rat Brain Microvessel Endothelial Cells. Tox Sci 118 (1) 160-170

7.   Zhang Q, Hitchins VM, Schrand AM, Hussain SM, Goering PL. Uptake of Gold Nanoparticles in Murine Macrophage Cells Without Cytotoxicity or Production of Pro-inflammatory Mediators. *Nanotoxicology (Epub ahead of print Sept 2010)*

8.   Schrand AM, Lin JB, Ciftan Hens S, Hussain SM. (2010) Temporal and Mechanistic Tracking of Cellular Uptake Dynamics with Novel Surface Fluorophore-bound Nanodiamonds. *Nanoscale, DOI: 10.1039/c0nr00408a*

9.   Schrand AM, Schlager JJ, Dai L and Hussain SM. (2010) Preparing Cells Dosed with Nanomaterials for Assessment of Internalization and Localization with Transmission Electron Microscopy. *Nature Protocols 5, 744–757.*

10.   Nishanth, Reddy P; Jyotsna, Radhika G; Schlager, John J; Hussain, Saber M; Pallu, Reddanna (2011) Inflammatory responses of RAW 264.7 macrophages upon exposure to nanoparticles: Role of ROS-NFkB signaling pathway. *Nanotoxicology (Epub ahead of print March 2010)*

2011:

1.   Schaeublin NM, Braydich-Stolle LK, Schrand AM, Miller JM, Hutchinson J, Schlager JJ, and Hussain SM. (2010). Surface Charge of Gold Nanoparticles Mediates Mechanism of Toxicity. *Nanoscale 3, 410-420.*

One of the Top 25 most read papers for the first quarter of 2011.
Has already been cited by 14 other publications

2.   Grabinski CM, Schaeublin, NM, Wijaya, A, D'Couto H, Baxamusa SH, Hamad-Schifferli K., and Hussain SM. (2011) Effect of Gold Nanorod Surface Chemistry on Cellular Response. *ACS Nano, 5 (4), pp. 2870–2879.*

3.   Castle AB, Gracia-Espino E, Nieto-Delgado C, Terrones H, Terrones M, and Hussain SM. (2010). Hydroxyl-Functionalized and N-Doped Multiwalled Carbon Nanotubes Decorated with Silver Nanoparticles Preserve Cellular Function. *ACS Nano, 5 (4), pp. 2458–2466*

4.   Schaeublin NM, Braydich-Stolle LK, Schrand AM, Miller JM, Hutchinson J, Schlager JJ, and Hussain SM. (2011). Surface Charge of Gold Nanoparticles Mediates Mechanism of Toxicity. *Nanoscale 3(2):410-20.*

5.   Braydich-Stolle LK, Castle AB, Maurer EI, and Hussain SM. (2011) Advantages of Using Imaged Based Fluorescent Analysis for Nanomaterial Studies. *Journal of Experimental Nanoscience, In press.*

2012:

1.   Schaeublin N, Braydich-Stolle LK, Maurer EI, Park K, MacCuspie RI, Afrooz AN, Saleh NB, Vaia RA, Hussain SM. (2012) Does Shape Matter? Bioeffects of Gold Nanomaterials in a Human Skin Cell Model. *Langmuir. 2012 Feb 14;28 (6):3248-58.*

2.   *Trickler W J , Lantz S M , Schrand A M , Robinson B L , Newport G D , Schlager JJ, Paule MG, Slikker W, Biris AS, **Hussain SM**(2012) Effects of copper nanoparticles on rat cerebral microvessel endothelial cells. Nanomedicine. 2012 Feb 16.*

 Major Reviews in Peer Reviewed Journals:
1.   *Schrand AM, Rahman MF, Hussain SM, Schlager J, Smith DA, Ali SF. (2010) Metallic Nanoparticles and Their Toxicity Assessment. Wiley Interdiscip Rev (WIREs) Nanomedicine & Nanobiotechnology 2 (5):544-68.*

2.   *Hussain SM, Braydich-Stolle LK, Schrand AM, Murdock RC, Yu KO, Mattie DM, Schlager JJ, Mauricio Terrones (2009) Toxicity Evaluation for Safe Use of Nanomaterials: Recent Achievements and Technical Challenges . Advanced Materials 21: 1549-1559. Impact factor Journal 8.4.*

3.   *Hussain SM, and Schlager J J. (2009) Safety Evaluation of Silver Nanoparticles: Inhalation Model for Chronic Exposure. Toxicol Sci 108(2):223-224 Invited Review*

List of Book Chapters:

1.   *Schrand AM, Rahman MF, Hussain SM, Schlager J, Smith DA, Ali SF (2010) Metallic Nanoparticles and Their Toxicity Assessment. Nanomedicine & Nanobiotechnology 2(5):441-568.*

2.   *Braydich-Stolle LK, Murdock RC, and Hussain SM. (2010) Development of In Vitro Models to Assess Toxicity of Engineered Nanomaterials. In: Principles and Practice of Mixtures Toxicology. Moiz M, ed. WILEY-VCH Verlag GmbH & Co. KGaA. Weinheim, Germany.*

3.   *Yu KO, Braydich-Stolle LK, Mattie DM, Schlager JJ, and Hussain SM. (2009). In vitro and in vivo models for nanotoxicity testing. In: Nanotoxicity: From In Vivo and In Vitro Models to Health Risks. Sahu SC and Casciano DA, eds. John Wiley & Sons, Chichester, UK. pp. 335-348.*

Appendix III: Supplemental Information

A.   Supplemental Information:
Gold Nanoparticle Fractal Dimension Induced Different Biological Responses

Cell Viability Assay

The MTS cell viability assay was performed on cultured human keratinocytes exposed to 30nm and 60nm AuNPs at concentrations ranging from 0µg/mL to 6.25µg/mL in RPMI culture media (+1% penicillin/streptomycin, no serum) in order to determine changes in the cell viability after AuNP exposure. Briefly, the cells were seeded at 50,000 cells/well into 96-well plates and allowed to adhere for 24h. Nanoparticles in exposure media were added to the cells at increasing concentrations and incubated for 24h followed by the addition of the MTS reagent. The optical density (OD490 nm) of the resultant solution was determined at 0 and 1h by using a microplate

absorbance reader (SpectraMAX 340pc, Molecular Devices, CA). We found low levels of absorbance at 0h, which then were subtracted from 1h to normalize for any interference caused by the absorbance of the AuNPs themselves. As shown in Figure S1, at concentrations up to and including 6.25µg/mL, no significant (P<0.05) decrease in cell proliferation compared to the control was observed for any of the nanoparticles tested. Therefore, in vitro exposures for the purpose of gene expression analysis were conducted at the mid-range sub toxic concentration of 2.5µg/mL.
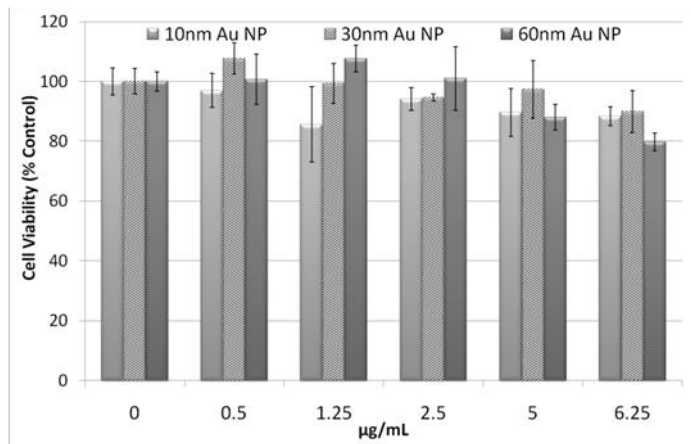
Figure S1. Cell Viability After 24h Exposure to Gold Nanoparticles. MTS assay results for HaCaT cells dosed with AuNPs for 24 hours. Cell viability measurements expressed as percent (%) of control. No significant change in cell viability was observed at concentrations up to 6.25 µg/mL.

Cellular Uptake and Quantification:

Thin sections of resin-embedded cells were prepared according to previously established techniques (Schrand et al., 2010). Imaging of the cells was performed with high angle angular dark field scanning transmission electron microscopy (HAADF-STEM) at 300kV on a FEI/Titan transmission electron microscope (TEM) and with bright-field TEM (BF-TEM) imaging on a Phillips/FEI Lab6 instrument at 200kV. Energy dispersive x-ray spectra (EDXS, EDAX system) were taken at distinct spots to verify the elemental composition of the internalized AuNPs or osmium-based background signal.
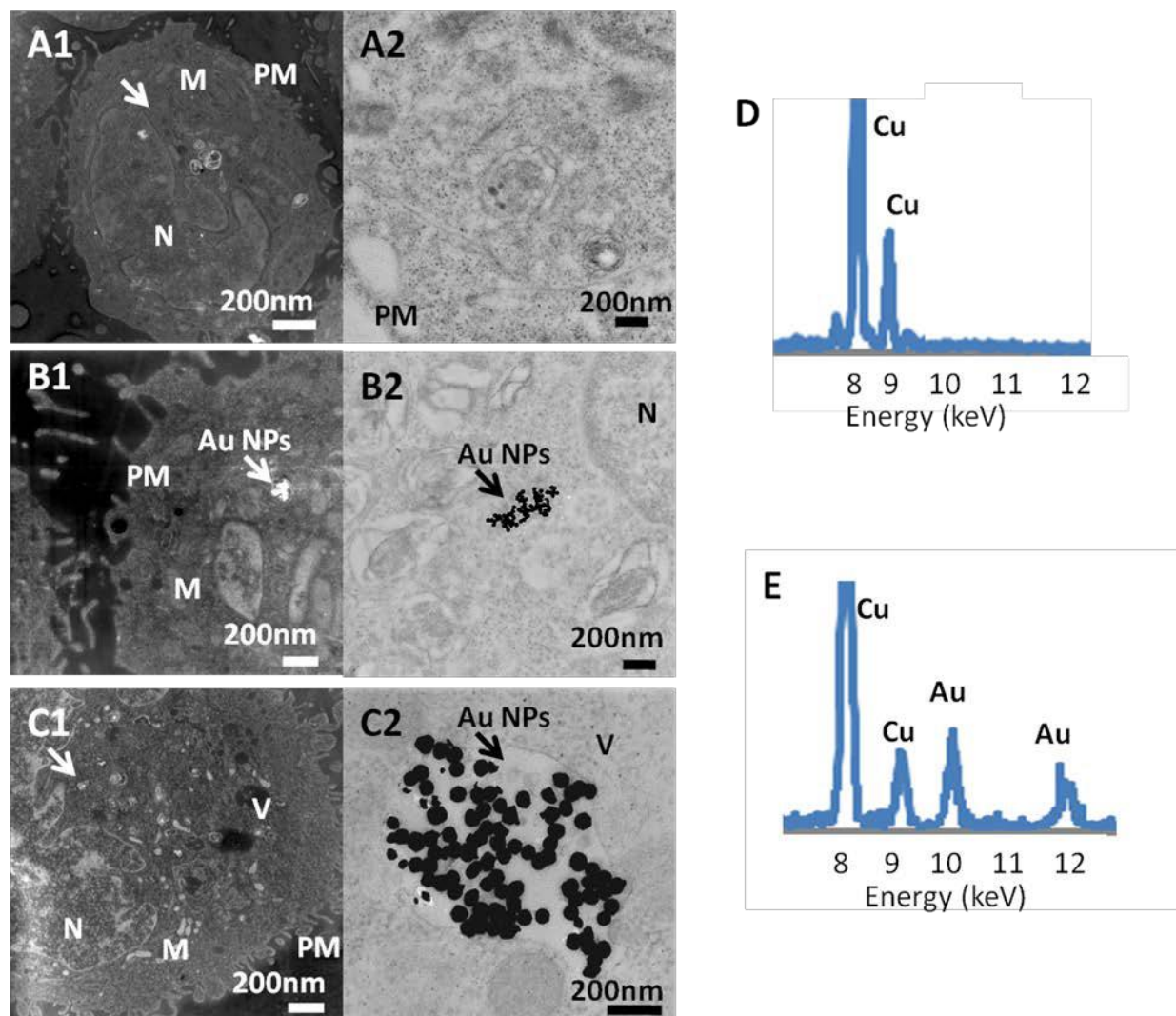
Figure S2. Representative high angle angular dark field (HAADF) scanning transmission electron microscopy (STEM) images (A1-C1) and bright-field transmission electron microscope (BF-TEM) images (A2-C2) of cells incubated with (A1-2) Control, (B1-2) 30nm AuNPs, and (C1-2) 60nm AuNPs for 24h at a concentration of 2.5µg/ml. White arrows in A1-C1 denote intracellular areas selected for energy dispersive x-ray analysis (EDXS). (D, E) EDXS to verify the elemental composition of selected areas of high contrast in cells. (D) Control cell only displaying signal from Cu TEM grid, (E) Representative spectra of AuNPs and Cu signal from TEM grid. Abbreviations: (PM) plasma membrane, (N) nucleus, (M) mitochondria, (V) vacuole and (KM) knife mark. Scale bars are 200nm.

The amount of AuNP uptake into the HaCaT cells was quantified with inductively-coupled plasma optical emission spectroscopy (ICP-OES). Briefly, HaCaT cells were plated at a density of 50,000 cells/mL and grown overnight in 6 well plates. The next day the cells were dosed with 2.5 µg/ml AuNPs of each size in RPMI dosing media in triplicate. After 24h, the cells were rinsed with warm media and thermocycled through freezing-thawing 2X to lyse the cells and release the AuNP cargo. The final samples were digested in acid media (2:1 HCl:HNO3) and run on a Thermo iCAP 6500 ICP-OES machine after dilution in water. Results are reported using the Au 267.5 nm wavelength in ppm or equivalent µg/ml.

Table S1 presents the data for quantification of cellular uptake of AuNPs after 24h of exposure. Data was normalized for total amount of Au/mL of sample as well as % uptake compared to original dose, number of original particles in applied dose and the number of particles internalized per individual cell.

Table S1.

Sample	Average Uptake (ng/mL)	% Uptake (Original Dose)	# Particles in Dose	# Particles Uptake/Cell
Au 30	67 ± 18	2.7%	2.0×10^{10}	1.0×10^{3}
Au 60	69 ± 13	2.8%	2.0×10^{9}	1.4×10^{2}

Dynamic Light Scattering Profiles for Aggregate Size Behavior In Biological Media

Upon dispersion into biological media, the AuNP form aggregates, which increase in size over the duration of the experiments up to 24h (Figure S3). Figure S3A, C represent a 0-6 hr timeframe for the 30 and 60 nm gold, while Figure S3B,D represents a 7-24 hr timeframe post dispersion in media.
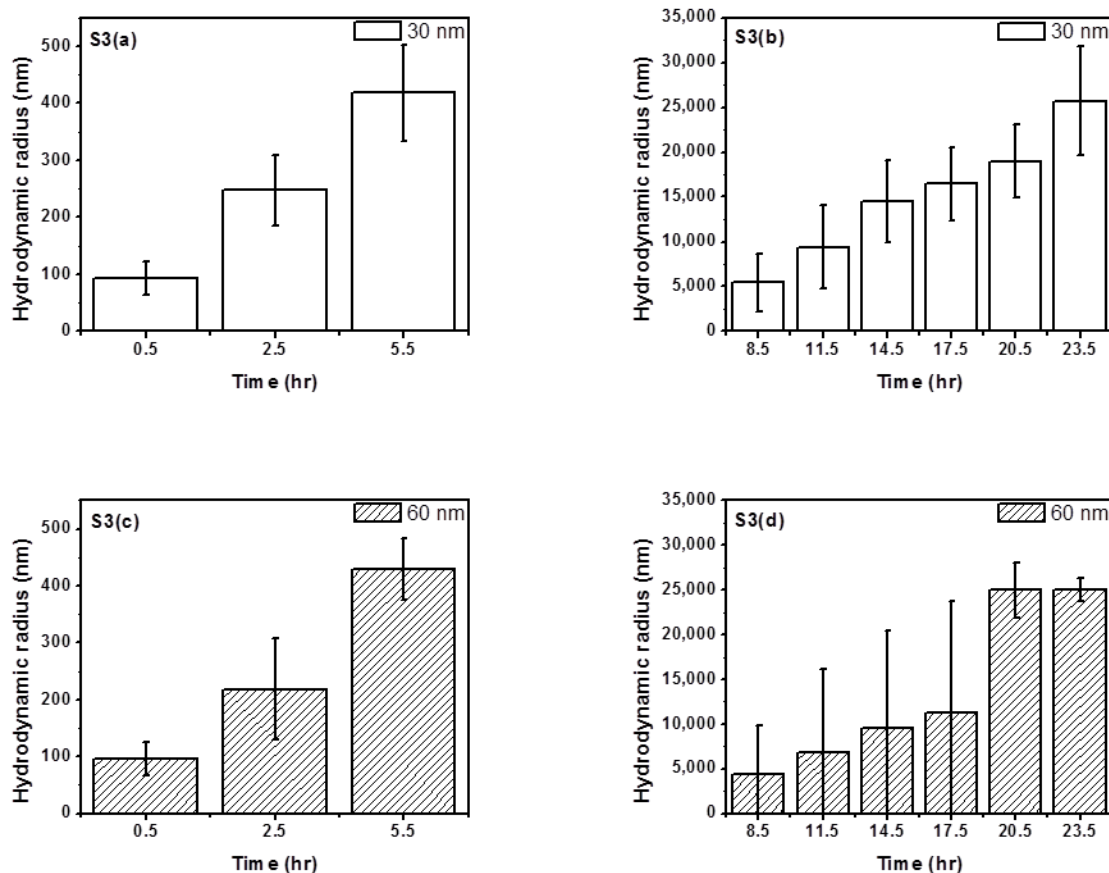
Figure S3. Aggregation Trends over Time for the 30nm and 60 nm AuNPs. Average hourly particle size for 0-6 hours (a) and (c) and 7-24 hours (b) and (d) for 30 and 60 nm, particles respectively. Error bars represent one standard deviation for average size of particles measured for that hour.

Genes Commonly and Uniquely Changed as a Result of Treatment with Gold Nanoparticles
Tables S2 and S3 list the genes commonly changed as a result of treatment with AuNPs including gene IDs, degree of upregulation or down regulation, function and location within the cell.

***Table S2. Genes Commonly Changed as a Result of Treatment with Gold Nanoparticles.
Selected genes significantly changed following exposure to AuNPs and possible molecular
consequences of regulation.***

Gene ID	Name	Response	Function	Location
BNIP3	BCL2/adenovirus E1B 19kDa interacting protein 3		apoptosis; ROS metabolic processes	cytoplasm
CD44	CD44 molecule (Indian blood group)		barrier disruption and inflammation	plasma membrane
CTTN	Cortactin		organizing the cytoskeleton and cell adhesion structures of	actin filaments; plasma membrane
DCN	Decorin		growth, differentiation, adhesion	extracellular space
DSG4	Desmoglein 4		differentiation, adhesion, proliferation	plasma membrane
EPHA4	Ephrin receptor A4		signal transduction	plasma membrane
EPPK1	Epiplakin 1		stress response, structural organization	cytoplasm
IL6ST	interleukin 6 signal transducer (oncostatin M		signal transduction	extracellular space; plasma membrane
ITGB1	integrin, beta 1		adhesion, tissue repair, immune response	plasma membrane
JAK1	Janus kinase 1		signal transduction	nucleus; cytoplasm
MBNL1	muscleblind-like		differentiation, regulation of mRNA splicing	Cytoplasm, Nucleus
MBNL2	muscleblind-like 2		mRNA processing; regulation of RNA splicing	cytoplasm, nucleus
NRG1	neuregulin 1		cell to cell signaling	extracellular space; nucleus; plasma membrane
OSMR	oncostatin M receptor		inflammation; cell signaling	plasma membrane
PI3K	phosphoinositide-3-kinase		apoptosis, proliferation, differentiation	cytoplasm
PIK3r1	phosphoinositide-3-kinase, regulatory subunit 1		signal transduction	cytoplasm
RASAL2	RAS protein activator like 2		signal transduction	intracellular
RhoA	RAS homolog member A		stress fiber formation	plasma membrane
S100A8	S100 calcium binding protein A8		inflammation	cytoplasm
S100A9	S100 calcium binding protein A9		hyper-proliferation of keratinocytes	nucleolus, cytoplasm
SCAMP1	Secretory carrier membrane protein 1		cell surface recycling; response to insult	cytoplasm
STAT1	signal transducer and activator of transcription 1		transcription activators; response to stimuli	nucleus; cytoplasm
TGFBR	transforming growth factor, beta receptor 1		signal transduction	plasma membrane

Table S3. Genes Uniquely Changed by Different Sizes of AuNPs.

Gene ID	Name	Response	Function	Location
30nm Au NP				
PTGER3	prostaglandin E receptor 3		ligand-dependent nuclear receptor activity; G-protein coupled receptor activity;	Plasma Membrane
60nm Au NP				
MDFIC	MyoD family inhibitor domain containing		activation of JUN kinase activity; regulation of Wnt receptor signaling pathway	Cytoplasm, nucleoli
RPH3A	rabphilin 3A homolog (mouse)		intracellular protein transport	Plasma Membrane
SEMA5B	sema domain, seven thrombospondin repeats (type 1		cell differentiation and development	Plasma Membrane
NDUFA11	NADH dehydrogenase (ubiquinone) 1 alpha subcomplex, 11, 14.7kDa		electron transport chain	Cytoplasm, mitochondri
PIP	prolactin-induced protein		actin binding; protein binding	Endoplasmi c Reticulum,
TCEANC	transcription elongation factor A (SII) N-terminal and central domain		transcription; regulation of transcription from RNA polymerase II promoter	Unknown
EML2	echinoderm microtubule associated protein like 2		proteolysis	Cytoplasm, microtubule
MUC8	mucin 8			Extracellular Space
CCDC56	coiled-coil domain containing 56			Unknown
CAPN2	calpain 2, (m/II) large subunit		response to hypoxia	Cytoplasm, Endoplasmi
STAT5B	signal transducer and activator of transcription 5B		response to hypoxia; JAK-STAT cascade; cytokine-mediated signaling pathway	Cytoplasm, Nucleus
DIAPH1	diaphanous homolog 1 (Drosophila)		actin cytoskeleton organization; actin filament polymerization	Cytoplasm, Plasma
SLFN5	schlafen family member 5		cell differentiation	Nucleus
CSNK1G1	casein kinase 1, gamma 1		protein amino acid phosphorylation; Wnt receptor signaling pathway	Cytoplasm
UGGT1	UDP-glucose glycoprotein glucosyltransferase 1		protein amino acid glycosylation; 'de novo' posttranslational protein folding	Cytoplasm, Endoplasmi
C5ORF41	chromosome 5 open reading frame 41		regulation of transcription, DNA-dependent	Unknown
TPM4	tropomyosin 4		response to oxidative stress	Cytoplasm, nuclear

B. Supplemental Information:
Relationship Between Physicochemical Properties and Nanotoxicity of CuNPs Nanoparticles

Dynamic Light Scattering (DLS):

Particle solutions were prepared and analyzed as previously described (Murdock et al., 2008). Briefly, solutions of Cu particles in DMEM/F12 cell culture media were made at 50 µg/mL of Cu particles, immediately analyzed for initial agglomerate sizes at 0 h, and then incubated at 37°C for 3 h to observe

alterations in agglomerate size in solution. Data are presented as the most prevalent agglomerate size over 3 h based on scattering intensity. Notice that Cu 480 has some primary sized ~500nm Cu NPs at the 0 h time point compared to Cu 90, which contains agglomerates of Cu NPs immediately after preparation >600nm in size (Fig S1).
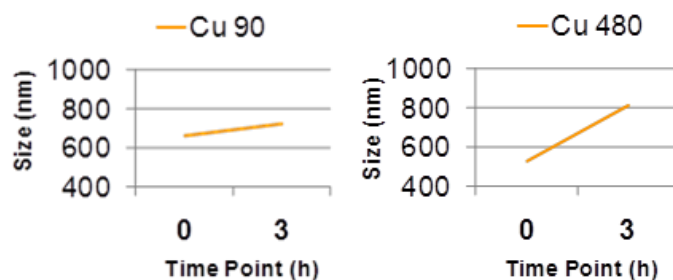

Figure S1. Dynamic light scattering of Cu NPs under cell culture conditions and over the duration of the dosing period (0-3 h).

Acellular ROS:

In order to measure the amount of ROS generated by Cu NPs independently of the cellular system, an acellular ROS was performed as described in Braydich-Stolle et al., 2009 and Venkatachari et al. 2005. The ROS probe was made by deacetylating the 2',7'-dichlorofluorescein diacetate (DCFH-DA) probe in NaOH. Immediately prior to analysis, horseradish peroxidase (HRP) reagent was added to the DCFH-DA solution. To measure ROS, the DCFH-HRP probe was added to different concentrations of nanoparticles in cell culture media and incubated at 37°C for 30 min. The plate was then read on a BioTek Synergy HT microplate reader at a 485 nm excitation wavelength and a 528 nm emission wavelength. The data presented below in Figure S2 demonstrate a baseline amount of ROS produced by Cu NPs after a very short time point of 30 min, which is significantly reduced upon the addition of 25 µM Dynasore.
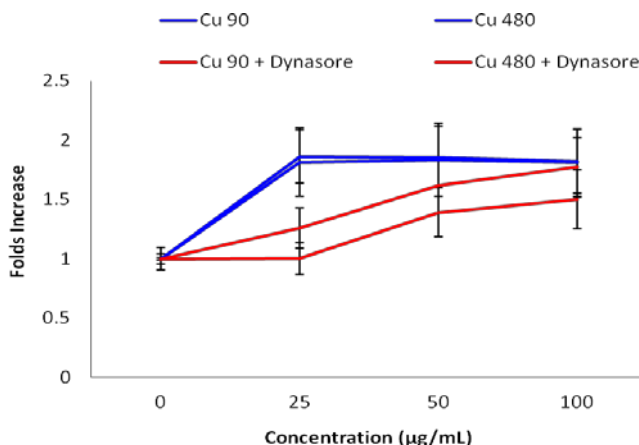

Figure S2. Acellular ROS data demonstrating a quenching effect after addition of 25 µM Dynasore to solutions of Cu NPs under cell culture conditions (i.e., in cell culture media, incubated at 37°C). There is a significant decrease in acellular ROS produced by 25 µg/mL of Cu 90 and Cu 480 when Dynasore is added compared to the control (paired t-test one-tailed, $p < 0.05$).

Cell Culture and Related Experiments:

Endocytosis Inhibitor Dynasore:

In this study, murine neuroblastoma (N2A) cells were pre-treated with 25 µM Dynasore for 1 h followed by 3 h of exposure to Cu NPs. This concentration was chosen based on literature values and control experiments. In these control experiments, we collected cell viability data in the N2A cell line after pre-treatment with various concentrations of Dynasore (0, 10, 25, 50 µM) for 1 h, followed by incubation under control conditions (dosing cell culture media without Cu NPs) for 3 h. High cell viability was maintained until the dose of 50 µM, which was significantly lower than the control (as assessed with the MTS assay, described below; Fig S3). By comparison, continuous incubation of the cells with Dynasore for 3 h led to significant decreases in cell viability at the lower concentration of 25 µM. In fact, continuous co-incubation of the cells with 25 µM Dynasore and Cu NPs led to further decreases in viability compared to the Cu NPs alone at the higher concentrations of 50-100 µg/ml (Fig S4). Therefore, the pretreatment methodology was a critical component of the rescue effect and is consistent with experiments conducted by other groups (Macia et al., 2006)(Newton et al., 2006)(Martinez-Argudo and Jepson 2008)(Gratton et al., 2008)(Jiang et al., 2010)(Soriano et al., 2010).
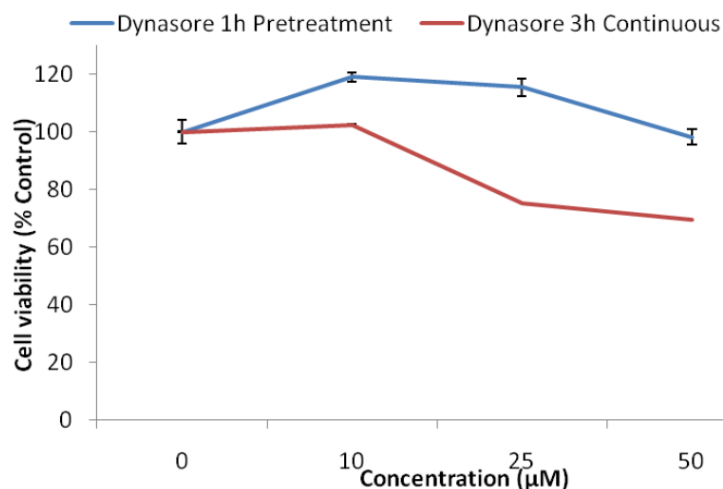

Figure S3. Cell viability for different concentrations of Dynasore in N2A cells assessed with the MTS assay. There was no significant difference for 25 µM Dynasore pretreatment for 1 h compared to the control whereas continuous incubation led to significant decreases in cell viability at concentrations >25 µM (paired t-test two-tailed, $p < 0.05$).
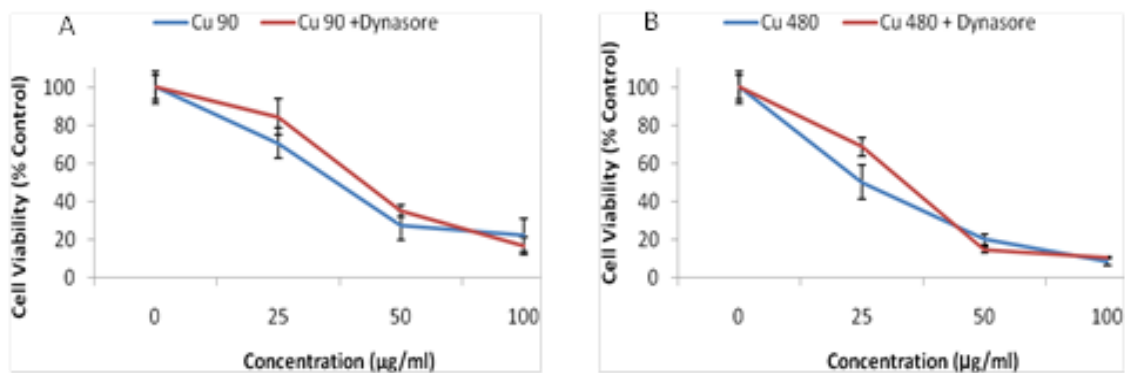
Figure S4. Cell viability data demonstrating a lesser degree of cell rescue by 25 µM Dynasore under co-incubation conditions for cells exposed to (A) Cu 90 and (B) Cu 480 at concentrations from 25-100 µg/ml over 3 h of continuous exposure.

MTS Assay for Mitochondrial Function:

In addition to cellular experiments presented in the main text of the paper (Figure 2A-B), we demonstrated that cells exposed to the soluble copper salt ($CuCl_2$) for 3 h could be rescued with 25 µM Dynasore pretreatment for 1 h (Fig S5).
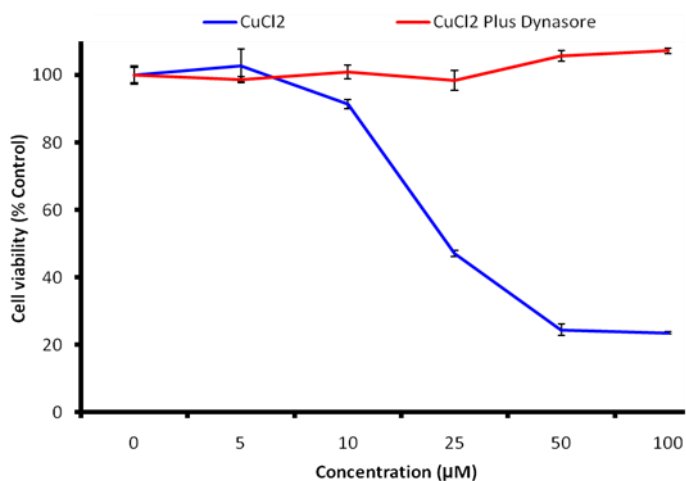
Figure S5. Dose-dependent cell viability of soluble copper salt sample ($CuCl_2$) representative of Cu ions in N2A cells assessed with the MTS assay. All samples pre-incubated with 25 µM Dynasore produced significantly greater viability results compared to cells continuously incubated with $CuCl_2$ (paired t-test two-tailed, $p < 0.05$.)

Cellular Reactive Oxygen Species (ROS):

The generation of intracellular reactive oxygen species (ROS) was determined using the fluorescent probe 2,7-dichlorohydrofluorescein diacetate (DCHF-DA) under a light controlled environment as described by Wang and Joseph (1999) with minor modifications as previously described by Hussain and Frazier (2002). The reactivity of the DCFH probe was evaluated with the positive control, hydrogen peroxide, by serial dilutions of stock 30% H_2O_2 (Sigma) in dosing media (Fig S6).
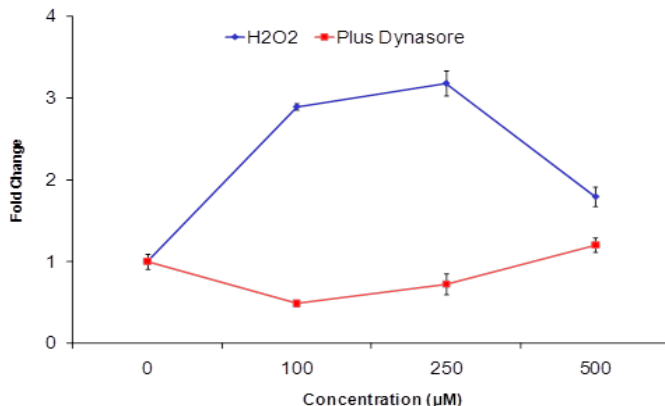
Figure S6 Dose-dependent increase in ROS production with the positive control hydrogen peroxide (H_2O_2) and demonstration of ROS quenching with 25 µM Dynasore pretreatment for 1 h. ROS production was significantly reduced at all H_2O_2 concentrations following the addition of Dynasore (paired t-test one-tailed, $p < 0.05$).

High-Performance Liquid Chromotography (HPLC):

Solutions were prepared and incubated at 5% CO_2 and 37ºC in dosing media to simulate the potential reaction conditions during chemical bio-modulation. Samples were analyzed using Zorbax XDB-C_{18} columns and the Agilent 1100 series liquid chromatography system coupled with UV detection. The mobile phases were A) water with 0.1& Trifluoro acetic acid (TFA) and B) 100% methanol with 0.1% TFA, with an initial concentration of 100% A increasing up to 100% B in 40 minutes. Detection was carried out with UV at 254 nm. Dynasore was identified using from serial standard dilutions ranging from 1-500 µM (Fig S7C). Representative HPLC spectra for the 10 µm and 25 µM Dynasore samples are shown in Figure S7A and S7B, which demonstrate a peak at ~20.64-20.67 min.
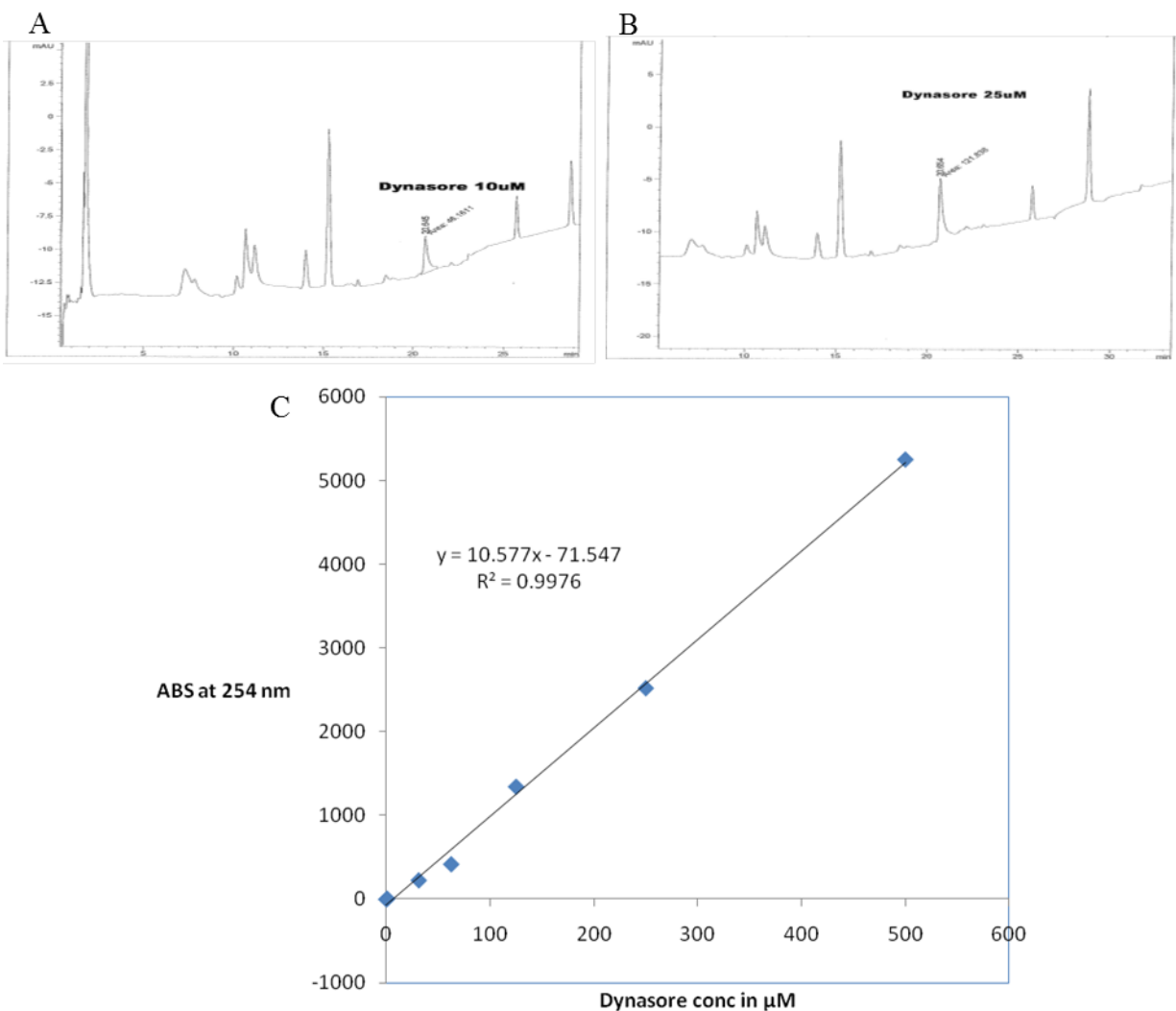
Figure S7. HPLC spectrographs for (A) 10 μm and (B) 25 μM Dynasore and (C) standard dilution graph for Dynasore obtained at peak value of 20.64-20.67 min.

Background spectra were taken of the cell culture media and each of the particles/ions in order to ensure that the Dynasore peak was not being affected by the mere presence of other chemicals but instead an actual chemical interaction.
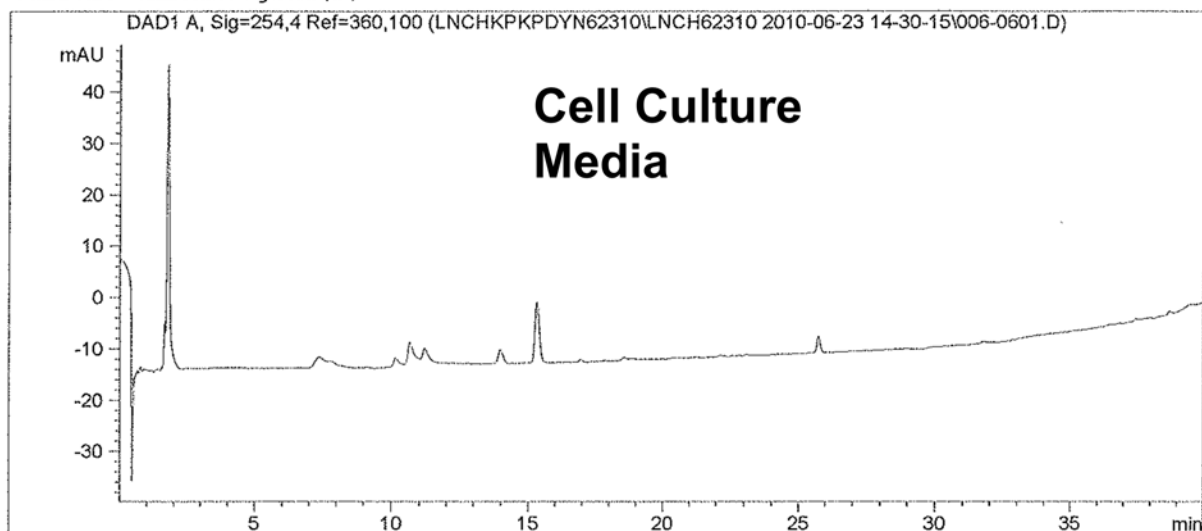
Current Chromatogram(s)

DAD1 A, Sig=254,4 Ref=360,100 (LNCHKPKPDYN62310\LNCH62310 2010-06-23 14-30-15\006-0601.D)

Cell Culture Media

Figure S8. HPLC spectrograph for cell culture media (DMEM/F12 + 1% penicillin/streptomycin). Notice there is no peak near that of Dynasore (~20.64-20.67 min).
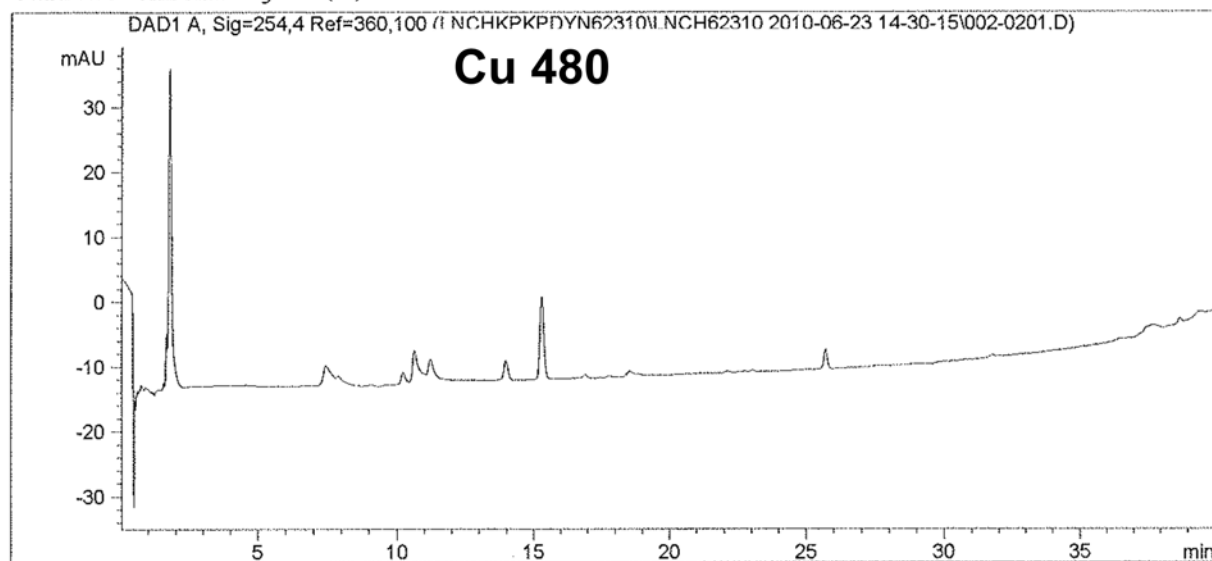
Current Chromatogram(s)

DAD1 A, Sig=254,4 Ref=360,100 (LNCHKPKPDYN62310\LNCH62310 2010-06-23 14-30-15\002-0201.D)

Cu 480

Figure S9. HPLC spectrograph for Cu 480 in cell culture media(DMEM/F12 + 1% penicillin/streptomycin). Notice there is no peak near that of Dynasore (~20.64-20.67 min).
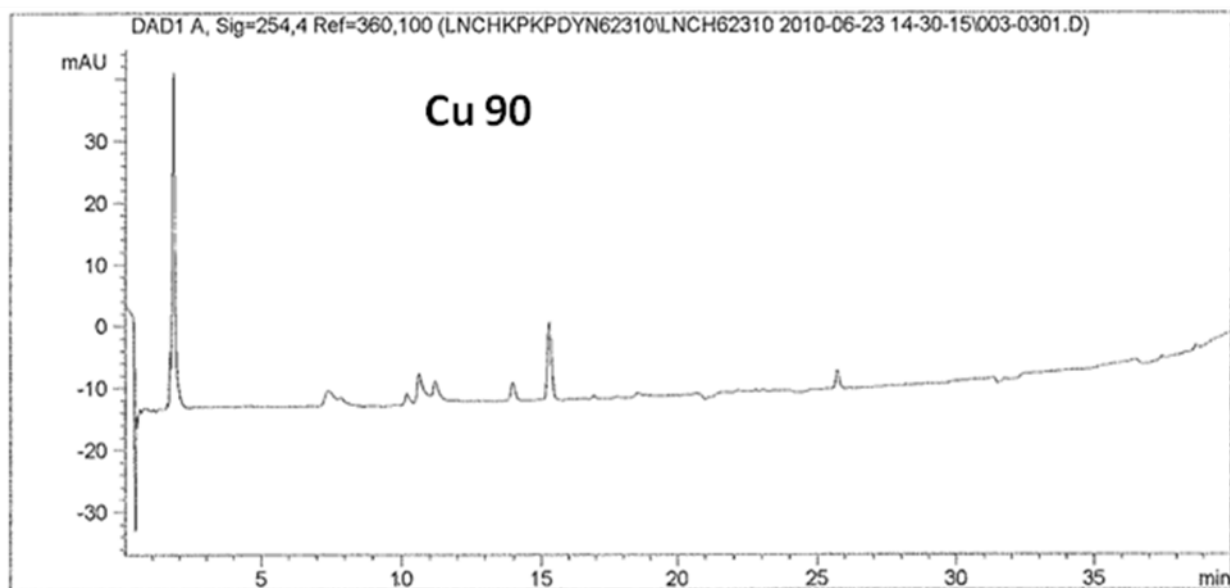
Figure S10. HPLC spectrograph for Cu 90 in cell culture media (DMEM/F12+1%penicillin/streptomycin). Notice there is no peak near that of Dynasore (~20.64-20.67 min).
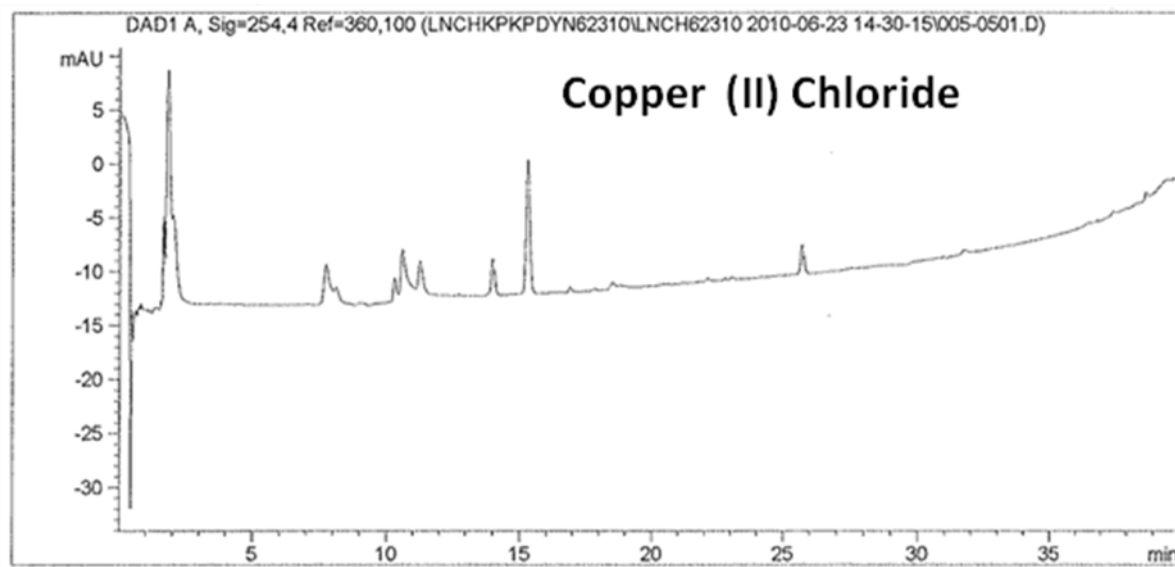

Figure S11. HPLC spectrograph for $CuCl_2$ in cell culture media (DMEM/F12 + 1% penicillin/streptomycin). Notice there is no peak near that of Dynasore (~20.64-20.67 min)